DOCTOR OF SCIENCES

Fundamental study of weak values and post-selected measurements from geometry and quantum foundations to quantum information and open systems

Ballesteros Ferraz, Lorena

Award date:
2023

Awarding institution:
University of Namur

Fundamental study of weak values and post-selected measurements: from geometry and quantum foundations to quantum information and open systems

Lorena Ballesteros Ferraz

A thesis submitted in fulfillment of the requirement of the degree of Doctor in Science.

Members of the jury:
Prof. Alexandre Mayer (President)
Prof. Pérola Milman
Prof. Alexandre Matzkin
Prof. John Martin
Prof. Dominique Lambert
Prof. Timoteo Carletti (Co-supervisor)
Prof. Yves Caudano (Supervisor)

Department of Physics
University of Namur
Namur, Belgium
Public defense - 13th of September 2023

Abstract

The second quantum revolution has arrived, and quantum physics is revealing an increasing number of practical applications every day. At the heart of quantum physics lies a foundational question: the measurement problem. What exactly happens when we measure quantum systems? Despite the fact that quantum theory provides a framework for measurements, many scientists and philosophers continue to debate the consequences of measuring to this day.

The focus of this thesis is on weak measurements—a type of quantum measurement where the interaction strength between the measuring device and the system being studied is very small. After the weak interaction, post-selection takes place, requiring a projective measurement and filtering on the desired final state. Ultimately, the shift in the ancilla's wavefunction is proportional to the weak value—a complex and unbounded number. In recent years, weak measurements have garnered significant attention due to their amplification power and fundamental properties.

In this study, we specifically focus on the polar description of weak values. Initially, we delve into the geometrical properties of weak values. The argument of the weak value corresponds to a geometric phase associated with the symplectic area of a triangle formed by the geodesics between the pre-selected state, a state involving the observable, and the post-selected state. To enhance visual comprehension, we also apply the Majorana description to the three states involved in the weak value. Our analysis shows then that the argument of the weak value is related to the sum of two solid angles on the Bloch sphere.

Next, we examine the modulus of weak values. We demonstrate that weak values can be expressed as the expectation value of a non-normal operator. We prove that weak values can differ from the observable's eigenvalues only if the operator is non-normal. Moreover, we establish strong correlations between the Henrici departure from normality—a parameter that indicates how far a matrix deviates from normality—and the modulus of the weak value in the strong amplification regime. These findings shed further light on the nature of weak values and their relationship with non-normal operators.

Looking at the weak value from a different angle, we can express it as the expectation value of the observable using a pseudo-Hermitian projector. We further demonstrate that, by modifying the Hilbert space standard metric, weak values can be described as expectation values in an indefinite metric space, where the metric has signature $(-1,1,\ldots,1)$. We establish a link between this space and non-classical logics and find that the emerging logic is paraconsistent and paracomplete. These new insights provide a fresh perspective that may inspire further research in the field of quantum foundations.

In quantum mechanics, a state can never be truly isolated and constantly interacts with its environment. In this study, we explore the effects of weak measurements with dissipation between the weak interaction and post-selection. Our investigation reveals that as the dissipation duration increases towards infinity, weak values tend to the expectation value of the observable in the pre-selected state. However, we observe anomalous weak values, even at infinite dissipation time, in cases where the ground state is degenerate. By examining the system at short dissipation times with weak measurements in the amplification regime, we can extract valuable information about the dissipative dynamics, including the dissipation rate and whether the system is Markovian or non-Markovian.

Quantum computing is among the most sought-after applications of quantum physics. In this study, we explore a protocol for implementing quantum algorithms using modular values. Specifically, we apply this protocol to the Deutsh-Jozsa algorithm, the Grover algorithm, and the phase estimation protocol. To assess the feasibility of our approach, we report experimental results obtained from the IBM quantum computer.

In summary, weak measurements hold great promise for both their amplification properties and their potential to deepen our understanding of fundamental quantum properties. We believe that our work will serve as a foundation for future studies exploring the polar description of weak values and their application to quantum foundations, as well as investigations into the effects of dissipation on weak measurements. Additionally, our exploration of modular values in quantum computing holds significant potential for advancing the field and driving progress towards practical quantum technologies.

Personal and original contributions

Chapter 2 – Introduction to quantum measurements

- Original idea and execution: Real weak values of opposite sign with their respective expectation values are proportional to the negative Kirwood-Dirac pseudo-probabilities, which are connected to non-classical states.

Chapter 4 – Geometrical interpretation of the argument of weak values

- Original idea and execution: The foundational notion and subsequent execution involve the observation that the weak value of any operator maintains a proportional relationship to the weak value of a highly specific projector.
- Computation of the formulas depicting the argument of weak values, framed within the context of vectors in the complex projective space. Help in the interpretation of these formulas as a symplectic area, as they are associated with Bargmann invariants.
- Original idea and execution: Study of two-level observables on the Bloch sphere.

Chapter 5 – Geometry of N-level operators weak values on the Bloch sphere

- Original idea and execution: Studying the argument of the weak value on the Bloch sphere by applying Majorana representation thanks to connection of weak values of arbitrary observables to weak values of projectors.
- Original idea and execution: Study of the spin-1 operator.
- Original idea and execution: Study of entanglement applying Majorana representation.

Chapter 6 – Revisiting weak value from a non-normal perspective

- Original idea and execution: Relationship between weak values and non-normality through the Henrici departure from normality.

- Numerical study of the correlation between the Henrici departure of normality and modulus of the weak value.
- Original idea and execution: Study of the nilpotent point, the derivatives of the weak value and the Henrici departure from normality, and study of the point of the maximum of weak values and nilpotent point.

Chapter 7 – Quantum weak values: paraconsistency and paracompletness

- Calculations of the properties of weak values as expectation values using an η-Hermitian pseudo-projectors.
- Calculation of the subspaces in the three-box paradox.
- Original idea and implementation: Change of basis of the boxes in the three-box paradox and study of this new basis in terms of a parameter.
- Helping in the interpretation.

Chapter 8 – Weak measurements in dissipative quantum systems

- Original idea to study weak measurements under dissipation.
- Analytical calculations of the weak measurement under dissipation.
- Original idea and execution: limit of the weak value when dissipation tends to infinity for degenerate and non-degenerate ground states.
- Original idea and execution: Measuring the amplified dissipation rate and differentiating Markovianity from non-Markovianity.

Chapter 9 – Exploiting modular values in quantum algorithms

- Original idea to use modular values to tackle quantum algorithms.
- Choice of the studied quantum algorithms.
- Designed of the model to implement quantum algorithms using modular values.
- Analytical calculations for each algorithm and implementation of the Deutsch-Jozsa algorithm on the IBM Quantum Computer.

Publications linked to this thesis

- **BALLESTEROS FERRAZ, Lorena**; LAMBERT, Dominique L.; CAUDANO, Yves. Geometrical interpretation of the argument of weak values of general observables in N-level quantum systems. Quantum Sci. Technol. 7 045028 (2022)
  This publication is linked to Chapter 4.

- **BALLESTEROS FERRAZ, Lorena**; MOUCHET, Sébastien R.; MUOLO, Riccardo. Let "Matildas" get the place in science classes that they deserve. Europhysics News 53 (5), 11 (2022)

- **BALLESTEROS FERRAZ, Lorena**; CAUDANO, Yves.; MARTIN, John. On the relevance of weak measurements in dissipative quantum systems, pre-print arXiv 2308.00722 (2023). Under review.
  This publication is linked to Chapter 8.

- **BALLESTEROS FERRAZ, Lorena**; MUOLO Riccardo; CAUDANO, Yves; CARLETTI, Timoteo. Effects of non-hermicity and non-normality on quantum weak values, pre-print arXiv 2306.01392 (2023). Under review.
  This publication is linked to Chapter 6.

- **BALLESTEROS FERRAZ, Lorena**; LAMBERT, Dominique L.; CAUDANO, Yves. Geometrical interpretation of the argument of Bargmann invariants and weak values in N-level quantum systems using Majorana representation, pre-print, arXiv 2211.05692 (2022). Under review.
  This publication is linked to Chapter 5.

- **BALLESTEROS FERRAZ, Lorena**; CARLETTI, Timoteo.; CAUDANO, Yves. Tackling quantum algorithms using modular values. In preparation.
  This publication is linked to Chapter 9.

Acknowledgment

First and foremost, I would like to express my sincere gratitude to all the members of the WeaM project for providing me with the invaluable opportunity and means to pursue my PhD thesis.
I am thankful to my supervisor, Yves Caudano, for his meticulous examination of my work and for granting me the freedom to explore my own research interests.
I would also like to extend my appreciation to the entire jury for dedicating their time to read and provide feedback on this manuscript.
Special thanks go to the collaborators whose insights and support have made this journey a little bit easier: Dominique Lambert, John Martin, Riccardo Muolo, and Timoteo Carletti. I would particularly like to thank Dominique Lambert for reviewing the work in the field of logic in Chapter 7.
I am also grateful to all the members of the LLS research unit for engaging great conversations, with special mentions to Muriel Lepère and Francesca Cecchet, who provided support during my lowest moments. I would like to extend my thanks to the few office mates with whom I had the opportunity to share moments: Mathilde, Chiara, and Freeda.
During the past year, I had the privilege of participating in a research exchange at the University of Liège within John Martin's group. I would like to express my thanks to him and all the group members—Jerôme, Baptiste, François, Eduardo, and Lukas—for their warm welcome, stimulating discussions, and showing me the dynamics of a collaborative research group.
One project that holds a special place in my heart is Women and Girls in Science at UNamur. I am deeply grateful to all my friends and colleagues who joined me on this journey: Aish, Riccardo, Seb, Matteo, Charlotte, Manel, Hala, Coraline, and Karin. This project truly illuminated my PhD experience.
Life in Namur as a non-French speaker has not always been easy. I would like to thank all the international researchers who made these four years a joyful adventure. I especially want to mention Aish, with whom I shared many great moments during the Covid-19 period.
My deepest gratitude goes to my family, particularly my mum, whose unwavering support has made it possible to achieve the distinction of having the first doctor in our family.
I would like to extend my heartfelt appreciation to my partner, Seb, for consistently being there for me, unwaveringly supportive during both the highs and lows of this journey, and steadfastly standing by my side.
Subsequently, I would like to acknowledge and thank all the individuals who have fought, are fighting, and will continue to fight for amplifying the voices of minorities and striving to create a

world where everyone has their rightful place. I extend a special thanks to the pioneering women who fought for recognition in academia and served as examples, making me realize that a PhD was within my reach. Without them, I would not be here today.
Last but undoubtedly of utmost importance, I am profoundly grateful to the European society for making my educational journey possible through the funding provided by taxes and the fellowships I have been fortunate to receive, starting from my final years of secondary school up to this PhD. Without their generosity, I would have never had the opportunity to reach the position I am in today.
Obrigada, gracias, gràcies, merci, thank you!

Only with the contributions of people from all backgrounds, genders, and sexual orientations science will advance. For a diverse and inclusive scientific future!

Quantum weak values: all you can do!

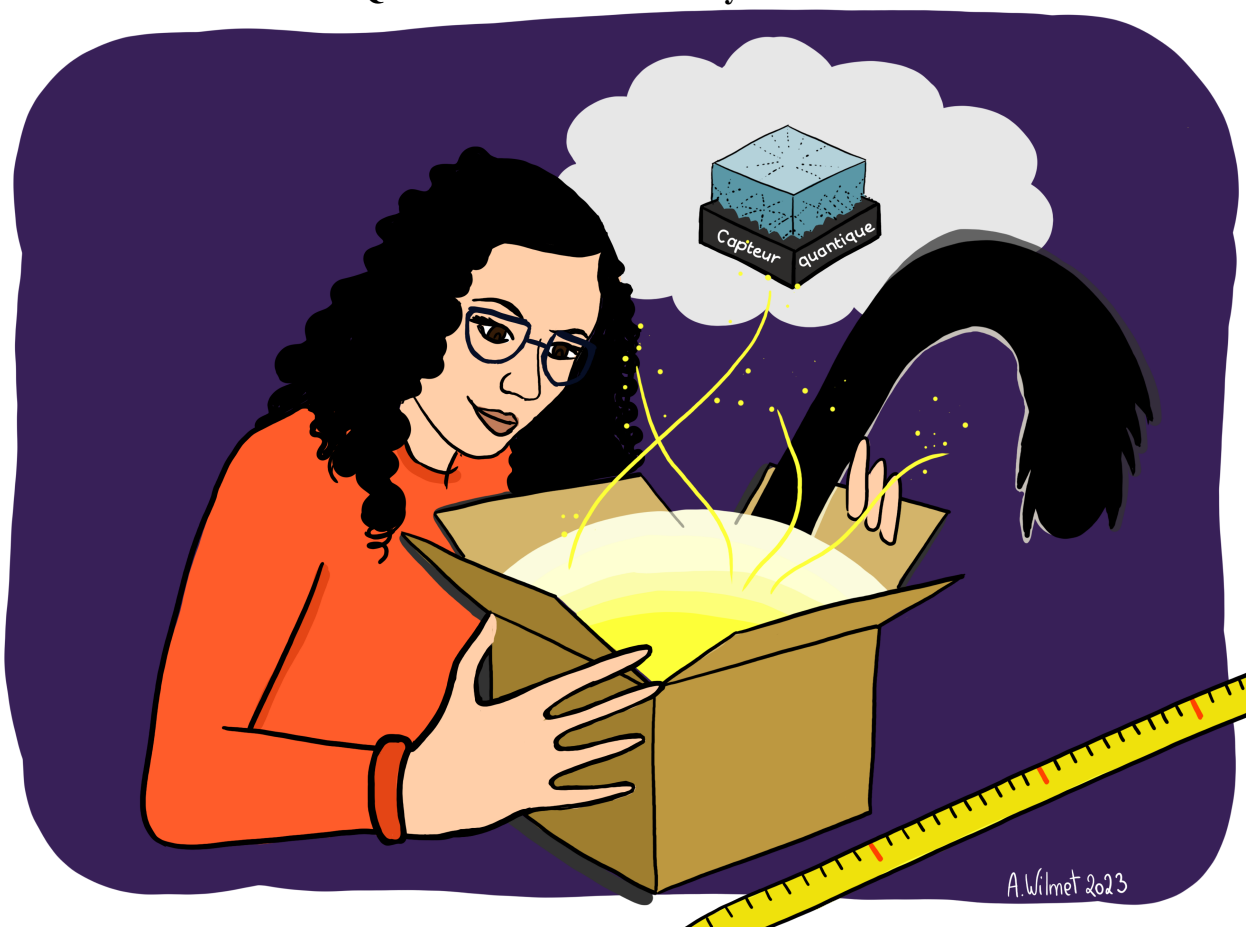

Contents

Chapter 1

Introduction

Quantum mechanics is a field with enormous potential. Although it initially began as a fundamental investigation, it has since yielded a plethora of possible applications [1, 2, 3], including the development of quantum clocks [4] and the highly sought-after quantum computer [5]. Additionally, quantum physics has been successful in making very precise predictions, particularly in the realm of quantum electrodynamics [6]. At the heart of quantum mechanics lies the issue of quantum measurement [7], and with it, the foundational question of how to interpret it [8, 9, 10]. The simplest type of measurement in quantum mechanics is the projective measurement, which is an ideal irreversible measurement that destroys all coherences and reduces the initial state of the system to an eigenvector of the measured observable [11]. In a projective measurement, the measuring device is typically treated classically.

Nonetheless, projective measurements are not the sole type of measurements in quantum physics. The von Neumann protocol, which involves describing both the measuring device (or ancilla) and the system using quantum states, offers an alternative approach to modeling measurements. This method can describe any type of measurement, ranging from weak (with a very small interaction strength) to projective (with an interaction strength that is very large) [12]. To further elaborate on this protocol, we can examine the Stern-Gerlach experiment [13]. Historically, this experiment was designed to determine the continuous or discrete character of spin. The experiment involves a beam of silver atoms, prepared in an oven, which passes through a magnet that generates a variable magnetic field, Fig. 1.1. This field couples the position of the beam with the spin. By detecting the position of the beam on the screen, information about the spin (up or down) can be obtained, Fig. 1.1. The magnetic field interaction can be modeled using a unitary operator. Depending on the interaction strength, which is determined by the intensity of the magnetic gradient, the degree of separation between the beam of spin up and spin down can vary. In the case of very weak interaction strength, the separation may not be easily observable, and the beam after interaction would remain almost unperturbed.

When the interaction strength in the Stern-Gerlach experiment is very weak, the quantum state after the experiment remains almost unperturbed. The shift between the spin states up and down is tiny, making it difficult to extract much information about the spin of the system. However, it is possible to obtain more information by applying a post-selection protocol known as a weak measurement, Fig. 1.2. This protocol consists of four steps: pre-selection of the system, weak interaction via a unitary operator, post-selection of the system, and finally, reading out the ancilla's

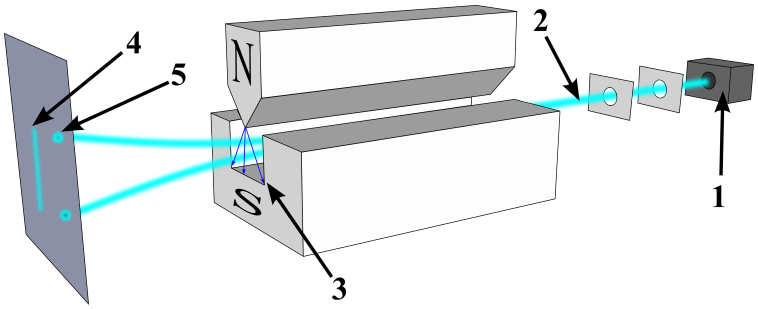

Figure 1.1: The Stern-Gerlach experiment involves a beam of silver atoms (2) that is first prepared in an oven (1) and then passed through a variable magnetic field (3). The beam ultimately reaches a screen, where the classical description predicts it will arrive in a vertical line (4). However, because spin is a quantum variable, the beam only reaches two points on the screen (5): they correspond to spin up and down. Reproduced from Tatoute, https://commons.wikimedia.org/wiki/File:Stern-Gerlach_experiment_svg.svg, accessed on the 20th of May 2023.

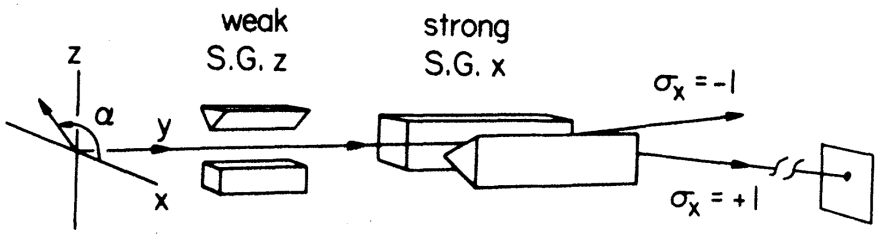

Figure 1.2: The weak measurement of the Stern-Gerlach experiment involves using two magnets. The first magnet couples the position and spin in the z direction weakly, while the second magnet post-selects the spin in the x direction as down. Reprinted from [17] with permission from The American Physical Society (APS).

wave-function, Fig. 1.2. In the Stern-Gerlach experiment, the weak interaction is achieved using a variable magnet field in the z direction, while the post-selection is performed using a variable magnetic field in the x direction. The ancilla's wave-function position is then measured on a screen, as shown in Fig. 1.2. The shift in the wave-function is proportional to a complex and unbounded number called weak value. The concept of weak measurements was first introduced in the late 1980s by Yakir Aharonov, David Albert, and Lev Vaidman to address fundamental questions and paradoxes in quantum mechanics [14]. In particular, weak measurements have shed light on the nature of quantum measurements and the role of the observer in the measurement process [15, 16]. Weak values are complex and unbounded numbers that are typically studied in terms of their real and imaginary parts, as it is most useful in experiments. However, like any other complex number, weak values can also be investigated in the polar representation, in terms of their modulus and argument. In this thesis, we focus on studying the argument of weak values for any N-level discrete observable, building upon previous results on the argument of weak values of projectors in two-level systems [18]. It was found that the argument of the weak value of a two-level projector describes a geometric phase that is associated with the solid angle on the Bloch sphere of the triangle formed by the pre-selected state, the weakly measured projector state, and the post-

selected state. We expand this work to N-level projectors and general observables, establishing a link between the argument of the weak value of an N-level projector and the third-order Bargmann invariant. Specifically, the argument of the weak value of an N-level projector is equivalent to the argument of the third-order Bargmann invariant involving the pre-selected state, the measured projector state, and the post-selected state. The third-order Bargmann invariant also describes a geometric phase, which is associated with the symplectic area of the geodesic triangle between the three quantum states in the complex projective space $\mathbb{C}\mathrm{P}^{N-1}$. As a result, we find that the argument of the weak value of any projector describes a geometric phase that is associated with the symplectic area of the geodesic triangle formed by the pre-selected state, the projector state, and the post-selected state in the complex projective space [19].

To tackle the general observable case, we showed that the weak value of any observable is proportional to the weak value of a projector that arises from the normalized application of the observable over the pre-selected state. The constant of proportionality between the weak value of the general observable and the one of the projector is real. Consequently, the argument of the weak value of any observable describes a geometric phase that is associated with the symplectic area of the triangle formed by the geodesics connecting the pre-selected state, the state obtained by applying the observable to the initial state, and the post-selected state in the complex projective space $\mathbb{C}\mathrm{P}^{N-1}$ [19].

Thanks to our study, we now have a complete understanding of the geometrical properties of the argument of weak values of general discrete observables. However, visualizing this geometry can be challenging in the general case. To address this, we can use the Majorana representation, which maps an N-level system state to $N-1$ qubit states, for the three projectors involved in the argument of the weak value. With this approach, the argument of the weak value of any observable can be expressed as the sum of $N-1$ arguments of weak values of qubit projectors. Each of these arguments of weak value of a two-level projector is associated with a solid angle on the Bloch sphere. Therefore, we can represent the argument of any weak value using $N-1$ solid angles on the Bloch sphere. Additionally, as weak values are invariant under unitary transformations, we can always transform any weak value to a three-level system weak value. Using this approach, we can represent the argument of any weak value as the sum of two solid angles on the Bloch sphere [20]. The choice between representing the weak value in the initial space ($\mathbb{C}\mathrm{P}^{N-1}$) or on the Bloch sphere by utilizing the Majorana representation depends on the specific problem at hand. In cases where the focus is on the N-level system, working in the initial space is necessary, even though visualization can be challenging. However, when visualization is crucial for understanding the system under study, the Majorana representation is the most suitable choice.

While the geometrical properties of the argument of weak values are interesting, most applications focus on the amplification power of weak values. To study amplification, it is best to examine the modulus of the weak value. In a typical weak measurement without post-selection, the resulting shift is proportional to the expectation value. However, when post-selection takes place after the weak interaction, the shift becomes proportional to the weak value. Consequently, the weak value replaces the expectation value. We can express the weak value as an expectation value of a non-Hermitian operator, which is not only non-Hermitian but also non-normal. This condition is stronger than simply being non-Hermitian because not all non-Hermitian operators are non-normal, but all non-normal operators are non-Hermitian. In this thesis, we demonstrate that the new operator must be non-normal to obtain a weak value that differs from one of the observable's eigenvalues. Additionally, we discovered that, for specific cases, the largest weak value is achieved

when the parameters exhibit the highest non-normality, as measured by the Henrici departure from normality [21].
Following a similar approach, by rewriting weak values as expectation values with a pseudo-Hermitian projector, instead of an expectation value of a non-Hermitian operator, allows us to investigate the weak value in a new space defined by the metric η under which the projector is Hermitian (actually, η-Hermitian). Interestingly, we found that any weak value can be described in an indefinite metric space, also known as a Krein space. This space can be linked to a paraconsistent and paracomplete logic, where a property and its negation can both be true, and a property with its negation might not necessarily encompass the whole space. This implies that a property or its negation (the logical union) might not necessarily hold true. Thanks to this description, we were able to provide a fresh perspective on the quantum three-box paradox.
Furthermore, quantum systems are inherently never completely isolated, and weak measurements are no exception as they interact with the surrounding environment. Therefore, it is crucial to study the effects of dissipation on weak measurements as it can destroy the anomalous properties of weak values. In this study, we investigate the behavior of weak values under dissipation and demonstrate that, regardless of the system, weak values tend to converge to the expectation value of the initial state under infinite dissipation duration, except in cases where the ground state is degenerate. Weak values can still exhibit anomalous properties even at infinite dissipation time under when degenerate fundamental states are present. Furthermore, we can use weak values in the amplification regime at short dissipation times to extract valuable information about the system's dynamics, such as the dissipation rate and whether the dynamics are Markovian or non-Markovian [22].
Moreover, quantum computing holds immense potential for advancing various fields, and weak values or modular values, related concept that arise when the operator is unitary, could potentially contribute to this progress. In this study, we propose a versatile configuration using modular values that can be applied to any algorithm that involves an oracle, which is a gate used to describe unknown operators in computing. In this case, the protocol consists of measuring the modular value of the oracle. To test the effectiveness of this protocol, we apply it to the Deutsch-Jozsa, Grover's algorithms, and the quantum phase estimation protocol. As a proof of concept, we implement the Deutsch-Jozsa algorithm on the IBM quantum computer, but our preliminary results do not indicate any significant advantage over traditional quantum algorithms. Nevertheless, we believe that exploring the potential of weak values in quantum computing can lead to exciting discoveries and applications in the future.
The thesis is structured as follows: Chapter 2 provides an introduction to weak measurements and their applications. In Chapter 3, we describe the properties of the N-dimensional quantum spaces and introduce the necessary mathematical tools to follow the thesis. Chapter 4 focuses on the geometrical interpretation of the argument of weak values in the complex projective space, while Chapter 5 provides a similar description but on the Bloch sphere. In Chapter 6, we investigate the non-normal properties of weak values, and in Chapter 7, we explore the connection between weak values and paraconsistent logic. Chapter 8 is devoted to the study of weak values under dissipation, while in Chapter 9, we apply modular values to quantum algorithms, including a general configuration that can be applied to any algorithm involving an oracle, such as the Deutsch-Jozsa and Grover's algorithms. Finally, in Chapter 10, we provide the conclusions and perspectives.

Chapter 2

Introduction to quantum measurements

Measurements play an indispensable role in many aspects of our daily lives. From determining the speed of a car to detecting cancer or monitoring oven temperature, accurate measurements are crucial. In scientific experiments, these same questions of what to measure and how to measure it arise. What type of microscope should be used? What information will it provide? Should the focus be on measuring particle size or density of particles? Obtaining precise and relevant information from the system under study is key to advancing scientific knowledge and discovery.
In classical systems, measuring a system is usually viewed as a technical challenge to be tackled. The main focus is often on improving the precision, speed, or signal-to-noise ratio of measuring devices, i.e., the quality, without much intrinsic philosophical consideration. For instance, when measuring the size of a particle, the instrument provides a measurement result with an uncertainty that is associated with the precision of the instrument. Importantly, the size of the particle does not typically change as a consequence of being measured.
In the quantum realm, the measurement process has been a fascinating and contentious issue, unlike its classical counterpart. Fundamentally, measuring a quantum system inevitably alters it. When starting with a state that is a linear combination of states in a given basis, after the measurement, the final state collapses into one of the eigenstates of the measured operator, destroying the superposition. This is a destructive measurement. The interpretation of this collapse and the measurement process has been a crucial question in the field of quantum foundations, and it has sparked a lot of debate [9, 10, 23].
Projective measurements, as described above, are considered ideal. Their typical description does not include the measuring device within the quantum formalism: only its effects on quantum states (the projection) are considered. However, they are not the only scheme available for measuring in quantum physics.
In this chapter, we aim to present an overview of the various types of measurements in quantum physics that are most relevant to our discussion. Although we do not aim to provide an exhaustive list, as there are numerous other measurement protocols in quantum physics [11, 24], we present some fundamental techniques. Firstly, we introduce the projective measurement and the POVM scheme. Subsequently, we explore measurement protocols that consider both the measuring device and the system, such as the von Neumann protocol. In the third section, we explain the basics of weak measurements, and in the fourth section, we derive the complete procedure of weak measurements. Finally, in sections 2.4 and 2.5, we introduce a few properties and applications of weak

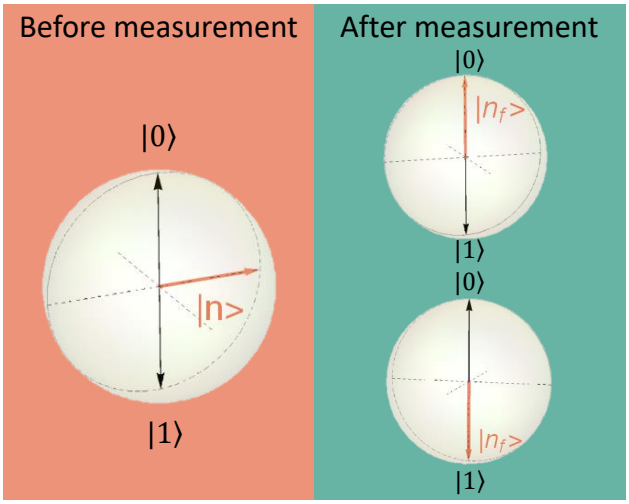

Figure 2.1: Representation on the Bloch sphere of the quantum state $\frac{1}{\sqrt{2}}(|0\rangle + |1\rangle)$ before the measurement and the states $|0\rangle$ and $|1\rangle$ after the projective measurement.

values.

2.1 Projective measurements

The projective measurement is the simplest type of measurement in quantum physics. This measurement is considered ideal and results in the collapse of the system into one of the eigenvectors of the observable being measured. For instance, suppose we have an atom initially in a linear combination of excited and ground states, represented as $|\psi\rangle = \frac{1}{\sqrt{2}}(|e\rangle + |g\rangle)$. Upon measuring the energy of the atom, the resulting state would be one of the two energy levels and not a superposition of both. The state is said to be completely collapsed. Fig. 2.1, depicts an example before and after the measurement on the Bloch sphere. The measurement in the basis $(|0\rangle, |1\rangle)$ collapses the state to one of the poles of the Bloch sphere. The Bloch sphere is introduced in section 3.1.
Let us delve deeper into the formal definition of projective measurements. In quantum mechanics, pure states of an N-level system can be represented as an N-component normalized complex vector in a given basis. However, not all quantum states are pure. Mixed states can be described using a density operator, $\hat{\rho} = \sum_i p_i |\phi_i\rangle \langle\phi_i|$, where $\sum_i p_i = 1$. An introduction to density operators can be found in appendix A. Observables in quantum physics are typically represented by Hermitian operators since their spectra should be real and the eigenstates orthogonal. Let us consider the operator $\hat{A}$ to be measured,

$$\hat{A} = \sum_i \alpha_i |a_i\rangle \langle a_i| , \tag{2.1}$$

where α_i are the eigenvalues of the operator $\hat{A}$ and $|a_i\rangle$ the orthonormal eigenvectors. We assume that the operator is non-degenerate.
When measuring the observable $\hat{A}$ in the state $\hat{\rho}$, the possible outcomes correspond to the eigenvalues of the operator $\hat{A}$, α_i, with probabilities,

$$P(\alpha_i) = \mathrm{Tr}\left(\hat{\Pi}_i \hat{\rho}\right), \tag{2.2}$$

where $\hat{\Pi}_i$ is the projection operator linked to the eigenstate $|a_i\rangle$, $\hat{\Pi}_i = |a_i\rangle \langle a_i|$.
The state of the system after the measurement is

$$\hat{\rho}_i = \frac{\hat{\Pi}_i \hat{\rho} \hat{\Pi}_i}{\mathrm{Tr}\left(\hat{\Pi}_i \hat{\rho}\right)}. \tag{2.3}$$

The expectation value of the observable $\hat{A}$ is

$$\langle \hat{A} \rangle = \mathrm{Tr}\left(\hat{A}\hat{\rho}\right), \tag{2.4}$$

for a more comprehensive elaboration on this formula, please refer to appendix A.
The projective measurement does not considered the measuring device. The measurement is strong and ideal - there is no error - the state is always completely collapsed. After the measurement, it is not possible to extract any more information from it. The maximum amount of information has already been extracted from the system and it cannot provide any further information.
The positive operator-valued measurement (POVM) is a generalization of the projective measurement. POVMs are defined by a set of operators, $\hat{F}_i$, where the operators are Hermitian and non-negative, and the set is complete,

$$\sum_i \hat{F}_i = \hat{I}, \tag{2.5}$$

where $\hat{I}$ is the identity operator. The probability to measure outcome i is

$$\mathrm{prob}\,(i) = \mathrm{Tr}\left(\rho \hat{F}_i\right). \tag{2.6}$$

The POVM framework doesn't directly yield the resultant state; rather, the specific measurement outcome, denoted as i, dictates the final state. Given an initial quantum state $\hat{\rho}$ and an outcome i, the ensuing quantum state is determined by the equation:

$$\hat{\rho}_{f_i} = \frac{\hat{M}_i \hat{\rho} \hat{M}_i^\dagger}{\mathrm{Tr}\left[\hat{M}_i \hat{\rho} \hat{M}_i^\dagger\right]}, \tag{2.7}$$

where $\hat{M}_i^\dagger \hat{M}_i = \hat{F}_i$.
Consequently, the final state remains dependent on the initial state, evading a complete collapse. This dynamic preserves more information post-POVM since the measurement process gathers less information. The POVM's advantageous features render it a prevailing choice in the realm of quantum information theory.

2.2 Von Neumannn protocol

Von Neumann developed a protocol for measuring properties of a quantum system that involves an ancilla-based approach [25]. The system and the ancilla (or measuring device) are both treated as quantum systems, and the protocol consists of three main steps, as shown in Fig. 2.2. Initially, the system is prepared in its initial state, and the ancilla's wave function is centered on zero in the position basis. Then, a unitary operator is applied to both the system and the ancilla, entangling the two components of the full system. Finally, the ancilla's wave function is readout, and the

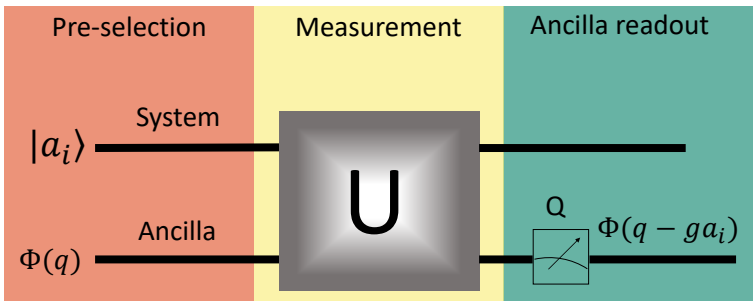

Figure 2.2: This figure illustrates the von Neumann protocol scheme, when the system's initial state is an eigenstate of the observable $|a_i\rangle$. The measurement process involves the use of a unitary operator entangling the ancilla and the system, and in the final step, the ancilla is read out to extract the corresponding eigenvalue.

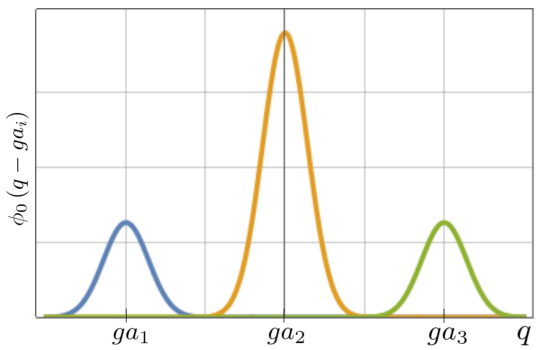

(a) The wave functions of shifted ancilla have been affected by a strong interaction, where the interaction strength ($g = 10$) far exceeds the width ($\Delta = 1$). The resulting eigenvalues are distinguishable, and include -1, 0, and 1.

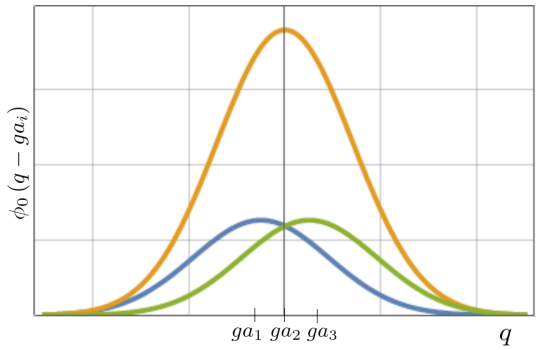

(b) The wave functions of shifted ancilla have been subjected to a relatively weak interaction strength ($g = 0.5$), which is small compared to the width ($\Delta = 1$). As a result, the wave functions cannot be distinguished after a single measurement.

Figure 2.3

wave function is shifted by an amount proportional to the eigenvalues of the observable to be measured. Depending on the interaction strength, denoted as g, the shifted wave functions may be fully distinguishable or not, as illustrated in Fig. 2.3. When the interaction strength times the eigenvalue is larger than the width of the measuring device, none of the shifted wave functions overlap (Fig. 2.3(a)), whereas if the interaction strength times the eigenvalue is smaller than the width of the the measuring device wave function, the shifts are not distinguishable (Fig. 2.3(b)). This protocol offers a measurement approach that covers a range of measurement strengths, from very weak (where the system is almost not perturbed) to ideal strong measurements.
Let us move to a detailed derivation of the protocol's procedure [12]. The ancilla state is described in the continuous space in terms of a wave function as,

$$\left|m^{(0)}\right\rangle = \int dq\,|q\rangle \left\langle q\middle|m^{(0)}\right\rangle = \int dq\,|q\rangle\,\phi_0(q)\,, \tag{2.8}$$

where the the wave function should be centered on 0. For example, the following function [26],

$$\phi_0(q) = \sqrt{\frac{1}{\sqrt{2\pi\Delta^2}} e^{-\frac{q^2}{2\Delta^2}}}. \tag{2.9}$$

The square of Eq. 2.9, the probability density $|\phi_0(q)|^2$, is a Gaussian function with width Δ. Considering that the observable to be measured is $\hat{A}$, the interaction Hamiltonian applied in the second step is

$$H_{\text{int}} = \gamma \hat{A} \otimes \hat{P}, \tag{2.10}$$

where γ is the coupling constant and $\hat{P}$ is the meter momentum, conjugate to the meter position $\hat{Q}$. As the measuring time slot δt is very short, the free evolution Hamiltonian of both the system and the ancilla can be neglected and the unitary operator governing the dynamics of the system is

$$\hat{U} = e^{-i\int_0^{\delta t} dt \hat{H}_{\text{int}}} = e^{-ig\hat{A}\otimes\hat{P}}, \tag{2.11}$$

where $g = \gamma\delta t$ and $\hbar = 1$. Considering the initial state of the system to be an eigenstate of the observable to be measured, $|a_i\rangle$, the total state after the application of the unitary operator is, $|a_i\rangle \otimes \left|m^{(0)}\right\rangle \rightarrow |a_i\rangle \otimes \left|m^{(i)}\right\rangle$

$$|a_i\rangle \otimes \left|m^{(i)}\right\rangle = \hat{U}\left(|a_i\rangle \otimes \left|m^{(0)}\right\rangle\right) = e^{-ig\hat{A}\otimes\hat{P}} |a_i\rangle \otimes \left|m^{(0)}\right\rangle = |a_i\rangle \otimes \left(e^{-iga_i\hat{P}} \int dq\, |q\rangle\, \phi_0(q)\right). \tag{2.12}$$

The operator $e^{-i\lambda\hat{P}}$ acts as a translation operator on a wave function in the position basis $\phi(q)$, $e^{-i\lambda\hat{P}}\phi(q) = \phi(q-\lambda)$. Hence, the complete state after the application of the unitary operator is

$$|a_i\rangle \otimes \left|m^{(i)}\right\rangle = |a_i\rangle \otimes \int dq\, |q\rangle\, \phi_0(q - ga_i). \tag{2.13}$$

The protocol induces a shift in the ancilla's wave function, which is proportional to the corresponding eigenvalue a_i. In the last step of the protocol, the ancilla's wave function is measured, and the resulting shifts provide a measurement of the observable. However, as shown in Fig. 2.3, the eigenvalues can only be distinguished when the strength of the interaction is sufficiently large. When the interaction strength is weak, the measurement becomes less precise, and the extracted information is reduced. Nonetheless, this approach, known as the von Neumann protocol, accounts for both the system and the measuring device, allowing for any type of measurement, from ideal to weak, to be performed.

If the initial state is a pure state, which can be expressed in terms of the observable's basis as:

$$|\psi\rangle = \sum_i \beta_i |a_i\rangle, \tag{2.14}$$

where $|a_i\rangle$ are normalized vectors and $\sum_i \beta_i = 1$.

Then the full state after applying the von Neumann protocol is given by:

$$|\psi\rangle \otimes \left|m^{(f)}\right\rangle = \sum_i \beta_i |a_i\rangle \otimes \int dq\, |q\rangle\, \phi_0(q - ga_i), \tag{2.15}$$

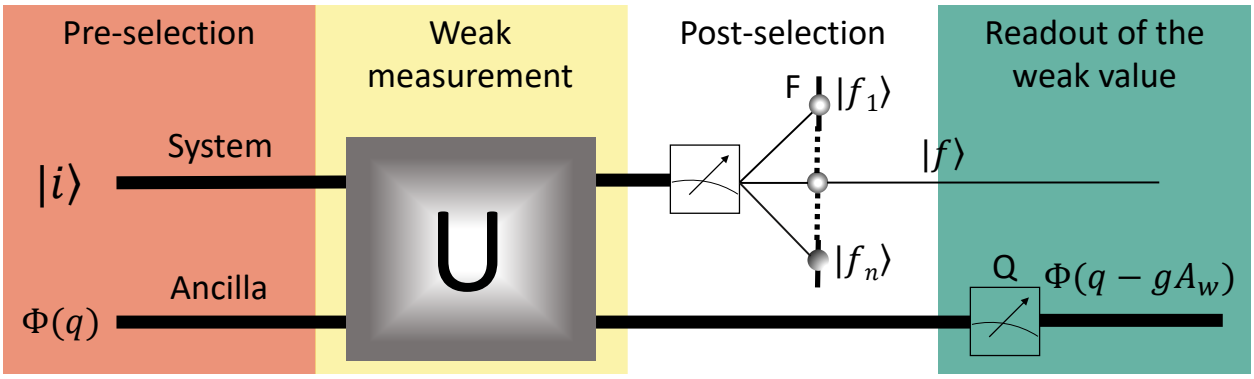

Figure 2.4: This is a schematic of the weak measurement process, which consists of four steps. First, the system is pre-selected in a chosen initial state. Second, a unitary operator is applied with a small interaction strength during a short period of time δt. Third, the system undergoes post-selection, which involves a projective measurement and a filtering procedure to extract only the information related to the desired final state. Finally, the ancilla's wave function is readout, and in the case of weak measurement, the shift is proportional to the weak value, A_w.

The final wave function of the measuring device is obtained by summing all the shifted wave functions weighted by the coefficients β_i. When a state is very close to an eigenvector, but has a small component of another eigenvector, the corresponding peak in the measurement outcome would be too small to be detectable. If the interaction strength between the system and the measuring device is very small compared to the width of the measuring device's wave function, the shift is proportional to the expectation value of the observable.

2.3 Weak measurements

Introduced in the 1980s and inspired by the von Neumann protocol [17], weak measurements have become an essential tool in quantum mechanics. As shown schematically in Fig. 2.4, unlike the von Neumann protocol, the weak measurement process involves four steps, including post-selection, which is not present in the von Neumann protocol and plays a crucial role. In the first step, the initial pure state of the system is chosen, $|\psi_i\rangle$, (pre-selection) and the initial ancilla's wave function, $|\phi_0\rangle$ centered on 0. The total state is,

$$|\psi\rangle = |\psi_i\rangle \otimes |\phi_0\rangle\,, \tag{2.16}$$

The second step consists of the application of a unitary operator, $\hat{U} = e^{-ig\hat{A}\otimes\hat{P}}$, where $\hbar = 1$, $g = \int_0^{\delta t} \gamma dt$, with γ being the coupling constant. $\hat{A}$ is the observable of interest, it belongs to the space of the system. $\hat{P}$ is the pointer, in this case, momentum, and it belongs to the ancilla's space. The joint system-meter state evolves thus according to

$$|\psi\rangle \to \hat{U}\left(|\psi_i\rangle \otimes |\phi_0\rangle\right) = e^{-ig\hat{A}\otimes\hat{P}}\left(|\psi_i\rangle \otimes |\phi_0\rangle\right). \tag{2.17}$$

As the measurement is weak, both the coupling constant and the time δt should be small. Hence, g is very small and the unitary operator is expanded in Taylor series until the first order in g,

$$\hat{U}\left(|\psi_i\rangle \otimes |\phi_0\rangle\right) = \left(\hat{I}\otimes\hat{I} - ig\hat{A}\otimes\hat{P}\right)\left(|\psi_i\rangle \otimes |\phi_0\rangle\right) + o\left(g^2\right). \tag{2.18}$$

During the time of the unitary operator application, both the ancilla and the system are not considered to evolve independently due to the short time of interaction.
However, after the unitary operation, only a weak interaction is performed. As a result, the system undergoes only a small perturbation, and the measurement protocol would provide limited information. Despite this, post-selection can still be applied to amplify the effect. The final state of the system is imposed to be $\left|\psi_f\right\rangle$, after a projective measurement with filtering, so that the final meter state is

$$\begin{aligned}\left|\mu_f\right\rangle &\approx \left\langle\psi_f\right|\left(\hat{I}\otimes\hat{I}-ig\hat{A}\otimes\hat{P}\right)\left(\left|\psi_i\right\rangle\otimes\left|\phi_0\right\rangle\right)=\left\langle\psi_f\middle|\psi_i\right\rangle\left|\phi_0\right\rangle-ig\left\langle\psi_f\right|\hat{A}\left|\psi_i\right\rangle\hat{P}\left|\phi_0\right\rangle \quad (2.19)\\ &= \left\langle\psi_f\middle|\psi_i\right\rangle\left(\hat{I}-ig\frac{\left\langle\psi_f\right|\hat{A}\left|\psi_i\right\rangle}{\left\langle\psi_f\middle|\psi_i\right\rangle}\hat{P}\right)\left|\phi_0\right\rangle,\end{aligned}$$

where A_w is the weak value,

$$A_w=\frac{\left\langle\psi_f\right|\hat{A}\left|\psi_i\right\rangle}{\left\langle\psi_f\middle|\psi_i\right\rangle}. \quad (2.20)$$

The operator $\hat{P}$ is a translation operator for the operator position, as seen in the previous section. Consequently, the wave function in the position representation presents a shift that is proportional to the weak value, A_w,

$$\phi_f(q)=\left\langle q\middle|\mu_f\right\rangle=\phi_0(q-gA_w), \quad (2.21)$$

where the weak value, A_w, is assumed to be real for this example. Nevertheless, it should be noted that in general, this quantity is a complex number. When both the real and imaginary parts of A_w are considered, two shifts appear in the ancilla's wave function. The shift in the position representation is proportional to the real part of A_w, while the shift in the momentum representation is proportional to the imaginary part of A_w. In the next section, we will consider this possibility along with more general operators as pointers.
In Eq. 2.20, the weak value can be much larger than the eigenvalues of the operator $\hat{A}$ due to the denominator. This property makes weak measurements a valuable tool for enhancing signals that would otherwise be difficult to measure. However, in order to achieve this enhancement, the pre- and post-selected states should be almost perpendicular, leading to a very small probability of post-selection, which is proportional to $|\left\langle\psi_f\middle|\psi_i\right\rangle|^2$ at zeroth order in g. Although the shift can be very large, to extract information about the weak value, the experiment needs to be repeated several times.
In this thesis, the term "weak measurements" will refer specifically to measurements with post-selection involving weak values. However, if we refer to a measurement with a weak coupling strength but without post-selection, we will make it explicit.

2.4 General description of weak measurements

In the previous section, we introduced the concept of weak values in the simplest possible way. Here, we develop the full theory considering complex weak values and any observable as pointer (not needing to be described in the continuous space) [26]. Both the state of the system and the meter are considered as density operators. Density operators are the generalization of pure quantum states. They are formed as a linear combination of projectors representing pure states.

Density operators are a classical statistical mixture of quantum projectors. For a more detailed explanation, read appendix A.
Let us consider the full system, formed by the system of interest described as a density operator, $\hat{\sigma}_i$ and an ancilla density operator, $\hat{\mu}_0$, $\hat{\rho}_0 = \hat{\sigma}_i \otimes \hat{\mu}_0$. The measurement is performed by applying a unitary operator. Taking inspiration from the von Neumann protocol, the chosen unitary operator is

$$\hat{U} = e^{-i\int_0^{\delta t} dt H_{\text{int}}} = e^{-i\int_0^{\delta t} dt \gamma \hat{A}\otimes\hat{N}} = e^{-ig\hat{A}\otimes\hat{N}}, \tag{2.22}$$

where $g = \int_0^{\delta t} \gamma dt$ with γ being the coupling constant, and $\hbar = 1$, $\hat{A}$ is the observable to be measured belonging to the system space, and $\hat{N}$ is the pointer belonging to the ancilla's space. In the von Neumann protocol, the duration of interaction δt is chosen to be small enough such that the system and the meter do not evolve independently. Similarly, in the weak measurement protocol, δt is also chosen to be small to ensure that there is no free evolution. However, in addition to this, the interaction strength g should also be small, i.e., $g \ll 1$, so that the unitary operator $\hat{U}$ can be expanded in a Taylor series up to the first order, given by:

$$\hat{U} = e^{-ig\hat{A}\otimes\hat{N}} \approx \hat{I} - ig\hat{A}\otimes\hat{N} - g^2\left(\hat{A}\otimes\hat{N}\right)^2 + O\left(g^3\right). \tag{2.23}$$

The full density operator is, after the application of the unitary operator, $\hat{\rho}_1$, in terms of $\hat{X} = \hat{A}\otimes\hat{N}$,

$$\begin{aligned}
\hat{\rho}_1 &= e^{-i\int dt\gamma\hat{A}\otimes\hat{N}}\hat{\rho}_0 e^{i\int dt\gamma\hat{A}\otimes\hat{N}} \\
&\approx \left(\hat{I} - ig\hat{X} - \frac{g^2}{2}\hat{X}^2\right)\hat{\rho}_0\left(\hat{I} + ig\hat{X} - \frac{g^2}{2}\hat{X}^2\right) \\
&= \hat{\rho}_0 + ig\left[\hat{\rho}_0, \hat{X}\right] - \frac{g^2}{2}\left(\hat{X}^2\hat{\rho}_0 + \hat{\rho}_0\hat{X}^2 - 2\hat{X}\hat{\rho}_0\hat{X}\right) \\
&= \hat{\rho}_0 + ig\left[\hat{\rho}_0, \hat{X}\right] - \frac{g^2}{2}\left[\left[\hat{\rho}_0, \hat{X}\right], \hat{X}\right],
\end{aligned} \tag{2.24}$$

where $\left[\hat{Y}, \hat{Z}\right]$ is the commutator of the operators $\hat{Y}$ and $\hat{Z}$. The density operator is

$$\hat{\rho}_1 \approx \hat{\rho}_0 + i\left[\hat{\rho}_0, g\hat{A}\otimes\hat{N}\right] - \frac{1}{2}\left[\left[\hat{\rho}_0, g\hat{A}\otimes\hat{N}\right], g\hat{A}\otimes\hat{N}\right]. \tag{2.25}$$

After the application of the unitary operator, a weak interaction has been implemented. The system has only been slightly modified. However, only a little bit of information could be extracted from the system. This could be interesting in specific cases in which the experimentalist possesses a lot of copies of the system and does not want to destroy them.
However, this type of measurement find many more application when post-selection is applied to the system, after the weak interaction. In this case, a projective measurement is executed on the system, projecting the state to the chosen density operator, $\hat{\sigma}_f$, while the ancilla's state is left unchanged. The measuring device density operator after the post-selection on the system is

$$\hat{\mu}_f = \frac{\text{Tr}_S\left[\left(\hat{\sigma}_f\otimes\hat{I}\right)\hat{\rho}_1\right]}{\text{Tr}\left[\text{Tr}_S\left[\left(\hat{\sigma}_f\otimes\hat{I}\right)\hat{\rho}_1\right]\right]}, \tag{2.26}$$

where Tr_S is the partial trace over the system, and the term $\mathrm{Tr}_S\left[\left(\hat{\sigma}_f \otimes \hat{I}\right)\hat{\rho}_1\right]$ is,

$$\begin{aligned}
&\mathrm{Tr}_S\left[\left(\hat{\sigma}_f \otimes \hat{I}\right)\hat{\rho}_1\right] \approx \mathrm{Tr}_S\left[\left(\hat{\sigma}_f \otimes \hat{I}\right)\left(\hat{\sigma}_i \otimes \hat{\mu}_0 + ig\left[\hat{\sigma}_i \otimes \hat{\mu}_0, \hat{X}\right] - \frac{g^2}{2}\left[\left[\hat{\sigma}_i \otimes \hat{\mu}_0, \hat{X}\right], \hat{X}\right]\right)\right] \qquad (2.27)\\
= \;& \mathrm{Tr}_S\left[\left(\hat{\sigma}_f \otimes \hat{I}\right)\left(\hat{\sigma}_i \otimes \hat{\mu}_0 + ig\hat{\sigma}_i \otimes \hat{\mu}_0\hat{X} - ig\hat{X}\hat{\sigma}_i \otimes \hat{\mu}_0 - \frac{g^2}{2}\left(\left[\hat{\sigma}_i \otimes \hat{\mu}_0\hat{X} - \hat{X}\hat{\sigma}_i \otimes \hat{\mu}_0, \hat{X}\right]\right)\right)\right]\\
= \;& \mathrm{Tr}_S\left[\left(\hat{\sigma}_f \otimes \hat{I}\right)\left(\hat{\sigma}_i \otimes \hat{\mu}_0 + ig\hat{\sigma}_i \otimes \hat{\mu}_0\hat{X} - ig\hat{X}\hat{\sigma}_i \otimes \hat{\mu}_0 - \frac{g^2}{2}\left(\hat{\sigma}_i \otimes \hat{\mu}_0\hat{X}^2 - 2\hat{X}\hat{\sigma}_i \otimes \hat{\mu}_0\hat{X} + \hat{X}^2\hat{\sigma}_i \otimes \hat{\mu}_0\right)\right)\right]\\
= \;& \mathrm{Tr}\left(\hat{\sigma}_f\hat{\sigma}_i\right)\hat{\mu}_0 + ig\left(\mathrm{Tr}\left[\hat{\sigma}_f\hat{\sigma}_i\hat{A}\right]\hat{\mu}_0\hat{N} - \mathrm{Tr}\left[\hat{\sigma}_f\hat{A}\hat{\sigma}_i\right]\hat{N}\hat{\mu}_0\right)\\
- \;& \frac{1}{2}g^2\left(\mathrm{Tr}\left[\hat{\sigma}_f\hat{\sigma}_i\hat{A}^2\right]\hat{\mu}_0\hat{N}^2 + \mathrm{Tr}\left[\hat{\sigma}_f\hat{A}^2\hat{\sigma}_i\right]\hat{N}^2\hat{\mu}_0 - 2\mathrm{Tr}\left[\hat{\sigma}_f\hat{A}\hat{\sigma}_i\hat{A}\right]\hat{N}\hat{\mu}_0\hat{N}\right),
\end{aligned}$$

where the trace property $[A+B,C] = [A,C] + [B,C]$ has been invoked.
We will also consider two assumptions in our analysis. Firstly, we assume that the initial average value of the particle number is zero, denoted as $\langle N\rangle_0 = 0$. This assumption ensures that our shift is taken from the origin, and is equivalent to centering the wave function in position representation at 0. Secondly, we assume that the initial average value of the particle number squared is non-zero, denoted as $\langle N^2\rangle_0 \neq 0$. This assumption is essential for obtaining a shift proportional to the imaginary part of the weak value. The denominator of Eq. 2.26 is

$$\mathrm{Tr}\left[\mathrm{Tr}_S\left[\left(\hat{\sigma}_f \otimes \hat{I}\right)\hat{\rho}_1\right]\right] = \mathrm{Tr}\left[\hat{\sigma}_f\sigma_i\right]\left[1 - g^2\langle N^2\rangle_0\left[\mathrm{Re}\left(\frac{\mathrm{Tr}\left[\hat{\sigma}_f\hat{A}^2\hat{\sigma}_i\right]}{\mathrm{Tr}\left[\hat{\sigma}_f\hat{\sigma}_i\right]} - \left|\frac{\mathrm{Tr}\left[\hat{\sigma}_f\hat{A}\hat{\sigma}_i\right]}{\mathrm{Tr}\left[\hat{\sigma}_f\hat{\sigma}_i\right]}\right|^2\right)\right]\right]. \qquad (2.28)$$

In equations Eq. 2.27 and Eq. 2.28, one can notice that the final ancilla's state is proportional to the initial ancilla's state plus a shift. In Eq. 2.27, one can see that this shift can be written in terms of weak values of $\hat{A}$, as it can be written in terms of density operators as[1],

$$A_w = \frac{\mathrm{Tr}\left[\hat{\sigma}_f\hat{A}\hat{\sigma}_i\right]}{\mathrm{Tr}\left[\hat{\sigma}_f\hat{\sigma}_i\right]}. \qquad (2.29)$$

While Eq. 2.28 contains other terms that are proportional to g^2, we assume that g is small enough to neglect all terms of order g^2.
The shift arising from Eq. 2.27 is, in general, a linear combination of the real and imaginary parts of the weak value. Nonetheless, for experimental purposes, it is often desirable to separate these two parts. This can be achieved by considering two special cases of meter observables. The first case occurs when the meter observable is proportional to the pointer observable, that is, $\hat{L} = \hat{N}$. In this case, the shift is proportional to the imaginary part of the weak value. The second case occurs when the meter observable is the canonical conjugate of the pointer, that is, $\left[\hat{M},\hat{N}\right] = i\hat{I}$. In this case, the shift is proportional to the real part of the weak value. In the context of the von

[1] Weak values find their origins within the realm of quantum pure states, their definition expressed as $\frac{\langle\psi_f|\hat{A}|\psi_i\rangle}{\langle\psi_f|\psi_i\rangle}$. This concept can be trivially rephrased using projectors, $\hat{\Pi}_a = |\psi_a\rangle\langle\psi_a|$, resulting in $\frac{\mathrm{Tr}\left[\hat{\Pi}_f\hat{A}\hat{\Pi}_i\right]}{\mathrm{Tr}\left[\hat{\Pi}_f\hat{\Pi}_i\right]} = \frac{\langle\psi_f|\hat{A}|\psi_i\rangle\langle\psi_i|\psi_f\rangle}{|\langle\psi_f|\psi_i\rangle|^2} = \frac{\langle\psi_f|\hat{A}|\psi_i\rangle}{\langle\psi_f|\psi_i\rangle}$. This paves the way for the natural extension of weak values to density operators, yielding $\frac{\mathrm{Tr}\left[\hat{\sigma}_f\hat{A}\hat{\sigma}_i\right]}{\mathrm{Tr}\left[\hat{\sigma}_f\hat{\sigma}_i\right]}$.

Neumann protocol, the first case corresponds to using the position $\hat{Q}$ as the meter observable, while the second case corresponds to using the momentum $\hat{P}$ as the meter observable. The expectation value of $\hat{N}$ is proportional to the imaginary part of the weak value,

$$\langle \hat{N} \rangle_f \approx 2g\langle \hat{N}^2 \rangle \mathrm{Im}\left(\frac{\mathrm{Tr}\left[\hat{\sigma}_f \hat{A} \hat{\sigma}_0\right]}{\mathrm{Tr}\left[\hat{\sigma}_f \hat{\sigma}_0\right]} \right) D^{-1}, \tag{2.30}$$

with,

$$D = \left[1 - g^2 \langle N^2 \rangle_0 \left[\mathrm{Re}\left(\frac{\mathrm{Tr}\left[\hat{\sigma}_f \hat{A}^2 \hat{\sigma}_i\right]}{\mathrm{Tr}\left[\hat{\sigma}_f \hat{\sigma}_i\right]} - \left| \frac{\mathrm{Tr}\left[\hat{\sigma}_f \hat{A} \hat{\sigma}_i\right]}{\mathrm{Tr}\left[\hat{\sigma}_f \hat{\sigma}_i\right]} \right|^2 \right) \right] \right]. \tag{2.31}$$

The expectation value of $\hat{M}$ is proportional to the imaginary part of weak value,

$$\langle \hat{M} \rangle_f \approx \left[g\mathrm{Re}\left(\frac{\mathrm{Tr}\left[\hat{\sigma}_f \hat{A} \hat{\sigma}_0\right]}{\mathrm{Tr}\left[\hat{\sigma}_f \hat{\sigma}_0\right]} \right) + g\langle \{\hat{N}, \hat{M}\} \rangle_0 \mathrm{Im}\left(\frac{\mathrm{Tr}\left[\hat{\sigma}_f \hat{A} \hat{\sigma}_0\right]}{\mathrm{Tr}\left[\hat{\sigma}_f \hat{\sigma}_0\right]} \right) \right] D^{-1}, \tag{2.32}$$

where $\langle \hat{M} \rangle_0 = 0$ has been assumed.
The weak value appears in the shift of the ancilla's state independently of the observable being measured and the pointer used. It is not necessary to have the configuration in which they were introduced [17]. Moreover, the weak value has been found to play a crucial role in other types of measurements, such as homodyne measurements [27]. Homodyne measurements are a type of interferometric measurement commonly used in optics [11]. In this case, the measurement is weak, and post-selection is performed by photon counting. Even in the von Neumann scheme with strong measurements, weak values still play an important role [28]. Thus, the concept of weak values has far-reaching implications beyond the weak von Neumann measurement scheme, and is a key tool for understanding quantum measurements in a variety of contexts.

2.5 Weak values

Weak values, denoted as $A_w = \frac{\langle \psi_f | \hat{A} | \psi_i \rangle}{\langle \psi_f | \psi_i \rangle}$, are complex and unbounded quantities. In the von Neumann measurement scheme with post-selection, weak values replace the eigenvalues of the observable in the meter shift. However, weak values can lie outside the observable's spectrum.
Despite this, weak values can be interpreted as a quasiprobability distribution. In fact, we showed that any weak value is proportional to the weak values of a specific projector, defined as the normalized application of the observable on the pre-selected state [19]. More precisely, we have $A_w \propto \Pi_{i'w}$, where $|\psi_{i'}\rangle = \frac{1}{\sqrt{N}} \hat{A} |\psi_i\rangle$ [19].

$$\Pi_{i',w} = \frac{\mathrm{Tr}\left[\hat{\Pi}_f \hat{\Pi}_{i'} \hat{\Pi}_i\right]}{\mathrm{Tr}\left[\hat{\Pi}_f \hat{\Pi}_i\right]}, \tag{2.33}$$

where the numerator, $\mathrm{Tr}\left[\hat{\Pi}_f \hat{\Pi}_n \hat{\Pi}_i\right]$ is the Kirkwood-Dirac quasiprobability distribution [29]. This distribution provides information about the state non-classicality. If the quasiprobability is negative or complex, the state is non-classical. In this cases, quantum states can provide quantum advantage

in quantum metrology and information [30].
A weak value can be expressed as,

$$A_w = \frac{\langle \psi_i | \hat{A}^2 | \psi_i \rangle}{\langle \psi_i | \hat{A} | \psi_i \rangle} \frac{\mathrm{Tr}\left[\hat{\Pi}_f \hat{\Pi}_{i'} \hat{\Pi}_i\right]}{\mathrm{Tr}\left[\hat{\Pi}_f \hat{\Pi}_i\right]}, \tag{2.34}$$

where $\hat{\Pi}_{i'} = \frac{\hat{A}|\psi_i\rangle\langle\psi_i|\hat{A}}{\langle\psi_i|\hat{A}|\psi_i\rangle}$. It is worth noting that the expectation value of $\hat{A}^2$ is always real and positive, while the expectation value of $\hat{A}$ is real but may be negative.
A weak value is considered anomalous if it is complex or if its absolute value is either greater than the largest eigenvalue of the observable being measured or smaller than the smallest eigenvalue.
Upon examination of Eq. 2.34, it becomes evident that due to the real nature of both expectation values, $\langle \psi_i | \hat{A} | \psi_i \rangle$ and $\langle \psi_i | \hat{A}^2 | \psi_i \rangle$, along with the probability of post-selection $\mathrm{Tr}\left[\hat{\Pi}_f \hat{\Pi}_i\right]$, a complex weak value establishes a direct connection to a complex Kirkwood-Dirac quasi-probability. This quasi-probability, in turn, serves as a hallmark of a non-classical state.
Furthermore, in cases where the weak value is real, a weak value A_w that holds the opposite sign of the initial state's observable expectation value, $\langle \psi_i | \hat{A} | \psi_i \rangle$, correlates with a negative Kirwood-Dirac quasi-probability $\mathrm{Tr}\left[\hat{\Pi} f \hat{\Pi} i' \hat{\Pi}_i\right]$, link to a non-classical state, Eq. 2.34. It is worth emphasizing that $\langle \psi_i | \hat{A}^2 | \psi_i \rangle$ consistently remains positive.
Therefore, a deeper investigation of this relationship between weak values and Kirkwood-Dirac quasiprobability is needed in future research.
Anomalous weak values have been shown to provide evidence of contextuality, which is another important feature of quantum processes [31, 32]. Quantum contextuality defines an aspect within the structure of quantum mechanics, where the act of measuring quantum observables transcends a simple unveiling of predetermined values. The outcome of measuring a quantum observable becomes contingent on the presence of other commuting observables within the same measurement set. This interdependence becomes pronounced in scenarios involving quantum weak measurements, where the result becomes intricately linked to the specific post-selected state chosen.
The numerator in Eq. 2.33 is a third-order Bargmann invariant, which takes the form of $\mathrm{Tr}\left(\hat{\Pi}_1 \hat{\Pi}_2 \hat{\Pi}_3\right)$. It is important to note that all three states used in this invariant must not be orthogonal to each other. This invariant is noteworthy because it remains unchanged under both gauge transformation and re-parametrization, as Bargmann originally noted in [33]. While it is possible to define Bargmann invariants of any order, only third-order invariants like this one are fundamental, since any higher-order invariant can be expressed in terms of third-order ones [34]. The significance of this invariant extends beyond its mathematical properties, as it plays a crucial role in quantum computing, specifically in determining the indistinguishability of states [35]. We'll delve into this topic further in chapter 3.
There exists a wide range of opinions among researchers on the meaning of weak values in quantum mechanics. The debate concerning the meaning of weak values is rooted in the fact that weak values cannot be directly observed in experiments and must instead be inferred using post-selection techniques. This method of inference makes the interpretation of weak values susceptible to various assumptions and mathematical manipulations that can influence their meaning.
Some prominent researchers, including Yakir Aharonov, Lev Vaidman, and Jeff Tollaksen, suggest that weak values represent a fundamental property of quantum systems and could lead to the development of new technologies. They propose a time-symmetric framework in which the initial and final states can be chosen, and they argue that weak values arise from this description [36, 37, 38].

On the other hand, some researchers disagree that weak values are a fundamental aspect of quantum physics. They argue that weak values cannot be used to reinterpret quantum paradoxes and consider them a mere mathematical construction [39, 40].
Moreover, the interpretation of the imaginary part of weak values remains a fundamental question. Some studies suggest that the imaginary part does not provide information about the observable but only about the pointer [41].
The issue of the meaning of weak values in quantum mechanics is a complex and multifaceted topic. Nonetheless, we believe that weak values are a fundamental aspect of quantum mechanics and play a crucial role in understanding non-classicality. Furthermore, they have a wide range of practical applications in various quantum technologies, as we will discuss in the next section.

2.6 Weak value applications

The weak value, A_w is a complex and unbounded quantity. These properties have been extensively used. Having pre- and post-selected states that are almost orthogonal provides a large weak value, Eq. 2.20. This property can be used to enhance tiny signals that otherwise could not be measured [17, 42]. To benefit from this amplification, the experiment should be repeated several times, as the probability of post-selection is very small, Eq. 2.28. Metrology [43, 44, 45], sensing [46, 47, 48, 49] and control of tiny experimental parameters [50, 51] benefit largely from weak value amplification [52, 53].
Weak measurements evidenced new physical phenomena, such as minute optical effects in beam propagation [54, 55, 56]. For instance, the spin Hall effect of light, a phenomenon in which a beam of light undergoes a shift dependent on the polarization upon passing through a crystal, has been measured for the first time using amplifying weak measurements. This effect arises due to the spin-orbit coupling between the light's spin angular momentum and the medium momentum. Because the resulting shift is extremely small, the measurement can be classified as weak. However, by selecting a pre-determined beam with horizontal polarization and a post-selection of nearly vertical polarization, the shift can be significantly magnified, allowing the experimenters to measure it using commonly available technological platforms [57].
Weak values offer invaluable insights into various quantum foundation issues, including the non-perturbative sensing of quantum particles along trajectories [58, 59, 60]. Weak values also offer a reinterpretation of paradoxes that have intrigued scientists for decades [61, 62, 63, 64]. For instance, the three-box paradox deals with a photon that can be present in one of three boxes labeled A, B, and C. By conducting a weak measurement, interesting results can be obtained, such as a pseudo-probability of one for the photon being present in boxes A and B, and a pseudo-probability of -1 for it being in box C. However, to interpret these weak values correctly, weak values should be regarded as pseudo-probabilities rather than actual probabilities [65].
Weak values, being complex numbers, offer a unique way to access the complex components of quantum states in quantum tomography [66, 67]. In fact, the wave function of photons was first measured using weak measurements, by post-selecting photons with null momentum, resulting in a weak value that was directly proportional to the wave function in position representation. By measuring the real and imaginary components of the weak value, the experimentalists could determine the real and imaginary parts of the wave function, which is a departure from the conventional method of measuring the amplitude of the wave function [68]. In addition, weak values have also

been utilized to measure the expectation values of non-Hermitian operators, by leveraging their complex properties [69].
As complex numbers, they can be studied in terms of real and imaginary parts, but also in terms of modulus and argument. The argument of a weak value represents a Berry phase, as we will discuss in the chapters 4 and 5. Consequently, the arguments of weak values can be employed to measure Berry phases [70].

Chapter 3

Quantum space

Selecting the appropriate coordinate system is a pivotal factor in addressing Physics challenges. Cartesian coordinates are the most intuitive to us, as our planet's curvature is almost negligible at our scale, despite being almost spherical in shape. In fact, certain physical scenarios demand venturing beyond familiarity and embracing alternative coordinate systems, spherical coordinates being a prominent example. For instance, when calculating the distance between two points on Earth, taking into account the planet's curvature by using the great circle method, namely, a geodesic between two points on a sphere, instead of a straight line is paramount. This means that relying on Euclidean geometry alone is not sufficient anymore. Therefore, switching to a spherical coordinate system becomes absolutely indispensable in order to ensure accurate calculations of distances and directions.

Governments, companies, and scientific institutions consider, nowadays, quantum physics as a key field for the advancement of technology [71, 72, 73]. A growing number of applications has recently appeared, such as quantum sensing, quantum random numbers generators, atomic clocks, or the long-sought-after quantum computer [74, 75, 76, 77]. Most of these applications are based on qubits, namely, two-level quantum systems. The quantum state of such a system can be in a superposition of two different states, for example, excited and ground states of an atom. Two-level quantum systems are chosen for these applications, among others, due to the simplicity of the their quantum space.

A pure two-level state is represented as a two-component normalized complex vector, generating a three-dimensional space. However, a global phase can be ignored as it does not change the physical properties of the quantum state. Using this property, the qubit space is the complex projective space $\mathbb{C}\mathrm{P}^1$, a two-dimensional space. $\mathbb{C}\mathrm{P}^1$ is bijectively mapped to the surface of a unit 2-sphere. This sphere is called after Felix Bloch, the Bloch sphere [78]. Quantum physicists are most familiar with the Bloch representation. It simplifies the visualization and study of many processes and calculations.

Nevertheless, there are instances where venturing beyond the familiar confines becomes essential. For instance, consider the realm of quantum error correction, a technique crucial for safeguarding quantum information against errors stemming from decoherence or various forms of quantum noise. In such scenarios, the utilization of larger discrete quantum systems, specifically N-level systems, can prove beneficial [79]. In these cases, moving to an unfamiliar space, as in the Earth surface, might be the key element to be successful.

Pure quantum states of N-level systems are defined in Hilbert space as an N-component normalized complex vector, denoted by $|\psi\rangle$. An N-level pure state, represented by an N-component complex vector, generates a $2N-1$ space. Omitting a global phase, the pure states generate a complex projective space, $\mathbb{C}\mathrm{P}^{N-1}$. This space is a $2N-2$ dimensional space. Unlike the two-level quantum space, mapping this space to the surface of a higher dimensional sphere is not possible. Although all pure states are on the surface of the sphere, not all points on the sphere are quantum pure states [80]. In fact, quantum pure states are mapped to only a subset of the sphere surface, making the representation and visualization of states much more challenging. The two-level quantum space is a special case. In general, the dimension of $\mathbb{C}\mathrm{P}^{N-1}$ is $2N-2$, while the dimension of the higher dimensional sphere, $\mathbb{S}^{N^2-2}$ is N^2-2, as one can appreciate, in the two-level case $(N=2)$, both spaces are of dimension 2. This means that the representation and visualization of states become increasingly complex as the number of levels is larger than two. The two-level quantum space is a very special case.
Within this chapter, we delve into diverse facets of both two-level and N-level quantum spaces. Serving as an introductory compass, our exploration unveils key concepts and properties poised to underpin forthcoming chapters' intricate analyses. First, we introduce the geometry of the two-level quantum space, using the Bloch sphere. Subsequently, we describe the case of N-level systems, working on the complex projective space $\mathbb{C}\mathrm{P}^{N-1}$, providing more details to understand larger quantum spaces. To do so, we study the star and wedge products, symmetric and anti-symmetric vectorial products, that are essential to N-level systems. We also introduce a simple representation of three-level systems on a spherical octant. Afterwards, we introduce the formalism of geometric phases. Finally, Bargmann invariants will be treated, as they will turn out to be a necessary tool to study the argument of weak values.

3.1 Exploring the Bloch Sphere: visualizing quantum two-level states

Two-level systems are usually represented using a unit 2-sphere, the Bloch sphere. Quantum two-level pure states are on the surface of the unit sphere. Any point of the surface of the Bloch sphere represent a pure quantum state and all pure quantum states are on the surface of the sphere. There is a bijective map between $\mathbb{C}\mathrm{P}^1$ and the Bloch sphere. Each point on the Bloch sphere corresponds to a family of vectors in Hilbert space rather than a single one. This sphere is independent of global phase, meaning that if we multiply a quantum state, $|\psi\rangle$, by a phase factor $e^{i\phi}$, the state remains represented by the same point on the sphere surface. The physical meaning of a quantum state does not vary when multiplying the quantum state by a phase, that is the motivation to use the complex projective space instead of the Hilbert space. Therefore, we use the Bloch sphere to represent projectors or, equivalently, the complex projective space $\mathbb{C}\mathrm{P}^1$. A projector of a pure state is defined as $\hat{\Pi} = |\psi\rangle\langle\psi|$. Importantly, projectors are invariant to the global phase of the quantum state, so if we multiply $|\psi\rangle$ by $e^{i\phi}$, the projector remains exactly the same. In order to incorporate the global phase into the Bloch sphere representation, an additional circle must be linked to each point on the sphere's surface. The point on the circle associated with a quantum state within the Hilbert space represents the global phase of that state. A pure state projector, denoted by $\hat{\Pi}$, satisfies two

important conditions: first, $\hat{\Pi}^2 = \hat{\Pi}$, indicating that the corresponding quantum state in Hilbert space is normalized. Second, $\hat{\Pi}$ is Hermitian, meaning that $\hat{\Pi} = \hat{\Pi}^\dagger$.
Mixed states, which are represented by density operators, are a linear combination of pure state projectors. Density operators are also Hermitian, but unlike pure state projectors, their square is not equal to themselves. In the Bloch ball representation, the vector representing a mixed quantum state is located inside the sphere. The closer this vector is to the surface of the sphere, the purer the state is. This means that if the vector is located near the center of the sphere, the state is closer to a complete classical mixture of all pure states [81]. Importantly, any point on the surface or inside of the unit sphere represents a quantum state.
Let us now study in detail the Bloch sphere. Two-level states are, in the most general case, defined as a two-component complex vector,

$$|\psi\rangle = \frac{1}{\sqrt{M}} \begin{pmatrix} a+ib \\ c+id \end{pmatrix}, \tag{3.1}$$

where a, b, c, and d are real numbers, and $\sqrt{M}$ serves as the normalization constant for the quantum state, thereby imposing a constraint on one of the four parameters.
By omitting the global phase, thus limiting to the complex projective space $\mathbb{C}\mathrm{P}^1$, a normalized quantum state can be expressed only using two variables. In terms of two angles, we obtain

$$|\psi\rangle = \begin{pmatrix} \cos\frac{\theta}{2} \\ e^{i\phi}\sin\frac{\theta}{2} \end{pmatrix}, \tag{3.2}$$

where the polar angle is defined in the range $0 \leq \theta \leq \pi$, and the azimuthal one in the interval $0 \leq \phi \leq 2\pi$. The chosen basis vectors are: $|0\rangle = \begin{pmatrix} 1 \\ 0 \end{pmatrix}$, $|1\rangle = \begin{pmatrix} 0 \\ 1 \end{pmatrix}$.
Both conditions, the normalization and the omission of the global phase, constrain the quantum state to the complex projective space, $\mathbb{C}\mathrm{P}^1$. Any state in the complex projective space is associated with a family of vectors in Hilbert space, by adding a global phase. This group represents two-level quantum states independently on the global phase, if we multiply a quantum state $|\psi\rangle$ by a unitary complex number, $e^{i\phi}$ the quantum state remains identical in the complex projective space. This convention is commonly used in quantum mechanics, as it reflects the fact that the physical properties of a quantum state remain unchanged when a global phase is added.
The projector corresponding to any pure state $|\psi\rangle$ (Eq. 3.2) is $\hat{\Pi} = |\psi\rangle\langle\psi|$. Consequently, any projector on a pure two-level system state can be written in terms of the identity and the traceless Pauli matrices, the chosen generators of the special unitary group $\mathrm{SU}(2)$[1], as

$$\hat{\Pi}_a = \frac{1}{2}\left(\hat{I} + \vec{a}\cdot\vec{\hat{\sigma}}\right), \tag{3.3}$$

where $\vec{a}$ is a real normalized three component vector, and the Pauli matrices are

$$\hat{\sigma}_1 = \begin{pmatrix} 0 & 1 \\ 1 & 0 \end{pmatrix} \qquad \hat{\sigma}_2 = \begin{pmatrix} 0 & -i \\ i & 0 \end{pmatrix} \qquad \hat{\sigma}_3 = \begin{pmatrix} 1 & 0 \\ 0 & -1 \end{pmatrix}. \tag{3.4}$$

The normalization of the vector $\vec{a}$ is a necessary and sufficient condition to ensure that the projector

[1] $\mathrm{SU}(N)$ is the N-dimensional special unitary group formed by all the $N \times N$ complex unitary matrices. The group can be generated by the complex exponential of all possible linear combinations of the generators of the group, which

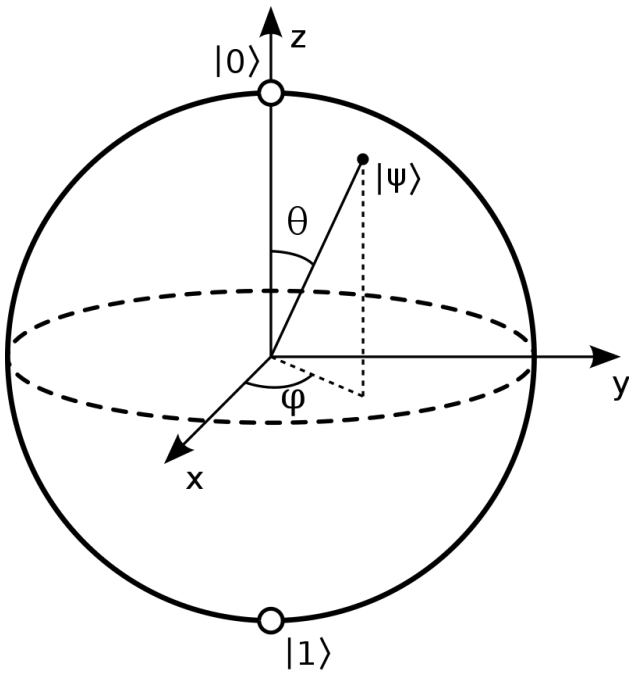

Figure 3.1: Quantum pure states are represented as vectors on the surface of a unit sphere, namely, the Bloch sphere. Each states depends on two parameters, polar and azimuthal angles. Reproduced from Smite-Meister, https://commons.wikimedia.org/wiki/File:Bloch_sphere.svg, accessed on the 22nd of May.

corresponds to a pure state. Using this condition, the projector to the square is equal to itself, $\hat{\Pi}^2 = \hat{\Pi}$. We can express the vector, $\vec{a}$, as a function of the polar and azimuthal angles as,

$$\vec{a} = (\cos\phi \sin\theta, \sin\phi \sin\theta, \cos\theta)\,. \tag{3.5}$$

The expression of the vector multiplying the Pauli matrices in Eq. 3.5 represents, when varying the angles in their ranges, the set of points of the surface of a unit sphere, the Bloch sphere. The vector, $\vec{a}$ represents a pure quantum state, $|\psi\rangle$, associated with the projector $\hat{\Pi}_a$, on the surface of the Bloch sphere.
In Fig. 3.1, the state $|0\rangle$ is placed at $(0,0,1)$ of the Bloch sphere, while the state $|1\rangle$ is positioned at $(0,0,-1)$. These states are placed at the poles of the sphere. Linear combinations with the same weight of $|0\rangle$, and $|1\rangle$, $\frac{1}{\sqrt{2}}(|0\rangle \pm |1\rangle)$, are placed at both intersections of the equator of the sphere with the y axis, $(0,\pm 1,0)$. Two orthogonal states present an angle of π on the Bloch sphere.
A mixed state is a statistical mixture of two or more pure states. It can be written as a weighted sum of the pure states, where the weights are probabilities that represent the likelihood of finding the system in each of the pure states. One common way to create a mixed state is through decoherence. It appears when a quantum system interacts with its environment, for example, a quantum system exposed to thermal fluctuations or other sources of noise in its environment. A mixed state is

are $2N-1$ traceless Hermitian matrices. The exponential of a Hermitian matrix is always a unitary matrix. For instance, in SU(2), the Pauli matrices may serve as generators. Similarly, in SU(3), the Gell-Mann matrices are a possible choice for the generators.

represented as a density operator, $\hat{\rho}$, which is a linear combination of pure quantum state projectors,

$$\hat{\rho} = \sum_s p_s \left|\psi_s\right\rangle \left\langle\psi_s\right|, \tag{3.6}$$

where p_s is the weight of each pure state and they should be positive $\left|\psi_s\right\rangle$, and the density operator should be normalized, $\sum_s p_s = 1$, which implies that $\mathrm{Tr}\left(\hat{\rho}\right) = 1$.
The density operator can also be expressed in terms of the identity and the Pauli matrices (generators of $\mathrm{SU}\left(2\right)$) as

$$\rho = \frac{1}{2}\left(\hat{I} + \vec{\beta}\cdot\vec{\hat{\sigma}}\right). \tag{3.7}$$

Unlike projectors of pure quantum states, when considering mixed states, $\vec{\beta}$ is not a normalized vector, having a norm smaller or equal to 1, $\|\vec{\beta}\| \leq 1$. Comparing the vector $\vec{\beta}$ multiplying the Pauli matrices to a general vector in a sphere $\vec{\Gamma} = (r\cos\phi\sin\theta, r\sin\phi\sin\theta, r\cos\theta)$, one can extract the radius as well as the angles in the Bloch ball. The smaller the radius, the more mixed the state is. At the limits, if the radius is $r = 1$, the state is pure, while a radius equal to $r = 0$ corresponds to a completely mixed state, which is a statistical combination of all possible pure states with equal probabilities. Therefore, a point at the center of the sphere has zero coherence. All points inside the Bloch sphere represent quantum mixed states and all quantum mixed states can be represented in the Bloch sphere.
Mixed states find applications not only in quantum mechanics but also in other fields such as optics. In this field, the polarization of light can be described in terms of basis vectors corresponding to vertical and horizontal polarizations, denoted by $(\left|V\right\rangle, \left|H\right\rangle)$. The polarized state of light can be represented on the surface of a unit sphere, known as the Poincaré sphere, which is the optical analog of the Bloch sphere used in quantum mechanics. However, not all light is polarized. Natural sources of light, such as sunlight or firelight, can be described as unpolarized light. The properties of unpolarized light can also be described using the Poincaré sphere, where the degree of polarization is reflected in the radius. The completely unpolarized state, which is the optical analog of a completely incoherent state, corresponds to the center of the sphere.
In this section, we have introduced a powerful tool for representing any two-level state, whether pure or mixed; namely the Bloch sphere and ball. This elegant representation allows the visualization of quantum states as points in a unit sphere, providing valuable insights into their properties and behaviors. It is worth noting that this mapping is only applicable to two-level systems, and as we delve deeper into the topic, we will encounter more complex challenges when dealing with N-level systems. In the following sections, we explore these challenges and introduce new tools and techniques to tackle them.

3.2 N-level quantum states: mapping quantum states onto the generalized Bloch sphere

The geometry of two-level pure states is intuitive and visualizable due to the elegant mapping between $\mathbb{C}\mathrm{P}^1$ and the surface S^2, the Bloch sphere. However, for specific applications such as error correction, it may be necessary to extend our understanding of quantum states to larger systems known as qudits, d-level systems [82, 83]. In higher-dimensional systems, the mathematical and

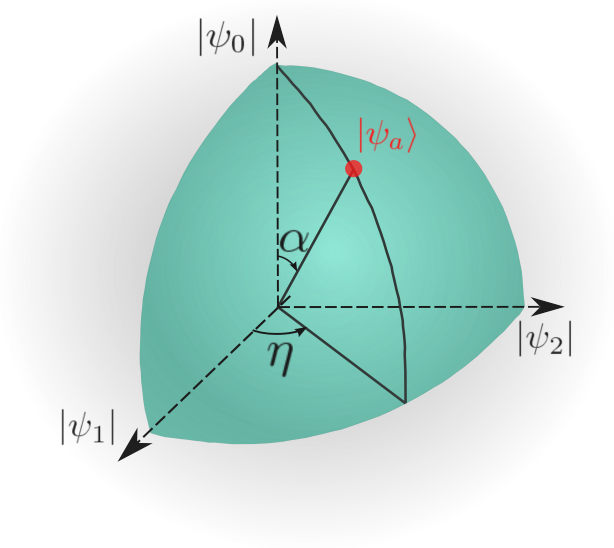

Figure 3.2: A three-level quantum state can be represented in the complex projective space $\mathbb{C}\mathrm{P}^2$ through a spherical octant projection.

geometrical representations become more complex, but they also provide us with more degrees of freedom and potentially more powerful computational capabilities.
Let us consider pure states of three-level quantum systems. Any three-level pure state, after normalization and ignoring a global phase, can be expressed in terms of four angles,

$$|\psi_a\rangle = \left(\cos\theta_a, e^{i\chi_{1,a}}\cos\varepsilon_a \sin\theta_a, e^{i\chi_{2,a}}\sin\varepsilon_a \sin\theta_a\right)^{\mathrm{T}}, \tag{3.8}$$

where $0 \leq \theta_a \leq \frac{\pi}{2}$, $0 \leq \varepsilon_a \leq \frac{\pi}{2}$, $0 \leq \chi_{1,a} \leq 2\pi$, and $0 \leq \chi_{2,a} \leq 2\pi$.
In a similar way to the previous section, a three-level pure projector can always be expressed in terms of the identity and the traceless Gell-Mann matrices, for more details see appendix B, the chosen generators of $\mathrm{SU}(3)$ as

$$\hat{\Pi}_a = \frac{1}{3}\left(\hat{I} + \sqrt{3}\vec{a}\cdot\hat{\vec{\lambda}}\right), \tag{3.9}$$

where $\hat{I}$ is the identity matrix, and $\hat{\vec{\lambda}}$ is a vector, the components of which are the eight Gell-Mann matrices, and $\vec{a}$ is an eight-component, normalized[2], real vector [84, 85]. The Gell-Mann matrices play a crucial role in the description of three-level systems, serving as the analog of the Pauli matrices for two-level systems. A three-level system projector is typically represented as a 3×3 Hermitian matrix. The most natural choice for a basis to describe any 3×3 Hermitian matrix is one that is spanned by the identity and the generators of $\mathrm{SU}(3)$, as they can generate the entire space of Hermitian 3×3 matrices. However, to describe a pure state, the projector must satisfy the condition $\hat{\Pi}^2 = \hat{\Pi}$. For systems with more than two levels, this condition reduces the size of the space to $2N-2$, while there are N^2-1 generators of the group.
The vector $\vec{a}$ represents the projector on the surface of the unit 7-sphere. Its expression can be found in appendix E. Nevertheless, this vector only depends on four free parameters, whereas a

[2]In this work, we chose the convention of normalized vectors on a single unit sphere. See appendix C for more details.

full surface of the sphere $\mathbb{S}^7$ depends on 7 free parameters. Consequently, only a subset of the 7-sphere represents quantum states. All pure states are on the surface of the unit 7-sphere, but not all points of the surface of the sphere are quantum states [80, 86].
As mentioned in the previous section, a projector of a pure quantum state should fulfill that the square of the projector is equal to itself, $\hat{\Pi}^2 = \hat{\Pi}$. Consequently, in the three-level case, contrary to the two-level case, this normalization imposes two conditions,

$$\vec{a}\cdot\vec{a} = 1 \qquad \text{and} \qquad \vec{a}\star\vec{a} = \vec{a}. \tag{3.10}$$

The first condition in Eq. 3.10 simply identifies the vector representing the projector as one vector belonging to the unitary 7-sphere, which represents the surface of a unitary 8-dimensional sphere. The second condition restricts the space of the 7-sphere that represents pure states. It creates a mapping of $\mathbb{C}\mathrm{P}^2$ to a four dimension subset of S^7. The star ($\star$) product is a symmetric vectorial product [84, 85, 87, 88, 89, 90, 91]. This product and the wedge ($\wedge$) product, anti-symmetric vectorial product, are defined from the structure constants of the group $\mathrm{SU}(3)$ as

$$\left(\vec{a}\star\vec{b}\right)_k = \sqrt{3}d_{ijk}a^i b^j \qquad \text{and} \qquad \left(\vec{a}\wedge\vec{b}\right)_k = f_{ijk}a^i b^j, \tag{3.11}$$

where the Einstein summation has been used, and the structure constants are defined as

$$d_{abc} = \frac{1}{4}\mathrm{Tr}\left(\hat{\lambda}_a\{\hat{\lambda}_b,\hat{\lambda}_c\}\right) \qquad \text{and} \qquad f_{abc} = -\frac{i}{4}\mathrm{Tr}\left(\hat{\lambda}_a\left[\hat{\lambda}_b,\hat{\lambda}_c\right]\right), \tag{3.12}$$

with the Gell-Mann matrices defined in appendix B.
In addition, two vectors $\vec{r_\psi}$ and $\vec{r_\phi}$ representing two orthogonal three-level quantum states present an angle of 120°. Therefore, the three vectors of a basis are in a plane with 120° between them. Furthermore, there is no equivalent of the $\star$ product in $\mathrm{SU}(2)$. For this reason, we discuss a few essential properties of the state representation as generalized Bloch spheres in appendix D and appendix E to provide more context. Note that the $\star$ and $\wedge$ products generate vectors that are both outside of $\mathbb{C}\mathrm{P}^2$ and not normalized in general (so they do not represent states). The vector $\vec{\alpha}\wedge\vec{\beta}$ produced by the wedge product is orthogonal to the two initial vectors $\vec{\alpha}$ and $\vec{\beta}$. Also, the two products are orthogonal: for any pre- and post-selected states $(\vec{i}\wedge\vec{f})\cdot(\vec{i}\star\vec{f}) = 0$.
Three-level states cannot be represented directly on the surface of the 7-sphere, as $\mathbb{C}\mathrm{P}^2$ cannot be mapped to S^7. However, it is possible to represent the complex projective space $\mathbb{C}\mathrm{P}^2$ in a spherical octant projection [84, 92]. In Fig. 3.2, we have depicted the representation of the state $|\psi_a\rangle = \left(\cos\alpha, \sin\alpha\cos\eta, e^{i\chi_2}\sin\alpha\sin\eta\right)^T$ in the spherical octant projection. When treating with the Bloch sphere, each point is associated with a circle related to global phase. In the three-level systems case, each point of the spherical octant is associated with a torus formed by the two phases present in the Hilbert space, χ_1, and χ_2, $|\psi\rangle = \left(|\psi_0|, e^{i\chi_1}|\psi_1|, e^{i\chi_2}|\psi_2|\right)^T$. The state $|\psi\rangle$ is projected to the point, $q = (|\psi_1|, |\psi_2|, |\psi_0|)$. Using the spherical octant projection, one can achieve a representation of three-level states in terms of two angles, η, and α. To consider all parameters, apart from the location on the spherical octant, the point in the torus should be precised.
In N-level systems, the representation of states is very similar to the one of three-level states. A general normalized quantum pure state depends on $2N-2$ parameters, after having omitted a global phase. Quantum states can be represented on a $2N-2$ subset of the surface of the $\mathbb{S}^{N^2-2}$

sphere, as there are N^2-1 traceless generators of SU(N). The expression of an N-level projector, can be expressed in terms of the identity and the generators of SU(N),

$$\hat{\Pi}_r = \frac{1}{N}\hat{I} + \sqrt{\frac{N-1}{2N}}\vec{r}\cdot\hat{\vec{L}}, \tag{3.13}$$

where $\hat{I}$ is the $N\times N$ identity matrix and $\hat{\vec{L}}$ are the N^2-1 generators of the group SU(N).
The projector in Eq. 3.13 represents a pure state when $\vec{r}\cdot\vec{r}=1$ that brings the vector to the surface of the sphere S^{N^2-2}, and $\vec{r}\star\vec{r}=\vec{r}$ that restricts the surface of the sphere S^{N^2-2} to the $(2N-2)$-dimensional subset. Both required conditions are fulfilled. Using these restrictions, the complex projective space $\mathbb{C}P^{N-1}$ that is built by all quantum states (disregarding a global phase) is mapped to a subset of the surface of the unit sphere S^{N^2-2}. The $\star$ and $\wedge$ products are defined in SU(N) as

$$(\vec{q}\star\vec{r})_c = \sqrt{\frac{N(N-1)}{2N}}\frac{1}{N-2}d_{abc}q_a r_b \qquad \text{and} \qquad (\vec{q}\wedge\vec{r})_c = f_{abc}q_a r_b, \tag{3.14}$$

where the structure constants of the group SU(N) are,

$$d_{abc} = \frac{1}{4}\mathrm{Tr}\left(\hat{L}_a\{\hat{L}_b,\hat{L}_c\}\right) \qquad f_{abc} = -\frac{i}{4}\mathrm{Tr}\left(\hat{L}_a\left[\hat{L}_b,\hat{L}_c\right]\right). \tag{3.15}$$

The anti-symmetric wedge product is defined similarly to the qutrit case, three-level system, using the structure constants of SU(N). It produces a vector with components $(\vec{\alpha}\wedge\vec{\beta})_c = f_{abc}\alpha_a\beta_b$, which is orthogonal to both $\vec{\alpha}$ and $\vec{\beta}$. Two vectors representing orthogonal N-level quantum states present an angle of $\pi - \arccos\frac{1}{N-1}$. When treating with two-level systems, the corresponding angle is π. Furthermore, when N tends to infinity, the angle between vectors representing two orthogonal quantum states tends to $\frac{\pi}{2}$
Plotting these states, even restricting to the angles that are not phases, is not possible in general. In Chapter 5, we study the Majorana symmetric representation of states [93], allowing the representation of N-level states as $N-1$ stars (or vectors) on the Bloch sphere.

3.3 Introduction to the formalism of geometric phases

When a quantum state follows a cyclic adiabatic evolution, starting and ending at the same point in the quantum state space, it acquires two global phases: the dynamical phase and the geometric phase (Fig. 3.3). The dynamical phase arises due to the time evolution of the quantum state and depends on the Hamiltonian governing the evolution. Consequently, the dynamical phase can vary depending on the specific nature of the evolution undergone by the quantum state. In contrast, the geometric (Berry-Pancharatnam) phase is only dependent on the geometry of the space and the followed path in quantum state space [94, 95]. Independently on how fast or slow the evolution path occurs, the added geometric global phase is the same.
Assuming the cyclic adiabatic trajectory depicted in Fig. 3.3, the state starts at the north pole of the Bloch sphere $|0\rangle$. Afterward, it presents an evolution passing by the equator and it ends up back at the initial state $|0\rangle$. As we can see, due to the curvature of the space, the Bloch sphere ($\mathbb{C}P^1$),

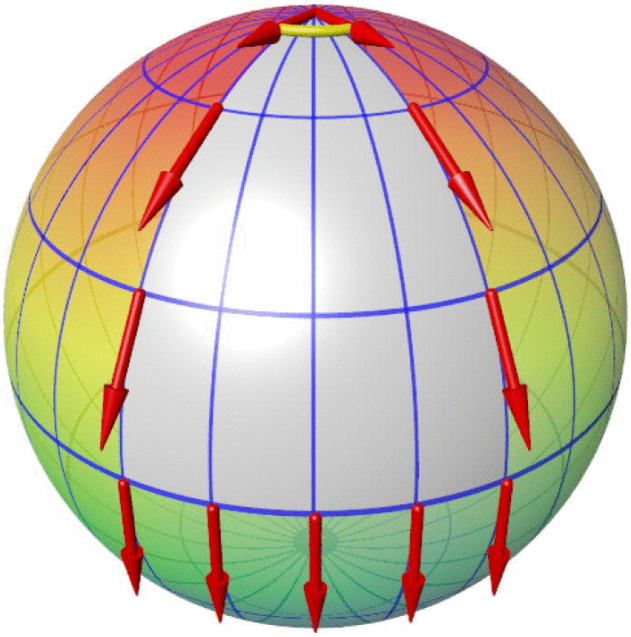

Figure 3.3: A geometric phase of a two-level quantum state corresponds to the global phase acquired by the state along an adiabatic cyclic trajectory. Reprinted from [96], with the permission of AIP Publishing.

without taking into account the possible phase that the state has acquired due to the Hamiltonian, a difference of phase is present between the initial and final state, even though the initial and the final states correspond to the same point on the Bloch sphere $|0\rangle$. The global phase that is acquired can be represented, as explained in the previous section, with the direction in a circle associated with each point on the Bloch sphere. In Fig. 3.3, this is depicted using an arrow.
Let us consider a quantum system that is governed by a Hamiltonian, $\hat{H}$, that depends on a vector of parameter, $\vec{R} = (X, Y, ...)$, $\hat{H}\left(\vec{R}(t)\right)$. The considered movement is cyclical. Hence, $\hat{H}\left(\vec{R}(T)\right) = \hat{H}\left(\vec{R}(0)\right)$, where T is the period. The state, $|\psi(t)\rangle$ evolves following the time dependent Schrödinger equation,

$$\hat{H}\left(\vec{R}(t)\right)|\psi(t)\rangle = i\frac{\partial|\psi(t)\rangle}{\partial t}, \tag{3.16}$$

where $\hbar = 1$. The discrete spectrum of the Hamiltonian can be expressed as

$$\hat{H}\left(\vec{R}\right)\left|n\left(\vec{R}\right)\right\rangle = E_n(R)\left|n\left(\vec{R}\right)\right\rangle. \tag{3.17}$$

The system is prepared initially in a state that corresponds to an eigenvector of the Hamiltonian, $|\psi(0)\rangle = \left|n\left(\vec{R}(0)\right)\right\rangle$. Consequently, the evolution of the quantum state is,

$$|\psi(t)\rangle = e^{-i\int_0^t dt' En\left(\vec{R}(t')\right)} e^{i\gamma_n(t)}\left|n\left(\vec{R}(t)\right)\right\rangle \tag{3.18}$$

The first exponential in the evolution of the quantum state (Eq. 3.18) is the dynamic phase [94]. The second exponential is the geometric phase. Imposing that the state obeys the Schrödinger

equation, one can determine that the evolution of the geometric phase is,

$$\frac{\partial \gamma_n(t)}{\partial t} = i\left\langle n\left(\vec{R}(t)\right)\middle|\nabla_{\vec{R}} n\left(\vec{R}(t)\right)\right\rangle \cdot \frac{\partial \vec{R}(t)}{\partial t}. \tag{3.19}$$

The geometric phase is in parameter space,

$$\gamma_n(C) = i\oint_C \left\langle n\left(\vec{R}\right)\middle|\nabla_{\vec{R}} n\left(\vec{R}\right)\right\rangle \cdot \frac{\partial \vec{R}(t)}{\partial t}. \tag{3.20}$$

The geometric phase, denoted by $\gamma_n(C)$, is defined as a line integral over the parameter space. This integral is independent of the specific path taken, as long as the evolution is adiabatic. An evolution is deemed adiabatic when neither heat nor mass experiences transfer between the system and the environment during the process. The Berry phase is an intrinsic characteristic of quantum systems. Samuel and Bhandari demonstrated that the Berry-Pancharatnam phase is not limited to cyclic or adiabatic evolutions [97]. In fact, any quantum system that evolves from an initial state to a final state acquires a geometric phase [98]. This phase is an intrinsic property of the geometry of quantum states and arises in various contexts. In the next section, we explore its significance in the context of Bargmann invariants.

3.4 Significance of the geometric phase in the context of Bargmann invariants

Geometric phases arise in several contexts. Among others, the argument of a Bargmann invariant describes a geometric phase. This property will be utilized in the next chapter in connection with the argument of weak values.
Bargmann invariants were defined in the context of the Wigner's theorem on symmetry operations [33]. This quantity is invariant under gauge transformation and re-parametrization. The invariant can present different order, depending on the number of involved quantum states. The Bargmann invariant of order N is defined as,

$$\Delta_m(\psi_1, \psi_2 \ldots \psi_{N-1}, \psi_N) = \mathrm{Tr}\left(\hat{\Pi}_1 \hat{\Pi}_2 \ldots \hat{\Pi}_{N-1} \hat{\Pi}_N\right), \tag{3.21}$$

where each projectors $\hat{\Pi}_a$ represents a pure quantum state.
The argument of an N-order Bargmann invariant is associated with the geometric phase that a state would get by performing a closed loop between $|\psi_1\rangle$ and $|\psi_N\rangle$,

$$\gamma_g[C_{12} \cup C_{23} U \ldots \cup C_{N1}] = -\arg\Delta_m(\psi_1, \psi_2 \ldots \psi_{N-1}, \psi_N), \tag{3.22}$$

where $C_{12} \cup C_{23} \cup \ldots \cup C_{N1}$ is a closed loop and each C_{ij} is a section of the circuit.
The argument of any N-order Bargmann invariant can be expressed as a sum of the arguments of third-order Bargmann invariants, $\mathrm{Tr}\left(\hat{\Pi}_1 \hat{\Pi}_2 \hat{\Pi}_3\right)$ [34], giving to third-order Bargmann invariants a special importance. Consequently, these invariants are directly linked to the Kirkwood-Dirac quasi-probability distribution, defined in the previous chapter 2.5.
The representation of a Bargmann invariant depends on the dimension of the involved quantum

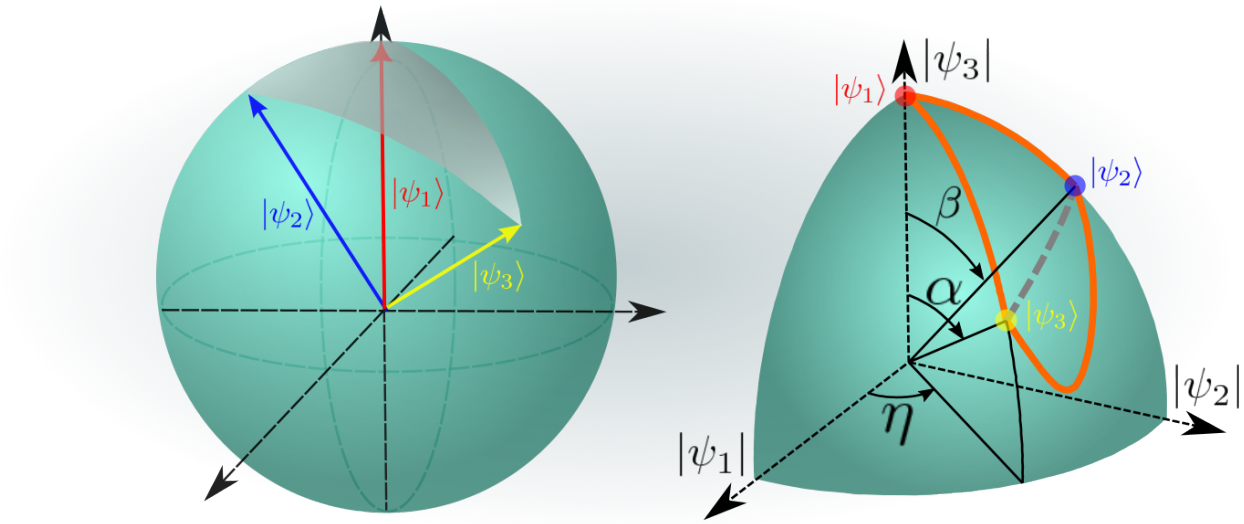

Figure 3.4: a) Representation of the solid angle associated with the two-level third-order Bargmann invariant. b) Representation of the projection of the geodesics used to compute the symplectic area associated with the three-level third-order Bargmann invariant. Modified from [19].

states. When treating with two-level systems the geometric phase is associated with the solid angle on the Bloch sphere of the triangle spanned by the vectors representing the three involved quantum states, $|\psi_1\rangle$, $|\psi_2\rangle$, and $|\psi_3\rangle$ [99]. Pure state projectors can always be expressed in terms of the identity and the Pauli matrices as expressed in Eq. 3.3. The vector $\vec{a}$, defined in Eq. 3.5, represents the state on the Bloch sphere. Hence, the argument of the third-order Bargmann invariant is,

$$\mathrm{Tr}\left[\hat{\Pi}_a\hat{\Pi}_b\hat{\Pi}_c\right] = \arctan\frac{\vec{a}\cdot\left(\vec{b}\times\vec{c}\right)}{1+\vec{c}\cdot\vec{b}+\vec{b}\cdot\vec{a}+\vec{c}\cdot\vec{a}} = -\frac{\Omega_{abc}}{2}. \tag{3.23}$$

The argument of the third-order Bargmann invariant of two-level systems is associated with half the solid angle on the Bloch sphere spanned by the three vectors representing the quantum states. Two-level projective space, $\mathbb{C}\mathrm{P}^1$, is bijectively mappable to the surface of a unit sphere. The mapping makes the geometry of the invariant specially simple. In Fig. 3.4, we plotted a representation of the solid angle associated with a geometric phase and thus with a Bargmann invariant involving the three two-level states $|\psi_1\rangle$, $|\psi_2\rangle$, and $|\psi_3\rangle$.

In three-level or higher-level systems, the projective space $\mathbb{C}\mathrm{P}^{N-1}$ cannot be mapped to the surface of the sphere $\mathbb{S}^{N^2-2}$. Consequently, the third-order Bargmann invariant is not associated anymore with the solid angle, but with the symplectic area[3] of the triangle spanned by the three states, $|\psi_1\rangle$, $|\psi_2\rangle$, and $|\psi_3\rangle$ in $\mathbb{C}\mathrm{P}^{N-1}$ [84]. The symplectic area is defined in an even manifold that is formed by pairs of directions: for example, symplectic areas in classical mechanics are specified in terms of position and momentum [100]. Here, we note that $2N-2$ free parameters describe the states in an N-dimensional complex Hilbert space (considering the global phase and the normalization),

[3]The symplectic area is defined in an even manifold constructed from direction pairs; in the phase space of classical mechanics, it is often related to position and momentum. This area is computed by integrating along boundary geodesics of a curve. Remarkably, this area is independent on the specific surface chosen for its calculation.

which accounts for the even number of dimensions.
In the two-level quantum space, the Riemannian and the symplectic areas coincide. Consequently, we can represent a symplectic area using the common Riemennian area on the Bloch sphere, the solid angle. However, in $\mathbb{C}\mathrm{P}^{N-1}$, the two areas do not coincide.
In Fig. 3.4b), we represented the projection of geodesics on $\mathbb{C}\mathrm{P}^2$ linked to the Bargmann invariant of the three three-level quantum states, $|\psi_1\rangle$, $|\psi_2\rangle$, and $|\psi_3\rangle$. To do so, we have employed the octant of the sphere, already introduced in the previous section.
It is important to note that the geodesics of the quantum state manifold do not correspond to geodesics of $\mathbb{S}^7$: they are not arcs of great circles of $\mathbb{S}^7$. In particular, the geometric phase is not equivalent to the Riemannian area of the $\mathbb{S}^7$ spherical triangle defined by the three vertices (which could include points that are not states), nor to the Riemannian area of a surface built from geodesics linking one vertex to the opposite side of the geodesic triangle (which is not unique as the surface generally depends on the chosen vertex in the triangle).

Chapter 4

Geometrical interpretation of the argument of weak values

Weak values are commonly investigated by analyzing their real and imaginary components, a convenient approach for experimental research [26, 42, 101]. Nevertheless, a recent surge in interest within the quantum community has centered on the geometrical interpretation of weak values [18, 102, 103, 104, 105, 106, 107]. This attraction to the geometrical aspect is driven by the profound link between geometric phases and weak values, a connection that underscores one of quantum mechanics' most unique attributes. Geometric phases emerge due to the intricate geometry of the Hilbert space, offering a striking contrast between quantum and classical physics. Unlike conventional dynamic phases stemming from temporal evolution, geometric phases arise from a quantum system's state space geometry. In Newtonian mechanics, state spaces are typically smooth manifolds devoid of non-trivial geometry. This contrast underscores the fundamental disparity between quantum mechanics and classical physics, underscoring the importance of geometric phases in quantum information and computation. Bridging these concepts entails the study of weak values in polar representation, in terms of complex number modulus and argument—to establish a cohesive connection.

In this chapter, we will link the argument of the weak value to geometric phases. We will also provide a geometrical interpretation of this argument in the complex projective space, $\mathbb{C}\mathrm{P}^{N-1}$.

We hope that these studies will help us to understand the meaning of weak values and their general role in quantum mechanics.

The chapter starts by introducing the geometrical interpretation of weak values of projectors in two- and three-level systems. Then, we move to weak values of projectors in N-level systems. The weak value of the generators of the $\mathrm{SU}(N)$ group will also be studied. Eventually, we move to weak values of general observables. At the end on the chapter, we will explain a few applications of the calculations.

4.1 Weak values of projectors in $\mathbb{C}^2$

We introduce here the basics of the geometric representation on the Bloch sphere of the argument of weak values of qubit (two-level systems) pure projectors. Then, we relate the argument

of the weak value of projectors to Bargmann invariants and geometric phases (in all dimensions). Throughout this chapter, we will always consider pure pre- and post-selected states.
Most generally, pure quantum states are represented by projectors $\hat{\Pi}_r = |\psi_r\rangle\langle\psi_r|$ in complex projective space (they verify $\hat{\Pi}_r^2 = \hat{\Pi}_r$). The state space of two-level quantum systems corresponds to the complex projective line $\mathbb{C}\mathrm{P}^1$. It is topologically equivalent to the two-dimensional sphere with unit radius in three dimensions, noted S^2 Fig. 3.1. Therefore, pure states in two-level quantum systems can be represented by a unit, three-dimensional, real vector $\vec{r}$ on the surface of the Bloch sphere. A two-level projector is then written in terms of the identity $\hat{I}$ and the traceless generators of SU(2) Eq. 3.3. Using the properties of the Pauli matrices, the calculation of the weak value $\Pi_{r,w} = \mathrm{Tr}\big(\hat{\Pi}_f\hat{\Pi}_r\hat{\Pi}_i\big)/\mathrm{Tr}\big(\hat{\Pi}_f\hat{\Pi}_i\big)$ is straightforward [18]:

$$\Pi_{r,w} = \frac{1+\vec{f}\cdot\vec{r}+\vec{r}\cdot\vec{i}+\vec{f}\cdot\vec{i}+i\,\vec{f}\cdot\left(\vec{r}\times\vec{i}\right)}{\frac{1}{2}\left(1+\vec{f}\cdot\vec{i}\right)}, \tag{4.1}$$

and the formula resulting for the argument [18] is

$$\arg\Pi_{r,w} = \arctan\frac{\vec{f}\cdot\left(\vec{r}\times\vec{i}\right)}{1+\vec{f}\cdot\vec{r}+\vec{r}\cdot\vec{i}+\vec{f}\cdot\vec{i}} = -\frac{\Omega_{irf}}{2}, \tag{4.2}$$

where $\vec{i}$ represents the pre-selected state and $\vec{f}$ the post-selected state, while $\vec{r}$ corresponds to the observable projector that is weakly probed. This purely geometric expression of the argument corresponds to minus one half of the solid angle Ω_{irf} intercepted on the Bloch sphere by the tetrahedron spanned from the three state vectors (where the path is followed in the order $i \to r \to f \to i$), as depicted in Fig. 4.1 (a). Incidentally, we note that the numerator in Eq. 4.2 corresponds to twice the signed volume of this tetrahedron. When calculating the solid angle in Eq. 4.2, the signs of the numerator and denominator should be taken into account to determine the appropriate quadrant. The geodesics between quantum states correspond to arcs of great circles on the Bloch sphere. Thus, for two-level systems, the argument of the weak value of a projector corresponds to a solid angle [18, 102, 103], the latter is also equal to the surface of the Bloch sphere inside the geodesic triangle, i. e. to the area of a spherical triangle. Let us note that, using Stokes' theorem, the solid angle can be computed from any closed surface bounded by the geodesic triangle. It can thus be seen as a contour integration along the geodesic path.
We now reformulate these insights by analyzing the argument of the Bargmann invariant $\mathrm{Tr}\,(\hat{\Pi}_f\hat{\Pi}_r\hat{\Pi}_i)$ [33], introduced in section 3.4, that appears in the numerator of the weak value expression $\Pi_{r,w}$. Because the denominator $\mathrm{Tr}\,(\hat{\Pi}_f\hat{\Pi}_i) = |\langle\psi_f|\,\psi_i\rangle|^2$ is always positive, the argument of the weak value is equal to the argument of the Bargmann invariant associated with the initial state, the projector state weakly measured and the final state [18, 102, 103, 108]. In any dimension, as mentioned in section 3.4, this invariant is linked to the geometric phase $\varphi_g = \arg\mathrm{Tr}\big(\hat{\Pi}_f\hat{\Pi}_r\hat{\Pi}_i\big) = \arg(\langle\psi_i|\psi_f\rangle\langle\psi_f|\psi_r\rangle\langle\psi_r|\psi_i\rangle)$ that would arise from a parametric evolution of the quantum system along the closed geodesic triangle (in the sequence $|\psi_i\rangle \to |\psi_r\rangle \to |\psi_f\rangle \to |\psi_i\rangle$) [109]:

$$\varphi_g = -\oint_{C_\Delta}\mathrm{Im}\langle\psi(s)|\frac{d\psi(s)}{ds}\rangle\,ds = -2\iint_{\Sigma(C_\Delta)}\mathrm{Im}\langle\frac{d\psi(s,t)}{dt}|\frac{d\psi(s,t)}{ds}\rangle\,ds\,dt, \tag{4.3}$$

where we chose to describe states in Hilbert space for the convenience of readers familiar with the Hilbert space description of geometric phases. The first integral is the integral of the Berry connec-

tion along the closed geodesic triangle C_Δ parametrized by $|\psi(s)\rangle$. The last member of Eq. 4.3 is a surface integral over any closed surface $\Sigma(C_\Delta)$ bounded by the geodesic triangle C_Δ, where $|\psi(s,t)\rangle$ is an arbitrary parametrization of the surface $\Sigma(C_\Delta)$. This is the integral of the Berry curvature. In any dimension, the argument of the weak value is thus identical to the Pancharatnam-Berry phase that a quantum state would pick up from a parametric state evolution along the closed geodesic triangle. We note however that weak values arise in many contexts in physics and we should not assume here that the geometric phase associated with the argument of the weak value is actually acquired by a quantum state evolving during the physical process described by the weak value.
The quantum state manifolds of $N-$level systems correspond to the complex projective spaces $\mathbb{C}\mathrm{P}^{N-1}$. They are Kähler manifolds [92], which means that they are equipped with a Hermitian form that provides both a Riemannian metric (Fubini-Study) and a symplectic form. The geometric phase Eq. 4.3 is linked to the symplectic area computed on the geodesic triangle using the symplectic form. In the qubit case, the Riemannian and symplectic areas of geodesic triangles are equivalent (they are equal up to a constant factor that depends on the normalization convention for the total areas). However, this is no longer the case in $\mathbb{C}\mathrm{P}^{N-1}$ with $N \geq 3$. For this reason, in three-level systems and beyond, the weak value argument cannot be as straightforwardly interpreted, nor as a solid angle, nor as a Riemannian area of a geodesic surface, as it is possible in the qubit case. Nevertheless, the symplectic area is independent of the particular surface on which it is computed. The argument of the weak value of the projector is thus appropriately seen as arising from a contour integral along the boundary geodesics of the triangle, which accumulates the incremental geometric phase changes along the closed path. The argument of the weak value of any projector on pure state is a three-point invariant of the geodesic triangle.

4.2 Weak values of projectors in $\mathbb{C}^3$

We now generalize our geometric description to three-level systems. This is not trivial as the state manifold cannot be mapped bijectively to a (larger) sphere, contrary to the two-level case. In three-level systems, pure states are then associated with rays that are points of the projective plane $\mathbb{C}\mathrm{P}^2$, more details can be found in section 3.2. In $\mathbb{C}\mathrm{P}^1$, we used the identity and three (N^2-1 with $N=2$) 2×2 traceless generators of SU(2) (the three Pauli matrices) as a basis to expand the projectors. In $\mathbb{C}\mathrm{P}^2$, we expand projectors in terms of the eight (N^2-1 with $N=3$) 3×3 traceless Gell-Mann matrices $\hat{\lambda}_i$, a representation of the Lie algebra SU(3) [110] (we define the generators in appendix B). However, the quantum state manifold $\mathbb{C}\mathrm{P}^2$ is not equivalent to the surface of the 7-sphere S^7 in eight dimensions: all three-level states are on the sphere surface but most points on the surface of the 7-sphere are not proper quantum states. A projector on a pure state is defined in Eq. 3.9. We use the properties of the generators of the Lie algebra of SU(3) to calculate the expression of the weak value of a three-level system projector from Eq. 2.20: $\Pi_{r,w} = \mathrm{Tr}\left(\hat{\Pi}_f\hat{\Pi}_r\hat{\Pi}_i\right)/\mathrm{Tr}\left(\hat{\Pi}_f\hat{\Pi}_i\right)$. Applying the definition of projectors in terms of Gell-Mann matrices Eq. 3.9, we find

$$\Pi_{r,w} = \frac{1+2\vec{f}\cdot\vec{r}+2\vec{r}\cdot\vec{i}+2\vec{f}\cdot\vec{i}+2\vec{f}\cdot\left(\vec{r}\star\vec{i}\right)+i2\sqrt{3}\vec{f}\cdot\left(\vec{r}\wedge\vec{i}\right)}{3+6\vec{f}\cdot\vec{i}}, \tag{4.4}$$

where the 8-dimensional real vectors $\vec{i}$, $\vec{f}$ and $\vec{r}$ represent the pre- and post-selected states and the weakly measured projector state, respectively. The qutrit (three-level) weak value Eq. 4.4 bears similarities with the qubit case Eq. 4.1: for SU(2), the structure constants f_{abc} are given by the Levi-Cevita symbol while $d_{abc} = 0$, so that the wedge product reduces to the usual cross-product in three dimensions while the star product contribution disappears. We discuss additional properties of the $\star$ and $\wedge$ products in appendix D and we provide detailed calculations leading to Eq. 4.4 in appendix F.

Weak values are regularly considered in terms of their real and imaginary parts because this is how they affect typical weak measurements. Nonetheless, interpreting weak values in terms of their modulus and argument provides us more insight about their geometrical properties. Considering the real and imaginary parts of Eq. 4.4, the weak value argument is,

$$\arg \Pi_{r,w} = \arctan \frac{2\sqrt{3}\,\vec{f}\cdot\left(\vec{r}\wedge\vec{i}\right)}{1+2\left(\vec{f}\cdot\vec{r}+\vec{r}\cdot\vec{i}+\vec{f}\cdot\vec{i}\right)+2\,\vec{f}\cdot\left(\vec{r}\star\vec{i}\right)} + \phi\left(\Pi_{r,w}\right), \tag{4.5}$$

where the term ϕ essentially determines the appropriate quadrant (which depends on the signs of the real and imaginary parts of the weak value):

$$\phi(f) = \begin{cases} 0 \text{ if } \mathrm{Re}(f) > 0 \\ \pi \text{ if } \mathrm{Re}(f) < 0 \end{cases} \tag{4.6}$$

As discussed previously, this argument represents a geometric phase because it is equal to the argument of the Bargmann invariant [33] associated with the initial state, the projector state weakly measured and the final state [18, 102, 103, 108] as expressed in Eq. 4.3. It corresponds to a symplectic area evaluated on the geodesic triangle using the symplectic form of the projective space $\mathbb{C}\mathrm{P}^2 = \mathrm{SU}(3)/\mathrm{U}(2)$ [84], whose expression depends only on the vertices $\vec{i}$, $\vec{r}$ and $\vec{f}$ (which confirms the purely geometric origin of the argument). It is important to note that the geodesics of the quantum state manifold do not correspond to geodesics of S^7: they are not arcs of great circles of S^7. In particular, the geometric phase is not equivalent to the Riemannian area of the S^7 spherical triangle defined by the three vertices (which could include points that are not states), nor to the Riemannian area of a surface built from geodesics linking one vertex to the opposite side of the geodesic triangle (which is not unique as the surface generally depends on the chosen vertex in the triangle).

In Fig. 4.1, we represent the geodesic triangle spanned by three quantum states associated with a projector weak value, in $\mathbb{C}\mathrm{P}^1$ for qubit systems and in $\mathbb{C}\mathrm{P}^2$ for qutrit systems. For two-level systems, the three quantum states lay on the surface of the Bloch sphere and the argument is connected to the area of the spherical triangle, equivalent to the solid angle. For three-level systems, the geometry is more complicated. We can represent $\mathbb{C}\mathrm{P}^2$ graphically using a three-dimensional sphere octant, for more details see Fig. 3.2. Beware that the geodesics connecting the triangle vertices on the octant do not typically appear as spherical arcs. Each pair of vertices generates a unique complex projective line (i.e. a two dimensional subspace isomorphic to a Bloch sphere) in the complex projective plane $\mathbb{C}\mathrm{P}^2$. Topologically, the three geodesics connecting the vertices are thus arcs of great circles in each of these three distinct (in general) $\mathbb{C}\mathrm{P}^1$ subspaces. However, when projected on the sphere octant, the geodesic triangle is inevitably distorted. On the S^7 sphere, these geodesics would appear as circle arcs connecting the vertices. However these circle arcs

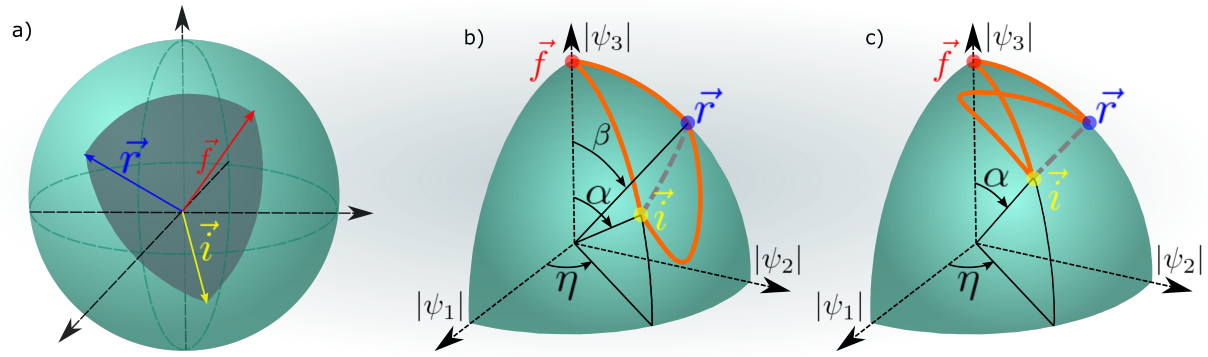

Figure 4.1: Representation of the geodesic triangle generated by the initial state ($\vec{i}$), the observable state ($\vec{r}$) and the final state ($\vec{f}$) in the complex projective spaces $\mathbb{C}\mathrm{P}^1$ (a) and $\mathbb{C}\mathrm{P}^2$ (b and c). The argument of the weak value of a projector is associated with the symplectic area of the triangle. (a) For two-level systems, the argument is also linked to the area and solid angle of the spherical triangle spanned by the three $\mathbb{R}^3$ vectors representing states on the Bloch sphere. (b) and (c) Depiction of two different geodesic triangles of three-level systems, using the spherical octant projection. Reproduced from [19].

would not be arcs of great circles because the geodesics of $\mathbb{C}\mathrm{P}^2$ are not those of S^7 (which is a reminder that the points of $\mathbb{C}\mathrm{P}^2$ are constrained to a four-dimensional subset of S^7 equipped with the Fubini-Study metric and not with the metric of the round sphere). Considering the invariance under unitary transformations, the most general geodesic triangle can be represented by the states $|f\rangle = (0,0,1)^T$, $|r\rangle = (0,\sin\beta,\cos\beta)^T$ and $|i\rangle = \left(\sin\alpha\cos\eta, e^{i\chi_2}\sin\alpha\sin\eta,\cos\alpha\right)^T$, as depicted in Fig. 4.1. The general expression of a state on S^7 and of the geodesic arc linking $\vec{r}$ and $\vec{f}$ are given in appendix E for reference.

4.3 Weak values of projectors in $\mathbb{C}^N$

Our results on three-level systems can be easily generalized to $N-$level systems. Projectors on pure states in $\mathbb{C}^N$ are associated with straight complex lines passing through the origin or, equivalently, with rays that are points of the projective space $\mathbb{C}\mathrm{P}^{N-1}$. We describe them in terms of the N^2-1 generators of the Lie algebra of $\mathrm{SU}(N)$ that generalize the Pauli and Gell-Mann matrices (see appendix G for details). In that case, a projector on a pure state is expressed as in Eq. 3.13(see appendix C).
The argument of the weak value of a projector $\hat{\Pi}_r$ on a pure state of an $N-$level system is expressed using the properties of the generators of $\mathrm{SU}(N)$ as,

$$\begin{aligned}\arg\Pi_{r,w} &= \arctan\frac{2\left(\frac{N-1}{2N}\right)^{\frac{3}{2}}\vec{f}\cdot\left(\vec{r}\wedge\vec{i}\right)}{\frac{1}{N^2}+\frac{N-1}{N^2}\left(\vec{f}\cdot\vec{r}+\vec{r}\cdot\vec{i}+\vec{f}\cdot\vec{i}\right)+\frac{(N-1)(N-2)}{N^2}\vec{f}\cdot\left(\vec{r}\star\vec{i}\right)} \\ &+ \phi\left(\Pi_{r,w}\right), \end{aligned} \tag{4.7}$$

where $\phi\left(\Pi_{r,w}\right)$ selects the appropriate quadrant and is specified in Eq. 4.6. Detailed calculations leading to Eq. 4.7 are provided in appendix F. The expression Eq. 4.7 of the argument of the weak

value generalizes the one obtained for three-level systems Eq. 4.5 to the case of $N-$level system projectors on pure states. Taking $N = 3$ and $N = 2$, we recover the results for three-level system projectors and qubit systems, respectively. As explained previously, the argument of the weak value of a projector is equal to the argument of the Bargmann invariant of the three states involved. Therefore, the argument Eq. 4.7 represents a geometric phase connected to the symplectic area of the geodesic triangle in $\mathbb{C}\mathrm{P}^{N-1}$.
To conclude this section, we first would like to emphasize that, using an appropriate unitary transformation, any set of three states of $\mathbb{C}\mathrm{P}^{N-1}$ and the geodesics linking them can always be mapped to a $\mathbb{C}\mathrm{P}^2$ subspace. Therefore, all observations valid for the weak value of qutrit projectors on pure states extend to arbitrary larger dimensions. In particular, Fig. 4.1 provides a valid representation of geodesic triangles in $\mathbb{C}\mathrm{P}^{N-1}$. Furthermore, from a geometric point of view, all weak values of projectors in any finite dimension can be described using 8-dimensional, normalized real vectors using the formulas Eq. 4.4 and Eq. 4.5 valid for $\mathbb{C}\mathrm{P}^2$. We also note that there are two three-point invariants that contribute to the geometric phase: $\vec{f}\cdot(\vec{r}\wedge\vec{i}) = f_{abc}f_a r_b i_c$ and $\vec{f}\cdot(\vec{r}\star\vec{i}) = \sqrt{\frac{N(N-1)}{2}}\frac{1}{N-2}d_{abc}f_a r_b i_c$. Both are invariant under cyclic permutations of the three vectors and under unitary transformations. However, the former is anti-symmetric under the permutation of two vectors, while the latter is symmetric.

4.4 Weak values of general observables

Weak measurement are not confined to projectors on pure states. In practice, experiments also deal with the weak values of arbitrary observables, such as the spin of a particle, projectors on degenerate subspaces or compound observables in multipartite systems to name a few. In this section, we study the weak value of a general Hermitian observable $\hat{A}$ of an $N-$level system. We will show that the weak value of any observable can be expressed in terms of the weak value of a very specific projector that will provide us with a geometrical description in the spirit of what we did before. We decompose the observable in terms of the $N\times N$ identity operator and a traceless operator from the generators of $\mathrm{SU}(N)$:

$$\hat{A} = a_I\hat{I}_N + a_L\,\vec{\alpha}\cdot\hat{\vec{L}}, \tag{4.8}$$

where $\hat{\vec{L}}$ is a vector whose N^2-1 components are the generators of the $\mathrm{SU}(N)$ Lie group (see appendix G), a_I and a_L are real constants and $\vec{\alpha}$ is a normalized vector with N^2-1 real components. Using the properties of the generators $\hat{\vec{L}}$ to compute the traces appearing in the definition Eq. 2.29, we obtain the weak value of a general observable (as shown in appendix F):

$$\begin{aligned} A_{\alpha,w} &= \frac{1}{\frac{1}{N}+\frac{N-1}{N}\vec{f}\cdot\vec{i}}\left[i\frac{a_L(N-1)}{N}\vec{f}\cdot\left(\vec{\alpha}\wedge\vec{i}\right)\right. \\ &+ \frac{a_I}{N}+\frac{a_I(N-1)}{N}\vec{f}\cdot\vec{i}+\frac{a_L\sqrt{2(N-1)}}{N\sqrt{N}}\left(\vec{f}\cdot\vec{\alpha}+\vec{\alpha}\cdot\vec{i}\right) \\ &+ \left.\frac{a_L\sqrt{2(N-1)}(N-2)}{N\sqrt{N}}\vec{f}\cdot\left(\vec{\alpha}\star\vec{i}\right)\right]. \end{aligned} \tag{4.9}$$

This expression generalizes our previous results on projectors, which we recover by setting the appropriate coefficients a_I and a_L from Eq. 3.13 and by constraining the operator using $\vec{\alpha} = \vec{\alpha} \star \vec{\alpha}$. It is thus crucial to note that, in Eq. 4.9, the vectors $\vec{i}$ and $\vec{f}$ must obey the constraints $\vec{i} = \vec{i} \star \vec{i}$ and $\vec{f} = \vec{f} \star \vec{f}$ because they represent states, while $\vec{\alpha}$ is allowed to range freely on the whole surface of the S^{N^2-2} sphere (for this reason, we denote the latter vector with a greek letter, while the former are identified by roman letters). Our normalization conventions for the projector definition Eq. 3.13 allowed us to express the weak values in terms of the geometrical properties of three vectors that all belong to the same unit sphere (see appendix C).
By considering the ratio of the imaginary and real parts of Eq. 4.9, we find the argument of the weak value of an arbitrary Hermitian observable:

$$\arg\left(A_{\alpha,w}\right) = \phi\left(A_{\alpha,w}\right) + \arctan \frac{\frac{a_L(N-1)}{N} \vec{f} \cdot \left(\vec{\alpha} \wedge \vec{i}\right)}{\frac{a_I}{N} + \frac{a_I(N-1)}{N} \vec{f} \cdot \vec{i} + \frac{a_L\sqrt{2(N-1)}}{N\sqrt{N}} \left(\vec{f} \cdot \vec{\alpha} + \vec{\alpha} \cdot \vec{i}\right) + \frac{a_L\sqrt{2(N-1)}(N-2)}{N\sqrt{N}} \vec{f} \cdot \left(\vec{\alpha} \star \vec{i}\right)}, \tag{4.10}$$

where $\phi\left(A_{\alpha,w}\right)$ specifies the quadrant according to Eq. 4.6. This expression bears similarities to the argument of the weak value of a projector on a pure state Eq. 4.7. Notwithstanding the appearance of the constant factors a_I and a_L, the essential differences are the new term a_I/N in the denominator and the fact that $\vec{\alpha}$ does not represent a state in general. We notice that the numerator is fully antisymmetric under permutations of vectors, while the denominator is symmetric under permutations of the initial and final states. The term involving the star product is even fully symmetric under permutations of the three vectors.
In order to interpret this argument in terms of a geometric phase, we relate it to the weak value of a particular projector on a pure state (we call it $\hat{\Pi}_{i'}$). This approach allows us to link the argument to the Bargmann invariant of the pre-selected state, the projector $\hat{\Pi}_{i'}$ and the post-selected state, and, therefore, to a symplectic area in $\mathbb{C}\mathrm{P}^{N-1}$. We define this projector by

$$\hat{\Pi}_{i'} = \frac{\hat{A}\left|\psi_i\right\rangle \left\langle\psi_i\right| \hat{A}}{\left\langle\psi_i\right| \hat{A}^2 \left|\psi_i\right\rangle} \tag{4.11}$$

when $\hat{A}\left|\psi_i\right\rangle \neq 0$ (else the weak value is 0 and the argument is undefined anyway). The state $\left|\psi_{i'}\right\rangle$ results from the application of the observable to the initial state. Since the argument of the weak value of a projector is equal to the argument of the Bargmann invariant, we have

$$\arg \Pi_{i',w} = \arg[\mathrm{Tr}\left(\hat{\Pi}_f \hat{\Pi}_{i'} \hat{\Pi}_i\right)] = \arg \frac{\left\langle\psi_f\right| \hat{A}\left|\psi_i\right\rangle \left\langle\psi_i\right| \hat{A}\left|\psi_i\right\rangle \left\langle\psi_i \middle| \psi_f\right\rangle}{\left\langle\psi_i\right| \hat{A}^2 \left|\psi_i\right\rangle}. \tag{4.12}$$

The expectation value of $\hat{A}^2$ in the pre-selected state is strictly positive and does not contribute to the total argument: $\arg\left\langle\psi_i\right| \hat{A}^2 \left|\psi_i\right\rangle = 0$. The average value $\langle A\rangle_{\psi_i} = \left\langle\psi_i\right| \hat{A}\left|\psi_i\right\rangle$ is a real number: its argument is 0 if it is positive and π if it is negative. Hence, the argument of the weak value of the observable $\hat{A}$ is equivalent to the argument of the weak value of the projector $\hat{\Pi}_{i'}$ modulo π:

$$\arg A_w = \arg \Pi_{i',w} - \arg \langle A\rangle_{\psi_i}. \tag{4.13}$$

We find two contributions. First, the geometric phase arising from the geodesic triangle in $\mathbb{C}\mathrm{P}^{N-1}$ whose vertices correspond to the vectors $\vec{i}$, $\vec{i}'$ and $\vec{f}$ on the S^{N^2-2} sphere. It is connected to the

symplectic area of the geodesic triangle and can alternatively be computed from Eq. 4.3. Second, another geometric phase that is given by the sign of average value of the observable in the initial state. It can easily be expressed in the present formalism, on S^{N^2-2}, in terms of the vectors $\vec{i}$ and $\vec{\alpha}$ by setting $\vec{i} = \vec{f}$ in Eq. 4.9, as done later in section 4.8 with Eq. 4.28.
Describing geometrically the relationship existing between an arbitrary initial state $|\psi_i\rangle$ and the quantum state associated with the projector $\hat{\Pi}_{i'}$ produced by an observable $\hat{A}$ according to Eq. 4.11 is far from a trivial task in general. In the case of the Pauli observables $\vec{\alpha}\cdot\hat{\vec{\sigma}}$, the vector $\vec{i}'$ corresponds to the mirror image of the initial state $\vec{i}$ with respect to the axis $\vec{\alpha}$ of the Pauli operator (i. e. the direction of the spin measurement). However, these particular observables are also unitary operators, which helps in determining their action on a general initial state. More complicated operators or families of operators should be studied on case by case basis. Subsequently in this chapter, we will consider in depth the situation of general observables of two-level systems and leave most higher dimensional cases for follow-up studies.
When the average value $\langle A\rangle_{\psi_i}$ equals zero, its argument can be 0 or π in Eq. 4.13. In this case, the projectors $\hat{\Pi}_i$ and $\hat{\Pi}_{i'}$ are also orthogonal. Therefore, they are linked by infinitely many geodesics and, at first, it is not clear how to define the geodesic triangle. However, the argument of the weak value on the left-hand side of Eq. 4.13 is well-defined since we assumed $A_w \neq 0$. This indicates that it is possible to select an appropriate geodesic to construct the geodesic triangle. This can be done by computing the limit of a family of geodesic triangles built from slightly perturbing the initial state $\hat{\Pi}_i = \lim_{\varepsilon\to 0}\hat{\Pi}_i(\varepsilon)$ so that $\mathrm{Tr}\hat{A}\,\hat{\Pi}_i(\varepsilon) = \langle A\rangle_{\psi_i(\varepsilon)} \neq 0$. There will be two choices for the geodesic (arising from the cases $\langle A\rangle_{\psi_i(\varepsilon)} > 0$ and $\langle A\rangle_{\psi_i(\varepsilon)} < 0$) that will give the correct value for the argument of the weak value using Eq. 4.13. Note that evaluating this limit would often occur automatically when studying the geodesic triangle as a function of the initial state (a natural use of the formalism). Alternatively, it is also possible to work with the projector $\hat{\Pi}_{f'}$ defined from the application of the operator on the post-selected state $\hat{A}\left|\psi_f\right\rangle$ (assuming $\langle A\rangle_{\psi_f} \neq 0$).

4.5 Weak values of the generators of the Lie group of SU(N)

As a relevant, direct application of the results obtained in the previous section, we express the weak values of the generators of the Lie algebra of SU(2) (Pauli matrices), SU(3) (Gell-Mann matrices) and SU(N) in general. Operators linked to these generators describe the spin of particles, light polarization, the orbital angular momentum of light and the polarization correlations in entangled photons, to cite the most typical laboratory use. They are also related to observables in particle physics and cosmology, where conceptual applications of weak measurements start to emerge [111]. We obtain the weak value and its argument, of all the generators, by setting $a_I = 0$ and $a_L = 1$ in the expressions Eq. 4.9 and Eq. 4.10, respectively.
First, we recover the weak value and its argument for two-level systems ($N = 2$) [112], which are

useful points of comparison:

$$\sigma_{r,w} = \frac{\vec{f}\cdot\vec{r}+\vec{r}\cdot\vec{i}+i\left[\vec{f}\cdot\left(\vec{r}\times\vec{i}\right)\right]}{1+\vec{f}\cdot\vec{i}}, \tag{4.14}$$

$$\arg\sigma_{r,w} = \arctan\frac{\vec{f}\cdot\left(\vec{r}\times\vec{i}\right)}{\vec{f}\cdot\vec{r}+\vec{r}\cdot\vec{i}}+\phi\left(\sigma_{r,w}\right), \tag{4.15}$$

where $\phi\left(\sigma_{r,w}\right)$ is defined in Eq. 4.6 and the generator is given by $\vec{r}\cdot\hat{\vec{\sigma}}$. In the particular case of SU(2), the star product is null and wedge product is equivalent to the cross product because the structure constants f_{abc} become the Levi-Civita symbol. Additionally, the vector $\vec{r}$ also represents a state and it is then possible to show that Eq. 4.15 is given by the sum of two solid angles connected to two Bargmann invariants [112]. These two solid angles correspond to the two contributions found in Eq. 4.13 when using the projector $\hat{\Pi}_{i'}$ to determine the geometric phase.

Second, we consider the generators $\vec{\alpha}\cdot\hat{\vec{\lambda}}$ of the Lie group SU(3), i. e. the Gell-Mann matrices [110]:

$$\lambda_{\alpha,w} = \frac{2}{\sqrt{3}}\frac{\vec{f}\cdot\vec{\alpha}+\vec{\alpha}\cdot\vec{i}+\vec{f}\cdot\left(\vec{\alpha}\star\vec{i}\right)+\sqrt{3}\,i\,\vec{f}\cdot\left(\vec{\alpha}\wedge\vec{i}\right)}{1+2\vec{f}\cdot\vec{i}}, \tag{4.16}$$

$$\arg\lambda_{\alpha,w} = \arctan\frac{\sqrt{3}\,\vec{f}\cdot\left(\vec{\alpha}\wedge\vec{i}\right)}{\vec{f}\cdot\vec{\alpha}+\vec{\alpha}\cdot\vec{i}+\vec{f}\cdot\left(\vec{\alpha}\star\vec{i}\right)}+\phi\left(\lambda_{\alpha,w}\right), \tag{4.17}$$

with $\phi\left(\lambda_{\alpha,w}\right)$ defined in Eq. 4.6 and where $\vec{\alpha}$ does not represent a state in general. We note the elegant similarities between the weak values of qubit and qutrit systems. However, the complexity introduced in particular by the additional term involving the star product makes it no longer possible to interpret straightforwardly the geometric phase Eq. 4.17. Indeed, in addition to the three initial vectors $\vec{i}$, $\vec{\alpha}$ and $\vec{f}$, we also have to consider the directions of $\vec{f}\wedge\vec{\alpha}$ and $\vec{f}\star\vec{\alpha}$, which prevent us from reducing the problem to the three dimensions spanned by $\vec{i}$, $\vec{\alpha}$ and $\vec{f}$.

Third, for the generators $\vec{\alpha}\cdot\hat{\vec{L}}$ of SU(N) generalizing the Pauli and Gell-Mann matrices, the weak value and its argument are

$$L_{\alpha,w} = \sqrt{2\frac{N-1}{N}}\frac{\vec{f}\cdot\vec{\alpha}+\vec{\alpha}\cdot\vec{i}+(N-2)\vec{f}\cdot\left(\vec{\alpha}\star\vec{i}\right)+i\sqrt{\frac{N^2-N}{2}}\vec{f}\cdot\left(\vec{\alpha}\wedge\vec{i}\right)}{1+(N-1)\vec{f}\cdot\vec{i}}, \tag{4.18}$$

$$\arg L_{\alpha,w} = \arctan\frac{\sqrt{\frac{1}{2}N(N-1)}\;\vec{f}\cdot\left(\vec{\alpha}\wedge\vec{i}\right)}{\vec{f}\cdot\vec{\alpha}+\vec{\alpha}\cdot\vec{i}+(N-2)\;\vec{f}\cdot\left(\vec{\alpha}\star\vec{i}\right)}+\phi\left(L_{\alpha,w}\right), \tag{4.19}$$

with $\phi\left(L_{\alpha,w}\right)$ defined in Eq. 4.6.

4.6 Weak value of a two-level system observable

We turn our attention to the weak values of arbitrary observables in two-level systems. In particular, we are interested in analyzing their connection to the projector $\hat{\Pi}_{i'}$ Eq. 4.11 that characterizes the

geometric phase associated with their argument Eq. 4.13. Advantageously, all operators and states of two-level systems are linked to a unit vector on the Bloch sphere. We note the initial and final states $\vec{i}$ and $\vec{f}$. Without loss of generality, we consider an observable of the form Eq. 4.8, written as

$$\hat{O}_r = a\left(\hat{I} + \gamma\,\vec{r}\cdot\hat{\vec{\sigma}}\right), \tag{4.20}$$

where $\vec{r}$ is a unit vector and a and γ are real constants. Later on, γ will appear as the relevant parameter for studying geometric phases. When $\gamma = 0$, the weakly measured observable is proportional to the identity. When $\gamma = 1$, it is proportional to a projector. Then, when $\gamma \to \infty$, it tends to a linear combination of the Pauli matrices, proportional to $\vec{r}\cdot\hat{\vec{\sigma}}$. From Eq. 4.9 and Eq. 4.10, we readily obtain the weak value and its argument:

$$O_{r,w} = a\frac{1 + \vec{f}\cdot\vec{i} + \gamma\left(\vec{f}\cdot\vec{r} + \vec{r}\cdot\vec{i}\right) + i\gamma\vec{f}\cdot\left(\vec{r}\times\vec{i}\right)}{1 + \vec{f}\cdot\vec{i}}, \tag{4.21}$$

$$\arg O_{r,w} = \arctan\frac{\gamma\vec{f}\cdot\left(\vec{r}\times\vec{i}\right)}{1 + \vec{f}\cdot\vec{i} + \gamma\left(\vec{f}\cdot\vec{r} + \vec{r}\cdot\vec{i}\right)} + \phi\left(O_{r,w}\right), \tag{4.22}$$

with $\phi\left(O_{r,w}\right)$ giving the appropriate quadrant for the argument, on the basis of the signs of the real and imaginary parts of the weak value Eq. 4.6. It should be highlighted that the argument of the weak value depends chiefly on γ. The parameter a only contributes a 0 or π term through $\phi\left(O_{r,w}\right)$, depending on its sign. Interestingly, the parameter γ plays a role similar to a measurement strength, from which the geometric phase Eq. 4.22 emerges [107].
The projector $\hat{\Pi}_{i'} = \hat{O}_r\hat{\Pi}_i\hat{O}_r / \operatorname{Tr}\hat{\Pi}_i\hat{O}_r^2$ Eq. 4.11 connects the geometric phase Eq. 4.22 to the argument of a Bargmann invariant. Its Bloch sphere vector is

$$\vec{i'} = \frac{1}{1 + 2\gamma\vec{r}\cdot\vec{i} + \gamma^2}\left[\left(1 - \gamma^2\right)\vec{i} + 2\gamma\left(1 + \gamma\vec{r}\cdot\vec{i}\right)\vec{r}\right]. \tag{4.23}$$

Fig. 4.2 depicts the evolution of the $\vec{i'}$ vector as a function of the observable parameter γ. When $\gamma = 0$, $\vec{i'}$ is the pre-selected state $\vec{i}$ because the observable is proportional to the identity. With $\gamma = 1$, $\vec{i'}$ corresponds to $\vec{r}$ since for that value of γ, the operator itself is equivalent to a projector. When $\gamma \to \infty$, the observable is proportional to the Pauli operator $\vec{r}\cdot\hat{\vec{\sigma}}$. Then, $\vec{i'}$ is the mirror image $\vec{i}_m$ of the initial vector $\vec{i}$ with respect to the direction $\vec{r}$ [112]:

$$\vec{i}_m = -\vec{i} + 2\left(\vec{i}\cdot\vec{r}\right)\vec{r}. \tag{4.24}$$

All the possible locations of $\vec{i'}$ form the great circle that connects the initial state $\vec{i}$ to the direction $\vec{r}$ associated with the operator. Positive values of γ correspond to the arc linking $\vec{i} \to \vec{r} \to \vec{i}_m$, while the negative values of gamma give the complementary arc $\vec{i} \to -\vec{r} \to \vec{i}_m$. Knowing $\vec{i'}$, it becomes possible to represent geometrically the argument of the weak value on the Bloch sphere, as a function of γ for fixed pre- and post-selected states, in a manner similar to Fig. 4.1 (a). This is the main appeal of this projector.

At a more quantitative level, Fig. 4.3 represents the smallest angles existing between the various

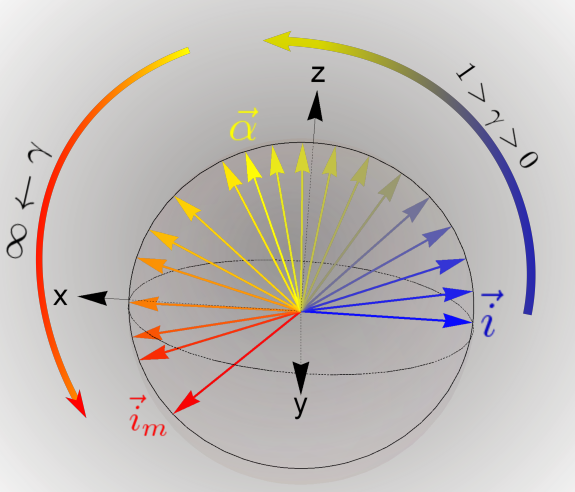

Figure 4.2: Representation of the vector $\vec{i}'$ on the Bloch sphere for positive values of the parameter γ. The blue vector is the initial state, the yellow vector is the vector $\vec{r}$ associated with the observable. The red vector $\vec{i}_m$ is the mirror image of the initial state with respect to the vector $\vec{r}$. Reproduced from [19].

relevant vectors. Two angles are constant: ϕ_{ir} between the initial state $\vec{i}$ and the operator vector $\vec{r}$, as well as ϕ_{ii_m} between the initial state and its mirror image $\vec{i}_m$ through $\vec{r}$. The evolution of the angle $\phi_{ii'}$ between the initial state $\vec{i}$ and the projector $\vec{i}'$ goes from 0 for $\gamma = 0$ (when the operator is proportional to the identity), to ϕ_{ir} for $\gamma = 1$ (when the operator $\hat{O}_r$ acts as the projector on $\vec{r}$), to the maximum value of π for $\gamma = -1/\cos\phi_{ir}$. The latter corresponds to $\hat{O}_r|\psi_i\rangle = 0$. In this case, both the weak value $O_{r,w}$ and the average value $\langle O_r\rangle_{\psi_i}$ are null, and the argument of the weak value is undefined. This value of γ delimits the parameter ranges for which the average value contributes with a factor 0 or π to the geometric phase Eq. 4.13, according to its sign. Beyond this critical value of γ, the value of the $\phi_{ii'}$ angle decreases and tends to ϕ_{ii_m}. We also see that the angle $\phi_{ri'}$ between $\vec{r}$ and $\vec{i}'$ is equal to ϕ_{ir} when $\gamma = 0$ or $\gamma \to \infty$, as these limiting cases correspond to mirror images with respect to $\vec{r}$. When the operator is proportional to a projector ($\gamma = 1$), $\phi_{ri'} = 0$. Finally, we observe that $\phi_{ii'}$ parametrizes the longitude along the great circle arc described by $\vec{i}'$. $\phi_{ii'}$ can be expressed solely in terms of ϕ_{ir} and γ by projecting Eq. 4.23 on the initial state.

4.7 Projectors on degenerate subspaces and Hermitian quantum gates

Sections 4.2 and 4.3 dealt with the weak values of projectors on pure states. However, projectors on degenerate subspaces also arise in practice. For example, the square of a spin-1 operator is associated with a doubly degenerate subspace, which plays an essential role in proofs of quantum contextuality [113]. As shown in appendix C, an arbitrary projector $\hat{P}$ on a k-degenerate subspace of $\mathbb{C}^n$ takes the form

$$\hat{P} = \frac{k}{N}\hat{I}_N + \sqrt{\frac{k(N-k)}{2N}}\vec{p}\cdot\vec{L}, \tag{4.25}$$

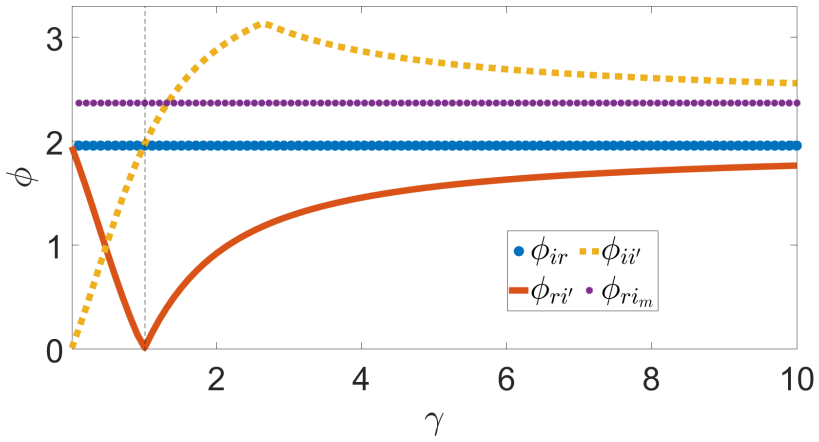

Figure 4.3: Evolution of the smallest angles subtended by the four vectors $\vec{i}$ (arbitrary initial state), $\vec{r}$ (vector associated with the arbitrary qubit operator $\hat{O}_r$), $\vec{i}_m$ (mirror image of $\vec{i}$ through the direction $\vec{r}$) and $\vec{i}'$ (Bloch sphere direction giving the geometric phase associated with the weak value as half a solid angle). In yellow: the angle $\phi_{ii'}$ between $\vec{i}$ and $\vec{i}'$. In dark orange: the angle $\phi_{ri'}$ between $\vec{r}$ and $\vec{i}'$. In blue and purple: the constant angles ϕ_{ir} and $\phi_{ri_m} = 2(\pi - \phi_{ir})$, between $\vec{i}$ and $\vec{r}$ and between $\vec{r}$ and $\vec{i}_m$, respectively. Reproduced from [19].

where the normalized, real vector $\vec{\rho}$ on the S^{N^2-2} sphere is constrained by the star product according to

$$\vec{\rho} \star \vec{\rho} = \frac{N-2k}{N-2}\sqrt{\frac{N-1}{k(N-k)}}\vec{\rho}. \tag{4.26}$$

Setting $k = 1$ in Eq. 4.25 and Eq. 4.26, we recover the projectors on pure states. Then, $\vec{\rho}$ is associated with a quantum state in $\mathbb{C}\mathrm{P}^{N-1}$, but not otherwise (see example in appendix C).
The specific expressions of the weak value and its argument can be deduced as a straightforward application of Eq. 4.9 and Eq. 4.10. The point we actually wish to stress here is that, for such observables, the projector $\hat{\Pi}_{i'}$ Eq. 4.13 of $\mathbb{C}\mathrm{P}^{N-1}$, whose argument of the Bargmann invariant with the pre- and post-selected states is linked to the weak value geometric phase, has a straightforward interpretation: it is simply the projection of the initial state on the degenerate subspace covered by $\hat{P}$. Its state vector is given by $\hat{P}|\psi_i\rangle = |\psi_{i'}\rangle$. Therefore, the argument of the weak value P_w is solely linked to the symplectic area of the geodesic triangle with vertices $|\psi_f\rangle$, $|\psi_i\rangle$ and $|\psi_{i'}\rangle$ and corresponds to the Pancharatnam-Berry phase Eq. 4.3. Indeed, the average value of a projector is always positive $\langle\psi_i|\hat{P}|\psi_i\rangle \geq 0$ and, thus, does not contribute to the geometric phase Eq. 4.13.
Another class of related observables gives rise to a nicely geometric interpretation of the projector $\hat{\Pi}_{i'}$ present in the effective Bargmann invariant. It comprises all the observables that are both unitary and Hermitian. Amongst them, we recover many multi-qubit quantum gates, such as the the CNOT, CZ, SWAP, Toffoli and CSWAP gates, as well as, obviously, the Hadamard gate and all the Pauli gates acting on single qubits. Interestingly all the Hermitian unitary operators are connected to the projectors defined herebefore Eq. 4.25. Indeed, from any projector, we can build

an observable $\hat{S} = 2\hat{P} - \hat{I}_N$ that is both Hermitian and unitary. Therefore,

$$\hat{S} = \frac{2k-N}{N}\hat{I}_N + \sqrt{\frac{2k(N-k)}{N}}\vec{\rho}\cdot\vec{L}, \tag{4.27}$$

where the unit vector $\vec{\rho}$ must obey the star product condition Eq. 4.26 since it is linked to a k-degenerate projector $\hat{P}$. The state produced by $(2\hat{P} - \hat{I}_N)|\psi_i\rangle = |\psi_{i'}\rangle$ results from a generalized reflection of the complex state vector $|\psi_i\rangle$ in $\mathbb{C}^N$ with respect to the subspace corresponding to $\hat{P}$. This provides us with a quite elegant interpretation of the state contributing to the effective Bargmann invariant, reminiscent of the role played by the mirror image of the initial vector on the Bloch sphere in the case of Pauli operators (see Fig. 4.2). For example, in qutrit systems, such an observable $\hat{S}$ would fundamentally flip the sign of one component of the state vector when it is expressed in the diagonal representation of the related projector $\hat{P}$. Therefore, the vector $\vec{i}'$ in S^7 would result from a peculiar reflection symmetry flipping the sign of the initial state vector components in four of the eight dimensions (in appendix E, see the expression Eq. E.1 of an arbitrary state on S^7 given as a function of its Hilbert space representation, where one should change the sign of a component n_i). Additionally, since the observable is unitary, the geodesic arc connecting the states $|\psi_i\rangle$ and $|\psi_{i'}\rangle$ in $\mathbb{C}\mathrm{P}^{n-1}$ could correspond to an actual progressive evolution of the system.

4.8 Beyond weak measurements: average values and quantum uncertainties

Finally, we point out that we recover useful quantum mechanical expressions pertaining to average values of observables by setting identical initial and final states in the weak value Eq. 4.9. It is also helpful to look at expressions involving the variance in order to see how their definitions involve the star $\star$ and wedge $\wedge$ products of SU(N).
We suppose that the quantum system is in the pure state $|\psi\rangle$, characterized by the vector $\vec{i} = \vec{i}\star\vec{i}$. We consider two general observables $\hat{A} = a_I\hat{I}_N + a_L\ \vec{\alpha}\cdot\hat{\vec{L}}$ and $\hat{B} = b_I\hat{I}_N + b_L\ \vec{\beta}\cdot\hat{\vec{L}}$, where we use greek letters for the operator vectors as they do not necessarily correspond to a state on the S^{N^2-2} sphere. Then the average value is related to the 8-dimensional Euclidean scalar product between the two vectors on the sphere:

$$\langle A\rangle = \langle\psi|\hat{A}|\psi\rangle = a_I + a_L\sqrt{2\frac{N-1}{N}}\vec{i}\cdot\vec{\alpha}, \tag{4.28}$$

where we set $\vec{f} = \vec{i}$ in Eq. 4.9. In appendix F, we compute the particular expressions of the squared operator $\hat{A}^2$, the commutator $[\hat{A},\hat{B}]$ and the anticommutator $\{\hat{A},\hat{B}\}$. These operators appear in the Heisenberg uncertainty relations as

$$\mathrm{Var}(A)\mathrm{Var}(B) - \mathrm{Cov}^2(A,B) \geq \frac{1}{4}|\langle[\hat{A},\hat{B}]\rangle|^2, \tag{4.29}$$

where the variance is defined as usually by $\mathrm{Var}(A) = \langle A^2\rangle - \langle A\rangle^2$ and the (symmetric) covariance by $\mathrm{Cov}(A,B) = \frac{1}{2}\langle\{\hat{A},\hat{B}\}\rangle - \langle A\rangle\langle B\rangle$. Using these definitions, we find

$$\mathrm{Var}(A) = \frac{2}{N}a_L^2[1-(N-1)(\vec{\alpha}\cdot\vec{i})^2 + (N-2)\ \vec{\alpha}\star\vec{\alpha}\cdot\vec{i}] \tag{4.30}$$

$$\mathrm{Cov}(A,B) = \frac{2}{N}a_L b_L[\vec{\alpha}\cdot\vec{\beta} - (N-1)(\vec{\alpha}\cdot\vec{i})(\vec{\beta}\cdot\vec{i}) + (N-2)\ \vec{\alpha}\star\vec{\beta}\cdot\vec{i}] \tag{4.31}$$

$$\langle[\hat{A},\hat{B}]\rangle = 2ia_L b_L\sqrt{2\frac{N-1}{N}}\ \vec{\alpha}\wedge\vec{\beta}\cdot\vec{i} \tag{4.32}$$

Thus the two invariants that involve the wedge and star products that are present in the argument of weak values emerge as well in the Heisenberg uncertainty relationship. In particular, we observe that the numerator of the argument of the weak value, which involves the wedge product, is therefore proportional to an average, in the initial state, of a commutator. The operators in this commutator are the weakly measured observable and the final state. (Note that the roles of the initial and final state could be switched using a cyclic permutation of the three vectors.) Ultimately, these two invariants are built to provide contribution involving the three vectors in a fully symmetric or anti-symmetric way. It is suggested in the literature that the average value of the square of the commutator is a predictor of quantum chaos [114]. This can also be evaluated to be

$$\langle|[\hat{A},\hat{B}]|^2\rangle = \frac{8}{N}a_L b_L[\|\vec{\alpha}\wedge\vec{\beta}\|^2 + (N-2)(\vec{\alpha}\wedge\vec{\beta})\star(\vec{\alpha}\wedge\vec{\beta})\cdot\vec{i}]. \tag{4.33}$$

4.9 Usefulness of the argument of the weak value

We wish now to reflect on the significance of the argument of the weak value as a geometric phase. For the weak value of a projector $\hat{\Pi}_r$, we saw that this geometric phase is equivalent to the Pancharatnam-Berry phase that a state would acquire during a parametric evolution along the closed geodesic triangle formed by the initial state, the projector state and the final state. Actually, this corresponds also to the geometric phase for the open curve built from the two successive geodesics connecting $|\psi_i\rangle\langle\psi_i|$ to $|\psi_r\rangle\langle\psi_r|$, and then $|\psi_r\rangle\langle\psi_r|$ to $|\psi_f\rangle\langle\psi_f|$ [109]. Thus, we could be naively tempted to attribute this geometric phase to the final state after a post-selected weak-measurement of the projector $\hat{\Pi}_r$. However, our preliminary investigation of geometric phases during actual weak measurements shows that the geometric phase imparted on the joint system and Gaussian meter state, after post-selection but before meter measurement, does not depend on the weak coupling parameter g to first order (note that this geometric phase arises from a non-cyclic evolution, along an open curve). Thus, the geometric phase acquired during a weak measurement with a Gaussian meter does not depend univocally on the associated weak value (to second order in the coupling parameter, it depends on the meter variance and on the imaginary part of weak value of the square of the observable: $\varphi_g \approx g^2\Delta^2 p\ \mathrm{Im}\langle A^2\rangle_w$). Nevertheless, it is well-known [101] that, after a weak measurement with a Gaussian meter, the average meter position $\langle x\rangle$ is given by $g\,\mathrm{Re}A_w$, while the average meter momentum $\langle p\rangle$ is given by $2g\Delta^2 p\,\mathrm{Im}A_w$. As a result, the argument of the weak value sets the angle pointing to the location of the centroid of the Gaussian Wigner function in the meter phase space after a weak measurement: $\arg A_w = \arctan\frac{\langle p\rangle\Delta x}{\langle x\rangle\Delta p}$ (this angle can be made equal to the geometric phase by an appropriate scaling of the phase space coordinates). Furthermore, Lundeen and Resch [115] showed that the weak value is proportional to

the average α (in the final state $|\phi_m(fi)\rangle$ of the meter) of the annihilation operator $\hat{a}$ associated with the meter phase space. To first order in the coupling, after post-selection, the meter is thus left in a coherent state $|\alpha\rangle \approx |0\rangle + \alpha|1\rangle$ given by the eigenvalue $\alpha = g\Delta p A_w$. Hence, the argument of the weak value appears as the phase of the coherent state, which is also the phase of its component in the first excited state $|1\rangle$. This approach provides as well a natural interpretation to the modulus of the weak value, as its square gives the average occupancy level in this coherent state: $\langle N\rangle_\alpha \approx g^2\Delta^2 p\,|A_w|^2$.

In many weak measurements applications, we are actually interested in the meter shifted averages and not only in the operator weakly measured. For example, when measuring tiny optical deviations of light beams upon reflection on an interface (effects known as the Goos-Hänchen and Imbert-Fedorov shifts), the argument of the weak value would give an indication of the ratio of the observed angular to spatial shifts of the light beam. In such an experiment, the transverse position of the beam plays the role of the meter (subjected to shifts), while the weakly measured operator is an effective observable related to the transfer function of the reflection process (that depends on the polarization) [55]. The principle of performing a (typically amplified) weak measurement of an effective observable derived from the transfer function of a physical process is quite general [116]. Here, we provide some thoughts for the analysis of such ratios arising from experimental observations. The interpretation of the real and imaginary parts of the weak value have been much discussed in the literature. A useful point of view is that the real part of the weak value gives the optimal conditional estimate of the observable given the knowledge imparted by the initial and final states of the pre- and post-selected measurement [41, 117, 118, 119]. Correspondingly, the imaginary part is related to the inaccuracy of the optimal estimate $\varepsilon^2(\hat{F}) = \sum_f \mathrm{Im}^2 A_w(f)$, where f runs over all possible final states of the measurement observable $\hat{F}$ used for post-selection [41, 117, 118, 119]. In some very broad sense, the ratio of the imaginary to the real part appears linked to the inverse of a signal-to-noise ratio. This observation can be made more precise by noting that the real part of the weak value has been linked in weak measurements to the role of the operator $\hat{A}$ as an observable, while the imaginary part has been associated with the operator $\hat{A}$ as the generator of infinitesimal unitary transformations $e^{-i\varepsilon\hat{A}}$, where it plays a dynamical role [41, 120]. The argument of the weak value conveys thus a direct indication of the relative importance of these two aspects of the operator $\hat{A}$ in the physical process giving rise to the weak value. We further evidence this by expressing the weak value as a logarithmic derivative $A_w = i\frac{d}{d\varepsilon}\ln\langle\psi_f|e^{-i\varepsilon\hat{A}}|\psi_i\rangle|_{\varepsilon=0} = i\frac{d}{d\varepsilon}\ln\langle\psi_f|\psi(\varepsilon)\rangle|_{\varepsilon=0}$. By writing $\langle\psi_f|\psi(\varepsilon)\rangle = R(\varepsilon)e^{iS(\varepsilon)}$ (with $R,S\in\mathbb{R}$), we find $A_w = -\frac{d}{d\varepsilon}S(\varepsilon) + i\frac{d}{d\varepsilon}\ln R(\varepsilon)$. The argument of the weak value reflects then how the amplitude of the complex overlap between the final and initial states varies with respect to its phase in the limit of a vanishing evolution: $\arg A_w = -\frac{d\ln R(\varepsilon)}{dS(\varepsilon)}|_{\varepsilon=0}$. We see that the derivative of the phase of the overlap encodes information about the observable (as the real part of the weak value corresponds to the best estimate), while the imaginary part of the weak value relates to the modification of the post-selection probability due to the unitary evolution through the logarithmic derivative of the overlap amplitude. The first aspect impacts the observed average meter position, while the second impacts its observed average momentum. As the argument is a geometric phase, we understand that the ratio of these very different aspects of the operator action in the weak value is fully determined by the geometry and can be represented and studied using geodesic triangles. This approach could be fruitful to study weak values arising from effective observables generated by unitary transfer functions [116], and even could be gener-

alized to non-Hermitian effective observables [55].
Although we were mainly concerned with discrete observables in this thesis, it is nevertheless enlightening to review the former expressions in the context of the weak value of the momentum post-selected on position: $p_w = i\frac{d}{d\varepsilon}\ln\langle x|\, e^{-i\varepsilon\hat{p}}\,|\psi_i\rangle\,|_{\varepsilon=0} = i\frac{d}{d\varepsilon}\ln\psi(x-\varepsilon)|_{\varepsilon=0} = -i\frac{d}{dx}\ln\psi(x)$, where now $R(x)$ and $S(x)$ are understood as the (real) amplitude and phase of the wavefunction $\psi(x)$ in the limit of an infinitesimal unitary transformation $e^{-i\varepsilon\hat{p}}$. The argument provides thus the ratio of the so-called osmotic momentum $p_o = -\frac{d}{dx}\ln R(x) = \mathrm{Im}\, p_w$ and Bohmian momentum $p_b = \frac{d}{dx}S(x) = \mathrm{Re}\, p_w$ at position x [41, 58, 118]. The osmotic momentum p_o appears in the stochastic interpretation of quantum mechanics (with p_b), where it compensates the stochastic diffusion, while p_b is central in the de Broglie-Bohm interpretation as it defines deterministic particle velocities. The ratio of these two momenta (or of the associated velocities) should thus be seen through the lens of geometric phases! The geometrical investigation of the argument of weak values advocates a holistic interpretation of the weak value as it describes the full observations in phase space, beyond the common dichotomy between the real and imaginary parts.
The geometric description applies to all weak values of discrete observables. Thus, it offers an extensive range of target applications. In particular, we believe our approach could prove useful to study the geometry of the connection between anomalous weak values and contextuality, which is a property describing that a quantum measurement goes beyond merely revealing pre-established values. In the realm of weak measurements, contextuality emerges as a consequence of the outcome being intricately linked to the specific post-selected state that is selected. Indeed, anomalous weak values, which are values outside the range of possible eigenvalues of the observable, are always a witness of contextuality [31, 32]. Additionally, anomalous weak values of arbitrary observables are necessarily linked to anomalous weak values of projectors [31, 32]. As the eigenvalue range of a projector is the $[0,1]$ interval, when the argument of a projector weak value is not equal to 0, the weak value is necessarily anomalous. Thus a non-zero argument of a projector weak value is an indicator of contextuality related to the emergence of a geometric phase. Furthermore, if the modulus of the weak value is larger than 1, this is also an indicator of contextuality. We could thus investigate from a geometrical viewpoint the nature of the contextuality that arise either from a non-zero argument or from an amplification effect. Beyond the projector case, any observable can be rescaled $(\hat{A}-\lambda_{\min}\hat{I})/(\lambda_{\max}-\lambda_{\min})$, so that its eigenvalue range belongs to the $[0,1]$ interval. Then, the argument and modulus of its weak values can be used similarly to the case of projectors to indicate contextuality.
Weak values also appear in dynamical processes [118], independently of weak measurements. For example, they determine the perturbed energy eigenvalues

$$E_n(g) = E_n(0) + \frac{\langle E_n(0)|\,\hat{\Delta}(g)\,|E_n(g)\rangle}{\langle E_n(0)|E_n(g)\rangle} \tag{4.34}$$

due to a perturbation $\hat{\Delta}(g)$, in terms of the initial unperturbed energies $E_n(0)$ [118]. Thus, the positive or negative contributions of the different weak values for all the eigenstates could be analyzed from their argument (which control if the energies increase or decrease), by considering jointly the various geodesic triangles involved. Our formalism provides a description of the relevant weak values quantities in a geometric way in $\mathbb{R}^{N^2-1}$ that helps to visualize physical processes influenced by phases, in a conceptually simpler approach than in the complex Hilbert vector space. In this context, let us restate that a single weak value is determined by three states only. As a result, in any

finite dimension, the geodesic triangle can be studied in a three dimensional subspace equivalent to $\mathbb{C}\mathrm{P}^2$. The geometric representation of a single weak value can thus be reduced to a qutrit case, which may simplify the geometric description (although not as much as in the qubit case). Focusing on qutrit systems is of prime importance to understand the geometry of weak values generally. In the example above, even if there are many energy eigenstates, for each of them, the problem reduces to a three dimensional subspace.
Finally, the appearance of geometric phases in weak values suggests that a geometric description of their argument should prove useful in fields in which the phase is essential, such as interferometry or quantum computing tasks. For example, beyond two-level systems, it would especially benefit to studies of the coupling of the three-dimensional polarization of light to its environment during propagation, of the orbital angular momentum of light beams used for quantum information processing tasks in large dimensions, of interferometers involving particles with spin larger than $\frac{1}{2}$, as well as of quantum paradoxes, where the phase plays an important role. Indeed, as we focused our attention to the argument of the weak value and its associated geometric phase, instead of the real part of the weak value (as is mostly done in the literature), we provide particular insight into the interferometric aspects of weak values and weak measurements.

4.10 Conclusions

We described on hyperspheres the geometrical properties of the weak values of general observables. For projectors on pure states of $N-$level systems, the argument of the weak value is the argument the Bargmann invariant of the initial, projector and final states. The argument of the Bargmann invariant and, hence, the argument of the weak value represent a geometric phase that is associated with the symplectic area of the geodesic triangle in the projective space $\mathbb{C}\mathrm{P}^{N-1}$. The states are constrained to a $(2N-2)$-dimensional subset of the unit sphere S^{N^2-2}, which generalizes the Bloch sphere. For all observables, we express the weak value and its argument in terms of three Euclidean vectors located on S^{N^2-2}: formulas involve the standard Euclidean scalar product, as well as two vectorial operations inherited from $\mathrm{SU}(N)$, represented by the star $\star$ and $\wedge$ products. We showed that the argument of the weak value is always related to a Bargmann invariant of three projectors, even when the observable probed by the weak measurement is not a projector. Thus we found a geometric depiction of the argument of any weak value in terms of a symplectic area of a geodesic triangle in complex projective space. For arbitrary observables of two-level systems, the geometric phase corresponds to minus half the solid angle subtended by the three vectors associated with the initial state, the effective projector linked to the weak value, and the final state. We studied on the Bloch sphere how the projector associated with the effective Bargmann invariant evolves as a function of the weakly probed observable in a two-level system. We also investigated the geometric operations behind this projector in higher dimensional systems, for arbitrary projectors on degenerate subspaces and for Hermitian quantum gates. We produced the weak values of the generators of $\mathrm{SU}(N)$, including the Pauli and Gell-Mann matrices, which are essential to all spin and polarization applications of weak measurements. The formalism used here applies to both weak and average values, and we illustrated its usefulness beyond weak measurements by expressing the quantities intervening in the Heisenberg inequalities.

Chapter 5

Geometry of N-level operators weak values on the Bloch sphere

In the previous chapter, we moved out of our quantum comfort zone by providing a geometrical description in $\mathbb{C}\mathrm{P}^{N-1}$. However, as the reader may have noticed, the visualization of the system in this space is still rather hard. In this chapter, we would like to go back to the quantum comfort zone, the Bloch sphere. We study the argument of weak values of general observables, succeeding to give a geometric description to this argument on the Bloch sphere, by applying the Majorana symmetric representation. The choice of whether to work on the Bloch sphere or on $\mathbb{C}\mathrm{P}^{N-1}$ depends on the specific system being studied and the properties that need to be retrieved. In other words, different systems and different goals may require different mathematical frameworks, and researchers may choose the one that is most suitable for their particular needs. For example, we will show in this chapter that, in the Majorana framework, it is possible to calculate the entanglement of the system. This study is not achievable straightforwardly in $\mathbb{C}\mathrm{P}^{N-1}$. Nonetheless, the starting space is $\mathbb{C}\mathrm{P}^{N-1}$. Hence, it is more suited to study properties intrinsically related to the complete complex projective space.

The weak value argument of two-level projectors is linked to a geometric phase that is associated with the solid angle on the Bloch sphere of a spherical triangle formed by the pre-selected, probed projector, and post-selected states [112]. In contrast, for N-level systems, the weak value argument of a projector represents a geometric phase, but it is associated with the symplectic area of a geodesic triangle formed by the pre-selected state, probed projector state, and post-selected state in $\mathbb{C}\mathrm{P}^{N-1}$, as demonstrated in the previous chapter [19]. This area-based geometric phase is distinct from the solid angle-based phase, which only applies in $\mathbb{C}\mathrm{P}^2$. Sometimes, we may not only be concerned with projectors, but with other observables as well. However, we can approach this issue by employing the fact that the weak value of any observable can be expressed as the weak value of a projector, as demonstrated in the preceding chapter.

Cormann et al showed that the argument of the weak value of N-level projectors can be expressed as the sum of $N-1$ solid angles on the Bloch sphere. For this, they applied Majorana representation to the three states (initial state, probed projector state, and post-selected state) [18]. Ettore Majorana introduced in the 1930s a mathematical procedure to describe systems larger than qubits (two-level systems) on the Bloch sphere. $N-1$ stars on the Bloch sphere represent an N-level system [121]. The Majorana representation is a powerful tool to get a geometrical insight and to

perform calculations [122, 123, 124]. Several studies, from purely theoretical to quantum computing, made use of this representation [125, 126, 127].
Visualizing a symplectic area in $\mathbb{C}\mathrm{P}^{N-1}$ is not an intuitive task, as it is not the usual Riemannian area. To tackle this problem, in this chapter, we show that, by applying the Majorana representation to the three states involved in the weak value of any N-level observable (pre-selected state, effective projector state [19], and post-selected state), the geometry of the full system is brought to the Bloch sphere. The argument of the weak value is the sum of $N-1$ solid angles on the Bloch sphere. The argument of the projector weak value is equivalent to the argument of the Bargmann invariant associated with the three states (invariant under gauge transformation and re-parametrization).
This chapter is structured as follows. In the first section, we introduce the symmetric Majorana representation formalism. Then, we present the geometric interpretation of weak values of N-level general observables, by applying the Majorana representation. In the third section, these calculations are applied to the specific case of 3-level systems. After this, we present the relevant example of spin-1 systems: we study the argument of the weak value of a spin-1 operator when the modulus of the weak value presents a divergence, a typical situation of an amplification effect appearing in a weak measurement with nearly orthogonal pre- and post-selected states.

5.1 Symmetric Majorana representation

This work will employ the symmetric Majorana representation of $\mathbb{C}\mathrm{P}^{N-1}$, which should not be confused with the Majorana representation of spinors. The representation maps N-level quantum states to $N-1$ stars on the Bloch sphere. To do so, it associates the basis of N-level systems with the symmetric tensorial products of two-level states [93].
Let us consider a four-level system. The Majorana representation maps each of the four pure states to one of the four possible symmetric states produced with three qubits,

$$\begin{aligned}
|0\rangle &\rightarrow |\Psi\rangle = |0\rangle|0\rangle|0\rangle \\
|1\rangle &\rightarrow |\Psi\rangle = \frac{1}{\sqrt{3}}\left(|1\rangle|0\rangle|0\rangle + |0\rangle|1\rangle|0\rangle + |0\rangle|0\rangle|1\rangle\right) \\
|2\rangle &\rightarrow |\Psi\rangle = \frac{1}{\sqrt{3}}\left(|1\rangle|1\rangle|0\rangle + |1\rangle|0\rangle|1\rangle + |0\rangle|1\rangle|1\rangle\right) \\
|3\rangle &\rightarrow |\Psi\rangle = |1\rangle|1\rangle|1\rangle
\end{aligned} \tag{5.1}$$

where the order of the basis can be chosen. This association is straightforwardly generalized to N-level systems,

$$\begin{aligned}
|0\rangle &\rightarrow |\Psi\rangle = \underbrace{|0\rangle\,|0\rangle\,....\,|0\rangle}_{N-1} \\
|1\rangle &\rightarrow |\Psi\rangle = \frac{1}{\sqrt{N-1}}\sum_P |1\rangle\,\underbrace{|0\rangle\,|0\rangle\,...\,|0\rangle}_{N-2} \\
&\vdots \\
|N-2\rangle &\rightarrow |\Psi\rangle = \frac{1}{\sqrt{N-1}}\sum_P |0\rangle\,\underbrace{|1\rangle\,|1\rangle\,...\,|1\rangle}_{N-2}, \\
|N-1\rangle &\rightarrow |\Psi\rangle = \underbrace{|1\rangle\,|1\rangle\,...\,|1\rangle}_{N-1},
\end{aligned} \tag{5.2}$$

where P runs through all the permutations of the states $|0\rangle$ and $|1\rangle$. In general, it is possible to calculate the Majorana stars (points on the Bloch sphere representing quantum pure state) of any N-level pure state, which can be expressed in a basis as,

$$|\psi\rangle = \sum_{i=0}^{N-1} c_i\,|i\rangle\,, \tag{5.3}$$

by using the following polynomial,

$$P(z) = \sum_{k=0}^{N-1} (-1)^k \sqrt{C_{N-1}^k}\, c_k z^{N-1-k}, \tag{5.4}$$

where the binomial coefficients $C_k^{N-1} = \frac{(N-1)!}{k!(N-1-k)!}$ and c_k are the coefficients of the state $|\psi\rangle$. The polar, θ_k, and azimuthal, ϕ_k, angles on the Bloch sphere depend respectively on the modulus and the phase of the roots z_k of the polynomial Eq. 5.4,

$$z_k = e^{i\phi_k} \tan\frac{\theta_k}{2}, \tag{5.5}$$

where $0 \leq \phi_k \leq 2\pi$, and $0 \leq \theta_k \leq \pi$.
This representation provides a method to describe any N-level system as $N-1$ qubits. These qubits can be easily represented as stars on the Bloch sphere. The manner in which the stars are displayed provides information about intrinsic properties of the system. For example, the angle between two stars belonging to the same three-level system provides information about the entanglement of the state. We will exploit these properties in the following sections to obtain a geometrical representation of weak values on the Bloch sphere.

5.2 Weak values of N-level observables in terms of Majorana stars

The initial state, the observable and the post-selected state constitute the required components of a weak value. Varying any of these parts can completely modify the quantity. In this section, we provide the theoretical framework to apply the Majorana representation to the different components of the weak value of an N-level observable.
As seen in the previous chapter, the weak value of any discrete observable is proportional to the weak value of a very specific projector with a constant of proportionality that is real [19],

$$A_w = \frac{\langle \psi_f | \hat{A} | \psi_i \rangle}{\langle \psi_f | \psi_i \rangle} = \frac{\langle \psi_i | \hat{A}^2 | \psi_i \rangle}{\langle \psi_i | \hat{A} | \psi_i \rangle} \frac{\langle \psi_f | \hat{\Pi}_{i'} | \psi_i \rangle}{\langle \psi_f | \psi_i \rangle}, \tag{5.6}$$

where $\hat{\Pi}_{i'} = |\psi_{i'}\rangle \langle \psi_{i'}|$, with,

$$|\psi_{i'}\rangle = \frac{1}{\sqrt{\langle \psi_i | \hat{A}^2 | \psi_i \rangle}} \hat{A} |\psi_i\rangle . \tag{5.7}$$

As the weak value is invariant under unitary transformations, two unitary operators are applied to take two states to separable states in the Majorana representation. It is always possible to map two states to separable states (degenerate stars, i.e. a coherent state) in the Majorana representation [99]. The pre-selected state is mapped to

$$|\psi_i\rangle \rightarrow |\Psi'_i\rangle = \underbrace{|0\rangle \ldots |0\rangle}_{N-1}, \tag{5.8}$$

via applying an appropriate unitary operator $\hat{U}^{(1)}$. Capital Greek letters are employed to symbolize states within the Majorana representation, particularly the tensorial product of two-level pure states. Conversely, lowercase Greek letters are utilized when dealing with systems of N-levels. The general form of the unitary operator to take a state $|\psi_1\rangle$ to another state $|\psi_2\rangle$ is,

$$\hat{U} = e^{-i \arg \langle \psi_2 | \psi_1 \rangle} \left(\hat{I} - 2 |\Delta\rangle \langle \Delta| \right), \tag{5.9}$$

where,

$$|\Delta\rangle = \frac{e^{-i \arg \langle \psi_2 | \psi_1 \rangle} |\psi_1\rangle - |\psi_2\rangle}{\sqrt{2 \left(1 - |\langle \psi_2 | \psi_1 \rangle|\right)}}. \tag{5.10}$$

The other components are also affected by the unitary transformation,

$$\hat{A} \rightarrow \hat{U}^{(1)} \hat{A} \hat{U}^{(1)^\dagger} = \hat{A}', \tag{5.11}$$

and

$$\hat{U}^{(1)} |\psi_f\rangle = |\psi'_f\rangle . \tag{5.12}$$

A second unitary operator $\hat{U}^{(2)}$ that leaves the pre-selected state invariant,

$$|\psi''_i\rangle = \hat{U}^{(2)} |\psi'_i\rangle = |\psi'_i\rangle , \tag{5.13}$$

is applied to map the state $|\psi_{i'}\rangle$ expressed in Eq. 5.7 to a second separable state,

$$|\psi'_{i'}\rangle \rightarrow |\Psi''_{i'}\rangle = \underbrace{|\phi_{i'}\rangle ... |\phi_{i'}\rangle}_{N-1}. \tag{5.14}$$

This unitary operator should also be applied to the post-selected state,

$$\hat{U}^{(2)} |\psi'_f\rangle = |\psi''_f\rangle . \tag{5.15}$$

After both unitary operators, the pure post-selected state is a general pure N-level state,

$$|\Psi''_f\rangle = \frac{1}{\sqrt{M}} \sum_P \hat{P} \left[\left|\phi_f^{(1)}\right\rangle ... \left|\phi_f^{(N-1)}\right\rangle \right], \tag{5.16}$$

where the sum runs through all the permutations. After removing the global phase [1], the state can be written as a symmetric state in the Majorana representation. Writing the state as,

$$|\psi''_f\rangle = \sum_{i=0}^{N-1} c_i |i\rangle , \tag{5.17}$$

and solving the Majorana polynomial, Eq. 5.4, one can express the state in the Majorana symmetric representation [93, 128].
The weak value is now calculated, following Eq. 5.6, as,

$$A_w = \frac{\left\langle \psi''_f \right| \hat{A}'' |\psi''_i\rangle}{\left\langle \psi''_f \middle| \psi''_i \right\rangle} = \frac{\langle \psi_i | \hat{A}^2 |\psi_i\rangle}{\langle \psi_i | \hat{A} |\psi_i\rangle} \Pi^{(1)}_{i',w} \Pi^{(2)}_{i',w} \dots \Pi^{(N-1)}_{i',w}, \tag{5.18}$$

where each two-level system weak value is,

$$\Pi^{(j)}_{i',w} = \frac{\left\langle \phi_f^{(j)} \middle| \phi_{i'} \right\rangle \langle \phi_{i'} | \phi_i \rangle}{\left\langle \phi_f^{(j)} \middle| \phi_i \right\rangle}. \tag{5.19}$$

The modulus of the weak value is thus the product of $N-1$ moduli of weak values of qubit projectors,

$$\begin{aligned} |A_w| &= \frac{\langle \psi_i | \hat{A}^2 |\psi_i\rangle}{|\langle \psi_i | \hat{A} |\psi_i\rangle|} |\Pi^{(1)}_{i',w}| \cdot |\Pi^{(2)}_{i',w}| ... |\Pi^{(N-1)}_{i',w}| \\ &= \sqrt{\langle \psi_i | \hat{A}^2 |\psi_i\rangle} \left| \frac{\left\langle \phi_f^{(1)} \middle| \phi_{i'} \right\rangle}{\left\langle \phi_f^{(1)} \middle| \phi_i \right\rangle} \right| \left| \frac{\left\langle \phi_f^{(2)} \middle| \phi_{i'} \right\rangle}{\left\langle \phi_f^{(2)} \middle| \phi_i \right\rangle} \right| \dots \left| \frac{\left\langle \phi_f^{(N-1)} \middle| \phi_{i'} \right\rangle}{\left\langle \phi_f^{(N-1)} \middle| \phi_i \right\rangle} \right|, \end{aligned} \tag{5.20}$$

[1] As the expressions of the weak value only depend on the projector, $\hat{\Pi}_{i'}$, this phase has no impact.

where the following property has been used $\langle\psi_{i'}|\psi_i\rangle = \underbrace{\langle\phi_{i'}|\phi_i\rangle\langle\phi_{i'}|\phi_i\rangle\ldots\langle\phi_{i'}|\phi_i\rangle}_{N-1} = \frac{\langle\psi_i|\hat{A}|\psi_i\rangle}{\sqrt{\langle\psi_i|\hat{A}^2|\psi_i\rangle}}$.
The argument of the weak value of $\hat{A}$ is the sum of $N-1$ arguments of weak values of qubit projectors and the argument of the expectation value of the operator $\langle\hat{A}\rangle_i = \langle\psi_i|\hat{A}\,|\psi_i\rangle$, which is either 0 or π.

$$\begin{aligned} & \arg A_w = \\ = \;& \arg\Pi^{(1)}_{i',w} + \arg\Pi^{(2)}_{i',w} + \ldots + \arg\Pi^{(N-1)}_{i',w} - \arg\langle\hat{A}\rangle_i, \\ = \;& -\frac{\Omega_{ii'_1 f}}{2} - \frac{\Omega_{ii'_2 f}}{2} - \ldots - \frac{\Omega_{ii'_{N-1} f}}{2} - \arg\langle\hat{A}\rangle_i \\ = \;& \sum_j \arg\left(\left\langle\phi_i\middle|\phi_f^{(j)}\right\rangle\left\langle\phi_f^{(j)}\middle|\phi_{i'}\right\rangle\right) - \arg\langle\hat{A}\rangle_i \end{aligned} \tag{5.21}$$

Each argument of a qubit projector weak value represents a geometric phase that is associated with the area of the solid angle on the Bloch sphere of the spherical triangle spanned by the vectors representing the pre-selected state, the application of the observable over the initial state and the post-selected state in the Majorana representation.
The argument of the weak value of an observable in N-level system represents a geometric phase that is associated with the symplectic area of the geodesic triangle spanned by the geodesics linking the three vectors representing the pre-selected state, the application of the observable over the pre-selected state and the post-selected state in $\mathbb{C}\mathrm{P}^{N-1}$. This space is a Kähler manifold, which means that there are three compatible structures: the complex structure, the symplectic structure and the Riemannian structure. In $\mathbb{C}\mathrm{P}^1$, the symplectic area and the Riemannian one coincide. Hence, the argument of the weak value of an observable in two-level systems can be described in terms of solid angles. Using Majorana's description, we succeed to associate a symplectic area in $\mathbb{C}\mathrm{P}^{N-1}$ with $N-1$ solid angles on the Bloch sphere. However, the spherical triangle associated with the solid angles, Ω, are not geodesic curves of $\mathbb{C}\mathrm{P}^{N-1}$ in the Majorana representation, apart in $\mathbb{C}\mathrm{P}^1$.
This description allows to visualize the argument of the weak value and Bargmann invariants as function of dynamical parameters, giving a direct intuition of the studied system. Sometimes, the studied systems are actually composed of k different particles. In this case, the Majorana representation would actually provide the geometry of these particles on the Bloch sphere. As we will see in the following sections, this approach allows us to study the entanglement of the system.

5.3 Majorana representation of weak values of observables in three-level systems

In this section, we focus on general weak values of three-level general observables, $\hat{A} = a_I\hat{I} + a_L\vec{\alpha}\cdot\vec{\hat{\lambda}}$, where $\vec{\hat{\lambda}}$ are the Gell-Mann matrices (appendix B). Three-level systems are specially relevant. On the one hand, there are several interesting observables in three-level systems, such as the spin-1 operators, the 3D Stokes parameter operators, or three-level projectors like those appearing in the three-box paradox [65, 129, 130, 131]. On the other hand, as weak values depend only on three vectors, the description of a single weak value is intrinsically a three-level problem.

As weak values are invariant under unitary transformations, it is feasible to apply three unitary operators to transform the three N-level vectors into three states with only three components different from zero. In practice, this maps the vectors and their associated geodesic triangles to a three-dimensional subspace of $\mathbb{C}\mathrm{P}^{N-1}$, equivalent to $\mathbb{C}\mathrm{P}^2$. By applying this procedure, any weak value of systems larger than three dimensions can be converted to a three-level weak value, providing a representation of its argument of the weak value as two solid angles on the Bloch sphere. Consequently, we can always choose to represent the argument with $N-1$ or two solid angles.
Any projector of a pure three-level state can be written in terms of the Gell-Mann matrices and the identity as $\hat{\Pi}_a = \frac{1}{3}\left(\hat{I} + \sqrt{3}\vec{a}\cdot\vec{\hat{\lambda}}\right)$. The weak value of $\hat{A}$ is $A_w = \frac{\langle\psi_f|\hat{A}|\psi_i\rangle}{\langle\psi_f|\psi_i\rangle} = \frac{\mathrm{Tr}\left[\hat{\Pi}_f\hat{A}\hat{\Pi}_i\right]}{\mathrm{Tr}\left[\hat{\Pi}_f\hat{\Pi}_i\right]}$, which is proportional to the weak value of the projector $\hat{\Pi}_{i'}$, where $|\psi_{i'}\rangle$ is defined in Eq. 5.7. Owing to this property, the weak values of general observables are directly linked to Bargmann invariants. The argument of the weak value is equal to the argument of a Bargmann invariant up to a phase of either 0 or π, as seen in the previous chapter.
Having a description of weak values of general observables in terms of projectors, the Majorana representation can be applied to all three states. In that case, the system is mapped from $\mathbb{C}\mathrm{P}^2$ to a representation on the Bloch sphere. The argument of the weak value of a projector of a pure state is the sum of the arguments of two weak values in two-level systems. Each of these arguments is associated with a solid angle on the Bloch sphere.
Let us consider a general pre-selected state $|\psi_i\rangle$ in $\mathbb{C}\mathrm{P}^2$ (removing the global phase),

$$|\psi_i\rangle = \left(\cos\theta_i, e^{i\chi_{1i}}\cos\varepsilon_i\sin\theta_i, e^{i\chi_{2i}}\sin\varepsilon_i\sin\theta_i\right)^T, \tag{5.22}$$

where i is the complex unit. As the weak value is invariant under unitary transformations, we choose to map the pre-selected state to the state,

$$\left|\psi_i'\right\rangle = (1,0,0)^T, \tag{5.23}$$

that is separable in the Majorana representation,

$$\left|\Psi_i'\right\rangle = |\phi_i\rangle\,|\phi_i\rangle, \tag{5.24}$$

with $|\phi_i\rangle = |0\rangle$, choosing,

$$|0\rangle = (1,0)^T \qquad |1\rangle = (0,1)^T. \tag{5.25}$$

The unitary operator that maps the pre-selected state to the state $|\psi_i'\rangle$ is,

$$\hat{U}^{(1)} = \begin{pmatrix} \cos\theta_i & e^{-i\chi_{1i}}\cos\varepsilon_i\sin\theta_i & e^{-i\chi_{2i}}\sin\varepsilon_i\sin\theta_i \\ \sin\theta_i & -e^{-i\chi_{1i}}\cos\varepsilon_i\cos\theta_i & -e^{-i\chi_{2i}}\sin\varepsilon_i\cos\theta_i \\ 0 & -e^{-i\chi_{1i}}\sin\varepsilon_i & e^{-i\chi_{2i}}\cos\varepsilon_i \end{pmatrix} \tag{5.26}$$

When applying this unitary operator to the system, the post-selected state and the observable are also modified, $\left|\psi_f\right\rangle \to \left|\psi_f'\right\rangle$ and $\hat{A} \to \hat{A}'$. After removing the phase on the first component of the state [2] arising from the application of the observable over the initial state, $\left|\psi_{i'}'\right\rangle$ can be written as,

$$\left|\psi_{i'}'\right\rangle = \left(\cos\theta_{i'}, e^{i\chi_{1i'}}\cos\varepsilon_{i'}\sin\theta_{i'}, e^{i\chi_{2i'}}\sin\varepsilon_{i'}\sin\theta_{i'}\right)^T. \tag{5.27}$$

[2] As the expressions of the weak value depend on the projector, $\Pi_{i'}$, this phase has no impact.

At this stage, we apply a second unitary operator $\hat{U}^{(2)}$ that leaves $|\psi_i'\rangle$ invariant and takes the state $|\psi_{i'}'\rangle$ to a separable state,

$$\hat{U}^{(2)} = \begin{pmatrix} 1 & 0 & 0 \\ 0 & e^{-i\chi_{1i'}}\cos\alpha & -e^{-i\chi_{2i'}}\sin\alpha \\ 0 & e^{-i\chi_{1i'}}\sin\alpha & e^{-i\chi_{2i'}}\cos\alpha \end{pmatrix}, \tag{5.28}$$

where $\alpha = -\varepsilon_{i'} + \arcsin\left(\tan\frac{\theta_{i'}}{2}\right)$. This unitary transformation maps $|\psi_{i'}'\rangle$ to,

$$|\psi_{i'}''\rangle = \left(\cos\theta_{i'}, \sqrt{2\cos\theta_{i'}\,(1-\cos\theta_{i'})}, 1-\cos\theta_{i'}\right)^T, \tag{5.29}$$

which, in terms of qubits, is $|\Psi_{i'}''\rangle = |\phi_{i'}\rangle\,|\phi_{i'}\rangle$, with,

$$|\phi_{i'}\rangle = \left(\sqrt{\cos\theta_{i'}}, \sqrt{1-\cos\theta_{i'}}\right)^T. \tag{5.30}$$

After applying both unitary transformations ($\hat{U}^{(1)}$ and $\hat{U}^{(2)}$), the post-selected state $|\psi_f''\rangle$ has the general form, $|\psi_f''\rangle = c_0\,|0\rangle + c_1\,|1\rangle + c_2\,|2\rangle$. To obtain the Majorana symmetrized state, one should solve the following polynomial [99],

$$c_2 - \sqrt{2}c_1 z + c_0 z^2 = 0 \tag{5.31}$$

The polar, θ_k, and azimuthal, ϕ_k, angles on the Bloch sphere can be calculated from the roots z_k of the polynomial, Eq. 5.31.
Once all the transformations are applied, the three states are easily mapped to the Bloch sphere,

$$\begin{aligned} |\psi_i\rangle &\rightarrow |\Psi_i\rangle = |0\rangle\,|0\rangle \\ |\psi_{i'}\rangle &\rightarrow |\Psi_{i'}\rangle = |\phi_{i'}\rangle\,|\phi_{i'}\rangle \\ |\psi_f\rangle &\rightarrow |\Psi_f\rangle = \frac{1}{\sqrt{M}}\left(|\phi_f^{(1)}\rangle\,|\phi_f^{(2)}\rangle + |\phi_f^{(2)}\rangle\,|\phi_f^{(1)}\rangle\right), \end{aligned} \tag{5.32}$$

with,

$$M = 2\left(1 + \left|\langle\phi_f^{(1)}|\phi_f^{(2)}\rangle\right|^2\right). \tag{5.33}$$

The weak value written in terms of the new states is,

$$\begin{aligned} A_w &= \frac{\langle\psi_i|\hat{A}^2|\psi_i\rangle}{\langle\psi_i|\hat{A}|\psi_i\rangle}\frac{\langle\phi_f^{(1)}|\phi_{i'}\rangle\langle\phi_f^{(2)}|\phi_{i'}\rangle\langle\phi_{i'}|\phi_i\rangle^2}{\langle\phi_f^{(1)}|\phi_i\rangle\langle\phi_f^{(2)}|\phi_i\rangle} \\ &= \frac{\sqrt{\langle\psi_i|\hat{A}^2|\psi_i\rangle}}{\langle\psi_i|\hat{A}|\psi_i\rangle}\Pi_{i',w}^{(1)}\Pi_{i',w}^{(2)}, \end{aligned} \tag{5.34}$$

where,

$$\Pi^{(n)}_{i',w} = \frac{\left\langle \phi^{(n)}_f \middle| \phi_{i'} \right\rangle \langle \phi_{i'} | \phi_i \rangle}{\left\langle \phi^{(n)}_f \middle| \phi_i \right\rangle}. \tag{5.35}$$

The quantity $\langle \psi_i | \hat{A}^2 | \psi_i \rangle$ is real and positive and the expectation value of the operator $\hat{A}$, $\langle \hat{A} \rangle_i = \langle \psi_i | \hat{A} | \psi_i \rangle$, is real, therefore, the argument of the weak value is the sum of the arguments of both weak values and an extra phase that is either 0 or π,

$$\arg A_w = \arg \Pi^{(1)}_{i',w} + \arg \Pi^{(2)}_{i',w} - \arg \langle \hat{A} \rangle_i, \tag{5.36}$$

The argument of the weak value of any three-level observable is the sum of two arguments of weak values of projectors of qubits. Each of these arguments is associated with the solid angle on the Bloch sphere of the triangle spanned by the vectors representing the states $|\phi_i\rangle$, $|\phi_{i'}\rangle$ and $\left|\phi^n_f\right\rangle$,

$$\arg A_w = -\frac{\Omega_{ii'f_1}}{2} - \frac{\Omega_{ii'f_2}}{2} - \arg \langle \hat{A} \rangle_i \tag{5.37}$$

The argument of general observable weak values in 3-level systems has two geometric descriptions, one in $\mathbb{C}\mathrm{P}^2$ and a second one on the Bloch sphere. The argument of the weak value of any 3-level observable is a geometric phase associated with the symplectic area in $\mathbb{C}\mathrm{P}^2$ of the triangle spanned by the geodesics connecting the three vectors representing the pre-selected state, the application of the observable over the initial state and the post-selected state. Additionally, this symplectic area can be mapped to a Riemannian area on the Bloch sphere thanks to the Majorana description. In this case, the argument of the weak value is the sum of two arguments that are associated with solid angles on the Bloch sphere.

Any weak value can be described using a three-level system, only three vectors are involved in the calculations. In consequence, the results presented in this section are pertinent for the weak value of any N-level observable. The argument of the weak value of any N-level observable is the sum of the argument of the weak value of two qubit projectors (up to a phase of 0 or π). Consequently, in this section, we have linked the symplectic area of a triangle in $\mathbb{C}\mathrm{P}^{N-1}$ to two solid angles on the Bloch sphere.

In Fig. 5.1, we depict the solid angles linked to the argument of the weak value of a chosen Hermitian operator, the controlled NOT gate, essential to produce entangled states in quantum computing,

$$CNOT = \begin{pmatrix} 1 & 0 & 0 & 0 \\ 0 & 1 & 0 & 0 \\ 0 & 0 & 0 & 1 \\ 0 & 0 & 1 & 0 \end{pmatrix}. \tag{5.38}$$

In Fig. 5.1a), we represent the three solid angles on the Bloch sphere in the Majorana representation and the three states involved in the weak value. Nevertheless, one can always reduce the size of the system to a three-level system (independently on the initial vector space size). In Fig. 5.1b), we depict the two solid angles induced by the argument of the weak value after reducing the size of the space from 4 levels (requiring 3 states) to 3 levels (involving only 2 states). In Fig. 5.1c), the geodesic triangle between the three involved vectors is represented in $\mathbb{C}\mathrm{P}^2$. To do so, we use the

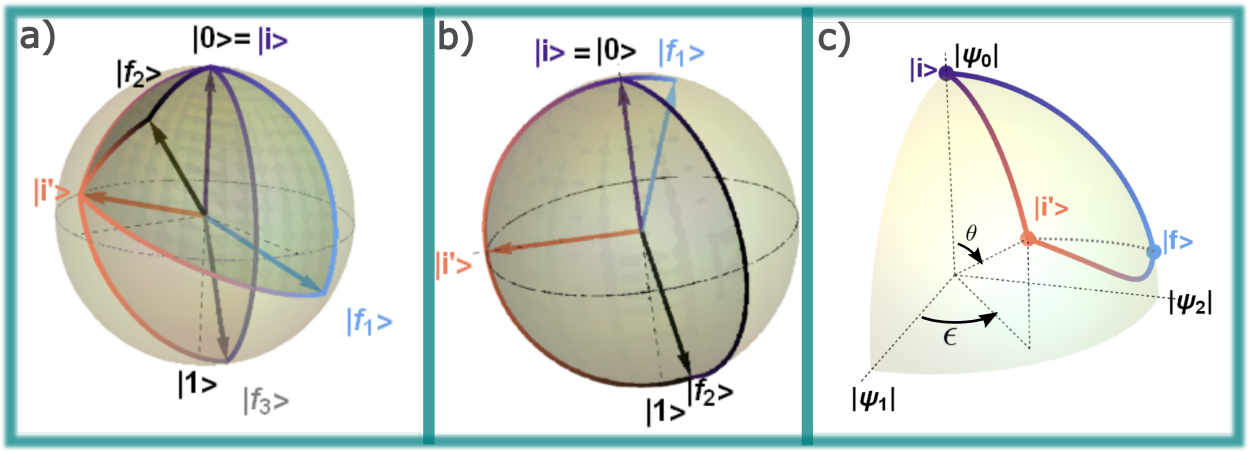

Figure 5.1: Representation of the argument of the weak value of the CNOT gate. The pre-selected state is $|\psi_i\rangle = \frac{1}{\sqrt{4}}(1,-i,1,-i)^T$ and the post-selected state is $|\psi_f\rangle = \frac{1}{\sqrt{5}}(1,0,-2,0)^T$. a) Representation of the three solid angles involved in $\arg(CNOT_w)$ on the Bloch sphere. b) Representation of two solid angles concerning the argument of the weak value of the $CNOT$ gate in the reduced approach (three-level system). c) Depiction of the geodesic triangle in the complex projective space $\mathbb{C}P^2$ between the initial state, the application of the CNOT gate over the initial state and the post-selected state, using the spherical octant projection. Reproduced from [20].

spherical octant projection. Each point of the octant is associated with a torus formed by the two phase components of the Hilbert space, χ_1 and χ_2, $|\psi\rangle = \left(|\psi_0|, e^{i\chi_1}|\psi_1|, e^{i\chi_2}|\psi_2|\right)^T$ [84]. The state $|\psi\rangle$ is projected to the real point $\vec{q} = (|\psi_1|, |\psi_2|, |\psi_0|)$. We also depicted the projected geodesics between each pair of states in three dimensions. The symplectic area is a contour integral along these geodesics, but it cannot be directly represented. The geodesics in $\mathbb{C}P^2$ do not correspond to great circles on the sphere S^7. Moreover, after applying the Majorana representation to the geodesic, it does not correspond to great circles on the Bloch sphere. Between separable states, geodesics correspond to circular segments on the Bloch sphere [132]. However, they can have very complicated shapes when it comes to states that are not separable. In Fig. 5.2, we depicted three three-level states on the octant sphere and on the Bloch sphere, after applying the Majorana representation. The geodesics between the three states have also been added. Furthermore, we mapped the $\mathbb{C}P^2$ geodesics on the Bloch sphere using the Majorana representation. We can see that the $\mathbb{C}P^2$ geodesic between the two separable states is a circular segment. However, the $\mathbb{C}P^2$ geodesics between separable and non-separable states have very complicated configurations.

5.4 Weak values of three-level systems: Spin-1

The spin, describing the intrinsic angular momentum of particles, has a central role in quantum physics. The spin operator depends on the type of particle. The Pauli matrices, the chosen generators of $SU(2)$, describe the spin-1/2 [133]. In the case of spin-1, the operators can be described in terms of generators of $SU(3)$. The spin operators along the three different axes are detailed in terms of the Gell-Mann matrices as, $\hat{S}_x = \frac{1}{\sqrt{2}}\left(\hat{\lambda}_1 + \hat{\lambda}_6\right)$, $\hat{S}_y = \frac{1}{\sqrt{2}}\left(\hat{\lambda}_2 + \hat{\lambda}_7\right)$, $\hat{S}_z = \frac{1}{2}\left(\hat{\lambda}_3 + \sqrt{3}\hat{\lambda}_8\right)$ [134],

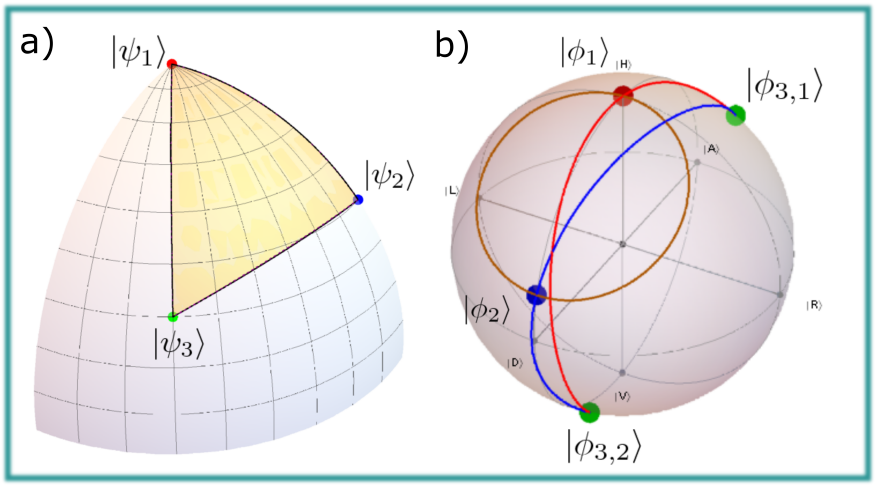

Figure 5.2: Representation of the states $|\psi_1\rangle = (0,0,1)^T$, $|\psi_2\rangle = \left(0, \cos\frac{2\pi}{9}, \sin\frac{2\pi}{9}\right)^T$ and $|\psi_3\rangle = \left(\frac{3}{4}, \frac{\sqrt{3}}{4}e^{\frac{i\pi}{4}}, \frac{1}{2}\right)^T$ in a) the spherical octant. b) Majorana stars representing the previous three-level states. We also added the three geodesics between the three-level states on the octant sphere b). Geodesics between quantum states in the Majorana representation. The represented geodesics in the Majorana representation are not great circles.

where the Gell-Mann matrices are defined in appendix B and $\hbar = 1$.
In several experiments, the weak value of the spin operators has a central role [17, 135]. The real and imaginary parts of the weak values of spin-$1/2$ operators have been theoretically studied, along with their modulus and argument [14, 17, 112, 102]. As the spin direction can be represented directly on the Bloch sphere, the situation is easy to visualize. However, the weak values of the spin-1 operators were much less studied, especially from a geometrical point of view. One possible method is their study in terms of vectors in $\mathbb{C}P^2$, with a generalization of the Bloch sphere [19]. Here, we focus on the description of weak values of the spin-1 operator on the Bloch sphere using the Majorana formalism introduced in the previous sections.
Let us consider the weak values of a linear combination of the three components of the spin, $\vec{\hat{S}} = n_x\hat{S}_x + n_y\hat{S}_y + n_z\hat{S}_z$. Without loss of generality, by setting an appropriate reference point, we rotate the direction $\vec{n} = (n_x, n_y, n_z)^T$ into $\vec{n} = (0,0,1)$. In consequence, we focus on the study of the weak values of $\hat{S}_z$, S_{z_w}. The general pre- and post-selected states have 4 independent parameters each. Owing to the substantial multitude of unconstrained parameters inherent in the general weak value of the spin-1 operator, our approach involves a strategic reduction of these unconfined variables by opting for a specific pre-selected state—a choice that streamlines the complexity while maintaining its nontrivial nature. It is essential to note that the outcomes detailed in this section pertain exclusively to this particular selection. To extrapolate these findings to broader scenarios, it becomes imperative to embark on further explorations. Yet, as we shall demonstrate, these outcomes hold profound intrigue; even in this straightforward scenario, a tapestry of intricate behaviors unfurls, underscoring the significance of delving deeper into the spin-1 illustration. The pre-selected state is chosen to be,

$$|\psi_i\rangle = \frac{1}{\sqrt{6}}(2,1,i)^T, \tag{5.39}$$

where we set the parameters in Eq. 5.22 to $\varepsilon_i = \frac{\pi}{4}$, $\chi_{1i} = 0$, $\chi_{2i} = \frac{3\pi}{2}$, and $\theta = \arccos\sqrt{\frac{2}{3}}$, a simple state, but not a trivial one. In the case of the post-selected state, only two parameters are fixed, $\varepsilon_f = \frac{\pi}{4}$, and $\chi_{2f} = 0$,

$$\left|\psi_f\right\rangle = \left(\cos\theta, \frac{1}{\sqrt{2}}\sin\theta e^{i\xi}, \frac{1}{\sqrt{2}}\sin\theta\right)^T. \tag{5.40}$$

These states provide a system with two independent parameters, θ and ξ, to study. The application of the spin operator to the pre-selected state is,

$$\left|\psi_{i'}\right\rangle = \frac{1}{\sqrt{5}}(2,0,-i). \tag{5.41}$$

Applying the appropriate unitary operators, the initial state is moved to,

$$\left|\psi_i''\right\rangle = (1,0,0) \rightarrow \left|\Psi_i''\right\rangle = \left|0\right\rangle\left|0\right\rangle, \tag{5.42}$$

and the state $\left|\psi_{i'}\right\rangle$ to,

$$\left|\psi_{i'}''\right\rangle = \left(\sqrt{\frac{3}{10}}, \sqrt{-\frac{3}{5}+\sqrt{\frac{6}{5}}}, 1-\sqrt{\frac{3}{10}}\right)^T \rightarrow \left|\Psi_{i'}''\right\rangle = \left|\phi_{i'}\right\rangle\left|\phi_{i'}\right\rangle, \tag{5.43}$$

where,

$$\left|\phi_{i'}\right\rangle = \left(\left(\frac{3}{10}\right)^{\frac{1}{4}}, \sqrt{1-\sqrt{\frac{3}{10}}}\right)^T. \tag{5.44}$$

Making use of these states and applying the Majorana representation to the post-selected state (in Eq. 5.4) one finds the Majorana polynomial that should be solved), we study the argument of the weak value of the spin-1 as the sum of two arguments of two-level projectors of pure states that are associated with two solid angles on the Bloch sphere.

One of the most useful characteristics of weak values is their ability to amplify minute phenomena thanks to their unbounded property. Identifying the behavior of the argument of the weak value when the absolute value tends to infinity is essential due to both the discontinuities that appear in that range and their usefulness.

We study the weak value of $\hat{S}_z$, as a function of a family of post-selected sates described by the parameters θ and ξ. In Fig. 5.3, we represent the maximum value of the modulus of the weak value of $\hat{S}_z$ for each value of ξ. The maximum of the modulus of the weak values takes place for a determined $\theta_{\max}(\xi)$. We use this value to plot the argument of the weak value at $\theta_{\max}(\xi)$ in terms of ξ. We also depict the angle between the two stars on the Bloch sphere representing the post-selected state, $\vec{f}_1$ and $\vec{f}_2$ at $\theta_{\max}(\xi)$ as a function of ξ. The angle between the two vectors on the Bloch sphere represents an entanglement measure of the two-qubit state. If the angle between the vectors is 0°, the state is separable and thus the entropy of entanglement is 0. On the opposite side, if the angle between the two vectors is 180°, the state is a maximally entangled Bell state. The modulus of the weak value presents a vertical asymptote at $\xi = \frac{\pi}{2}$ because the initial and final states are then orthogonal. At the divergence point, the argument of the weak value presents a π jump. This behavior is typical of the argument of the weak value when there is a divergence in the

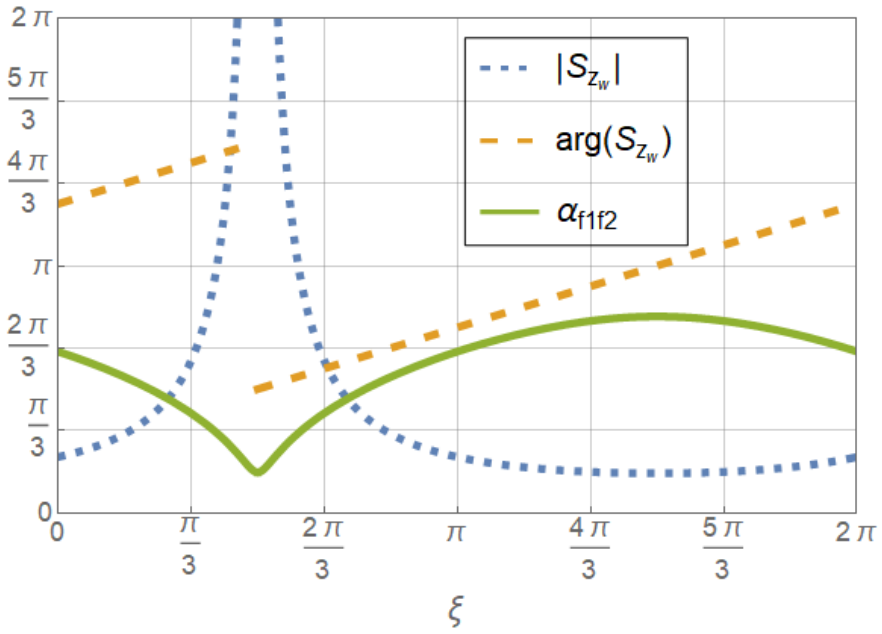

Figure 5.3: Representation of the maximum value of the modulus of the weak value for each value of ξ (blue), of the argument of the weak value for the value of $\theta_{max}(\xi)$ at the maximum of the modulus in terms of ξ (green) and of the angle between $\vec{f}_1$ and $\vec{f}_2$ at $\theta_{\max}(\xi)$ as a function of ξ (orange). Reproduced from [20].

modulus [18].

The two vectors on the Bloch sphere associated with the final state, $\vec{f}_1$ and $\vec{f}_2$, are the closest, 29.42°, where the maximum value of the modulus tends to infinity. Both the initial state and the application of the operator over the initial state present an entropy of entanglement equal to 0, as the states are separable. Hence, the angle between $\vec{f}_1$ and $\vec{f}_2$ represents the total entanglement of the system.

Having a minimum of entropy of entanglement at the divergence in the modulus of the weak values is counter-intuitive at first. Anomalous weak values are a proof of contextuality [31], a characteristic of non-classicality. Therefore, it could have been expected to find a maximum in the entanglement, which is also a characteristic of non-classicality, at the most anomalous weak value (divergence). To clarify if this is an intrinsic characteristic of the system, we depict the value of the angle between the vectors $\vec{f}_1$ and $\vec{f}_2$ for all values of θ and ξ in Fig. 5.4. We also include the value of θ at the maximum of the modulus of the weak value, $\theta_{\max}(\xi)$ (red line). We plot the same line for the minimum of the weak value $\theta_{\min}(\xi)$ (green line). There are two absolute minima of the entropy of entanglement. None of them is at the maximum of the modulus of the weak value (red line in the plot). However, the maximum of modulus of the weak value is always located near to the minimum of the entanglement, as it follows the bottom of the valley of minimal entanglement on Fig. 5.4 (slightly to the left). A very similar correlation links the minimum of the modulus of the weak value (green line) and the maximum of the entanglement. The trends are very similar, but slightly shifted. This behavior is very intriguing due to the correlation of the anomalous weak values and non-classicality. We think this should be explored further in the future.

The weak value diverges for $\xi = \frac{\pi}{2}$, $\theta = \frac{\pi}{2}$, as it can been seen in Fig. 5.3. In Fig. 5.5 and Fig. 5.6,

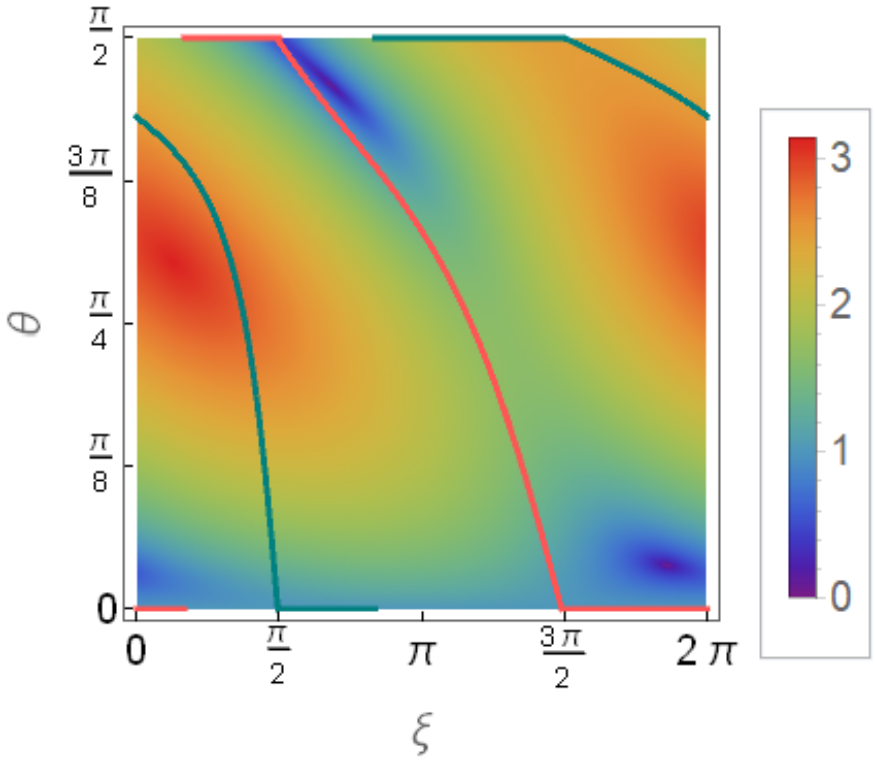

Figure 5.4: Color map of of the angle between the vectors representing the post-selected state on the Bloch sphere $\vec{f}_1$ and $\vec{f}_2$ as a function of θ and ξ. The red line represents the angle θ for which the modulus of the weak value is maximum for fixed values of ξ, $\theta_{\max}(\xi)$. The green line represents the angle θ for which the modulus of the weak value is minimum for fixed values of ξ, $\theta_{\min}(\xi)$. Reproduced from [20].

we depict the evolution of the argument of the weak value in the Majorana representation in terms of ξ (a), the representation on the Bloch sphere of the solid angles associated with the argument of the weak value for the maximum of the modulus of the weak value (b), and the evolution of the angles on the Bloch sphere as a function of ξ (c). In Fig. 5.5, we represent a case with θ smaller than at the divergence ($\theta = \frac{\pi}{2} - 0.2$) and in Fig. 5.6, a case very near the vertical asymptote, ($\theta = \frac{\pi}{2} - 10^{-11}$).

In Fig. 5.5a), one can perceive that, around $\theta = \frac{\pi}{2}$, the slope of the function is quite big. The closer the angle θ is from the divergence case, the larger the slope. In Fig. 5.6a), we represent the extreme case, when $\theta = \frac{\pi}{2}$. There, the slope is infinite, as the argument presents a π jump. In the first case, Fig. 5.5, the big slope in the argument of the weak value occurs when $\arg\Pi^{(2)}_{i',w}$ passes by 0, so that there is no discontinuity. The other projector presents an argument of the weak value that also has a smooth variation at that point. However, $\arg\Pi^{(1)}_{i',w}$ passes by 0 at $\xi = \frac{3\pi}{2}$. In the second case, Fig. 5.6, the argument varies linearly with ξ, except at the point of the maximum of the modulus of the weak value, where it exhibits a π jump. This jump is associated with a π jump in the argument of the weak value of the second projector, $\arg\Pi^{(2)}_{i',w}$. This jump is natural, as the vector is passing by the pole of the Bloch sphere. To observe a smooth movement of the star on the Bloch sphere (without change of sense of the movement), a π jump should be present in the

function of azimuthal angle, ϕ. The argument of $\Pi^{(2)}_{i',w}$ also passes by 0 at $\xi = \frac{3\pi}{2}$. It appears that the non-smooth behavior of the argument of the weak value induces a non-smooth behavior in one argument of the weak value of a projector in the Majorana representation, while the other argument keeps a smooth behavior.

In figures b) of Fig. 5.5 and Fig. 5.6, we represent the solid angles on the Bloch sphere associated with the argument of the weak value. In each figure, the solid angles correspond to the case in which the modulus of the weak value is maximum, $\{\theta = \pi/2 - 0.2, \xi = 2.09\}$ and $\{\theta = \frac{\pi}{2}, \xi = \frac{\pi}{2}\}$ respectively. The value of the maximum is highlighted with a vertical line (pink in Fig. 5.5 and green in Fig. 5.6). Far from the divergence, Fig. 5.5, there are clearly two solid angles. However, very close to the divergence, Fig. 5.6, all the vectors are nearly on the same plane on the Bloch sphere. One of the qubit states representing the post-selected state in the Majorana representation is orthogonal to the qubit state representing the initial state, a condition required for the appearance of a divergence. All vectors on the Bloch sphere are not necessarily on the same plane when a divergence is present. When the initial and final states are orthogonal, the great circle between $\vec{i}$ and $\vec{f}_2$ is not unique as there are different paths with the same distance. At $\theta = \frac{\pi}{2}$, in Fig. 5.6, the vectors $\vec{f}_1$ and $\vec{f}_2$ are the closest and thus the entanglement between them is the minimum.

In Fig. 5.5c, 5.6c, we depict both the azimuthal and the polar angles of the two qubits representing the final state, at the divergence position, $\theta = \frac{\pi}{2}$ in Fig. 5.6 and at a smaller value of θ, Fig. 5.5. In Fig. 5.5c, the polar angle θ_{f1} is approximately constant from $\xi = 0$ until the maximum of the modulus of the weak value (vertical line), $\xi = 2.09$. The maximum occurs at a value a bit larger than $\xi = 2.09$. Then, it decreases, presenting a minimum at $\xi = \frac{3\pi}{2}$, where the azimuthal angle, ϕ_{f1}, passes by 0. After that point, the polar angle increases until reaching the initial value. At the jump position, in Fig. 5.6. The polar angle of one of the qubits, θ_{f2}, representing the post-selected state has a maximum at the position of the maximum of the modulus of the weak value (vertical line), where it is orthogonal to the pre-selected state, $\langle f_2|i\rangle = 0$. The polar angle of the other qubit, θ_{f1}, is almost constant in terms of ξ for $\theta = \frac{\pi}{2}$. It exhibits a smooth maximum at $\xi = \frac{\pi}{2}$. At this point the two polar angles are the closest. In Fig. 5.5c, ϕ_{f2} has a large slope near the maximum of the modulus, similarly to the argument of the weak value. In Fig. 5.6c, ϕ_{f2} has a π jump at $\xi = \frac{\pi}{2}$, where the divergence takes place. It also presents a large slope when the argument of the weak value passes by π, when the weak value is purely real. It appears that the azimuthal angle presents a similar behavior as the argument of the weak value when a non-smooth behavior appears.

Using the Majorana representation, we studied different aspects of the weak values, such as the entropy of entanglement. We noticed that an interesting behavior occurs: a maximum (minimum) of the entanglement is near a minimum (maximum) of the modulus of the weak value. The entanglement of the Majorana stars has a clear meaning when the initial state is an actual 2-particle system in a symmetric state. Otherwise, the results can be interpreted following a single-particle entanglement formalism [136]. Only the Majorana approach allows this analysis. Simply visualizing the behavior of the qubits representing the different states on the Bloch sphere, we can interpret the evolution of the argument of the weak value.

5.5 Conclusions

In this chapter, we applied the Majorana symmetric representation to study the geometry of the argument of weak values of N-level general observables on the Bloch sphere. The weak value of

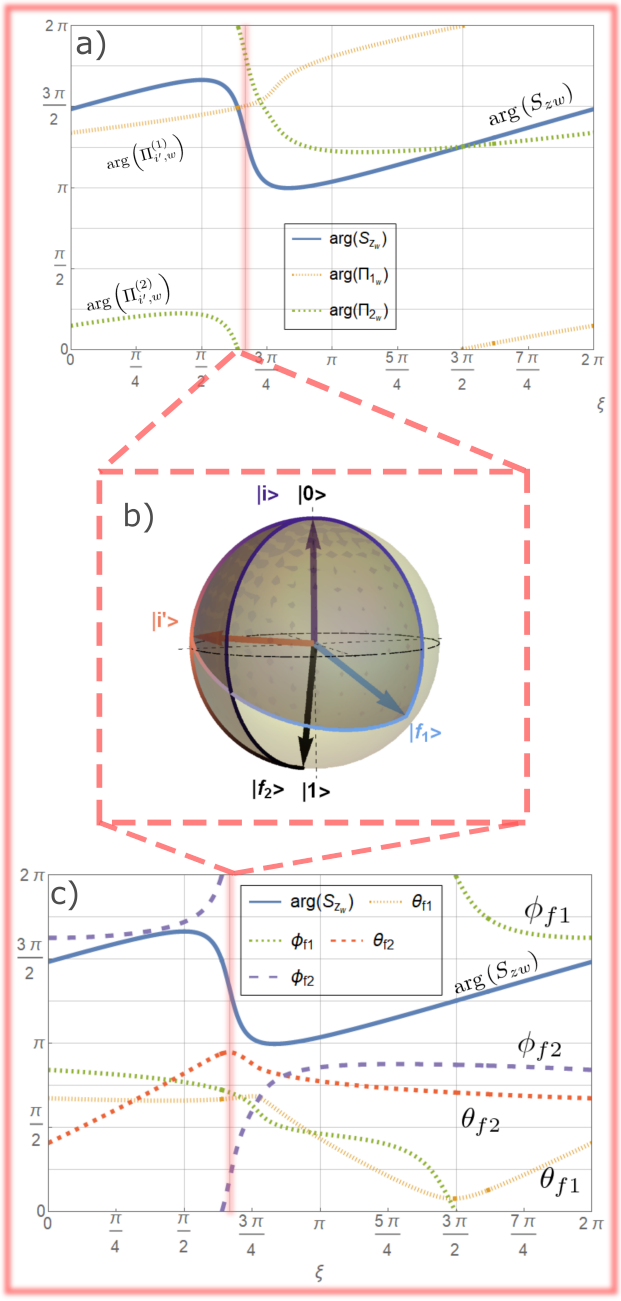

Figure 5.5: a) Argument of the weak value of the spin operator, S_{z_w}, in terms of ξ, argument of the weak value $\Pi^{(1)}_{i',w}$ and $\Pi^{(2)}_{i',w}$ in terms of ξ for $\theta = \frac{\pi}{2} - 0.2$. b) Solid angles on the Bloch sphere $\Omega_{ii'f_1}$ and $\Omega_{ii'f_2}$ for $\theta = \frac{\pi}{2} - 0.2$ and $\xi = 2.09$. c) Argument of the weak value of $\hat{S}_z$ and polar and azimuthal angles, θ and ϕ, of the vectors representing the post-selected state on the Bloch sphere for $\theta = \frac{\pi}{2} - 0.2$, in terms of ξ. A vertical line has been added in a) and c) at the value of ξ for which the modulus of the weak value is maximum, $\xi = 2.09$. Reproduced from [20].

any observable is proportional to the weak value of an effective projector that is defined as the normalized application of the observable over the pre-selected state. The constant of proportionality

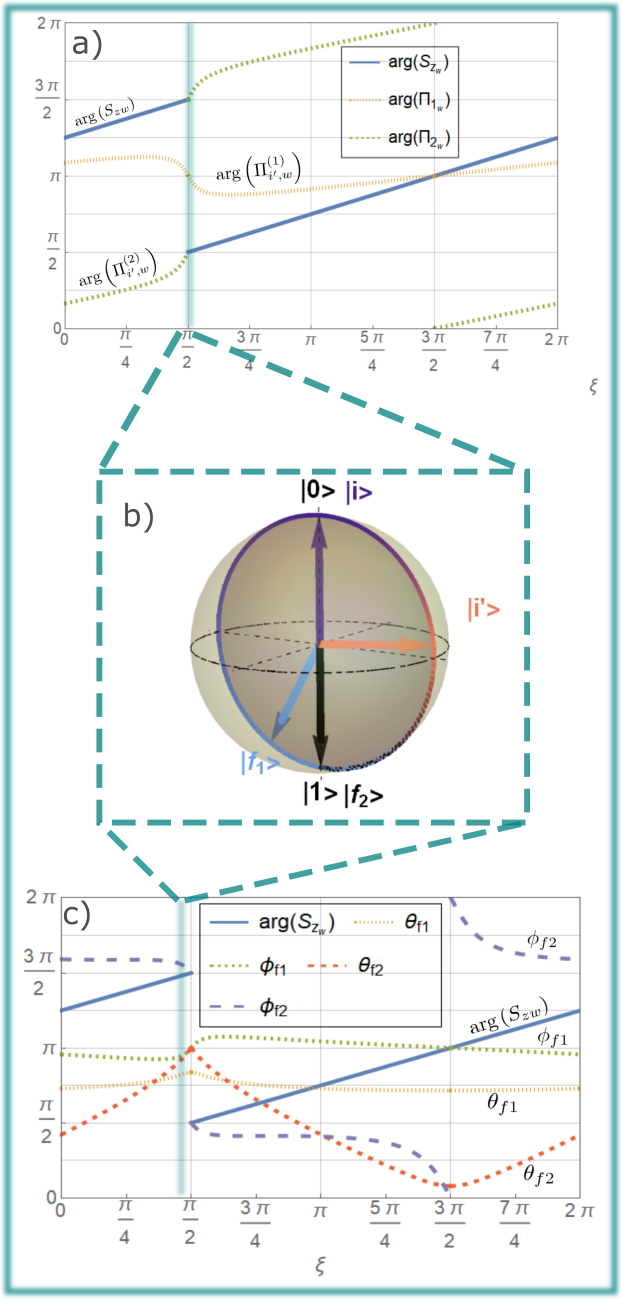

Figure 5.6: a) Argument of the weak value of of the spin operator, S_{z_w}, in terms of ξ, argument of the weak value $\Pi^{(1)}_{i',w}$ and $\Pi^{(2)}_{i',w}$ in terms ξ with $\theta = \frac{\pi}{2} - 10^{-11}$. b) Solid angles on the Bloch sphere $\Omega_{ii'f_1}$ and $\Omega_{ii'f_2}$ for $\xi = \frac{\pi}{2}$ and $\theta = \frac{\pi}{2}$. c) Argument of the weak value of $\hat{S}_z$ and polar and azimuthal angles, θ and ϕ, of the vectors representing the post-selected state on the Bloch sphere for $\theta = \frac{\pi}{2}$, in terms of ξ. A vertical line has been added in a) and c) at the value of ξ for which the modulus of the weak value is maximum, $\xi = \frac{\pi}{2}$. Reproduced from [20].

is real. Hence, the argument of the weak value of any observable is the argument of the weak value of a projector modulo π.

The modulus of the weak value of a general observable is the product of $N-1$ moduli of weak values of projectors in $\mathbb{C}\mathrm{P}^1$ and constants that are independent on the post-selected state. The argument of the weak value of any observable is the sum of $N-1$ arguments of 2-level systems, plus a phase that is either 0 or π. Each of these arguments represents a solid angle on the Bloch sphere. Any weak value depends only on three states. Thus, applying different unitary operators, it is possible to map these states to a three-level system, giving a special importance to the qutrit case. Doing so, we map a symplectic area in $\mathbb{C}\mathrm{P}^{N-1}$ to a sum of two solid angles, instead of $N-1$, on the Bloch sphere (up to a constant that is either 0 or π). The solid angles on the Bloch sphere are determined by the great circles between the four qubit vectors (the two degenerate states associated with the initial state, the two degenerate states linked to the observable, and the two entangled states describing the final state). However, these great circles are not geodesics between the states in $\mathbb{C}\mathrm{P}^{N-1}$.

We applied these results to the spin-1 operator for anomalous weak values in the region of weak value amplification. Using a specific case, we studied the argument of the weak value when the modulus tends to infinity (asymptotic behavior). We found that when the weak value diverges, the angle between the two vectors representing the post-selected state on the Bloch sphere presents a constrained minimum. The angle between the two qubits describing the post-selected state on the Bloch sphere gives a measure of the total entanglement of the system. The maximum value of the modulus is for any value of the angle ξ near the minimum of entanglement. The physical meaning of entanglement when the initial state is a 2-particle system in a symmetric state is straightforward. However, when this is not the case, studies should be performed in the light of single-particle entanglement [136]. The non-smooth behavior of the argument of the weak value seems to be associated with the evolution of the azimuthal angle of the qubits on the Bloch sphere. The azimuthal angle controls the phase of the qubit state components. Ultimately, it is thus responsible for any phase appearing in the qubit weak value.

Chapter 6

Revisiting weak value from a non-normal perspective

In the previous two chapters, our focus was primarily on exploring the concept of the argument of weak values. Now, we shift our attention towards examining the modulus of weak values—an essential element in amplifying weak values that enable the measurement of subtle signals.
Weak values play a role similar to expectation values in certain types of quantum measurements. However, they can be anomalous, meaning that they lie outside the range of eigenvalues of the measured operator, which represents a determined quantum property. Hence they can become complex numbers and unbounded [46, 50, 137]. Anomalous weak values are used to amplify signals [57], to measure complex properties such as wave functions [68] or expectation values of non-Hermitian operators [69], and to study fundamental quantum phenomena, like paradoxes [138, 139, 140, 141]. Anomalous weak values evidence an intrinsic property of non-classicality, called contextuality [31, 32]. A particular subset of anomalous weak values yields weak-value amplification. This phenomenon occurs when the modulus of the weak value is larger than the modulus of all the observable eigenvalues. Such weak values are said to be in the amplifying range.
The weak value can always be expressed as the expectation value of an operator, defined in terms of the pre-selected state, the observable and the post-selected state, $O_w = \mathrm{Tr}\left[\hat{\Pi}_i \hat{A}\right]$, with $\hat{A} = \frac{\hat{O}\hat{\Pi}_i}{\mathrm{Tr}\left[\hat{\Pi}_f \hat{\Pi}_i\right]}$. This operator is not necessarily Hermitian. Most non-Hermitian operators are also non-normal, meaning that $\hat{A}\hat{A}^\dagger \neq \hat{A}^\dagger \hat{A}$. The choice of definition of $\hat{A}$ is arbitrary to some extent, as the weak value can also be defined in terms of an operator involving the post-selected state $\hat{A}'$, $O_w = \mathrm{Tr}\left[\hat{\Pi}_f \hat{A}'\right]$, with $\hat{A}' = \frac{\hat{\Pi}_f \hat{O}}{\mathrm{Tr}\left[\hat{\Pi}_f \hat{\Pi}_i\right]}$. In the framework of matrices, relevant to this chapter, the above definition of non-normality implies that the matrix cannot be diagonalized through an orthonormal transformation [142]. Non-normality is a stronger relation of asymmetry than simple non-Hermicity: in fact, all non-normal matrices are non-Hermitian, but there is a class of non-Hermitian matrices which are normal, the circulant matrices [143]. Such stronger asymmetry can be thought of as a hierarchical structure of the matrix. This clearly emerges when we consider networks: in such context, the adjacency matrix represents the way in which the nodes (i.e, the units of the network) are connected to each other; when the structure of the connections is hierarchical, the adjacency matrix is non-normal [144, 145]. The latter framework results are particularly interesting for applications, as real-world networks are non-normal [146].

In particular, this work shows that the operators $\hat{A}$ and $\hat{A}'$ must be non-normal for the weak value to become anomalous. When imposing an arbitrary post-selection, the weakly measured quantity changes from an expectation value of a Hermitian operator representing the observable of interest, to an expectation value of a specific non-normal operator. Interpreting weak values from this point of view might involve studying the energetics of the protocol, especially the post-selection process. Possible links with open systems and non-Hermitian quantum physics [147] might appear, as post-selection involves a discarding process.
Non-normality of matrices and operators has been studied in numerical analysis by Trefethen and collaborators [142, 148], triggered by the effects observed in fluid dynamics [149]. In fact, such property makes the matrix more sensible to perturbations, which results in an amplifying effect of the latter, with dramatic consequences on the dynamics. For example, in fluid dynamics, it gives rise to a premature emergence of turbulence [142], while in epidemics it may lead to a lower threshold for an outbreak [150]. Effects of non-normality have also been studied in ecology [151, 152], Turing pattern formation [153], chemical reaction networks [154], and synchronization dynamics [143]. Such a change in the behavior of the system can be ascribed to the possible emergence of an initial transient growth, whose intensity is proportional to the non-normality of the system [146]. The degree of non-normality is estimated by the spectral properties of the matrix, resulting in different metrics [142, 146]. Those metrics will be used in the following to assess the strength of the anomalous weak value. In particular, we will be interested in using the Henrici departure from normality.
In this chapter, we show that non-normality is a necessary condition for obtaining a weak value that is different from an eigenvalue of the observable. We will show that in order to have a large weak value, the operator $\hat{A}$ and $\hat{A}'$ must be non-normal; hence, the latter property is necessary to obtain amplification. Furthermore, by comparing the modulus of the weak value and the Henrici departure from normality with varying pre- and post-selected states, we make a direct connection between the degree of weak-value amplification and the degree of non-normality of the operator $\hat{A}$. As a next step, we vary the observable, which is the other component involved in the weak value. Ordinarily, experimenters select pre- and post-selected states that are nearly orthogonal in order to achieve amplification. However, in some cases, we have some freedom to choose the observable. In this study, we demonstrate the critical role that this choice plays in the amplification yield. By varying the observable, we discovered that the maximum weak value always occurs at the arithmetic average of the maximum Henrici departure from normality of both matrices $\hat{A}$ and $\hat{A}'$. Furthermore, the weak value tends toward infinity when the points at which the matrices $\hat{A}$ and $\hat{A}'$ are degenerate and nilpotent coincide.

6.1 Weak values as expectation values of non-normal operators

The aim of this section is to show the importance of non-normality for the emergence of weak values. To achieve this goal, we rewrite the weak value as the expectation value of a non-normal operator, $\hat{A}$. Then, we prove that when the latter operator is normal, the weak value is simply an eigenvalue of the observable, $\hat{O}$. This shows that weak values are directly linked to non-normal operators.

The weak value of the system using pure pre- and post-selected states can be expressed as

$$O_w = \frac{\langle \psi_f | \hat{O} | \psi_i \rangle}{\langle \psi_f | \psi_i \rangle} = \frac{\mathrm{Tr}\left[\hat{\Pi}_f \hat{O} \hat{\Pi}_i\right]}{\mathrm{Tr}\left[\hat{\Pi}_f \hat{\Pi}_i\right]}. \tag{6.1}$$

A simple algebraic manipulation[1] of the previous formula expresses the weak value in terms of the expectation value of the operator $\hat{A}$,

$$O_w = \langle \psi_f | \hat{A} | \psi_f \rangle, \tag{6.2}$$

where the non-normal operator $\hat{A}$ is defined in terms of the operator $\hat{O}$ and the pre- and post-selected states as follows:

$$\hat{A} = \frac{\hat{O}\hat{\Pi}_i}{\mathrm{Tr}\left[\hat{\Pi}_f \hat{\Pi}_i\right]}. \tag{6.3}$$

To measure the non-normality of a matrix M, we use the Henrici departure from normality, d_f, defined as

$$d_f(M) = \sqrt{||M||_F^2 - \sum_{i=1}^{n} |\lambda_i|^2}, \tag{6.4}$$

where λ_i are the eigenvalues and $||M||_F = \sqrt{\sum_{i,j=1}^{n} |m_{ij}|^2}$, the Frobenius norm of the matrix M whose elements are m_{ij} [142]. The Henrici departure from normality of the matrix $\hat{A}$ is thus,

$$d_f\left(\hat{A}\right) = \frac{\sqrt{\langle \psi_i | \hat{O}^2 | \psi_i \rangle - \langle \psi_i | \hat{O} | \psi_i \rangle^2}}{|\langle \psi_f | \psi_i \rangle|^2} = \frac{\Delta_i \hat{O}}{|\langle \psi_f | \psi_i \rangle|^2}, \tag{6.5}$$

where $\Delta_i \hat{O}$ is the uncertainty of the observable $\hat{O}$ in the initial state. The details on the derivation of this equation can be found in appendix H. The Henrici departure from normality of $\hat{A}$ vanishes and the matrix is normal, only when the expectation value of $\hat{O}^2$ in the initial state is equal to the square of the expectation of $\hat{O}$ in the initial state, namely

$$\langle \psi_i | \hat{O}^2 | \psi_i \rangle = \langle \psi_i | \hat{O} | \psi_i \rangle^2. \tag{6.6}$$

However the Cauchy-Schwarz inequality implies that,

$$\langle \psi_i | \hat{O}^2 | \psi_i \rangle \geq \langle \psi_i | \hat{O} | \psi_i \rangle^2, \tag{6.7}$$

where the equality holds true only when $|\psi_i\rangle$ is an eigenvector of $\hat{O}$, $\hat{O}|\psi_i\rangle = \lambda |\psi_i\rangle$. In that case, the operator is normal and the weak value is simply the eigenvalue λ.
Obviously, defining the operator $\hat{A}$ in terms of the final or the initial state is an arbitrary choice. Hence, following a very similar algebraic manipulation[2], the weak value can also be defined as the expectation value in the initial state,

$$O'_w = \langle \psi_i | \hat{A}' | \psi_i \rangle, \tag{6.8}$$

[1] $O_w = \frac{\langle \psi_f|\hat{O}|\psi_i\rangle}{\langle \psi_f|\psi_i\rangle} = \frac{\langle \psi_f|\hat{O}|\psi_i\rangle\langle \psi_i|\psi_f\rangle}{\langle \psi_f|\psi_i\rangle\langle \psi_i|\psi_f\rangle} = \frac{\langle \psi_f|\hat{O}\hat{\Pi}_i|\psi_f\rangle}{|\langle \psi_f|\psi_i\rangle|^2} = \langle \psi_f| \frac{\hat{O}\hat{\Pi}_i}{\mathrm{Tr}[\hat{\Pi}_f\hat{\Pi}_i]} |\psi_f\rangle = \langle \psi_f|\hat{A}|\psi_f\rangle$

[2] $O_w = \frac{\langle \psi_f|\hat{O}|\psi_i\rangle}{\langle \psi_f|\psi_i\rangle} = \frac{\langle \psi_i|\psi_f\rangle\langle \psi_f|\hat{O}|\psi_i\rangle}{\langle \psi_i|\psi_f\rangle\langle \psi_f|\psi_i\rangle} = \frac{\langle \psi_i|\hat{\Pi}_f\hat{O}|\psi_i\rangle}{|\langle \psi_f|\psi_i\rangle|^2} = \langle \psi_i| \frac{\hat{\Pi}_f\hat{O}}{\mathrm{Tr}[\hat{\Pi}_f\hat{\Pi}_i]} |\psi_i\rangle = \langle \psi_i|\hat{A}'|\psi_i\rangle$

of the operator $\hat{A}'$ given by

$$\hat{A}' = \frac{\hat{\Pi}_f \hat{O}}{\mathrm{Tr}\left[\hat{\Pi}_f \hat{\Pi}_i\right]}. \tag{6.9}$$

Weak values are called anomalous when the imaginary part is different from 0 or, otherwise, when their value lies outside the range of the spectrum of the Hermitian operator $\hat{O}$ [31, 155, 156], namely

$$\begin{aligned} &\mathrm{Im}\, O_w \neq 0 \\ \text{or} \quad &O_w > \max\left(\langle \hat{O} \rangle\right) = \mathrm{Tr}\left(\hat{\rho}\hat{O}\right) = \max\left(\lambda_i\right) \\ \text{or} \quad &O_w < \min\left(\langle \hat{O} \rangle\right) = \mathrm{Tr}\left(\hat{\rho}\hat{O}\right) = \min\left(\lambda_i\right), \end{aligned} \tag{6.10}$$

where λ_i are the eigenvalues of the operator $\hat{O}$ and $\hat{\rho}$ is an arbitrary (not necessarily pure) quantum state represented here as a density operator. Amplifying weak values correspond to $|O_w| > \max|\lambda_i|$. If $\hat{A}$ or $\hat{A}'$ are normal, the weak value cannot be anomalous. Moreover, the weak value is one of the eigenvalues of the observable $\hat{O}$. The operator $\hat{A}$, resp. $\hat{A}'$, have both eigenvalue zero with multiplicity $N-1$ and one eigenvalue equal to an expectation value of the observable in the initial state $\langle \psi_i | \hat{O} | \psi_i \rangle$, resp. final state $\langle \psi_f | \hat{O} | \psi_f \rangle$. Another interesting case arises when the expectation value is equal to 0. In such a setting, the weak value is not necessarily equal to zero, but the non-normal matrix has all eigenvalues equal to zero and it is degenerate, hence it is a nilpotent matrix [3].

We have thus shown that weak values can be different from an eigenvalue only if both operators $\hat{A}$ and $\hat{A}'$ are non-normal. Since the anomalous properties are fundamental in all applications of weak values, our setting becomes interesting when the involved operators are non-normal.

Beyond this chapter's specific focus on weak values, we would like to stress that our results also establish a truly general connection between quantum fluctuations and non-normality. Indeed, assuming identical initial and final pure states $\hat{\Pi}_f = \hat{\Pi}_i$, the weak value Eq. 6.1 is simply the expectation value $\langle \hat{O} \rangle_i$ of the observable in the considered quantum state $\hat{\Pi}_i$. We can as well express it as the average of the non-normal operator $\hat{A} = \hat{O}\hat{\Pi}_i$ in the initial state, given simply by the trace $\mathrm{Tr}\left(\hat{O}\hat{\Pi}_i\right)$. Then, Henrici's departure from non-normality becomes exactly equal to the uncertainty of the observable in the quantum state $d_f(\hat{O}\hat{\Pi}_i) = \Delta_i \hat{O}$. It appears thus that the non-normality of the operator $\hat{O}\hat{\Pi}_i$ is a measure of the quantum fluctuations around the observable expectation value evaluated through the trace of the same operator $\hat{O}\hat{\Pi}_i$. When the state $\hat{\Pi}_i$ is an eigenstate of the observable $\hat{O}$, the operator is normal and the quantum uncertainty is zero. Indeed, measurements of a quantum system in an eigenstate of the probed observable yield the associated eigenvalue with probability 1. This general link between quantum uncertainties and non-normality, and their relationship with Henrici's departure from normality in particular, does not seem to have been recognized in practice, to the best of our knowledge.

[3] The only matrix with a zero spectrum that is not nilpotent is the zero matrix, which is not degenerate, since it has full geometric multiplicity. Our case does not fall in the latter, our matrix being non-normal.

6.2 Correlation between non-normality and amplifying weak values

Non-normality, as we have shown in the previous sections, is necessary to obtain weak values different from an eigenvalue of the observable, and thus also to have amplifying and complex weak values. The goal of this section is to study the relation between the level of amplification of the modulus of the weak value, and the non-normality of the matrix $\hat{A}$, defined in Eq. 6.3. We show that there is a direct dependence between the two. The larger the amplification, the larger the level of non-normality. To measure the non-normality of a matrix, we use the Henrici departure from normality, d_f, defined in Eq. 6.4. For sake of clarity, we consider the case of two-level systems. A general qubit pure state $|\psi_a\rangle$ can be expressed as

$$|\psi_a\rangle = \begin{pmatrix} \cos\theta_a \\ e^{i\xi_a}\sin\theta_a \end{pmatrix}, \tag{6.11}$$

where $0 \leq \theta_a \leq \frac{\pi}{2}$ and $0 \leq \xi_a \leq 2\pi$.
The pre- and post-selected states, $|\psi_i\rangle$ and $|\psi_f\rangle$, are described similarly to Eq. 6.11. Each pure state, pre- and post-selected, depends on two free parameters and the measured operator depends on four free parameters. Consequently, the full description of the process depends on eight free parameters. In this section, we will vary the pre- and post-selected states and fix the observable, while in the next section, we will do the opposite. We restrict the parametric freedom of the states by imposing the absence of phase of the initial and final states, $\xi_i = 0$ and $\xi_f = 0$. We refer the interested reader to appendix I for the analysis of the general case.
To elucidate the correlation between amplifying weak values and non-normality, the modulus of the weak value is qualitatively and quantitatively compared to the Henrici departure from normality. The chosen observables to study are the Pauli matrices and a linear combination of them, $\hat{O} = \frac{1}{\sqrt{3}}(\hat{\sigma}_x + \hat{\sigma}_y + \hat{\sigma}_z)$, where the Pauli matrices have been defined in Eq. 3.4. Our choice has been motivated by the important role the latter play in quantum physics by describing the spin [157, 158, 159].
Let us consider the Pauli matrix σ_x. Then by using the previous definitions we get

$$d_f\left(\hat{A}_x\right) = \frac{|\cos(2\theta_i)|}{|\langle\psi_f|\psi_i\rangle|^2}, \tag{6.12}$$

where $\hat{A}_x$ denotes the operator $\hat{A}$ built from $\hat{\sigma}_x$,

$$\hat{A}_x = \frac{\hat{\sigma}_x\hat{\Pi}_i}{|\langle\psi_f|\psi_i\rangle|^2} \tag{6.13}$$

and the modulus of the weak value to the square is,

$$|\sigma_{x,w}|^2 = \frac{\sin^2(\theta_f+\theta_i)}{|\langle\psi_f|\psi_i\rangle|^2}, \tag{6.14}$$

with $|\langle\psi_f|\psi_i\rangle|^2 = \cos^2(\theta_f-\theta_i)$. The level curves of the latter are reported in Fig. 6.1 as a function of the angles θ_i and θ_f. The red line define the 1-level, where the modulus of the weak value

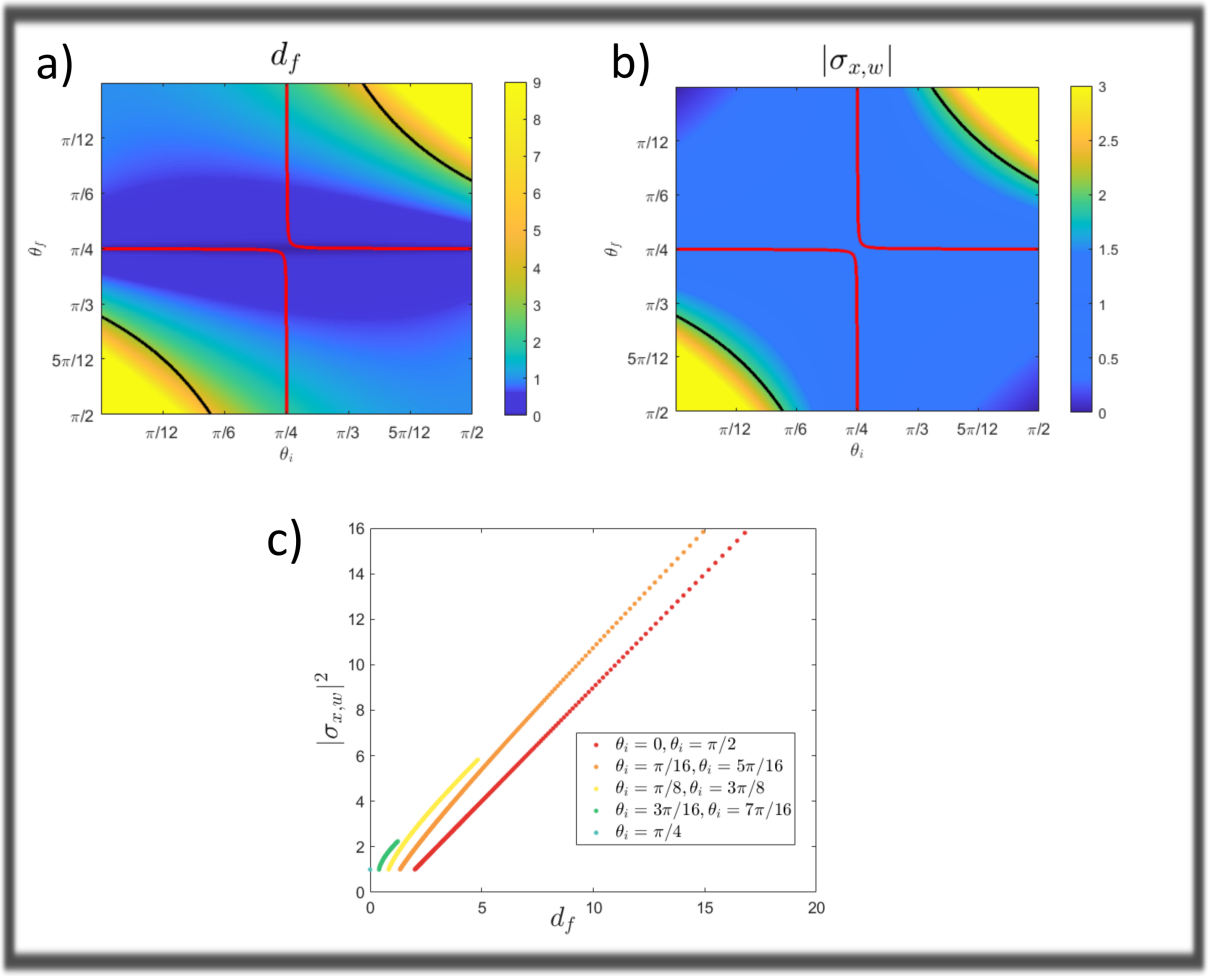

Figure 6.1: a) Color map of the modulus of the weak value of $\hat{\sigma}_x$ in terms of the polar angles of the pure pre- and post-selected states (θ_i, θ_f), imposing $\xi_i = 0$, $\xi_f = 0$. b) Color map of the Henrici departure from normality of the non-normal matrix $\hat{A}$ associated to the weak value $\sigma_{x,w}$. a,b) The red curve corresponds to the border of the area in which the modulus of the weak value is larger than 1. The black curve corresponds to the border of the area in which the modulus of the weak value is twice the maximum possible expectation weak value. c) Square modulus of the weak value as a function of the Henrici departure from normality for anomalous weak values, $|\sigma_{x,w}| > 1$, obtained by varying θ_f between 0 and $\frac{\pi}{2}$, while θ_i is fixed (colored dots in the legend).

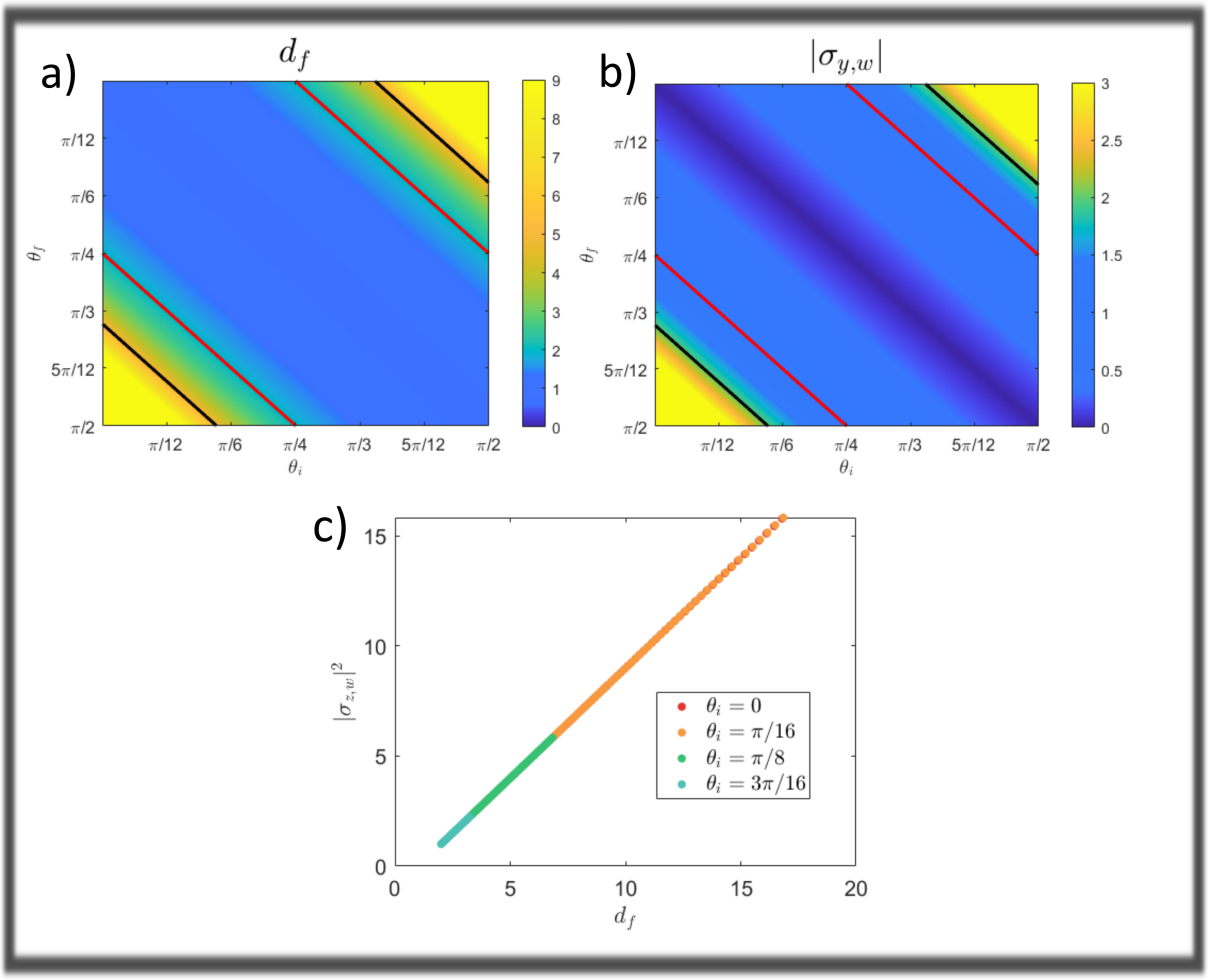

Figure 6.2: a) Color map of the modulus of the weak value of $\hat{\sigma}_y$ in terms of the polar angles of the pre- and post-selected states (θ_i, θ_f), imposing $\xi_i = 0$, $\xi_f = 0$. b) Color map of the Henrici departure from normality of the non-normal matrix associated to the weak value, $\hat{A}$. a,b) The red curve corresponds to the border of the area in which weak value amplification occurs. The black curve corresponds to the border of the area in which the modulus of the weak value is twice the maximum possible expectation value. c) Square modulus of the amplified weak value as function of the Henrici departure from normality, for various $0 < \theta_f < \frac{\pi}{2}$.

equals 1, while the black line denotes the 2-level. In the region beyond the 1-level, weak value amplification occurs (as the eigenvalues of Pauli matrices are ± 1). We can observe a very good agreement among the results shown in the two top panels. Since we are considering pure pre- and post-selected states with real coefficients, the 1-level curve also define the region beyond which weak values of $\hat{\sigma}_x$ are anomalous. In other words, all real, anomalous weak values of Pauli matrices provide amplification.
To strengthen this claim we can express $|\sigma_{x,w}|^2$ in terms of $d_f\left(\hat{A}_x\right)$ by eliminating, e.g., the variable θ_f and considering thus θ_i as a free parameter. We can thus obtain

$$|\hat{\sigma}_{x,w}|^2 = \frac{1}{1+\tan^2\theta_i}\frac{1}{1+\tan^2\theta_f}\frac{(\tan\theta_f+\tan\theta_i)^2}{|\cos(2\theta_i)|}d_f\,, \tag{6.15}$$

where $\tan\theta_f$ can be expressed as a function of d_f by using Eq. 6.12. The explicit formula can be found in appendix I. This relation is shown in panel c) of Fig. 6.1 for several values of the parameter θ_i and by restricting d_f to the range corresponding to anomalous weak values, i.e., $|\hat{\sigma}_{x,w}|^2 > 1$.
A similar analysis can be performed by using as observables the remaining Pauli matrices and a combination of them. In the following Figs. 6.2, 6.3, 6.4, we report the dependence of the modulus of the weak value of $\hat{\sigma}_y$, $\hat{\sigma}_z$ and $\hat{O} = \frac{1}{\sqrt{3}}(\hat{\sigma}_x + \hat{\sigma}_y + \hat{\sigma}_z)$ respectively, as a function of the parameters θ_i and θ_f by using adapted color maps to emphasize the level curves. In the same figures, we also show the Henrici departure from normality as a function of the same parameters. As in the case of the observable $\hat{\sigma}_x$, for $\hat{\sigma}_y$ and $\hat{O} = \frac{1}{\sqrt{3}}(\hat{\sigma}_x + \hat{\sigma}_y + \hat{\sigma}_z)$, we can observe (see top panels in Figs. 6.2, 6.4) a very good agreement between the square of the modulus of the weak value and the Henrici departure from normality. We have also shown the region in which the modulus of the weak value is larger than the absolute value of the largest eigenvalue of the observable (red curve) and the one for which the modulus is at least twice the maximum eigenvalue (black curve). Outside the regions bounded by the latter curves, i.e., the yellow regions, the weak value is amplifying. Inside the regions bounded by the red curve, i.e., the blue ones, the modulus of the weak value lies in the range of eigenvalues of the studied operator (but the weak value can still be anomalous, i.e. if it is a complex number).
In Fig. 6.1, we consider the case for the observable $\hat{\sigma}_x$ and we can observe that the Henrici departure from normality (panel a) and the pattern of the modulus of the weak value (panel b) exhibit a good correlation in the region of anomalous weak values, especially in the region where $|O_w| > 2$, namely associated to yellow values. Near the boundary between anomalous and non-anomalous weak values (red curves), some differences are appreciable: in particular, the value of the minimum of the Henrici departure from normality is smaller than the modulus of the weak value (the former is associated with a darker blue than the latter). On the other hand, considering the region associated to values that are not anomalous, i.e., the region bounded by the red curve and containing the point $(\pi/4, \pi, 4)$, the patterns are completely different, we can indeed appreciate the presence of minima in the top-left and bottom-right corners for the weak value (b) and in the center in the case of the Henrici departure from normality (a). In Fig. 6.1c), one can observe that the squared modulus of the weak value increases as a function of the Henrici departure from normality. The dependence appears linear once the weak value reaches large values (red and orange curves). The point of interception with the axis $\left(|\sigma_{x,w}|^2 = 0\right)$ depends on the initial angle, θ_i. However, when the weak value does not reach large values (green and yellow curves), the dependence is closer to quadratic. The analytical formulas can be found in appendix I. The behaviour of these functions is

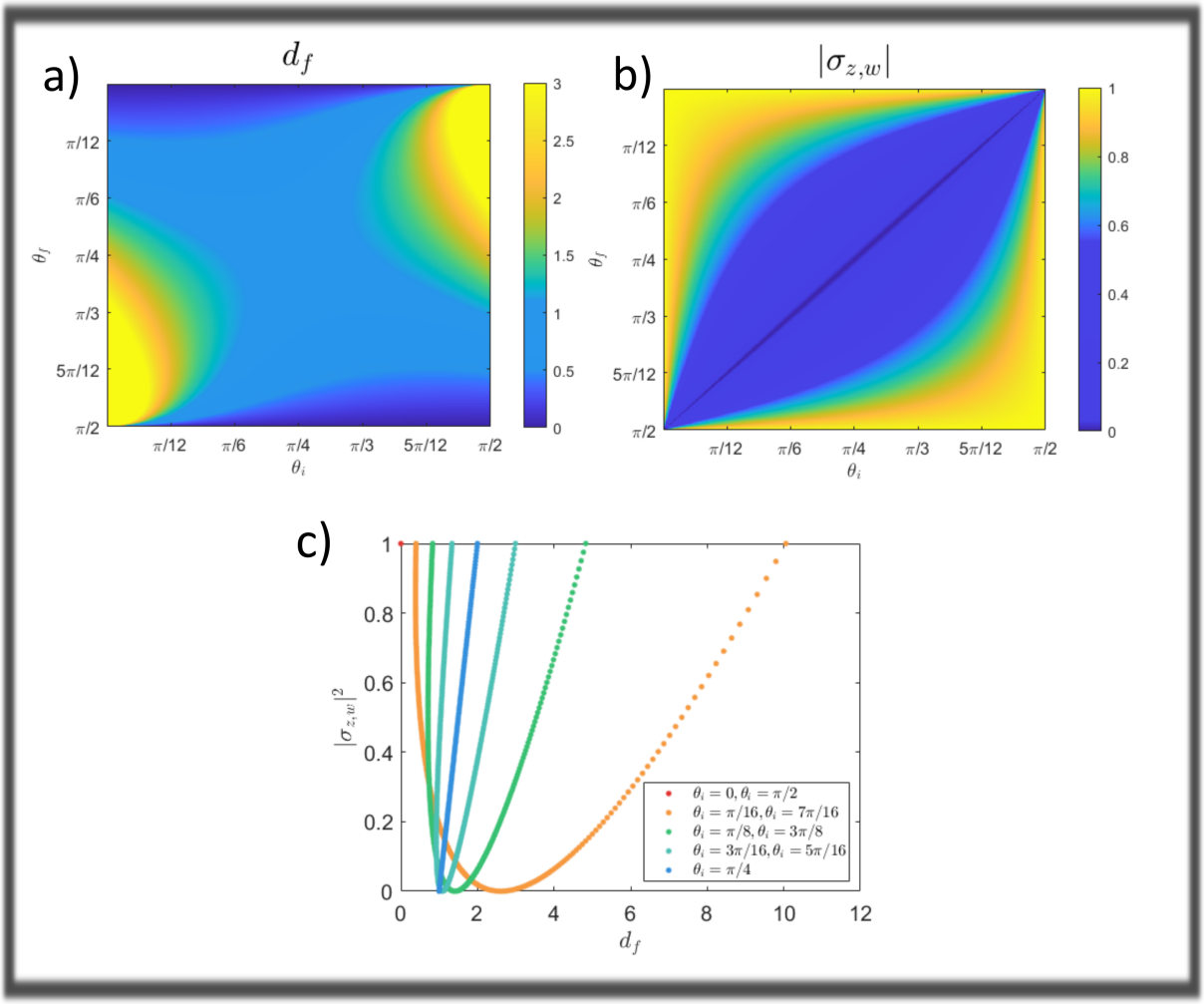

Figure 6.3: a) Color map of the modulus of the weak value of $\hat{\sigma}_z$ in terms of the polar angles of the pre- and post-selected states (θ_i, θ_f), imposing $\xi_i = 0$, $\xi_f = 0$. b) Color map of the Henrici departure from normality of the non-normal matrix associated to the weak value. c) Square modulus of the weak value as a function of the Henrici departure from normality, with $0 < \theta_f < \frac{\pi}{2}$.

very rich.

In Fig. 6.2, the chosen observable is $\hat{\sigma}_y$ and we report again the weak value and the Henrici departure from normality as a function of the angles by using a color code match. In this case too, we have a perfect agreement of the behavior of the two quantities in the parameter region associated to anomalous weak values. In the complementary region, a central minimum appears in the case of the weak value that is absent in the Henrici departure from normality plot. In Fig. 6.2c), the square of the modulus of the weak value depends linearly on the Henrici departure from normality, irrespective of the magnitude of the maximum weak value for the specific case. Furthermore, the slope and the point of interception with the axis ($\left(|\sigma_{y,w}|^2 = 0\right)$) are independent on the value of θ_i. In appendix J, one can find the analytical formula showing that the modulus of weak value to the square depends linearly on the Henrici departure from normality, when both phases are null. Note that in Fig. 6.2b), all non-zero weak values are anomalous because they are purely imaginary numbers (anomalousness is not equivalent with amplification in this case).

In Fig. 6.3, where the chosen observable is $\hat{\sigma}_z$, the patterns of both quantities do not exhibit similarities. This difference with respect to the other cases is due to the fact that no amplification occurs for this observable with the chosen pre- and post selected states. The weak value is real and never anomalous. In Fig. 6.3c), we have plotted the dependence of the modulus of the weak value on the Henrici departure from normality for many value of the angles. As one can see, a large weak value does not imply a large Henrici departure from normality, indeed there is a parabola-like behavior. The analytical formulas can also be found in appendix J.

In Fig. 6.4, we show the results for the observable $\hat{O} = \frac{1}{\sqrt{3}}(\hat{\sigma}_x + \hat{\sigma}_y + \hat{\sigma}_z)$. The pattern of the modulus of the weak value and the Henrici departure from normality show a good correlation in the region of weak value amplification, especially from $|O_w| > 2$ (black curve). Some differences can be appreciated near the boundary (red curves) separating the regions where amplification occurs or not, as the weak value and the departure from normality exhibit different patterns near that area. In the complementary region, i.e., inside the region bounded by the red curves and containing the point $(\pi/4, \pi/4)$, large differences can be appreciated: the level sets for the weak value show a ring-like shape absent in the Henrici departure from normality case. In Fig. 6.4c), there is a linear-like dependence of the modulus square of the weak value on the Henrici departure from normality. However, in this case, both the point of interception with the axis $\left(|O_w|^2 = 0\right)$ and the slope depend on θ_i. When the modulus of the weak value does not reach large values (green and blue lines), the dependence is quadratic and not linear. For this observable and the chosen pre- and post-selected states, the weak value is a complex number whenever $\theta_i \neq \theta_f$, and thus anomalous everywhere but on the descending diagonal of Fig. 6.4b).

For the sake of completeness, we have also computed the weak value and the Henrici departure from normality for a three-level system, whose general pure state is

$$|\psi_a\rangle = \left(\cos\theta_a, e^{i\chi_{1,a}}\cos\alpha_a \sin\theta_a, e^{i\chi_{2,a}}\sin\alpha_a \sin\theta_a\right)^\top . \tag{6.16}$$

The chosen three-level operator is the Gell-Mann matrix $\hat{O} = \hat{\lambda}_5$ (see appendix B). The Gell-Mann matrices are the traceless generators of the Lie group $\mathrm{SU}(3)$ that generalize the Pauli matrices, the traceless generators of $\mathrm{SU}(2)$. In Fig. 6.5, the weak value and the Henrici departure from normality have been depicted by using a color map scheme. As one can see, the plots match pretty well, with the exception of the angles located in the top-right corner, for which the Henrici departure from normality assumes larger values than the squared modulus of the weak value, in particular in the

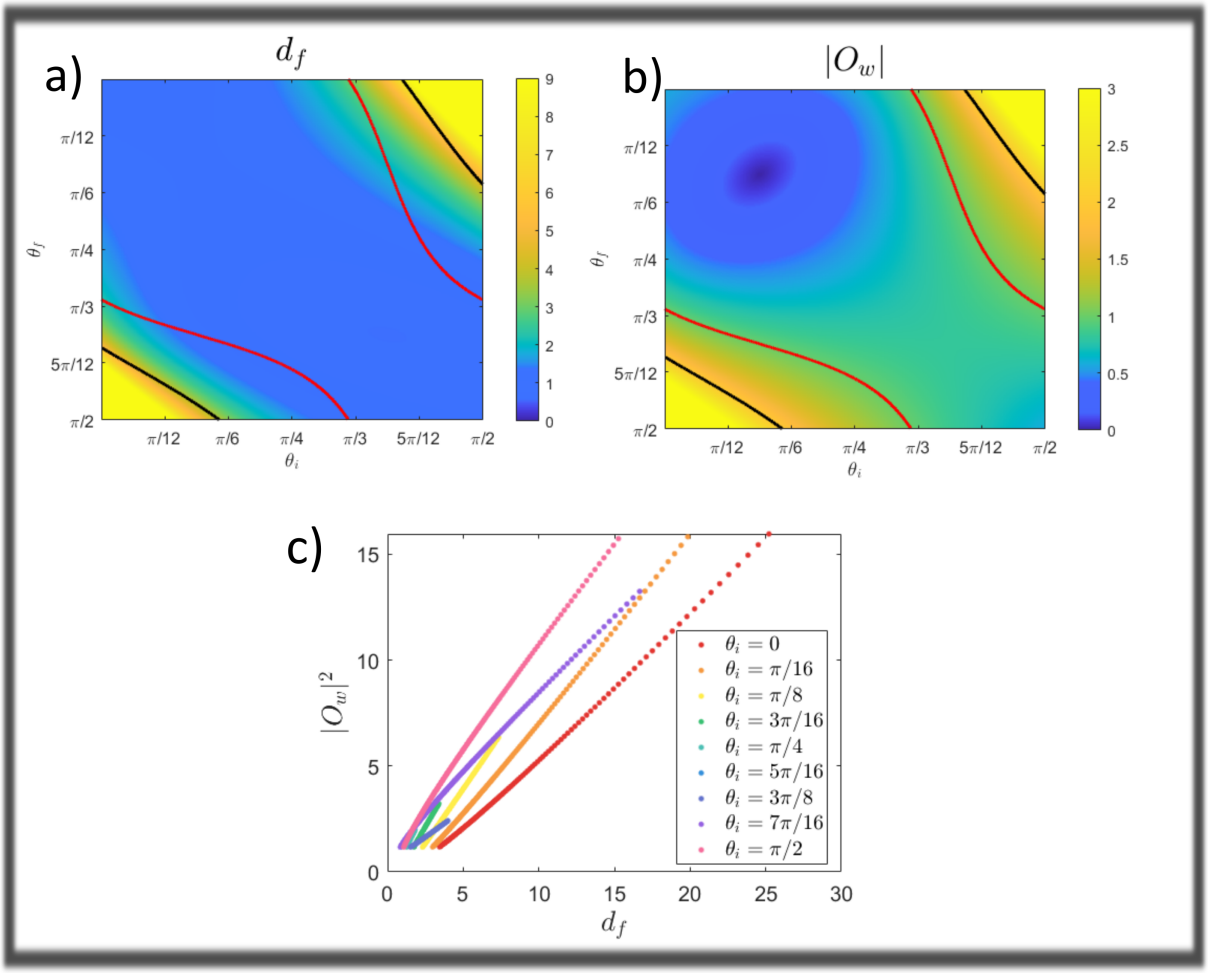

Figure 6.4: a) Color map of the modulus of the weak value of the operator $\hat{O} = \frac{1}{\sqrt{3}}(\hat{\sigma}_y + \hat{\sigma}_x + \hat{\sigma}_z)$ in terms of the polar angles of the pre- and post-selected states (θ_i, θ_f), imposing $\xi_i = 0$, $\xi_f = 0$. b) Color map of the Henrici departure from normality of the non-normal matrix associated with the weak value in terms of the polar angles of the pre- and post-selected states (θ_i, θ_f). a,b) The red curve corresponds to the border of the area in which the weak value amplification occurs. The black curve corresponds to the border of the area in which the modulus of the weak value is twice the maximum possible expectation value. c) Square modulus of the weak value as a function of the Henrici departure from normality for amplified anomalous weak values, $|O_w| > 1$, with $0 < \theta_f < \frac{\pi}{2}$.

strip contained between the red and black curves. The square of the modulus of the weak value depends linearly on the Henrici departure from normality. The slope and the point of interception $\left(|\lambda_{5,w}|^2 = 0\right)$ depend on the pre-selected polar angle.

In conclusion, we have shown that the amplification degree of the weak value depends on the non-normality of the matrix $\hat{A}$ when weak value amplification occurs (so that the weak value is necessarily anomalous, even if a real number). When one feature increases, the other does too. However, this does not happen when amplified weak values are not present. In general, the behaviour is complex, and there are cases in which some regions of discordance are present, as shown in appendix I.

6.3 A reformulation of the problem with a varying observable

In the previous section, we examined the relationship between the Henrici departure from normality and the weak value by varying the pre- and post-selected pure states. However, in some cases, we may have the freedom to select the observable for a given experiment. Here, we investigate how varying the observable impacts non-normality and the modulus of weak values, for given pre- and post selected pure states. To narrow our focus, we restrict our analysis to two-level systems. Specifically, we consider an observable that depends on two parameters,

$$\hat{O} = \sin\theta\cos\phi\ \hat{\sigma}_x + \sin\theta\sin\phi\ \hat{\sigma}_y + \cos\theta\ \hat{\sigma}_z\,, \tag{6.17}$$

where $0 \leq \theta \leq \frac{\pi}{2}$, $0 \leq \phi \leq 2\pi$, and $\hat{\sigma}_i$ are the Pauli matrices (Eq. 3.4). In the present analysis, we investigate the relationship between the weak value and the Henrici departure from normality for the two matrices: $\hat{A}$ and $\hat{A}'$, which are defined in Eq. 6.3 and Eq. 6.9, respectively. Because the denominators of the latter matrices do not vary by modifying the operator, we decided to compare, in this section, the normalized Henrici departure from normality – $d_{f,n}\left(\hat{A}\right)$ and $d_{f,n}\left(\hat{A}'\right)$ – with the modulus of the numerator of the weak value, $|\left\langle\psi_f\right|\hat{O}\left|\psi_i\right\rangle|$.

The results reported in Fig. 6.6a) show a clear trend. Since the operator $\hat{A}'$ does not depend on the initial state, the normalized Henrici departure from normality $d_{f,n}\left(\hat{A}'\right)$ does not vary when we change the pre-selected state, with a fixed final state $\theta_f = 0$; obviously, this is not the case for $d_{f,n}\left(\hat{A}\right)$, as the different black curves clearly show. When the initial state is completely orthogonal to the final one, i.e., $\theta_i = \frac{\pi}{2}$, the two Henrici indexes and the weak value coincide. Starting from this value, the two indexes differ from each other but evolve similarly, and the weak value also follows a similar trend in between both departures from normality in most of the range of values of θ.

In order to understand this behavior, we study the derivative of the three functions (see Fig. 6.6b)). As one can appreciate, the derivative of the weak value with respect to θ is always between the ones of the two normalized Henrici departures from normality, for the studied system. Consequently, the variation of the weak value is not only determined by the orthogonality of the pre- and post-selected states, as seen when varying θ_i, but also by the normalized non-normality of the operators $\hat{A}$ and $\hat{A}'$.

In some cases, the behavior of the numerator of the weak value and the normalized Henrici departures from normality can be vastly different, as shown in Fig. 6.7. For the chosen parameters in this scenario, the numerator of the weak value does not fall between the two normalized Henrici departures from normality of $\hat{A}$ and $\hat{A}'$. Moreover, as θ_i decreases, the curve of the weak value

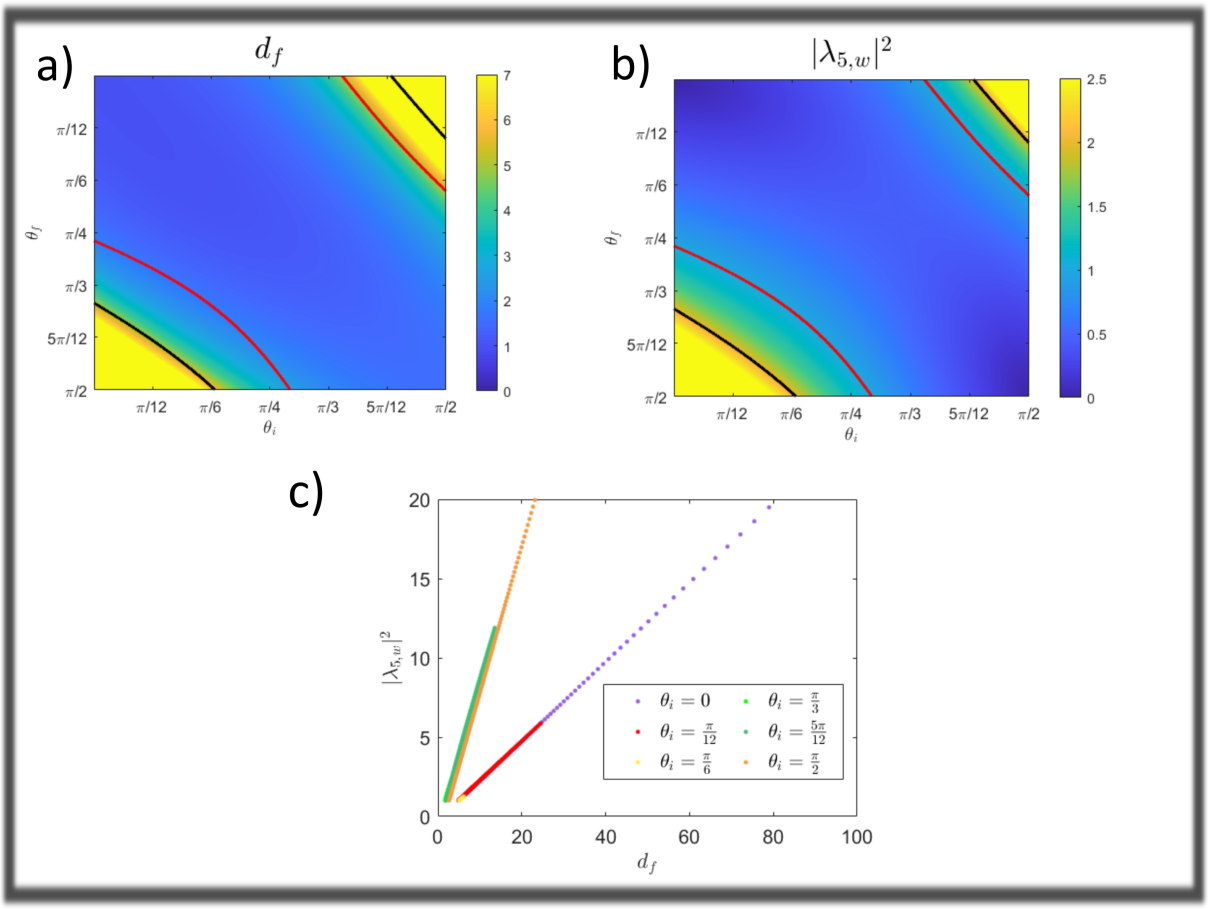

Figure 6.5: a) Color map of the modulus of the weak value of the operator $\hat{O} = \hat{\lambda}_5$, $\chi_{1,i} = \frac{\pi}{7}$, $\chi_{2,i} = \frac{\pi}{21}$, $\alpha_i = \frac{\pi}{8}$, $\chi_{1,f} = \frac{\pi}{4}$, $\chi_{2,f} = 0$, $\alpha_f = \frac{\pi}{3}$ in terms of the polar angles of the pre- and post-selected states (θ_i and θ_f), imposing $\xi_i = 0$, $\xi_f = 0$. b) Color map of the Henrici departure from normality of the non-normal matrix associated to the weak value, $\hat{A}$. a,b) The red curve corresponds to the border of the area in which the weak value is in the amplification range. The black curve corresponds to the border of the area in which the modulus of the weak value is twice the maximum possible expectation value. c) Square modulus of the weak value as function of the Henrici departure from normality for amplifying weak values, $|O_w| > 1$, having $0 < \theta_f < \frac{\pi}{2}$.

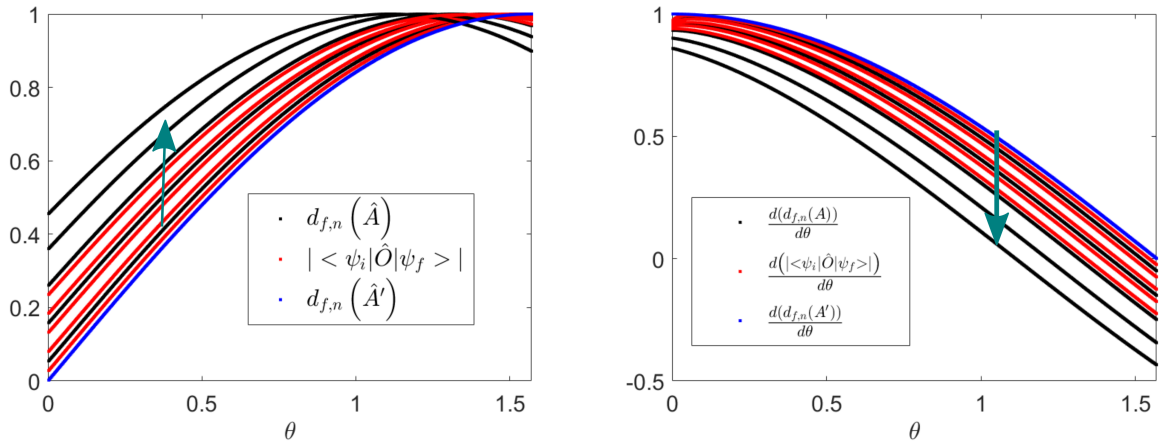

(a) (b)

Figure 6.6: a) For different initial states (θ_i), modulus of the numerator of the weak value (red), normalized Henrici departure from normality of $\hat{A}'$ (blue), and normalized Henrici departure from normality of $\hat{A}$ (black), all as a function of θ in the range of weak value amplification. b) For different initial states (θ_i), derivative of the modulus of the numerator of the weak value $|\langle\psi_f|\hat{O}|\psi_i\rangle|$ (red), the normalized Henrici departure from normality of $\hat{A}'$ (blue), and the normalized Henrici departure from normality of $\hat{A}$ (black), all as a function of θ in the range of weak value amplification. The chosen parameters are: $\theta_f = \xi_i = \xi_f = 0$, $\phi = \frac{\pi}{12}$, while θ_i varies from from 1.5446 to 1.3352. θ_i decreases in the direction of the green arrow.

moves down in the plot, whereas the normalized Henrici departure from normality of $\hat{A}$ moves in the opposite direction (see opposite orientations of the green arrows). It is worth noting that this type of behavior commonly occurs near the boundary of the amplification region of the weak values. Fig. 6.8 shows the modulus of the weak value plotted against θ. In the second case, the modulus of the weak value does not even reach twice the largest eigenvalue of the observable, whereas in the first case, the anomalous weak value is significantly larger. The intricate relationship between the weak value and the Henrici departure from normality of $\hat{A}$ and $\hat{A}'$ in two-level systems is an area that warrants further investigation. Detailed studies can uncover more about this behavior. The interested readers can find the expressions of the weak value, the Henrici departure from normality, and their derivatives in appendix L, with the assumption that $\xi_i = \xi_f = 0$.
As already stated, the operators $\hat{A}$, resp. $\hat{A}'$, have an eigenvalue equal to zero and the other one equal to $\frac{\langle\psi_i|\hat{O}|\psi_i\rangle}{\langle\psi_f|\psi_i\rangle}$, resp. $\frac{\langle\psi_f|\hat{O}|\psi_f\rangle}{\langle\psi_f|\psi_i\rangle}$. For the parameter value at which the expectation value of the operator is also equal to 0, the matrix is nilpotent. This is an interesting observation because it is well known that nilpotent matrices and operators affect the system dynamics [160, 161]. Furthermore, the 0 eigenvalue is now degenerate, as one can observe from Fig. 6.9, where the largest eigenvalue in absolute value and the angle between eigenvectors have been plotted for different initial states. As one can appreciate, for any value of the initial state, when the largest eigenvalue in absolute value is 0 (nilpotent matrix), the angle between the eigenvectors is null, and thus the matrix becomes degenerate.
Furthermore, the point of the maximum modulus of the numerator of the weak value in the ampli-

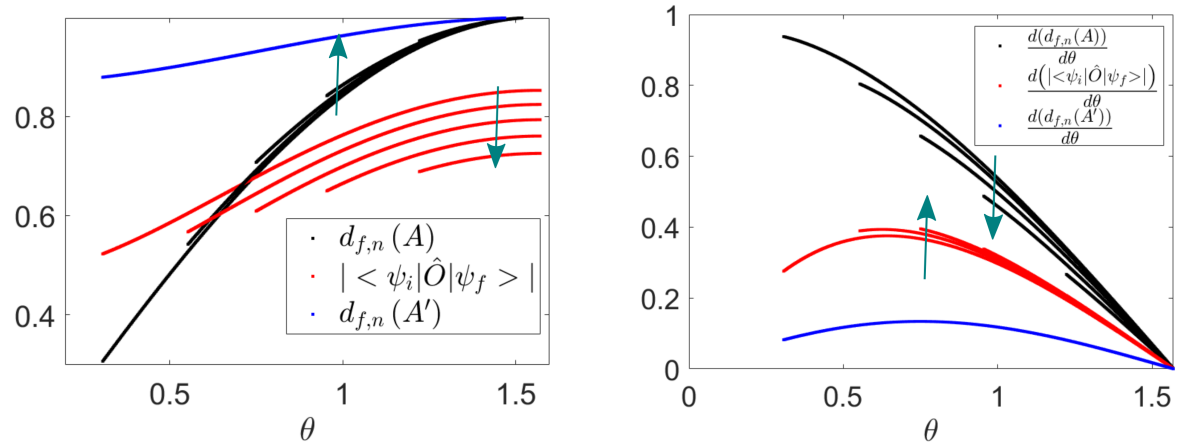

(a) (b)

Figure 6.7: a) For different initial states (θ_i), modulus of the numerator of the weak value (red), normalized Henrici departure from normality of $\hat{A}'$ (blue), and normalized Henrici departure from normality of $\hat{A}$ (black), all as a function of θ in the range of weak value amplification. b) For different initial states (θ_i), derivative of the numerator of the modulus of the weak value $|\langle\psi_f|\hat{O}|\psi_i\rangle|$ (red), the normalized Henrici departure from normality of $\hat{A}'$ (blue), and the normalized Henrici departure from normality of $\hat{A}$ (black), all as a function of θ in the range of weak value amplification. The chosen parameters are: $\theta_f = \xi_i = \xi_f = 0$, $\phi = 3\frac{\pi}{2}$, while θ_i varies from from 1.5446 to 1.3352. θ_i decreases in the direction of the green arrow.

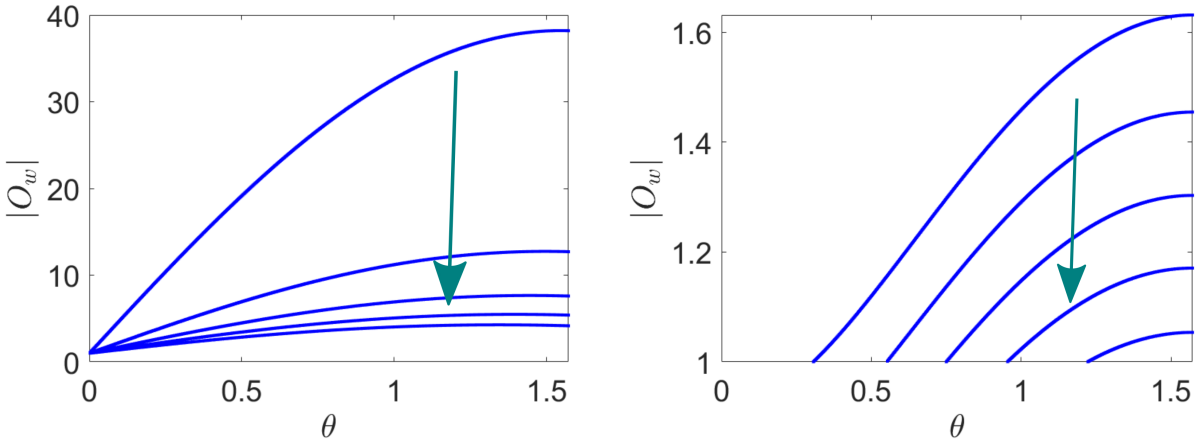

(a) (b)

Figure 6.8: a) Modulus of the weak value of $\hat{O}$ in terms of θ, for the cases of Fig. 6.6. The chosen parameters are: $\theta_f = \xi_i = \xi_f = 0$, $\phi = \frac{\pi}{12}$, while θ_i varies from from 1.5446 to 1.3352. b) Modulus of the weak value of $\hat{O}$ in terms of θ, for the cases of Fig. 6.7. The chosen parameters are: $\theta_f = \xi_i = \xi_f = 0$, $\phi = 3\frac{\pi}{2}$, while θ_i varies from from 1.5446 to 1.3352. θ_i decreases in the direction of the green arrow.

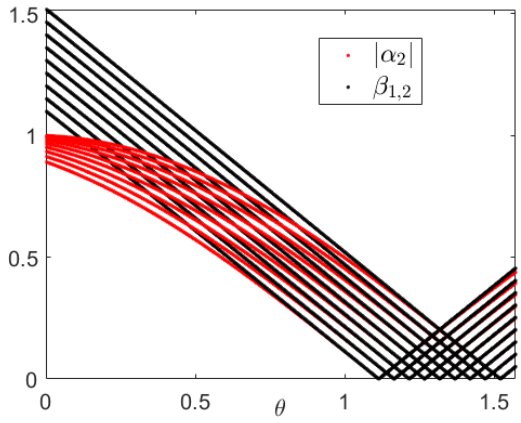

Figure 6.9: For any given polar initial angle, a completely degenerate nilpotent point exists. The largest eigenvalue in absolute value of $\hat{A}$, α_2, has been plotted in terms of θ and the angle between the eigenvectors of $\hat{A}$, $\beta_{1,2}$, in terms of θ. The chosen parameters are $\phi = \frac{\pi}{12}$, $\theta_f = 0$, $\xi_f = 0$, $\xi_i = 0$. The polar angle of the initial state varies between $\frac{\pi}{2}$ and $\frac{5\pi}{12}$.

fication regime (when the modulus of the weak value is largest than the maximum absolute value of the eigenvalues of the operator) is totally determined by the two points where the normalized Henrici departure from normality of the matrices $\hat{A}$ and $\hat{A}'$ reach their maximum values (this point is the same as the one in which the minimum of the absolute value of the eigenvalue different from 0 is reached, see appendix K). Indeed, the maximum modulus of the numerator of the weak value is always attained at the average of the two points where the normalized Henrici departure from normality reaches its maximum for the two matrices, Fig. 6.10. More details of these results can be found in appendix K.

As the angle θ_i increases, the parameter range in which weak value amplification occurs becomes more pronounced. From $\theta_i = \frac{\pi}{4}$, the degeneracy point, where both eigenvalues of $\hat{A}$ and $\hat{A}'$ are equal to zero, is located inside the amplification region, Fig. 6.11. Until this point, the maximum modulus of the weak value is smaller than twice the largest eigenvalue of $\hat{O}$. However, as θ_i increases beyond $\frac{\pi}{4}$, the maximum modulus of the weak value begins to rise much more rapidly. The closer the degeneracy points of the eigenvalues of the operators $\hat{A}$ and $\hat{A}'$, the larger the maximum of the modulus of the weak value. Actually, the maximum of the modulus of the weak value tends to infinity when the degeneracy points are identical (i.e. located at the same value of θ). In summary, the closer the degeneracy points of the eigenvalues of $\hat{A}$ and $\hat{A}'$ are to each other, the larger the maximum modulus of the weak value becomes. Ultimately, the maximum modulus of the weak value tends to infinity when the points of zero eigenvalues occur at the same angle θ.

6.4 Discussion and conclusions

In this chapter, we have shown the link existing between non-normality and anomalous weak values, with particular attention to weak values in the amplification regime. Weak values, unlike expectation values, can exhibit complex values and be outside the range of eigenvalues of the operator under scrutiny. A weak value is anomalous when it is complex or, if it is real, when its value

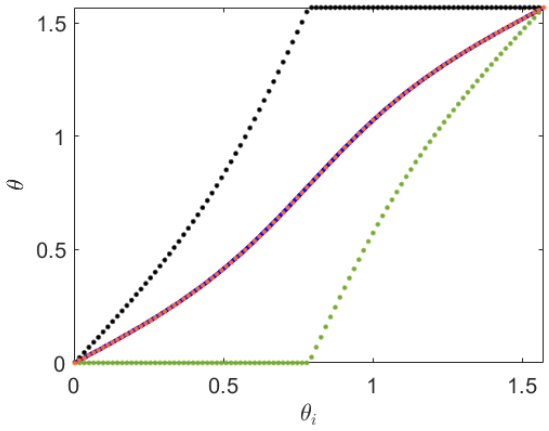

Figure 6.10: Value of θ from the observable $\hat{O}$ corresponding to the minimum of the largest eigenvalue in absolute value of $\hat{A}$, α_2 (green) and $\hat{A}'$, α_2' (black), and to the maximum modulus of the weak value (blue) as a function of θ_i, the polar angle of the pre-selected pure state, for anomalous weak values in the amplification range. The average of the value of θ corresponding to the minima of the maximum of the absolute value of eigenvalue of both matrices (orange) has also been included. The chosen parameters are $\phi = \frac{\pi}{4}$, $\theta_f = 0$, $\xi_f = 0$, $\xi_i = 0$.

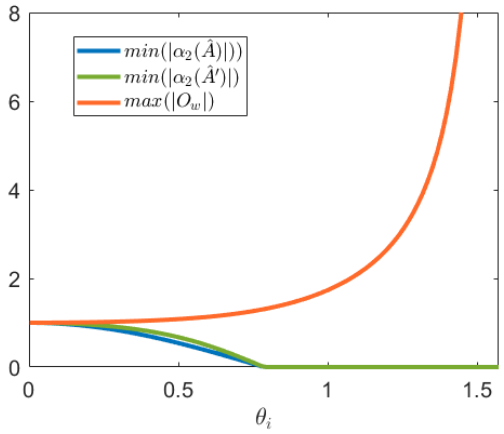

Figure 6.11: Largest value of the modulus of the weak value (orange), smallest value of the largest eigenvalue in absolute value of $\hat{A}$, α_2 (blue) and $\hat{A}'$, α_2'(green), as a function of the initial state (θ_i). The extremal values are computed over the range of all allowed values for the angle θ associated to the varying observable $\hat{O}$. The chosen parameters are $\phi = \frac{\pi}{4}$, $\theta_f = 0$, $\xi_f = 0$, $\xi_i = 0$.

is larger than the maximum eigenvalue or smaller than the minimum eigenvalue of the measured operator, $\hat{O}$. When the anomalous weak value has a modulus larger than the largest modulus of the eigenvalues, the weak value amplification regime is reached.

We have first proved that weak values can be expressed as the expectation value of a typically non-normal matrix, $\hat{A}$, Eq. 6.2 and Eq. 6.3. Then, we have shown that this matrix must be non-normal to obtain a weak value different from an eigenvalue of the observable. There are two arbitrary ways to define the non-normal matrix, in terms either of the initial, pre-selected pure state or of the final, post-selected pure state. Consequently, to obtain anomalous weak values, both matrices, called here $\hat{A}$ and $\hat{A}'$, must be non-normal. The non-normality is linked to the quantum fluctuations of the observable in the pre- or post-selected pure states. Actually, the quantum uncertainty of an arbitrary observable of any system in a given quantum state is exactly equal to Henrici's departure from normality of a specific operator built naturally from the product of the observable operator with the quantum state projector. This result highlights the importance of non-normality in quantum systems far beyond the specific context of weak measurements.

We showed for two-level systems that the two matrices $\hat{A}$ and $\hat{A}'$ can become simultaneously nilpotent, i.e., all the eigenvalues are null and both matrices are degenerate. For a given observable, this point is found by searching appropriate pre- and post-selected states. In the case of two-level systems, the matrices are completely degenerate.

We compared numerically the modulus of weak values and non-normality when varying the pre- and post-selected pure states. We have found a good correlation between such quantities once parameters allow for anomalous weak values firmly in the amplification regime.

Eventually, we have also analyzed the relation between the normalized Henrici departure from normality of both non-normal matrices $\hat{A}$ and $\hat{A}'$ when considering a 1-parameter family of observables in the weak-value amplification regime. In this case, the point of the maximum modulus of the numerator of the weak value is reached at the arithmetic average of the two points where the Henrici departure from normality of the matrices $\hat{A}$ and $\hat{A}'$ are maximal.

Non-Hermitian Hamiltonians describe the evolution of systems that are not isolated [147]. Even though in weak measurements the Hamiltonian of the weak process is Hermitian, post-selection seems to introduce non-normality in the process. It is interesting to observe the analogy with networks, where it is conjectured that non-normality (namely the presence of source and sink nodes) is correlated to the fact that the modeled system is an open one [145]. In weak measurements, it is clear that post-selection plays an important role by transforming an expectation values into weak values that can become anomalous. A reconsideration of weak measurements by viewing them as open rather than closed processes appears necessary.

Moreover, the fact that a non-normal matrix cannot be diagonalized through an orthonormal transformation means that the information encoded in the system cannot be completely disentangled. This is particularly interesting thinking about the present framework, as when post-selection is executed on the system, all the ancilla's wave-function shifts are projected on a common state and thus interfere. This interference seems to mix the information of the different shifts in a disentangled manner. To do so, the expectation value of the operator is transformed into a weak value that, as we have seen in this chapter, is strongly correlated to the non-normality of the operators $\hat{A}$ and $\hat{A}'$ in the amplification regime.

Lastly, let us recall that, in other fields, it has been observed that non-normal operators enhance the possibility of phase transitions to occur [143, 153]. Since phase transitions can be observed in post-selected measurements [162], we believe that revisiting quantum systems from this new perspective

could lead to the appearance of new, unexploited quantum phenomena linked to anomalous weak values.

Chapter 7

Quantum weak values: paraconsistency and paracompletness

Anomalous quantum weak values are values that fall outside the range of eigenvalues of the measured observable. These values provide evidence of contextuality [31, 32], a fundamental quantum property that challenges the classical notion of objective reality by showing that a measurement outcome cannot be reduced to pre-existing properties of the system. In fact, contextuality is mathematically equivalent to negativity in Wigner functions [163]. This intriguing feature has motivated many studies to investigate the role of contextuality in quantum computing, where it is believed to play a key role in achieving quantum speed-up [164, 165].

In this chapter, we explore the connection between weak values and paraconsistent logic. Paraconsistent logic is unique in that it tolerates contradictions, making it a valuable tool for examining the intrinsic logic of anomalous weak values. Specifically, we apply this logic to paradoxes involving weak values, such as the three-box paradox, to gain insights into the nature of anomalous weak values and their role in quantum mechanics.

In the previous section, we discussed weak values as the expectation value of a non-normal operator. However, it is also possible to view weak values from a different perspective, by considering the weak value as the expectation value of an observable, but considering an η-Hermitian pseudo-projector. This pseudo-projector is not Hermitian, but it is pseudo-Hermitian, satisfying the condition $\hat{\rho}^{\dagger}\eta = \eta\hat{\rho}$, where η represents the metric. When the metric satisfies $\eta^3 = \eta$, the density operator becomes Hermitian in an indefinite inner product space known as a Krein space [166, 167]. The inner product in this space is defined as

$$(x, y) := \langle x, \eta y \rangle, \tag{7.1}$$

which indicates that to calculate the scalar product, the second term should be multiplied by the metric η.

Krein spaces contain vectors that are orthogonal to themselves, similar to the case of special relativity, where the past and future events can be described in a light cone. In non-classical logic, orthogonality is interpreted as negation. Consequently, a vector orthogonal to itself in a Krein space can be used to represent a proposition equal to its negation, which supposes a contradiction intrinsic to the space. In classical logic, it should always be false. However, in paraconsistent logic, it is not, and the contradiction is accepted. The pseudo-projector can be described as an

η-Hermitian projector of the pre-selected state in Krein space. As a result, we can shift the entire problem to this new space and consider the weak value as an expectation value on the pre-selected state, but with an alternative metric.
With the tools to characterize weak values in paraconsistent logic, we can examine the three-box paradox with pre- and post-selection and observe how the contradiction arises naturally from the paradox. This discovery offers a new proof that weak values possess non-classical characteristics, in addition to contextuality [31, 32] and the requirement of coherence to achieve anomalous weak values [168].
This development takes us further by demonstrating that paraconsistency, unlike other non-classical properties, arises for any type of weak value, not just anomalous ones. The phenomenon of paraconsistency is related to post-selection in general and thus goes beyond the particular paradoxes case.

7.1 Weak values as expectation values employing η-Hermitian pseudo-projectors

In this section, we demonstrate how to re-express the weak value as the expectation value of an observable, using an η-Hermitian pseudo-projector. Additionally, we illustrate that it is always possible to select a metric $\hat{\eta}$ such that the pseudo-projector is Hermitian in an indefinite inner product space. Specifically, we examine a weak value A_w that can be represented as follows

$$A_w = \frac{\langle \psi_f | \hat{A} | \psi_i \rangle}{\langle \psi_f | \psi_i \rangle} = \mathrm{Tr}\left[\hat{A}\tilde{\rho}\right], \tag{7.2}$$

where the pseudo-projector $\tilde{\rho}$ is defined as

$$\tilde{\rho} = \frac{|\psi_i\rangle \langle \psi_f|}{\langle \psi_f | \psi_i \rangle}. \tag{7.3}$$

We observe that the operator $\tilde{\rho}$ is idempotent,

$$\tilde{\rho}^2 = \frac{|\psi_i\rangle \langle \psi_f|}{\langle \psi_f | \psi_i \rangle} \frac{|\psi_i\rangle \langle \psi_f|}{\langle \psi_f | \psi_i \rangle} = \frac{|\psi_i\rangle \langle \psi_f|}{\langle \psi_f | \psi_i \rangle} = \tilde{\rho}. \tag{7.4}$$

We would also like to remark that $\tilde{\rho}$ is not Hermitian,

$$\tilde{\rho} = \frac{|\psi_i\rangle \langle \psi_f|}{\langle \psi_f | \psi_i \rangle} \neq \tilde{\rho}^\dagger = \frac{|\psi_f\rangle \langle \psi_i|}{\langle \psi_i | \psi_f \rangle}, \tag{7.5}$$

where $\tilde{\rho}^\dagger$ is the conjugate transpose of the operator $\tilde{\rho}$. The operator $\tilde{\rho}$ is not Hermitian, but it is idempotent. We would like to find a metric, η such that,

$$\hat{\eta}\tilde{\rho} = \tilde{\rho}^\dagger \hat{\eta} \qquad \tilde{\rho}^\dagger = \hat{\eta}\tilde{\rho}\hat{\eta}^{-1}, \tag{7.6}$$

where $\hat{\eta}^{-1}$ is the inverse of $\hat{\eta}$.
The choice of $\hat{\eta}$ is not unique, there exist different metrics that fulfill Eq. 7.6. Despite the availability of various metrics to choose from, we opt to select the metric $\hat{\eta}$ with desirable mathematical properties, Hermiticity and unitarity,

$$\hat{\eta} = \hat{\eta}^{\dagger} = \hat{\eta}^{-1} \qquad \hat{\eta}^2 = \hat{I} \tag{7.7}$$

These mathematical properties guarantee, among other things, that the metric is invertible. These properties are very restrictive and highly desirable making the metric "ideal" in many respects. With these properties in mind, it is possible to express the metric $\hat{\eta}$ as a Householder transformation, which represents a reflection about a plane,

$$\hat{\eta} = \hat{I} - 2\,|\Delta\rangle\langle\Delta|, \tag{7.8}$$

where the state $|\Delta\rangle$ is,

$$|\Delta\rangle = \frac{e^{-i\alpha}\,|\psi_i\rangle - |\psi_f\rangle}{\sqrt{2\left(1 - |\langle\psi_i|\psi_f\rangle|\right)}}, \tag{7.9}$$

where

$$e^{i\alpha} = \frac{\langle\psi_f|\psi_i\rangle}{|\langle\psi_f|\psi_i\rangle|}. \tag{7.10}$$

As a result, the metric is expressed in terms of the pre- and post-selected state as

$$\hat{\eta} = \hat{I} - \frac{|\psi_i\rangle\langle\psi_i| + |\psi_f\rangle\langle\psi_f| - e^{-i\alpha}\,|\psi_i\rangle\langle\psi_f| - e^{i\alpha}\,|\psi_f\rangle\langle\psi_i|}{1 - |\langle\psi_f|\psi_i\rangle|}. \tag{7.11}$$

When applying the metric $\hat{\eta}$ to the pre-selected state, $|\psi_i\rangle$, we obtain

$$\hat{\eta}\,|\psi_i\rangle = |\psi_i\rangle - \frac{|\psi_i\rangle\left(1 - |\langle\psi_f|\psi_i\rangle|\right) + |\psi_f\rangle\, e^{i\alpha}\left(|\langle\psi_f|\psi_i\rangle| - 1\right)}{1 - |\langle\psi_f|\psi_i\rangle|} = e^{i\alpha}\,|\psi_f\rangle. \tag{7.12}$$

When applying the metric to the post-selected state, $\langle\psi_f|$, the result is

$$\langle\psi_f|\,\hat{\eta} = \langle\psi_f| - \frac{\langle\psi_i|\, e^{i\alpha}\left(|\langle\psi_f|\psi_i\rangle| - 1\right) + \langle\psi_f|\left(1 - |\langle\psi_f|\psi_i\rangle|\right)}{1 - |\langle\psi_f|\psi_i\rangle|} = \langle\psi_i|\, e^{i\alpha}. \tag{7.13}$$

First, it is essential to emphasize that $\hat{\eta}$ is Hermitian,

$$\hat{\eta}^{\dagger} = \hat{I}^{\dagger} - 2\left(|\Delta\rangle\langle\Delta|\right)^{\dagger} = \hat{I} - 2\,|\Delta\rangle\langle\Delta| = \hat{\eta}. \tag{7.14}$$

As the state $|\Delta\rangle$ is normalized, $\hat{\eta}$ is its own inverse, $\hat{\eta} = \hat{\eta}^{-1}$,

$$\hat{\eta}^2 = \hat{I} - 4\,|\Delta\rangle\langle\Delta| - 4\,|\Delta\rangle\langle\Delta|\Delta\rangle\langle\Delta| = \hat{I}. \tag{7.15}$$

Consequently, the metric $\hat{\eta}$ fulfills Eq. 7.6,

$$\hat{\eta}\,\tilde{\rho}\,\hat{\eta} = \frac{\hat{\eta}\,|\psi_i\rangle\langle\psi_f|\,\hat{\eta}}{\langle\psi_f|\psi_i\rangle} = \frac{|\psi_f\rangle\langle\psi_i|\, e^{2i\alpha}}{|\langle\psi_f|\psi_i\rangle|\, e^{i\alpha}} = \frac{|\psi_f\rangle\langle\psi_i|}{\langle\psi_i|\psi_f\rangle} = \tilde{\rho}^{\dagger}. \tag{7.16}$$

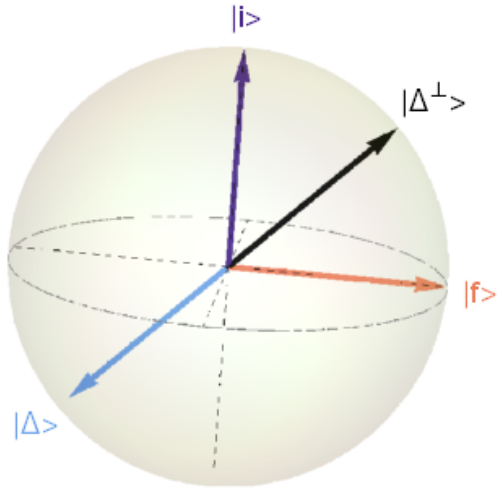

Figure 7.1: Representation of the initial state, post-selected state and the eigenvectors of $\hat{\eta}$, $|\Delta\rangle$ and $\left|\Delta^{\perp}\right\rangle$ on the Bloch sphere. The chosen state are: $|\psi_i\rangle = (1,0)^T$ and $\left|\psi_f\right\rangle = \frac{1}{\sqrt{2}}(1,i)^T$.

It is worth noting that since $\hat{\eta}$ satisfies $\hat{\eta} = \hat{\eta}^{-1}$ and $\hat{\eta}^3 = \hat{\eta}$, the metric establishes a Krein space. The metric $\hat{\eta}$ has always $N-1$ eigenvalues equal to 1 and one eigenvalue equal to -1. $\hat{\eta}$ has $N-2$ eigenvectors orthogonal to both $|\psi_i\rangle$ and $\left|\psi_f\right\rangle$ with eigenvalue equal to 1. It also has 2 eigenvectors in the span of $|\psi_i\rangle$ and $\left|\psi_f\right\rangle$ with eigenvalues 1 and -1. The eigenvalue -1 is associated with the state $|\Delta\rangle$,

$$\hat{\eta}\,|\Delta\rangle = \hat{I}\,|\Delta\rangle - 2\,|\Delta\rangle\langle\Delta|\Delta\rangle = -\,|\Delta\rangle\,. \tag{7.17}$$

One of the states orthogonal to $|\Delta\rangle$, $\left|\Delta^{\perp}\right\rangle$, $\left\langle\Delta\middle|\Delta^{\perp}\right\rangle = 0$ that is associated with an eigenvalue 1 is,

$$\hat{\eta}\left|\Delta^{\perp}\right\rangle = \hat{I}\left|\Delta^{\perp}\right\rangle - 2\,|\Delta\rangle\left\langle\Delta\middle|\Delta^{\perp}\right\rangle = \left|\Delta^{\perp}\right\rangle, \tag{7.18}$$

with the state $\left|\Delta^{\perp}\right\rangle$ given by

$$\left|\Delta^{\perp}\right\rangle = \frac{e^{-i\alpha}\,|\psi_i\rangle + \left|\psi_f\right\rangle}{\sqrt{2\left(1+|\left\langle\psi_i\middle|\psi_f\right\rangle|\right)}}. \tag{7.19}$$

Fig. 7.1 depicts the two-level scenario on the Bloch sphere, where the initial and post-selected states are presented alongside the two $\hat{\eta}$ eigenvectors, namely, $|\Delta\rangle$ and $\left|\Delta^{\perp}\right\rangle$. The state $\left|\Delta^{\perp}\right\rangle$ lies halfway between the initial and final states, whereas $|\Delta\rangle$ is orthogonal to the $\left|\Delta^{\perp}\right\rangle$.
We can explore the possibility of representing the operator $\tilde{\rho}$ as a projector in the Krein space, rather than the conventional complex projective space. To achieve this, we must re-express $\tilde{\rho}$ using a single state, $|\theta\rangle$, instead of the two-state formula we currently have, Eq. 7.3, but utilizing the metric $\hat{\eta}$,

$$\tilde{\rho} = \frac{|\psi_i\rangle\left\langle\psi_f\right|}{\left\langle\psi_f\middle|\psi_i\right\rangle} = \frac{|\theta\rangle\langle\theta|\,\hat{\eta}}{\langle\theta|\,\hat{\eta}\,|\theta\rangle}. \tag{7.20}$$

One can easily find that by employing the metric $\hat{\eta}$, the searched state $|\theta\rangle$ is equal to the pre-selected state,

$$|\theta\rangle = |\psi_i\rangle\,. \tag{7.21}$$

Therefore, it is possible to express the weak value as an expectation value by utilizing the pre-selected projector in Krein space.
In summary, we have expressed weak values in terms of expectation values using a novel peudo-projector, $\tilde{\rho}$, which maps the initial state onto a new space, the Krein space. In effect, we are relocating the problem from the Hilbert space to an indefinite inner product space. In the upcoming section, we will delve deeper into the subject of weak values in Krein spaces. The appeal of such spaces is that paraconsistency is an inherent feature of them, as we will explore further.

7.2 Linking Krein spaces with paraconsistent and paracomplete logic

In the previous section, we demonstrated that any weak value can be expressed as an expectation value on an indefinite inner product space (Krein space), denoted as $\mathscr{S}$. Specifically, the weak value corresponds to the expectation value of the observable under study, evaluated on the pre-selected state in this new space. To achieve this, we utilized the metric $\hat{\eta}$, whose signature for an N-level system is $(-1,1,\ldots,1)$. In this section, we explore the connection between Krein spaces and paraconsistent logic.
Let us consider a plane within the Krein space $\mathscr{L}_{0j}$, which is spanned by all possible linear combinations of the two states $|0\rangle$ and $|j\rangle$. Specifically, $|0\rangle$ is associated with the eigenvalue -1 in the metric, while $|j\rangle$ is one of the states associated with an eigenvalue of 1:

$$\mathscr{L}_{0j} = \alpha\,|0\rangle + \beta\,|j\rangle\,, \tag{7.22}$$

where α and β are complex numbers. The η-orthogonal space, $\mathscr{L}_{0j}^{\perp\eta}$, is formed by all vectors $|x\rangle = \sum_{i=0}^{N-1} x_i\,|i\rangle$ such that

$$-x_0\bar{\alpha} + x_j\bar{\beta} = 0 \qquad \forall\alpha,\beta\in\mathbb{C}, \tag{7.23}$$

where x_0 and x_j are the first and the $j+1$ components of the vector $|x\rangle$, associated with the states $|0\rangle$ and $|j\rangle$. In general, this condition is fulfilled when $x_0 = x_j = 0$. Hence, the space $\mathscr{L}_{0j}^{\perp\eta}$ is,

$$\mathscr{L}_{0j}^{\perp\eta} = \sum_{i=1,i\neq j}^{N-1} \alpha_i\,|i\rangle\,. \tag{7.24}$$

No non-zero vector of the subspace $\mathscr{L}_{0j}$ is η-orthogonal to all vectors of the $\mathscr{L}_{0j}$ subspace. Therefore, this subspace is non-degenerate. Furthermore, the only vector that lies in both $\mathscr{L}_{0j}$ and its orthogonal complement, $\mathscr{L}_{0j}^{\perp\eta}$, is the zero vector $|\varnothing\rangle$. The intersection of both spaces is the $|\varnothing\rangle$ vector,

$$\mathscr{L}_{0j} \cap \mathscr{L}_{0j}^{\perp\eta} = \{|\varnothing\rangle\}. \tag{7.25}$$

No vector within the subspace $\mathscr{L}_{0j}$ can be expressed as a linear combination of vectors from its orthogonal subspace, $\mathscr{L}_{0j}^{\perp\eta}$. This property is intuitive to us because we are familiar with Euclidean

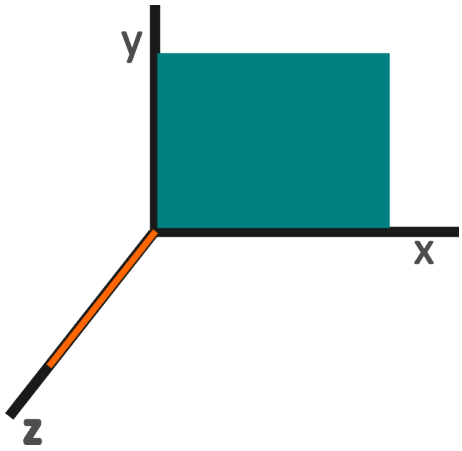

Figure 7.2: Representation of the three-dimensional Euclidean space. The green plane represents the x-y plane and the orange line is the orthogonal subspace, the z line.

spaces. To illustrate, consider a Euclidean 3-dimensional space. The intersection of the linear span of all real vectors in the x-y plane and the span of vectors with only a z component (the orthogonal space) is the zero vector $\vec{0}$. In Fig. 7.2, we have plotted the 3-dimensional Euclidean space with the x-y plane in green and the z line in orange. As you can see, the origin of the Euclidean coordinate system, the vector $\vec{0}$, coincides with the intersection of these two subspaces. In this context, orthogonality is defined with respect to the identity metric with signature $(1,1,1)$, which is the standard metric used in Newtonian physics.
Let us consider now two one-dimensional subspaces of $\mathscr{L}_{0j}$, $\mathscr{L}_{0j}^{\pm}$,

$$\mathscr{L}_{0j}^{\pm} = \pm\lambda\,|0\rangle + \lambda\,|j\rangle\,, \tag{7.26}$$

where λ is a complex number. The η-orthogonal subspaces to $\mathscr{L}_{0j}^{\pm}$ are composed by all vectors $|x\rangle$ fulfilling

$$\mp x_0\bar{\lambda} + x_j\bar{\lambda} = 0 \qquad \forall\lambda \in \mathbb{C}. \tag{7.27}$$

The subspaces formed by all vectors with $x_j = \pm x_0$ are the orthogonal subspaces of $\mathscr{L}_{0j}^{\pm}$, $\mathscr{L}_{0j}^{\pm\perp_\eta}$

$$\mathscr{L}_{0j}^{\pm\perp_\eta} = \left(\sum_{i=0,i\neq j}^{N-1} x_i\,|i\rangle\right) \pm x_0\,|j\rangle = \left(\sum_{i=1,i\neq j}^{N-1} x_i\,|i\rangle\right) + x_0\,|0\rangle \pm x_0\,|j\rangle\,, \tag{7.28}$$

this equation can be derived from a more general one, as found in the literature [167]. The intersection between the subspaces $\mathscr{L}_{0j}^{\pm}$ and $\mathscr{L}_{0j}^{\pm\perp_\eta}$ are the first subspaces themselves,

$$\mathscr{L}_{0j}^{\pm} \cap \mathscr{L}_{0j}^{\pm\perp_\eta} = \mathscr{L}_{0j}^{\pm}. \tag{7.29}$$

At first glance, this property may seem counterintuitive[1]. To better understand it, let us return to the Euclidean space but now consider a metric with signature $\hat{J} = (1,1,-1)$. Let us examine the

[1]It should be noted that this property only applies to subspaces built on the state $|\pm\rangle = \frac{\pm|0\rangle+|j\rangle}{\sqrt{2}}$, which is highly symmetric.

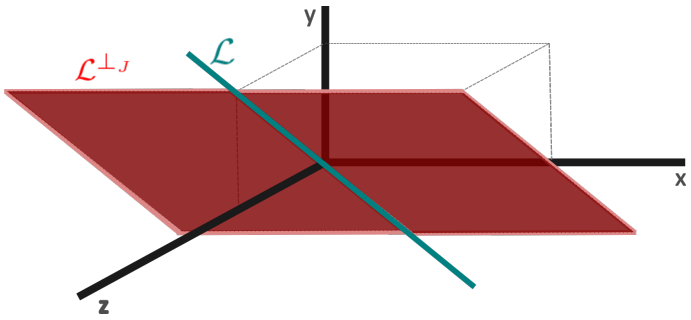

Figure 7.3: Representation of the J-orthogonal subspace to the line $y = z, x = 0$. The turquoise line is the intersection of the $y = z, x = 0$ line and the orthogonal subspace, the plane (x, y, y).

subspace defined by the line $y = z, x = 0$. The J-orthogonal subspace to this line is illustrated in Fig. 7.3, and it is the plane:

$$L^{\perp_J} = \left\{ \begin{pmatrix} x \\ y \\ y \end{pmatrix} \right\} \tag{7.30}$$

The intersection between this plane and the line $y = z, x = 0$ is the line itself, depicted in turquoise in Fig. 7.3. This case illustrates the main properties of the subspaces $\mathscr{L}_{0j}^{\pm}$ and the η metric, where the intersection of the $\mathscr{L}_{0j}^{\pm}$ with its orthogonal $\mathscr{L}_{0j}^{\pm\perp_\eta}$ is itself, $\mathscr{L}_{0j}^{\pm}$.
All vectors of $\mathscr{L}_{0j}^{\pm}$ are orthogonal to all vectors of $\mathscr{L}_{0j}^{\pm}$. Consequently, $\mathscr{L}_{0j}^{\pm}$ is an isotropic subspace of $\mathscr{L}_{0j}$.
We also notice a very general property of Krein spaces [167],

$$\left(\overline{\mathscr{L}_{0j}^{\pm} + \mathscr{L}_{0j}^{\pm\perp_\eta}}\right) \oplus \eta\mathscr{L}_{0j}^{\pm} = \mathscr{S}, \tag{7.31}$$

where $\eta\mathscr{L}_{0j}^{\pm}$ is the subspace generated by the application of η to all states of $\mathscr{L}_{0j}^{\pm}$, and $\oplus$ represents the direct sum, while $+$ represents the usual sum. As the metric is composed by ones and a minus one, it would imply,

$$\begin{aligned} \left(\overline{\mathscr{L}_{0j}^{+} + \mathscr{L}_{0j}^{+\perp}}\right) \oplus \mathscr{L}_{0j}^{-} &= \mathscr{S} \\ \left(\overline{\mathscr{L}_{0j}^{-} + \mathscr{L}_{0j}^{-\perp}}\right) \oplus \mathscr{L}_{0j}^{+} &= \mathscr{S} \end{aligned} \tag{7.32}$$

If we consider the Krein space, it turns out that the whole space cannot be generated using only the subspaces $\mathscr{L}_{0j}^{\pm}$ and $\mathscr{L}_{0j}^{\pm\perp}$. Instead, an additional subspace, namely $\eta\mathscr{L}_{0j}^{\pm}$, is required. This fact can be counterintuitive at first glance. To better understand this, let us return to the Euclidean space with the standard metric, the identity. In Fig. 7.3, we see that the x-y plane and its orthogonal complement, the z-axis, together generate the entire Euclidean space.

$$\left\{ \begin{pmatrix} x \\ y \\ 0 \end{pmatrix} \right\} \cup \left\{ \begin{pmatrix} 0 \\ 0 \\ z \end{pmatrix} \right\} = \left\{ \begin{pmatrix} x \\ y \\ z \end{pmatrix} \right\} = \mathbb{R}^3. \tag{7.33}$$

Nonetheless, if we consider the metric $\hat{J}$ and the Euclidean space depicted in Fig. 7.3, it is not possible to reconstruct the entire space using only the line $y = z, x = 0$ and its orthogonal complement, the plane $L^{\perp_J}$

$$\left\{ \begin{pmatrix} 0 \\ \lambda \\ \lambda \end{pmatrix} \right\} \cup \left\{ \begin{pmatrix} x \\ y \\ y \end{pmatrix} \right\} = \left\{ \begin{pmatrix} x \\ y+\lambda \\ y+\lambda \end{pmatrix} \right\} \neq \mathbb{R}^3. \tag{7.34}$$

To reconstruct the whole Euclidean space, we should add a line that is perpendicular to the plane. This line is actually J times the subspace defined by the line $y = z, x = 0$,

$$\left\{ \begin{pmatrix} 0 \\ \mu \\ -\mu \end{pmatrix} \right\}. \tag{7.35}$$

The whole Euclidean space is then build as

$$\left\{ \begin{pmatrix} 0 \\ \lambda \\ \lambda \end{pmatrix} \right\} \cup \left\{ \begin{pmatrix} x \\ y \\ y \end{pmatrix} \right\} \cup \left\{ \begin{pmatrix} 0 \\ \mu \\ -\mu \end{pmatrix} \right\} = \left\{ \begin{pmatrix} x \\ y+\lambda+\mu \\ y+\lambda-\mu \end{pmatrix} \right\} = \mathbb{R}^3. \tag{7.36}$$

Let us consider the propositional variable p_α. As usually done in quantum logic, this propositional variable can be linked to a closed subspace of the Krein space detailed before, $V\left(p_{0j}^{\pm}\right) = \mathscr{L}_{0j}^{\pm}$, where V is the function that links the propositional variables to the Krein subspaces. Thanks to this mapping, it is possible to define a semantic for the propositional variable in the Krein space. Specifically, this link provides a connection of any measurement result with a proposition. The conjunction of the probability of the propositional variables $p_{0j}^{\pm}$ and the paraconsistent negation of this variable can be mapped to the intersection of the subspaces $\mathscr{L}_{0j}^{\pm}$ and their orthogonal $\mathscr{L}_{0j}^{\pm\perp}$ as

$$p_{0j}^{\pm} \wedge \sim p_{0j}^{\pm} \rightarrow V\left(p_{0j}^{\pm}\right) \cap V\left(p_{0j}^{\pm}\right)^{\perp} = \mathscr{L}_{0j}^{\pm} \cap \mathscr{L}_{0j}^{\pm\perp} = \mathscr{L}_{0j}^{0} \neq \{|\varnothing\rangle\}, \tag{7.37}$$

where $\sim$ is a paraconsistent negation, and the paraconsistent negation is interpreted as the η-orthogonal, the pseudo-orthogonal subspace. The connection between negation and orthogonality is commonly utilized in quantum logics. As the intersection of the subspace and its negation (orthogonal) is not the null vector $|\varnothing\rangle$, $V\left(p_{0j}^{\pm} \wedge \sim p_{0j}^{\pm}\right) \neq |\varnothing\rangle$, there is an intrinsic contradiction in the Krein subspace. This implies that a proposition can be true and false at the same time, as the probability of having $p_{0j}^{\pm}$ and not $p_{0j}^{\pm}$ is not 0. These two properties are not orthogonal to each other. The non-classical logic is paraconsistent.

In classical logic, the conjunction of a variable and its negation is always false, since it is impossible to have a variable and its negation true at the same time. For example, it is not possible to have and to not have a bridge at the same time. However, in quantum mechanics, a probability amplitude different from zero can be assigned to both a property and its negation being true simultaneously. This phenomenon may appear counterintuitive, but it arises from the superposition principle of quantum mechanics. For instance, a quantum system can exist in a superposition of two states, such as a Schrödinger cat being both dead and alive (not dead) at the same time.

Furthermore, the disjunction of $p_{0j}^{\pm}$ and its paraconsistent negation $\sim p_{0j}^{\pm}$ that can be mapped to the sum of the subspaces $\mathscr{L}_{0j}^{\pm}$ and $\mathscr{L}_{0j}^{\pm\perp}$, that it is different from the complete space,

$$p_{0j}^{\pm}\vee \sim p_{0j}^{\pm} \to V\left(p_{0j}^{\pm}\right)+V\left(p_{0j}^{\pm}\right)^{\perp}=\mathscr{L}_{0j}^{\pm}+\mathscr{L}_{0j}^{\pm\perp}\neq\mathscr{S}. \tag{7.38}$$

The sum of both subspaces $\mathscr{L}_{0j}^{\pm}$ and $\mathscr{L}_{0j}^{\pm\perp}$ is different from the whole Krein space, $\mathscr{S}$. The sum of the probabilities of proposition $p_{0j}^{\pm}$ happening and $p_{0j}^{\pm}$ not happening is different from 1. The logic is paracomplete. The logics do not satisfy the excluded middle principle, which implies that either a proposition or its negation is true.
In classical logic the disjunction of a property and its negation is always equal to one. The probability of having a bridge or not having a bridge should be equal to one, there is not other possibility, either the bridge exits or it does not exist. In contrast, certain interpretations of quantum mechanics, such as hidden variable theories, could be based in paracompleteness. The logic that characterizes the Krein space, emerging from the framework of weak value representations and, by extension, general post-selected measurements, possesses a distinctly non-classical nature. This unique logic not only showcases paraconsistency but also unveils the facet of paracompleteness. Within the space, contradictions are inherent, as is the fact that the sum of all commonly considered probabilities is not equal to unity, which implies that other missing components should be considered. Many non-classical logics used to describe quantum mechanics are based solely on paraconsistency or paracompleteness [169]. In contrast, our new logic is both paraconsistent and paracomplete, offering a fresh perspective on the subject.

7.3 Three-box paradox

In the previous sections, we established a connection between weak values and Krein spaces by depicting the weak value as the expectation value of an observable in the initial state within the Krein space. Furthermore, we have successfully forged a connection between Krein spaces and the realms of paraconsistency and paracompleteness, implying that weak values can be described using a paraconsistent and paracomplete logic. Building on these findings, we now aim to apply them to the three-box paradox, taking into account pre- and post-selection, as explained in [65].
The quantum three box paradox considers a particle that can be in the three boxes noted by $|1\rangle$, $|2\rangle$, and $|3\rangle$. Let us consider that the particle is pre-selected in a state, $\left|\psi_i^{\text{box}}\right\rangle$, that is a linear combination of the three boxes

$$\left|\psi_i^{\text{box}}\right\rangle=\frac{1}{\sqrt{3}}\left(|1\rangle+|2\rangle+|3\rangle\right). \tag{7.39}$$

Thereafter, the particle is post-selected in a state, $\left|\psi_f^{\text{box}}\right\rangle$ that only differs from the initial state by a phase,

$$\left|\psi_f^{\text{box}}\right\rangle=\frac{1}{\sqrt{3}}\left(|1\rangle+|2\rangle-|3\rangle\right). \tag{7.40}$$

The paradox deals with the question of determining in which box the particle is located in-between pre- and post-selection. This issue can be tackled conceptually and experimentally by performing

a quantum weak measurement of the box projectors (the weak interaction should occur in-between pre- and post-selection). Let us suppose that, in the weak measurement, we query whether the particle is in box $|1\rangle$. Then, we would find that the weak value of the weakly probed projector $\hat{\Pi}_1 = |1\rangle\langle 1|$ is equal to 1. One interpretation of $\Pi_{1,w} = 1$ is that the particle was in box $|1\rangle$. Such an interpretation associates a "probability" (actually, a quasi-probability distribution) to the weak value of projector (an interpretation suggested by extending the standard probabilistic interpretation of the average value of a projector). Paradoxically, due to the symmetry of the situation, we will reach an equivalent conclusion if we query about box $|2\rangle$, as $\Pi_{2,w} = 1$ as well. How could the particle be in both boxes at the same time? This seems contradictory. What is even more surprising is that if we inquire about box $|3\rangle$, the resulting weak value is $\Pi_{3,w} = -1$. This negative "probability" may seem puzzling. However, the total "probability" of the particle existing in one of the three boxes sums up to 1, as expected.
Let us reconsider this paradox from a Krein space point of view. The weak value of the projector $\hat{\Pi}_i$, where i goes from 1 to 3, can be described as the expectation value of the pseudo-projector,

$$\tilde{\rho} = \frac{\left|\psi_i^{\text{box}}\right\rangle\left\langle\psi_f^{\text{box}}\right|}{\left\langle\psi_f^{\text{box}}\middle|\psi_i^{\text{box}}\right\rangle} = \begin{pmatrix} 1 & 1 & -1 \\ 1 & 1 & -1 \\ 1 & 1 & -1 \end{pmatrix}, \tag{7.41}$$

considering the basis

$$|1\rangle = \begin{pmatrix} 1 \\ 0 \\ 0 \end{pmatrix} \qquad |2\rangle = \begin{pmatrix} 0 \\ 1 \\ 0 \end{pmatrix} \qquad |3\rangle = \begin{pmatrix} 0 \\ 0 \\ 1 \end{pmatrix}. \tag{7.42}$$

The metric, $\hat{\eta}_{\text{box}}$, corresponding to the pre- and post-selected states is

$$\hat{\eta}_{\text{box}} = \begin{pmatrix} 1 & 0 & 0 \\ 0 & 1 & 0 \\ 0 & 0 & -1 \end{pmatrix}, \tag{7.43}$$

where Eq. 7.11 has been employed.
As one can appreciate, $\hat{\eta}^3 = \hat{\eta}$, and the space of the pseudo-operator is a Krein space, as expected. The projector in this space corresponds to the pre-selected state,

$$\tilde{\rho} = \frac{\left|\theta^{\text{box}}\right\rangle\left\langle\theta^{\text{box}}\right|\hat{\eta}_{\text{box}}}{\left\langle\theta^{\text{box}}\right|\hat{\eta}_{\text{box}}\left|\theta^{\text{box}}\right\rangle} = \frac{\left|\psi_i^{\text{box}}\right\rangle\left\langle\psi_i^{\text{box}}\right|\hat{\eta}_{\text{box}}}{\left\langle\psi_i^{\text{box}}\right|\hat{\eta}_{\text{box}}\left|\psi_i^{\text{box}}\right\rangle}. \tag{7.44}$$

We can now build two subspaces of the Krein space that are a homogenous linear combination of $|1\rangle$ and $|3\rangle$,

$$\mathscr{L}^{\pm}_{1,\text{box}} = \beta\,|1\rangle \pm \beta\,|3\rangle, \tag{7.45}$$

with β a complex number. The η_{box}-orthogonal subspace to $\mathscr{L}^{\pm}_{1,\text{box}}$ is

$$\mathscr{L}^{\pm\perp_{\eta_{\text{box}}}}_{1,\text{box}} = \beta\,|1\rangle + \alpha\,|2\rangle \pm \beta\,|3\rangle, \tag{7.46}$$

where α is a complex number. The intersection of the subspaces $\mathscr{L}^{\pm}_{1,\text{box}}$ and $\mathscr{L}^{\pm\perp_{\eta_{\text{box}}}}_{1,\text{box}}$ are the subspaces $\mathscr{L}^{\pm}_{1,\text{box}}$ themselves,

$$\mathscr{L}^{\pm}_{1,\text{box}} \cap \mathscr{L}^{\pm\perp_{\eta_{\text{box}}}}_{1,\text{box}} = \mathscr{L}^{\pm}_{1,\text{box}} \neq \{|\varnothing\rangle\} \tag{7.47}$$

Considering the subspaces as propositional variables, the variables can be true and false at the same time. The non-classical logic is paraconsistent.
Furthermore, two subspaces, $\mathscr{L}^{\pm}_{1,\text{box}}$ and $\mathscr{L}^{\pm\perp_{\eta_{\text{box}}}}_{1,\text{box}}$ do not generate the full Krein space $\mathscr{S}_{\text{box}}$,

$$\mathscr{L}^{\pm}_{1,\text{box}} + \mathscr{L}^{\pm\perp_{\eta_{\text{box}}}}_{1,\text{box}} \neq \mathscr{S}_{\text{box}} \tag{7.48}$$

To obtain the full Krein space we should add the subspace $\eta_{\text{box}}\mathscr{L}^{\pm}_{1,\text{box}}$,

$$\hat{\eta}_{\text{box}}\mathscr{L}^{\pm}_{1,\text{box}} = \mu\,|1\rangle \mp \mu\,|3\rangle\,, \tag{7.49}$$

with μ a complex number. The sum of the three subspaces builds the full Krein space

$$\left(\overline{\mathscr{L}^{\pm}_{1,\text{box}} + \mathscr{L}^{\pm\perp_{\eta_{\text{box}}}}_{1,\text{box}}}\right) \oplus \eta_{\text{box}}\mathscr{L}^{\pm}_{1,\text{box}} = \mathscr{S}_{\text{box}}. \tag{7.50}$$

The Krein space defining the three-box paradox is also paracomplete, as the sum of the probability of the proposition variable and its negation is different from the unity.
The three-box paradox can be described in a paracomplete and paraconsistent logic. In this type of logic, contradictions are intrinsic.
The paradox exhibits a remarkable symmetry, which allows for a similar approach to constructing the subspaces that result in the paracomplete and paraconsistent properties. In this scenario, the subspaces are formed by taking equally weighted linear combinations of the box states $|2\rangle$ and $|3\rangle$, incorporating both positive and negative signs, as follows,

$$\mathscr{L}^{\pm}_{2,\text{box}} = \beta\,|2\rangle \pm \beta\,|3\rangle\,. \tag{7.51}$$

The pseudo-orthogonal subspace is

$$\mathscr{L}^{\pm\perp_{\eta}}_{2,\text{box}} = \alpha\,|1\rangle + \beta\,|2\rangle \pm \beta\,|3\rangle\,. \tag{7.52}$$

From these subspaces arise the paracomplete and paraconsistent properties as

$$\begin{gathered}\mathscr{L}^{\pm}_{2,\text{box}} \cap \mathscr{L}^{\pm\perp_{\eta_{\text{box}}}}_{2,\text{box}} = \mathscr{L}^{\pm}_{2,\text{box}} \neq \{|\varnothing\rangle\} \\ \left(\overline{\mathscr{L}^{\pm}_{2,\text{box}} + \mathscr{L}^{\pm\perp_{\eta_{\text{box}}}}_{2,\text{box}}}\right) \oplus \eta_{\text{box}}\mathscr{L}^{\pm}_{2,\text{box}} = \mathscr{S}_{\text{box}}.\end{gathered} \tag{7.53}$$

In this particular paradox, there exist four distinct subspaces that give rise to both paracompleteness and paraconsistency. It is crucial to consider these subspaces when interpreting the paradox, as they play a significant role in understanding its counterintuitive properties. The remarkably high level of symmetry observed in this paradox is likely a contributing factor to the emergence of these counterintuitive properties.

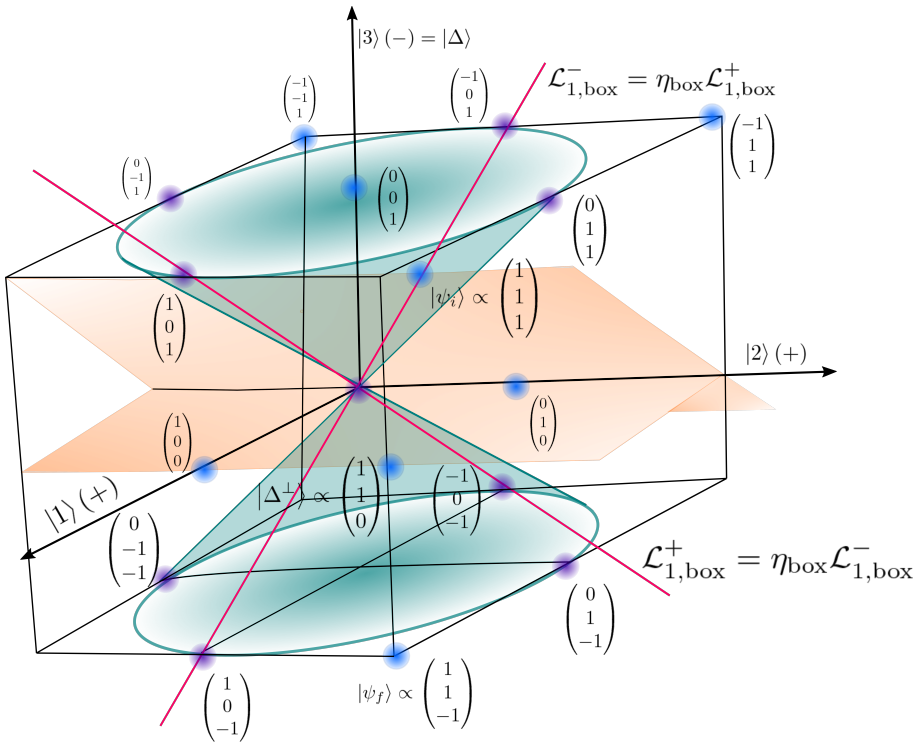

Figure 7.4: Krein space formed by quantum states with real components. The pink lines represent $\mathscr{L}_{\mathrm{box}}$ and $\hat{\eta}_{\mathrm{box}}\mathscr{L}_{\mathrm{box}}$. Several interesting points have been plotted, the purple ones are inside the cone, while the blue ones are outside. We have also included the plane $x = z$ in orange.

Fig. 7.4 illustrates the geometry of the Krein space determined by the three-box paradox, employing quantum states with real components only (in other words, it is actually a representation of the three-box paradox in $\mathbb{R}\mathrm{P}^2$ instead of $\mathbb{C}\mathrm{P}^2$). Notably, it resembles the light cone in Minkowski space. This similarity is not surprising, given that the metric is the same, as the light cone considers only two spatial dimensions. Neither the pre-selected state nor the post-selected one reside within the cone, and neither does any of the three boxes represented by $|1\rangle$, $|2\rangle$, and $|3\rangle$. Consequently, all components of the paradox lie outside this cone. The states $|\psi_i\rangle$ and $|\psi_f\rangle$ are positioned in a highly symmetrical manner relative to the plane defined by $\mathscr{L}^{+}_{1,\mathrm{box}}$ and $\mathscr{L}^{-}_{1,\mathrm{box}}$. This observation may help explain some of the counterintuitive properties of the paradox.
Let us reconsider the paradox by calculating the pseudo-probabilities of finding the particle in the boxes formed by the subspaces of the Krein space, namely $\mathscr{L}^{+}_{1,\mathrm{box}}$, $\mathscr{L}^{+\perp_\eta}_{1,\mathrm{box}}$, and $\eta_{\mathrm{box}}\mathscr{L}^{+}_{1,\mathrm{box}} = \mathscr{L}^{-}_{1,\mathrm{box}}$, as renamed $|\tilde{1}\rangle$, $|\tilde{2}\rangle$, and $|\tilde{3}\rangle$ as

$$\begin{aligned} |\tilde{1}\rangle &= \frac{1}{\sqrt{2}}(|1\rangle + |3\rangle) \\ |\tilde{2}\rangle &= \frac{1}{\sqrt{2+\alpha^2}}(|1\rangle + \alpha\,|2\rangle + |3\rangle) \\ |\tilde{3}\rangle &= \frac{1}{\sqrt{2}}(|1\rangle - |3\rangle) \end{aligned} \tag{7.54}$$

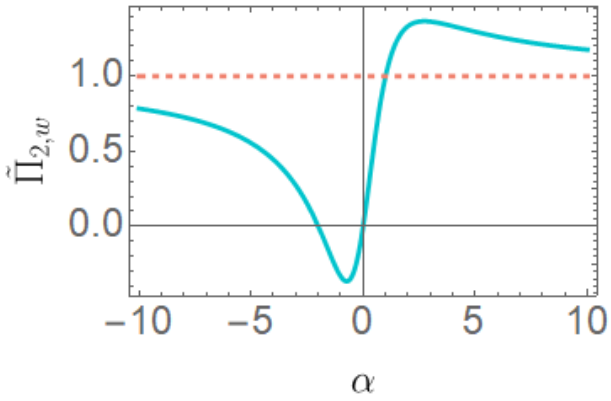

Figure 7.5: $\tilde{\Pi}_{2,w}$ in terms of α, where $\alpha \in \mathbb{R}$. When $\alpha = 0$, the weak value $\tilde{\Pi}_{2,w}$ equals zero. The minimum weak value is -0.366, which occurs when $\alpha = -0.732$, while the maximum weak value is 1.36, which occurs when $\alpha = 2.732$. Finally, the weak value is equal to 1 when $\alpha = 1$.

With these subspaces in mind, we can calculate the pseudo-probabilities, or weak values, of finding the particle in the corresponding boxes. The weak values of boxes $|\tilde{1}\rangle$ and $|\tilde{3}\rangle$ are 0, the pseudo-probability to find the particle in those boxes is 0. We might find the particle in box $|\tilde{2}\rangle$ with probability,

$$\tilde{\Pi}_{2,w} = \frac{\langle \psi_f|\tilde{2}\rangle\langle\tilde{2}|\psi_i\rangle}{\langle \psi_f|\psi_i\rangle} = \frac{\alpha(2+\alpha)}{2+\alpha^2}, \tag{7.55}$$

considering the values of $\alpha \in \mathbb{R}$. When $\alpha = 0$ (Fig. 7.5), the probability of finding the particle in $|\tilde{2}\rangle$ is zero, since the box $|\tilde{2}\rangle$ becomes equivalent to the box $|\tilde{1}\rangle$, and the particle is not found in any box. However, when $\alpha = 1$, the probability of finding the particle in box $|\tilde{2}\rangle$ becomes equal to one. In this case, the new basis is neither paracomplete nor paraconsistent, as we can be certain that the particle is located in box $|\tilde{2}\rangle$. The same holds true when α tends towards infinity or negative infinity. For other values of α, the probability ranges between negative values of -0.366 and positive values larger than 1.36.
The paradox initially appears to be paraconsistent in the system of boxes $|1\rangle$, $|2\rangle$, and $|3\rangle$, as the particle can be found in boxes $|1\rangle$ and $|2\rangle$ with a probability of 1, but the sum of all probabilities is equal to 1, suggesting that paracompleteness might not be inherent to the problem. However, by transitioning to the Krein space and calculating the probabilities there, we can eliminate the paraconsistent behavior by determining that the particle is in box $|\tilde{2}\rangle$, if it exists somewhere. However, this transition may also introduce paracompleteness, as the sum of all probabilities is no longer equal to 1.

7.4 Conclusions

In this chapter, we established a connection between quantum weak values and non-classical logics. The inherent logics governing weak values and, by extension, anomalous weak values, are characterized by both paraconsistency and paracompleteness. As a result, the same proposition can be both true and false simultaneously, while the probability of it being true or false need not necessarily be equal to 1.

The weak value can be described as the expectation value of a novel pseudo-projector, denoted as $\tilde{\rho}$, which is idempotent but not Hermitian. In fact, the operator $\tilde{\rho}$ is classified as pseudo-Hermitian, i.e., it is Hermitian with respect to a specific metric, denoted by $\hat{\eta}$. The metric $\hat{\eta}$ is not unique, and thus requires additional properties to be imposed for the selection of a specific metric. In our case, we decided to pick a unitary and Hermitian metric. This particular choice enables straightforward algebraic calculations, allowing for ease of computation. From a logical perspective, it imposes significant constraints on the associated logic, aiding in the identification of the most suitable and appropriate logic for the given context.
As demonstrated in this chapter, the metric $\hat{\eta}$ that corresponds to weak values satisfies the necessary conditions to describe an indefinite inner product space (Krein space).
In non-classical logics, it is possible to establish a correlation between orthogonality and negation, specifically the η-orthogonality in this case. By doing so, it can be inferred that certain intrinsic characteristics of a Krein space—such as having an intersection of η-orthogonal subspaces that are distinct from the null vector $|\varnothing\rangle$, and having a sum of η-orthogonal subspaces that are distinct from the entire Krein space—lead to the emergence of a paraconsistent and paracomplete logic.
Furthermore, it is noteworthy that the metrics linked to weak values take the form of $(-1,+1,+1,\ldots,+1)$ rather than $(-1,-1,-1,\ldots,+1,+1,\ldots,+1)$. This distinction holds significant importance. The metric associated with the weak value expression is a Minkowski-like metric, which characterizes special relativity! The existence of vectors with (pseudo-)norms that can be either positive or negative, as well as vectors that are not null but have zero norms (i.e., isotropic vectors that are pseudo-orthogonal to themselves), is significant in the context of paraconsistent logic.
A logic can be assigned to the Krein space used in weak value contexts, following a similar approach to that used in conventional quantum logic. In this case, a proposition p (from a non-classical propositional calculus) is linked to a closed subspace $\mathscr{L}(p)$ of the Krein space, which defines a semantics for this propositional calculus on the Krein space. Specifically, for any query about the outcome of measuring a particular observable, a proposition can be associated with it, indicating that certain physical states give rise to those measurement results.
The negation of a proposition is then associated with the pseudo-orthogonal space $\mathscr{L}_{\perp}$ (i.e. the orthogonal in the sense of the pseudo-euclidean metric defined on the Krein Space). The disjunction $p \vee q$ is linked to the closure of the direct sum of the subspaces $\mathscr{L}(p)$ and $\mathscr{L}(q)$, while the conjunction $p \wedge q$ is associated with the intersection of the subspaces $\mathscr{L}(p)$ and $\mathscr{L}(q)$. Using the properties of the Krein spaces, we discover that this logic is non-classical. It does not satisfy the "excluded middle principle" $((p \vee (\neg p)) \leftrightarrow$ tautology), and it is therefore a paracomplete logic. Furthermore, it does not satisfy the "non-contradiction principle" ($p \wedge (\neg p)$ is a contradiction), making it a paraconsistent logic. The conclusion of our analysis is the following: we discover a link between weak values and Minkowskian metric, giving rise to a link between those values and Krein spaces. Moreover, Krein spaces provide a semantic for a logic that is paracomplete and paraconsistent. This finding is relevant to the fundamental issue of interpreting quantum mechanics because quantum mechanics is sometimes considered to have an intrinsic paracomplete logic, where the "Tertium non datur" principle must be relinquished, neither a proposition nor its negation is necessarily true. Furthermore, in the context of weak measurements, pre- and post-selected states require us to abandon the non-contradiction principle. Thus, quantum mechanics can be associated with a logic that is both paracomplete and paraconsistent.
The situation may appear unsettling at first, but fortunately, mathematics provides us with tools to handle it. In particular, classical logic is associated with Boolean algebra, while intuitionistic

logic, which lacks the excluded-middle principle (Tertium non datur), is associated with Heyting algebra [2]. Similarly, we can associate paraconsistent logic with co-Heyting algebras, which is the dual algebra to Heyting albegras.

The algebra utilized in Krein spaces consists of all closed subspaces of the Krein space. Notably, this lattice diverges from the distributive properties. It also deviates from regularity, implying that the closure of the sum of two positive or negative definite subspaces (i.e., those containing solely vectors with positive or negative norms) no longer remains a positive or negative definite subspace. Moreover, this algebra departs from being Boolean, Heyting, and co-Heyting due to its non-distributive nature. Furthermore, the disjunction, represented by the closure of the sum, fails to adhere to the excluded middle principle, where the statement 'p OR NOT-p' does not hold true for the entire Krein space. Similarly, the conjunction, symbolized by the intersection of closed subspaces, does not satisfy the non-contradiction principle, as 'p AND NOT-p' does not yield the empty space. The introduction of this algebraic structure was initially documented in [170]. Despite its theoretical significance, it remains relatively uncommon in practical applications. Let us note that logic of indefinite metric space was deeply studied in the context of quantum mechanics and quantum field theory [171, 172]. However, in most cases, the subspaces associated with propositions of the propositional calculus are required to be regular, meaning they do not contain non-null vectors whose norm is zero. However, we are not required to limit ourselves to regular subspaces. On the contrary, the weak measurement situation leads us to consider subspaces that are not regular, and we can work with a lattice of non-regular subspaces. The three-box paradox shows precisely that we need to consider the logic of non-regular space.

To gain a better understanding of situations involving post-selected states, it may be beneficial to adopt a different logical framework and to utilize the algebra associated with Krein spaces, which arise naturally in the context of weak values expressed using Minkowskian metric. The aforementioned association can offer us an alternative perspective to comprehend well-established paradoxes. In this chapter, we directed our attention towards the three-box paradox and observed how paraconsistency and paracompleteness arise from the metric. This indicates that contradictions are inherent in this paradox, and, in fact, in all weak values.

This connection paves the way to an interpretation of all post-selected measurements as paraconsistent and paracomplete phenomena. This perspective is novel, as traditional philosophical discussions on quantum mechanics have focused on non-classical logics that are either paraconsistent or paracomplete. By exploring both properties simultaneously, we can acquire fresh insights and expand our comprehension of the foundational principles of quantum mechanics.

[2] A Heyting algebra, also known as a pseudo-Boolean algebra, is a bounded lattice with a partial order. In this algebraic structure, the greatest element is denoted as 1, and the least element is denoted as 0. The algebra is equipped with two fundamental operations: the meet operator $(\wedge)$ representing conjunction, and the join operator $(\vee)$ representing disjunction. Additionally, it features an implication operation. It is important to note that Heyting algebras do not necessarily adhere to the law of excluded middle. Heyting algebras are a generalization of Boolean algebras, with Boolean algebras being a specific type of Heyting algebra that adheres to the principle of excluded middle.

Chapter 8

Weak measurements in dissipative quantum systems

Weak values are widely used in the context of weak measurements for their amplification capacity [44, 57, 173] and the advantageous property of being complex numbers [68, 69]. However, as all quantum systems are open in practice, dissipative effects can affect the amplification qualities of weak values [174]. In this chapter, we explore the impact of dissipation on weak measurements. We also look at how weak values, because they are complex and unbounded, can be exploited to extract information on the dissipative dynamics of open quantum systems, such as the dissipation rate or non-markovianity [175].

In practice, quantum systems cannot be completely isolated. They always interact with the surrounding environment. The study of these dynamics falls within the scope of open quantum systems theory, which aims to understand how the interaction with the environment affects the system of interest [174, 176, 177]. The environment can usually be described in terms of bosonic modes and, in the Born-Markov and secular approximations, the system's dynamics can be modeled by a Lindblad master equation [178],

$$\dot{\hat{\rho}} = -i\left[\hat{H}_S, \hat{\rho}\right] + \sum_i \gamma_i \left(\hat{L}_i \hat{\rho} \hat{L}_i^\dagger - \frac{1}{2}\{\hat{L}_i^\dagger \hat{L}_i, \hat{\rho}\}\right) \equiv \mathscr{L}(\hat{\rho}), \tag{8.1}$$

where $\hat{L}_i$ are a set of jump operators, γ_i are dissipation rates, and $\hbar = 1$. In the following, to describe the time evolution over a time t of the operator $\hat{\rho}$ governed by the Lindblad master equation, we will use the superoperator notation $e^{\mathscr{L}t}\hat{\rho}$. This equation consists of two terms: the first term represents the unitary evolution of the density operator according to von Neumann's equation, while the second term, also noted $\mathscr{D}(\hat{\rho})$, accounts for the non-unitary dynamics resulting from dissipation, decoherence and dephasing. The dissipator $\mathscr{D}$ involves dissipation rates γ_i, one for each dissipation channel present [174].

Wiseman introduced the concept of weak values in dissipative systems in the context of homodyne measurements [11]. Since then, a few studies investigated weak measurements in open quantum systems. Two studies focused on the detrimental effects of decoherence on weak values, in particular, on the possibility that decoherence limits the sensitivity of sensors based on weak value amplification [179, 180]. Other research explored how Markovian environments prevent weak values from exhibiting anomalous properties and how quickly this process occurs [180, 181, 182, 183]

(an anomalous weak value has a value different from any average of the observable). Studies also sought to identify the optimal combination of a reservoir and a quantum system that minimizes the detrimental effects of dissipation on weak values at any given time. Non-Markovian environments appear to degrade the anomalous properties of weak values more slowly [184].
Our work expands upon previous studies by exploring the general limit of weak values at large dissipation times. Furthermore, we study the case of systems with degenerate ground states in the context of weak measurements and show that these systems can preserve the anomalous behaviour of weak values even in the limit of infinite dissipation times.
In addition, we leverage the amplification properties of weak values at short dissipation times and small dissipation rates to extract valuable information about the dissipation process. This approach serves as a valuable supplementary experiment, shedding light on the significance of incorporating dissipation rates in the modelling process of the main experimental setup, particularly when there is limited time available for dissipation. After a brief dissipation period, it enables an effective measurement of an amplified interaction rate, facilitating a comprehensive evaluation of its implications in the original experiment.
As after a short dissipation, one could measure an amplified interaction rate. Specifically, we focus on weak measurements where dissipation occurs after the weak interaction and before post-selection. The sequence involves pre-selecting the system, applying a general unitary operator $\hat{U} = e^{-igt\hat{A}_S \otimes \hat{N}}$, allowing for dissipative dynamics during a time τ, and finally performing post-selection. This scheme is present in any experimental setup with a time delay between the system-meter interaction and post-selection. We assume that the duration of the weak interaction is sufficiently short, so that any dissipation during this period is negligible.
We finally consider how our protocol would perform in a specific setup involving a two-level atom as the system and a single-mode cavity field as the meter. The weak measurement relies on a small interaction between the atom and the cavity field during the atom's short transit through the cavity. Subsequently, the atom undergoes dissipation through its interaction with the quantized radiation field of free space or another (leaky) cavity through which it passes. Post-selection is then performed and the real and imaginary parts of the weak value are measured by reading out the $\hat{Q}$ or $\hat{P}$ quadrature of the cavity field. The dissipation rate can be inferred by measuring the meter state with the benefits of weak value amplification. Additionally, if the dissipation process is non-Markovian, under certain circumstances, we show that it can be distinguished from a Markovian one based on the amplified weak value.

8.1 General weak measurements with dissipation

In this section, we consider the general theory of weak measurements, following the procedure of [26], but adding a dissipative evolution. The dissipation occurs during the time delay between the weak system–meter interaction and the post-selection. The protocol consists of five steps: system pre-selection, weak interaction, dissipative dynamics, post-selection on the system, and meter readout, as illustrated in Fig. 8.1. Consider that the initial state of the system is described by the density operator $\hat{\sigma}_i$ and that of the meter by $\hat{\mu}_0$. The tensor product of the states of the system and the meter provides the state of the full composite system, resulting in

$$\hat{\rho}_0 = \hat{\sigma}_i \otimes \hat{\mu}_0. \tag{8.2}$$

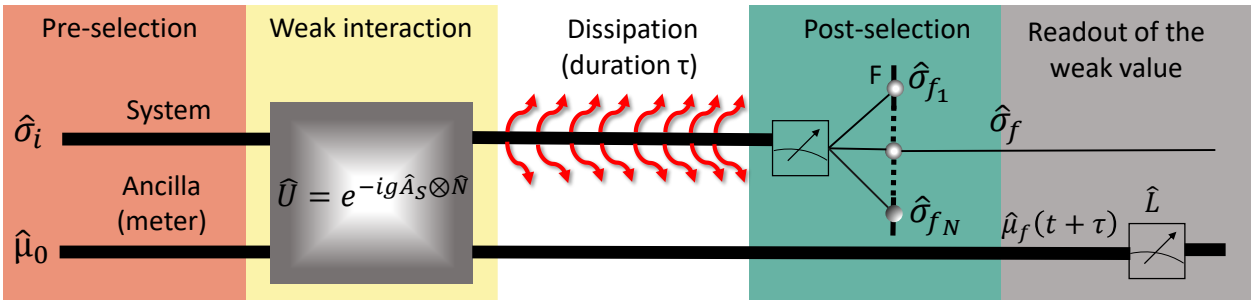

Figure 8.1: Overview of the steps involved in the dissipative weak measurement protocol. The process begins with pre-selection of the system, followed by the implementation of a weak measurement described through the unitary operator $\hat{U}$. After the weak interaction, the system undergoes dissipation for a duration τ before a post-selection. Finally, the meter is readout to extract information on the weak value.

The full system evolution depends on three components: the system Hamiltonian $\hat{H}_S$, the meter (or ancilla) Hamiltonian $\hat{H}_A$, and the interaction Hamiltonian

$$\hat{H}_{\text{int}} = g\hat{A}_S \otimes \hat{N}, \tag{8.3}$$

where $\hat{A}_S$ is the observable of interest acting in the system Hilbert space, $\hat{N}$ is an operator acting in the meter Hilbert space, g is the interaction strength, and $\hbar = 1$.
In the interaction picture with respect to $\hat{H}_0 = \hat{H}_S \otimes \hat{I} + \hat{I} \otimes \hat{H}_A$, the density operator of the composite system evolves as

$$\frac{d\hat{\rho}_I(t)}{dt} = -i\left[\hat{V}(t), \hat{\rho}_I(t)\right], \tag{8.4}$$

where the interaction Hamiltonian and the global density operator are given in the interaction picture by

$$\hat{V}(t) = e^{i\hat{H}_0 t}\hat{H}_{\text{int}}e^{-i\hat{H}_0 t}, \qquad \hat{\rho}_I(t) = e^{i\hat{H}_0 t}\hat{\rho}_0 e^{-i\hat{H}_0 t}, \tag{8.5}$$

where $\hbar = 1$.
The solution of Eq. 8.4 reads

$$\hat{\rho}_I(t) = \overrightarrow{\mathscr{T}}\exp\left[-i\int_0^t \hat{V}(t')\,dt'\right]\hat{\rho}_I(0)\exp\left[i\int_0^t \hat{V}(t')\,dt'\right]\overleftarrow{\mathscr{T}}, \tag{8.6}$$

where $\mathscr{T}$ is the time ordering operator. Given the small interaction strength g and the fact that $\hat{V}(t) \propto g$, we can expand the exponential in Eq. 8.6 in a Taylor series to first order in the interaction strength. As a result, we can express the density operator at time t as follows

$$\begin{aligned}
\hat{\rho}_I(t) &\approx \left[\hat{I} - i\int_0^t \hat{V}(t')\,dt'\right]\hat{\rho}_0\left[\hat{I} + i\int_0^t \hat{V}(t')\,dt'\right] \\
&\approx \hat{\rho}_0 + i\hat{\rho}_0\int_0^t \hat{V}(t')\,dt' - i\int_0^t \hat{V}(t')\,dt'\hat{\rho}_0 \\
&= \hat{\rho}_0 + i\left[\hat{\rho}_0, \int_0^t \hat{V}(t')\,dt'\right].
\end{aligned} \tag{8.7}$$

We assume that the weak interaction duration t is sufficiently short, so that the interaction Hamiltonian $\hat{V}(t)$ does not evolve much from $\hat{H}_{\text{int}}$ under the free evolution due to $\hat{H}_0$. In these circumstances, we can make a series development of $\hat{V}(t')$ around $t/2$ to first order:

$$\hat{V}\left(t'\right) \approx \hat{V}\left(t/2\right) + \dot{\hat{V}}(t/2)\left(t' - t/2\right) \tag{8.8}$$

with $\dot{\hat{V}}(t/2) = \frac{d\hat{V}}{dt'}\big|_{t'=t/2}$. Then, the density operator is given, at first order in time, by

$$\begin{aligned} \hat{\rho}_I(t) &\approx \hat{\rho}_0 + i\left[\hat{\rho}_0, \int_0^t dt' \left(\hat{V}\left(t/2\right) + \dot{\hat{V}}(t/2)\left(t' - t/2\right)\right)\right] \\ &= \hat{\rho}_0 + it\left[\hat{\rho}_0, \hat{V}\left(t/2\right)\right], \end{aligned} \tag{8.9}$$

since the integral of the second term is exactly 0. The first contribution neglected in Eq. 8.9 due to the approximation Eq. 8.8 is of the order $\left(\frac{i}{2}\right)^2 \frac{1}{3!} t^3 \left[\hat{H}_0, \left[\hat{H}_0, \hat{V}\left(t/2\right)\right]\right]$.
After the unitary evolution of the composite system, the system S follows a dissipative dynamics during a time interval τ, while it is assumed that the meter does not undergo any dissipative process. The total density operator $\hat{\rho}_I(t+\tau)$ is given, after the dissipative evolution, by

$$\hat{\rho}_I(t+\tau) = \left(e^{\mathscr{D}\tau} \otimes \hat{I}\right) \hat{\rho}_I(t) \approx \left(e^{\mathscr{D}\tau} \otimes \hat{I}\right) \left(\hat{\rho}_0 + it\left[\hat{\rho}_0, \hat{V}\left(t/2\right)\right]\right), \tag{8.10}$$

where the dissipator $\mathscr{D}$ has replaced the full Linbladian $\mathscr{L}$ because we are working in the interaction picture. Indeed, in the interaction picture, the evolution defined in Eq. 8.1 becomes $\dot{\hat{\rho}}_I = \mathscr{D}(\rho_I)$. Note that the dissipator remains identical to the one defined in the Schrödinger representation, as a result of the commutation rules obeyed by the jump operators $\hat{L}_i$ with the system Hamiltonian $\hat{H}_S$ [185]. After the dissipation time τ, the system is post-selected to the final state $\hat{\sigma}_f$. Post-selection is carried out by performing a projective measurement and filtering the information relevant to the state $\hat{\sigma}_f$. At this point, the meter state is, in the interaction picture,

$$\hat{\mu}_{fI}(t+\tau) = \frac{\text{Tr}_S\left[\left(\hat{\sigma}_{fI}(t+\tau) \otimes \hat{I}\right)\left(e^{\mathscr{D}\tau} \otimes \hat{I}\right)\hat{\rho}_I(t)\right]}{\text{Tr}\left[\left(\hat{\sigma}_{fI}(t+\tau) \otimes \hat{I}\right)\left(e^{\mathscr{D}\tau} \otimes \hat{I}\right)\hat{\rho}_I(t)\right]}, \tag{8.11}$$

where Tr_S is the partial trace over the system degrees of freedom, and the post-selection operator in the interaction picture depends on the post-selection time $t+\tau$ as

$$\hat{\sigma}_{fI}(t+\tau) = e^{i\hat{H}_S(t+\tau)} \hat{\sigma}_f e^{-i\hat{H}_S(t+\tau)}, \tag{8.12}$$

where $\hbar = 1$. In the remainder of this section, we will drop the explicit time dependence of $\hat{\sigma}_{fI}(t+\tau)$ and note it $\hat{\sigma}_{fI}$ for simplicity. The expression in the denominator of Eq. 8.11 corresponds to the probability of obtaining the post-selected state $\hat{\sigma}_f$, given the state of the composite system $\hat{\rho}_I(t+\tau)$. The denominator is equal to the trace of the numerator, ensuring that the trace of the meter state is equal to 1. Using $\hat{H}_{\text{int}} = 1g\hat{A}_S \otimes \hat{N}$, the denominator of Eq. 8.11 becomes, to first order in gt,

$$\begin{aligned} &\text{Tr}\left[\left(\hat{\sigma}_{fI} \otimes \hat{I}\right)\left(e^{\mathscr{D}\tau} \otimes \hat{I}\right)\hat{\rho}_I(t)\right] \\ &\quad\approx \text{Tr}\left[\hat{\sigma}_{fI}\, e^{\mathscr{D}\tau}\left(\hat{\sigma}_i\right)\right] + 2gt\,\text{Im}\left(\text{Tr}\left[\hat{\sigma}_{fI}\, e^{\mathscr{D}\tau}\left(\hat{A}_{SI}(t/2)\,\hat{\sigma}_i\right)\right]\text{Tr}\left[\hat{\mu}_0 \hat{N}_I(t/2)\right]\right) \\ &\quad= \text{Tr}\left[\hat{\sigma}_{fI}\, e^{\mathscr{D}\tau}\left(\hat{\sigma}_i\right)\right]\left(1 + 2gt\,\text{Im}\left[A_{S,w}(\tau)\right]\langle \hat{N}_I(t/2)\rangle_0\right), \end{aligned} \tag{8.13}$$

where we have defined the weak value with dissipation, denoted $A_{S,w}(\tau)$, as

$$A_{S,w}(\tau) = \frac{\mathrm{Tr}\left[\hat{\sigma}_{fI}\, e^{\mathscr{D}\tau}\left(\hat{A}_{SI}(t/2)\,\hat{\sigma}_i\right)\right]}{\mathrm{Tr}\left[\hat{\sigma}_{fI}\, e^{\mathscr{D}\tau}\left(\hat{\sigma}_i\right)\right]}, \tag{8.14}$$

and $\langle \hat{N}_I(t/2)\rangle_0 = \mathrm{Tr}\left[\hat{\mu}_0 \hat{N}_I(t/2)\right]$ corresponds to the expectation value of the operator $\hat{N}_I(t/2)$ in the initial meter state $\hat{\mu}_0$. Our definition (8.14) is very general and coincides with Wiseman's definition in the special case of homodyne measurements in cavity QED [27]. We stress that the weak value Eq. 8.14 has been calculated in the interaction picture and that the system and meter observables $\hat{A}_S$ and $\hat{N}$ appear thus as $A_{SI}(t/2)$ and $N_I(t/2)$, respectively. Their time dependence at $t/2$ results from the approximation Eq. 8.8. The operator $\hat{\sigma}_{fI}$ corresponds to the post-selected state $\hat{\sigma}_f$ at time $t+\tau$ in the interaction picture, as expressed in Eq. 8.12. If we revert to the Schrödinger picture, we see that $t/2$ corresponds to the effective time of the pre-selection and the post-selection for an instantaneous weak interaction that is symmetric with respect to pre- and post-selection. Advantageously, by setting the post-selection operator as a constant in the interaction picture, namely $\hat{\sigma}_{fI}(t+\tau) = \hat{\sigma}_{fI}(t/2)$ (the constant is defined with respect to the effective pre- and post-selection time), we can suppress in practice the effects of the system free evolution during time $\tau + t/2$ on the weak value, so that we can focus specifically on the repercussions of dissipation, as analyzed later on in this chapter.
Similarly, for the numerator of Eq. 8.11, we obtain

$$\begin{aligned}
&\mathrm{Tr}_S\left[\left(\hat{\sigma}_{fI}\otimes\hat{I}\right)\left(e^{\mathscr{D}\tau}\otimes\hat{I}\right)\hat{\rho}_I(t)\right] \\
&\quad\approx\ \mathrm{Tr}\left[\hat{\sigma}_{fI}\, e^{\mathscr{D}\tau}\left(\hat{\sigma}_i\right)\right]\hat{\mu}_0 + igt\left\{\mathrm{Tr}\left[\hat{\sigma}_{fI}\, e^{\mathscr{D}\tau}\left(\hat{\sigma}_i\hat{A}_{SI}\right)\right]\hat{\mu}_0\hat{N}_I - \mathrm{Tr}\left[\hat{\sigma}_{fI}\, e^{\mathscr{D}\tau}\left(\hat{A}_{SI}\hat{\sigma}_i\right)\right]\hat{N}_I\hat{\mu}_0\right\} \\
&\quad=\ \mathrm{Tr}\left[\hat{\sigma}_{fI}\, e^{\mathscr{D}\tau}\left(\hat{\sigma}_i\right)\right]\left[\hat{\mu}_0 + igt\left(\overline{A_{S,w}(\tau)}\hat{\mu}_0\hat{N}_I - A_{S,w}(\tau)\hat{N}_I\hat{\mu}_0\right)\right],
\end{aligned} \tag{8.15}$$

where the interaction picture operators $\hat{A}_{SI}$ and $\hat{N}_I$ should be evaluated at time $t/2$, and where we used the property $\left[e^{\mathscr{D}\tau}\left(\hat{O}\right)\right]^\dagger = e^{\mathscr{D}\tau}\left(\hat{O}^\dagger\right)$, valid for an arbitrary operator $\hat{O}$.
By combining the denominator Eq. 8.13 and the numerator Eq. 8.15, the final meter density matrix is, at first order in gt,

$$\hat{\mu}_{fI}(t+\tau) = \frac{\hat{\mu}_0 + igt\left(\overline{A_{S,w}(\tau)}\hat{\mu}_0\hat{N}_I(t/2) - A_{S,w}(\tau)\hat{N}_I(t/2)\,\hat{\mu}_0\right)}{1 + 2gt\,\mathrm{Im}\left[A_{S,w}(\tau)\right]\langle\hat{N}_I(t/2)\rangle_0}. \tag{8.16}$$

Up to a normalization constant, the final meter state can be expressed as the initial meter state $\hat{\mu}_0$ plus a term that depends on the pre-selected state, the observable, and the post-selected state. While this new term may seem small in principle, as it depends on a small parameter gt, there are cases where the weak value $A_{S,w}(\tau)$ becomes large, specifically when its denominator is close to zero due to the near-orthogonality of the pre- and post-selected states, resulting in a significant contribution to the meter state.
To actually perform the weak measurement, one should measure the expectation value of a meter observable, $\hat{L}$. The measurement result will depend on the weak value that appears in the meter final state, as described by Eq. 8.16. In the interaction picture, $\hat{L}$ is given by

$$\hat{L}_I(t+\tau) = e^{i\hat{H}_A(t+\tau)}\hat{L}\,e^{-i\hat{H}_A(t+\tau)}, \tag{8.17}$$

while its expectation value takes the form

$$\langle \hat{L} \rangle_f = \mathrm{Tr}\left(\hat{L}_I(t+\tau)\,\hat{\mu}_{fI}\right) = \frac{\langle \hat{L}_I(t+\tau)\rangle_0 + 2gt\,\mathrm{Im}\left[A_{S,w}(\tau)\,\langle \hat{L}_I(t+\tau)\,\hat{N}_I(t/2)\rangle_0\right]}{1+2gt\,\mathrm{Im}\left[A_{S,w}(\tau)\right]\langle \hat{N}_I(t/2)\rangle_0}, \tag{8.18}$$

where a procedure similar to [26] was followed to obtain the numerator expression. All expectation values are computed with respect to the initial meter state $\hat{\mu}_0$.
From now on, let us assume that the expectation value of the meter operator $\hat{N}_I(t/2)$ in the meter initial state is zero, that is, $\langle \hat{N}_I(t/2)\rangle_0 = 0$. If this is not the case, we could possibly redefine and translate the meter operator $\hat{N}$ to satisfy $\langle \hat{N}_I(t/2)\rangle_0 = 0$. When the meter free evolution is fully negligible during the short interaction time t, this assumption states that the expectation value of the meter observable is zero in the meter initial state, a natural calibration requirement imparted to the meter initial state. In the Schrödinger picture, the assumption requires the expectation value of the meter observable $\hat{N}$ to be zero in the state $\hat{\mu}_0(t/2)$ resulting from the free evolution for a duration $t/2$ of the meter initial state $\hat{\mu}_0$. In these conditions, the meter expectation value at the end of the measurement is simply the numerator of Eq. 8.18, namely

$$\langle \hat{L} \rangle_f = \mathrm{Tr}\left(\hat{L}_I(t+\tau)\,\hat{\mu}_{fI}\right) = \langle \hat{L}_I(t+\tau)\rangle_0 + 2gt\,\mathrm{Im}\left[A_{S,w}(\tau)\,\langle \hat{L}_I(t+\tau)\,\hat{N}_I(t/2)\rangle_0\right]. \tag{8.19}$$

In addition, if we select an initial meter density operator that commutes with the meter Hamiltonian, i.e. $\left[\hat{\mu}_0, \hat{H}_A\right] = 0$, the final meter average simplifies to

$$\langle \hat{L} \rangle_f = \langle \hat{L} \rangle_0 + 2gt\,\mathrm{Im}\left[A_{S,w}(\tau)\,\langle \hat{L}_I(t/2+\tau)\,\hat{N}\rangle_0\right], \tag{8.20}$$

where only the operator $\hat{L}_I$ remains in the interaction picture, evaluated at the effective time $t/2+\tau$. The latter reflects the natural evolution under $\hat{H}_A$ of the meter state perturbation due to the weak interaction. For short dissipation times τ, this time dependence could be neglected whenever $i(t/2+\tau)\,\langle\left[\hat{H}_A, \hat{L}\right]\hat{N}\rangle_0 \ll \langle \hat{L}\hat{N}\rangle_0$.
The shift in the expectation value of a general meter observable, $\hat{L}$, as given by Eq. 8.19, depends on both the real and imaginary parts of the weak value. It is enlightening to reformulate it the following way:

$$\langle \hat{L} \rangle_f = \langle \hat{L}_I \rangle_0 - igt\,\mathrm{Re}A_{S,w}(\tau)\,\langle\left[\hat{L}_I, \hat{N}_I\right]\rangle_0 + gt\,\mathrm{Im}A_{S,w}(\tau)\,\langle\left\{\hat{L}_I, \hat{N}_I\right\}\rangle_0, \tag{8.21}$$

where the interaction operators should be evaluated at the appropriate times $\hat{L}_I(t+\tau)$ and $\hat{N}_I(t/2)$. This expression makes the real and imaginary parts of the weak value appear explicitly. We can choose $\hat{L}$ such that $\langle \hat{L}_I(t+\tau)\rangle_0 = 0$, to ensure that the expectation value of $\hat{L}$ is now directly proportional to the terms which depend on the weak value. To separate the shifts due to the real and imaginary components, we can choose specific meter observables. For instance, when the meter observable at time $t+\tau$ is equal to the pointer at time $t/2$, i.e. $\hat{L}_I(t+\tau) = \hat{N}_I(t/2)$, the expectation value of the meter observable is proportional to the imaginary part of the weak value. Indeed, in this case, the expectation value Eq. 8.21 reads

$$\langle \hat{N} \rangle_f = 2gt\langle \hat{N}_I^2(t/2)\rangle_0\,\mathrm{Im}A_{S,w}(\tau), \tag{8.22}$$

where $\langle \hat{N}_I^2(t/2)\rangle_0 = \mathrm{Tr}\left[\hat{\mu}_0\hat{N}_I^2(t/2)\right] = \Delta^2\hat{N}_I(t/2) \neq 0$, considering that $\langle \hat{N}_I(t/2)\rangle_0 = 0$. On the other hand, when the meter observable, $\hat{L} = \hat{M}$, at time $t+\tau$ is the canonical conjugate of the pointer

at time $t/2$, such that $\left[\hat{M}_I(t+\tau),\hat{N}_I(t/2)\right]=i\hat{I}$, its expectation value has a term proportional to the real part of the weak value. More specifically, we have

$$\langle\hat{M}\rangle_f=\left[gt\ \mathrm{Re}A_{S,w}(\tau)+gt\ \langle\left\{\hat{M}_I(t+\tau),\hat{N}_I(t/2)\right\}\rangle_0\ \mathrm{Im}A_{S,w}(\tau)\right], \tag{8.23}$$

assuming that $\langle\hat{M}_I(t+\tau)\rangle_0=0$. It is sometimes possible to choose the observables and the initial state in such a way that we also have $\langle\left\{\hat{M}_I(t+\tau),\hat{N}_I(t/2)\right\}\rangle_0=0$. This then leads to the expectation value of $\hat{M}$ being directly proportional to the real part of the weak value. Using $\hat{N}$ and $\hat{M}$ as meter observables enables separating the real and imaginary components of the weak value, which is often desirable in many experimental setups. In addition, they enable describing the argument of the weak value [18, 112], here as a function of the dissipation time τ, in the meter phase space [19]. In section 8.3, we will show how Eq. 8.19 connects directly the meter measurement to the modulus and argument of the weak value. We remind the reader that equations Eq. 8.19–8.23) were obtained under the assumptions that the expectation value $\langle\hat{N}_I(t/2)\rangle_0=0$. If this is not the case, the denominator present in Eq. 8.18 should be kept. In particular, the general expression for Eq. 8.21 is

$$\langle\hat{L}\rangle_f=\frac{\langle\hat{L}_I\rangle_0-igt\,\mathrm{Re}A_{S,w}(\tau)\langle\left[\hat{L}_I,\hat{N}_I\right]\rangle_0+gt\,\mathrm{Im}A_{S,w}(\tau)\langle\left\{\hat{L}_I,\hat{N}_I\right\}\rangle_0}{1+2gt\,\mathrm{Im}\left[A_{S,w}(\tau)\right]\langle\hat{N}_I\rangle_0}, \tag{8.24}$$

with the appropriate time dependence $\hat{L}_I(t+\tau)$ and $\hat{N}_I(t/2)$.

The main results of this section, namely Eqs. 8.14, 8.19 and 8.21, as well as 8.24, describe the consequences on weak measurements of dissipation occurring after the weak interaction, before post-selection. These expressions ensue from the weak interaction approximation Eq. 8.8–8.9, that was used in Eq. 8.13 and Eq. 8.15 to evaluate the meter reduced density matrix Eq. 8.11 to first order in gt. By using expressions in the interaction picture, we also include the full treatment of the free Hamiltonian evolution of both the system and the meter, which is required for describing long dissipation times τ.

While there could also be dissipation during the time delay between pre-selection and the system–meter interaction, this would only alter the initial system state from $\hat{\sigma}_i(-T)$ to $\hat{\sigma}_i(0)$, where $\hat{\sigma}_i(-T)$ is the density operator produced by the pre-selection procedure at time $-T$ (either as characterized experimentally or as defined theoretically) and where T is the time delay between pre-selection and the application of the unitary operator at time 0. In that case, in the definition Eq. 8.14 of the weak value with dissipation, we should simply use $\hat{\sigma}_i(0)$ for the effectively pre-selected density operator: $\hat{\sigma}_i=\hat{\sigma}_i(0)=e^{\mathscr{L}T}(\hat{\sigma}_i(-T))=e^{\mathscr{D}T}(\hat{\sigma}_{iI}(-T))$, with the last equality expressed in the interaction picture. The effect of dissipation before the weak interaction is thus simply that the effective initial state $\hat{\sigma}_i(0)$ may differ from the desired initial state. As a result, it is generally possible to modify the post-selected state in order to partially preserve the amplification capabilities of the weak value (if this is the objective), provided that the evolution of the system is well-known and that the actual initial state $\hat{\sigma}_i(-T)$ is not completely mixed. In general, Eq. 8.19 does not account for dissipation occurring during the weak interaction, unless we assume that it is negligible because of the short duration t of the weak interaction.

As an illustration of the impact of dissipation before the weak interaction, let us consider the case of dissipation occurring only before the weak interaction (no dissipation in between the weak in-

teraction and post-selection). In that situation, the weak value would be

$$\widetilde{A_{S,w}}(T) = \frac{\mathrm{Tr}\left[\hat{\sigma}_{fI}(t+\tau)\hat{A}_{SI}(t/2)\,e^{\mathscr{D}T}\left(\hat{\sigma}_{iI}(-T)\right)\right]}{\mathrm{Tr}\left[\hat{\sigma}_{fI}(t+\tau)\,e^{\mathscr{D}T}\left(\hat{\sigma}_{iI}(-T)\right)\right]}, \tag{8.25}$$

where T is the dissipation duration. If the system state at time $-T$ is not completely mixed, the pre-selected state evolution under dissipation can be taken into account by modifying the post-selected state, in order to preserve some amplification, even at a very large dissipation time T. In other words, we can often choose a post-selected state that is sufficiently orthogonal to the pre-selected state after dissipation, $\hat{\sigma}_i(0)$. As an illustration, if the dissipation time is infinite and the system possesses a single non-degenerate ground state $|g\rangle$, considering a pure post-selected state $|\psi_f\rangle$, and ignoring the effects of the system free evolution, the weak value is

$$\lim_{T\to\infty} \widetilde{A_{S,w}}(T) = \frac{\langle\psi_f|\hat{A}|g\rangle}{\langle\psi_f|g\rangle}. \tag{8.26}$$

By choosing a post-selected state that is almost orthogonal to $|g\rangle$, we can find amplification even at infinite dissipation time. We will show in the next section that this is not the case when dissipation takes place after the weak interaction.

The consequences on the weak value of having dissipation before or after the weak interaction are completely different. Having dissipation before the weak interaction simply alters the initial state. However, having dissipation after the weak interaction destroys the coherences of the system, partially or completely, as we will show in the next section. Consequently, both types of dissipation should be studied separately. Furthermore, all the results of this chapter can be extended to the case in which there is dissipation before the weak interaction by changing the initial density operator, $\hat{\sigma}_i(-T)$ by an initial density operator after dissipation $\hat{\sigma}_i(0)$, just before the weak interaction.

8.2 Weak value evolution

In this section, we investigate the properties of the weak value of an arbitrary operator in the context of long dissipation times. Previous studies have suggested that dissipation can destroy the anomalous properties of the weak value [180, 179, 181, 182, 183, 184], which means that weak values converge to values within the range of the eigenvalues of the observable in the presence of dissipation. Our findings reveal that, in non-degenerate systems, the weak value approaches the expectation value of the operator as the dissipation time tends to infinity. Furthermore, we demonstrate that the anomalous properties of the weak value can persist at infinite dissipation time in systems with degenerate ground states. This suggests that dissipation does not always necessarily result in the loss of the amplification effect that the weak value can provide.

8.2.1 Non-degenerate ground state

Let us assume that the system under study possesses only one ground state, denoted by $|g\rangle$. In this case, the dissipative evolution invariably destroys anomalous properties of weak values at very

long times, regardless of the system's markovianity[1].
For simplicity of calculation, and without loss of generality, let us consider a two-level system. The excited state of the system is denoted by $|e\rangle$, and we assume that the pre- and post-selected states, $|\psi_i\rangle$ and $\left|\psi_f(\tau)\right\rangle$, are both pure states. We choose a post-selected state that depends on the dissipation duration τ in such a way that the post-selected state is constant in the interaction representation, noted $\left|\psi_{fI}\right\rangle$. This allows us to focus on analyzing the consequences of dissipation without observing effects of the free Hamiltonian evolution of the system during time τ. In practice, this is equivalent to ensuring that the effectively post-selected state at time $t/2$ does not depend on the dissipation duration. In this scenario, the weak value with dissipation can be expressed as follows

$$\begin{aligned} A_{S,w}(\tau) &= \frac{\mathrm{Tr}\left[\left|\psi_{fI}\right\rangle\left\langle\psi_{fI}\right| e^{\mathscr{D}\tau}\left(\hat{A}_{SI}\left|\psi_i\right\rangle\left\langle\psi_i\right|\right)\right]}{\mathrm{Tr}\left[\left|\psi_{fI}\right\rangle\left\langle\psi_{fI}\right| e^{\mathscr{D}\tau}\left(\left|\psi_i\right\rangle\left\langle\psi_i\right|\right)\right]} \\ &= \frac{\mathrm{Tr}\left[\left|\psi_{fI}\right\rangle\left\langle\psi_{fI}\right|\left(D_{ee}(\tau)\left|e\right\rangle\left\langle e\right| + D_{eg}(\tau)\left|e\right\rangle\left\langle g\right| + D_{ge}(\tau)\left|g\right\rangle\left\langle e\right| + D_{gg}(\tau)\left|g\right\rangle\left\langle g\right|\right)\right]}{\mathrm{Tr}\left[\left|\psi_{fI}\right\rangle\left\langle\psi_{fI}\right| e^{\mathscr{D}\tau}\left(\left|\psi_i\right\rangle\left\langle\psi_i\right|\right)\right]}, \end{aligned} \tag{8.27}$$

where

$$\hat{D}(\tau) = e^{\mathscr{D}\tau}\left(\hat{A}_{SI}\left|\psi_i\right\rangle\left\langle\psi_i\right|\right) \tag{8.28}$$

and the $D_{ij}(\tau)$ coefficients are the matrix elements of the operator $\hat{D}(\tau)$. The dissipator $\mathscr{D}$ represents the Lindbladian in the interaction picture. The observable $\hat{A}_{SI}$ is in principle evaluated in the interaction picture at time $t/2$. However, for the purpose of this discussion, we could neglect the small effect of the free evolution and consider that $\hat{A}_{SI}(t/2) = \hat{A}_S$ without loss of generality, since t is a small constant parameter. The trace of $\hat{D}(\tau)$, the result of the evolution of the operator $\hat{A}_{SI}\left|\psi_i\right\rangle\left\langle\psi_i\right|$, is preserved at all times τ, i.e., $\mathrm{Tr}\left(e^{\mathscr{D}\tau}\left(\hat{A}_{SI}\left|\psi_i\right\rangle\left\langle\psi_i\right|\right)\right) = \mathrm{Tr}\left(\hat{A}_{SI}\left|\psi_i\right\rangle\left\langle\psi_i\right|\right)$. Given that the Lindbladian dynamics associated with dissipation drives any operator to the ground state in the limit of infinite time (in other words, $\lim_{\tau\to\infty} e^{\mathscr{D}\tau}(\hat{O}) = \mathrm{Tr}[\hat{O}]\left|g\right\rangle\left\langle g\right|$), the coefficient that multiplies the ground density operator at long times should be equal to the expectation value of the operator $\hat{A}_{SI}$, i.e., $\lim_{\tau\to\infty} D_{gg}(\tau) = \mathrm{Tr}\left(\hat{A}_{SI}\left|\psi_i\right\rangle\left\langle\psi_i\right|\right)$. Therefore, the limit of the weak value can be expressed as

$$\begin{aligned} \lim_{\tau\to\infty} A_{S,w}(\tau) &= \frac{\mathrm{Tr}\left[\left|\psi_{fI}\right\rangle\left\langle\psi_{fI}\right| \mathrm{Tr}\left(\hat{A}_{SI}\left|\psi_i\right\rangle\left\langle\psi_i\right|\right)\left|g\right\rangle\left\langle g\right|\right]}{\left|\left\langle\psi_{fI}\middle|g\right\rangle\right|^2} \\ &= \mathrm{Tr}\left(\hat{A}_{SI}\left|\psi_i\right\rangle\left\langle\psi_i\right|\right)\frac{\mathrm{Tr}\left[\left|\psi_{fI}\right\rangle\left\langle\psi_{fI}\middle|g\right\rangle\left\langle g\right|\right]}{\left|\left\langle\psi_{fI}\middle|g\right\rangle\right|^2} = \mathrm{Tr}\left(\hat{A}_{SI}\left|\psi_i\right\rangle\left\langle\psi_i\right|\right)\frac{\left|\left\langle\psi_{fI}\middle|g\right\rangle\right|^2}{\left|\left\langle\psi_{fI}\middle|g\right\rangle\right|^2} \\ &= \mathrm{Tr}\left(\hat{A}_{SI}\left|\psi_i\right\rangle\left\langle\psi_i\right|\right) = \left\langle\psi_i\right|\hat{A}_{SI}\left|\psi_i\right\rangle. \end{aligned} \tag{8.29}$$

In conclusion, under dissipation, any weak value of a general observable approaches its expectation value on the initial state in the limit of infinite time. In particular, this result remains true regardless of the dimensionality of the quantum state and the chosen post-selected state, under the assumption of a unique steady state.

[1] Markovianity characterizes a process or system with memorylessness, meaning its state at time t is solely influenced by its state at time $t-1$, uninfluenced by preceding temporal stages. In contrast, a non-Markovian process relies on its entire historical sequence, diverging from the behaviour of a Markovian counterpart.

8.2.2 Degenerate ground state

We demonstrate that when a system's ground state is degenerate, amplification can occur at infinite dissipation times. Specifically, let us consider an N-level system that has a two-dimensional degenerate ground state. We chose the two orthogonal states $|g_1\rangle$ and $|g_2\rangle$ as a basis to describe the ground state. Depending on the initial state, the final evolution of the system can result in the final state being either $|g_1\rangle$, $|g_2\rangle$, a linear combination of the two, or a density matrix involving both states. In cases where the evolutions under dissipation in the denominator and numerator of the weak value yield the same final state, the weak value at infinite dissipation times tends towards the expectation value, as in Eq. 8.29. However, in cases where the final operators differ, amplification can occur at very long times. In this scenario, assuming pure pre- and post-selected states for simplicity, the weak value at infinite dissipation times can be expressed as follows,

$$\begin{aligned}\lim_{\tau\to\infty} A_{S,w}(\tau) &= \lim_{\tau\to\infty} \frac{\mathrm{Tr}\left[\left|\psi_{fI}\right\rangle\left\langle\psi_{fI}\right| e^{\mathscr{D}\tau}\left(\hat{A}_{SI}\left|\psi_i\right\rangle\left\langle\psi_i\right|\right)\right]}{\mathrm{Tr}\left[\left|\psi_{fI}\right\rangle\left\langle\psi_{fI}\right| e^{\mathscr{D}\tau}\left(\left|\psi_i\right\rangle\left\langle\psi_i\right|\right)\right]} \\ &= \frac{a_{11}\left|\left\langle\psi_{fI}|g_1\right\rangle\right|^2 + a_{22}\left|\left\langle\psi_{fI}|g_2\right\rangle\right|^2 + a_{21}\left\langle\psi_{fI}|g_2\right\rangle\left\langle g_1|\psi_{fI}\right\rangle + a_{12}\left\langle\psi_{fI}|g_1\right\rangle\left\langle g_2|\psi_{fI}\right\rangle}{b_{11}\left|\left\langle\psi_{fI}|g_1\right\rangle\right|^2 + b_{22}\left|\left\langle\psi_{fI}|g_2\right\rangle\right|^2 + b_{21}\left\langle\psi_{fI}|g_2\right\rangle\left\langle g_1|\psi_{fI}\right\rangle + b_{12}\left\langle\psi_{fI}|g_1\right\rangle\left\langle g_2|\psi_{fI}\right\rangle},\end{aligned} \tag{8.30}$$

where

$$\lim_{\tau\to\infty} e^{\mathscr{D}\tau}\left(\hat{A}_{SI}\left|\psi_i\right\rangle\left\langle\psi_i\right|\right) = \sum_{j=1}^{2}\sum_{k=1}^{2} a_{jk}\left|g_j\right\rangle\left\langle g_k\right|, \tag{8.31}$$

$$\lim_{\tau\to\infty} e^{\mathscr{D}\tau}\left(\left|\psi_i\right\rangle\left\langle\psi_i\right|\right) = \sum_{j=1}^{2}\sum_{k=1}^{2} b_{jk}\left|g_j\right\rangle\left\langle g_k\right|. \tag{8.32}$$

One can find amplification and complex weak values even at infinite time by choosing the appropriate post-selected state and observable. In that case, since these quantities cannot be any expectation value of the operator $\hat{A}_S$, the weak value is considered anomalous.
An alternative explanation stems from the decomposition of the unnormalized state $\hat{A}_{SI}\left|\psi_i\right\rangle = \left\langle\hat{A}_{SI}\right\rangle_i\left|\psi_i\right\rangle + \Delta_i\hat{A}_{SI}\left|\psi_i^{\perp}\right\rangle$, where the average is $\left\langle\hat{A}_{SI}\right\rangle_i = \langle\psi_i|\hat{A}_{SI}|\psi_i\rangle$, the quantum uncertainty is $\Delta_i\hat{A}_{SI} = \sqrt{\left\langle\hat{A}_{SI}^2\right\rangle_i - \left\langle\hat{A}_{SI}\right\rangle_i^2}$, and the normalized state $\left|\psi_i^{\perp}\right\rangle$ is orthogonal to the initial state $|\psi_i\rangle$. Therefore, considering the linearity of the dissipator evolution, we can write the weak value as

$$A_{S,w}(\tau) = \left\langle\hat{A}_{SI}\right\rangle_i + \Delta_i\hat{A}_{SI}\,\frac{\mathrm{Tr}\left[\left|\psi_{fI}\right\rangle\left\langle\psi_{fI}\right| e^{\mathscr{D}\tau}\left(\left|\psi_i^{\perp}\right\rangle\left\langle\psi_i\right|\right)\right]}{\mathrm{Tr}\left[\left|\psi_{fI}\right\rangle\left\langle\psi_{fI}\right| e^{\mathscr{D}\tau}\left(\left|\psi_i\right\rangle\left\langle\psi_i\right|\right)\right]}, \tag{8.33}$$

where the second term is responsible for any anomalousness of the weak value. We note that the trace of the coherence $\left|\psi_i^{\perp}\right\rangle\left\langle\psi_i\right|$ is zero. When the ground state is not degenerate, the operator $e^{\mathscr{D}\tau}\left(\left|\psi_i^{\perp}\right\rangle\left\langle\psi_i\right|\right)$ can only decay to 0 in the ground state and this second term does not contribute to the weak value. As explained previously, the weak values then decays to the average value. However, when the ground state is degenerate, depending on the nature of the various dissipation channels, the non-Hermitian operator $\left|\psi_i^{\perp}\right\rangle\left\langle\psi_i\right|$ can decay to a mixture of the zero operator and coherences in the ground state manifold. The part that decays to zero does not contribute to the weak value in the limit of infinite dissipation time, similarly to the non-degenerate case. However,

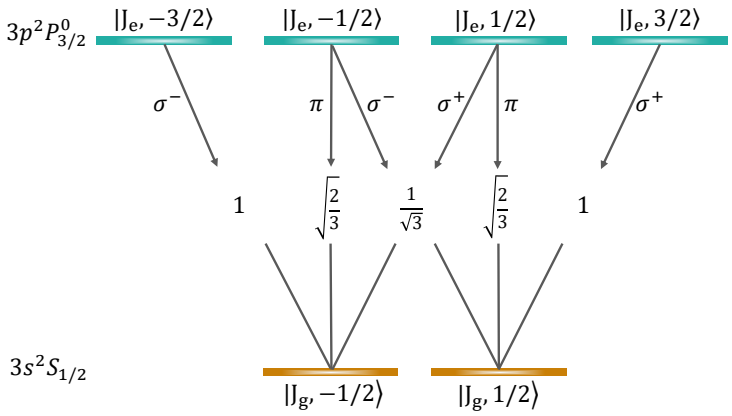

Figure 8.2: Atomic transition $J_g = \frac{1}{2} \leftrightarrow J_e = \frac{3}{2}$. The Clebsch-Gordan coefficients for each transition, $C^{J_g,1,J_e}_{m_g,q,m_e} = \langle J_g, m_g; 1, q | J_e, m_e \rangle$ are shown for each allowed transition.

the part that decays to non-Hermitian coherences of the type $|g_m\rangle\langle g_n|$ (with $\langle g_m|g_n\rangle = 0$) has trace zero but does contribute to the weak value, even in the limit of infinite dissipation time. This argument can easily be generalized to mixed initial states, beyond the pure state case examined here. Analyzing the evolution of the coherence $e^{\mathscr{D}\tau}\left(|\psi_i^\perp\rangle\langle\psi_i|\right)$ under dissipation may help find specific initial and final states to evidence anomalous weak values in degenerate systems.

As an example to demonstrate the anomalous properties of weak values in systems with degenerate ground states, we examine a simple case involving a sodium atom. Specifically, we consider a situation in which the orbitals $1s$, $2s$, and $2p$ are all fully occupied, and there is one electron in the degenerate level $3s$. When this electron is excited, it can undergo a transition to the nearby $3p$ level. In particular, one of the most intense transitions is the $J_g = \frac{1}{2} \leftrightarrow J_e = \frac{3}{2}$ transition that produces the main spectral line in the sodium doublet. In this system, the ground state is degenerate, while there are four possible excited states, making it a six-level system, Fig. 8.2.

The Lindbladian governing the de-excitation of the atom can be expressed in the interaction picture as

$$\mathscr{D}(\hat{\sigma}_I) = \Gamma \sum_{q=0,\pm} \left(\hat{L}_q \hat{\sigma}_I \hat{L}_q^\dagger - \frac{1}{2}\{\hat{L}_q^\dagger \hat{L}_q, \hat{\sigma}_I\} \right), \tag{8.34}$$

where Γ is a characteristic spontaneous emission rate for the transition $J_g = \frac{1}{2} \leftrightarrow J_e = \frac{3}{2}$, and

$$\hat{L}_q \left| J_e, m_e = m_g + q \right\rangle = C^{J_g,1,J_e}_{m_g,q,m_e} \left| J_g, m_g \right\rangle, \qquad \hat{L}_q \left| J_g, m_g \right\rangle = 0. \tag{8.35}$$

For more details on the expression of $\hat{L}_q$, see appendix M. To give a concrete example of the anomalous weak value generated by dissipation, let us consider the following pre- and post-selected states,

$$\begin{aligned} |\psi_i\rangle &= \frac{1}{2}\left(|J_e,-3/2\rangle + i\,|J_e,-1/2\rangle + |J_e,1/2\rangle + |J_e,3/2\rangle\right), \\ \left|\psi_{fI}\right\rangle &= \alpha\,|J_e,-3/2\rangle + -0.995\,|J_e,-1/2\rangle - \alpha\,(1+i)\,|J_e,3/2\rangle + \alpha\left|J_g,-1/2\right\rangle \\ &\quad + (-0.00734 + 0.00114i)\left|J_g,1/2\right\rangle, \end{aligned} \tag{8.36}$$

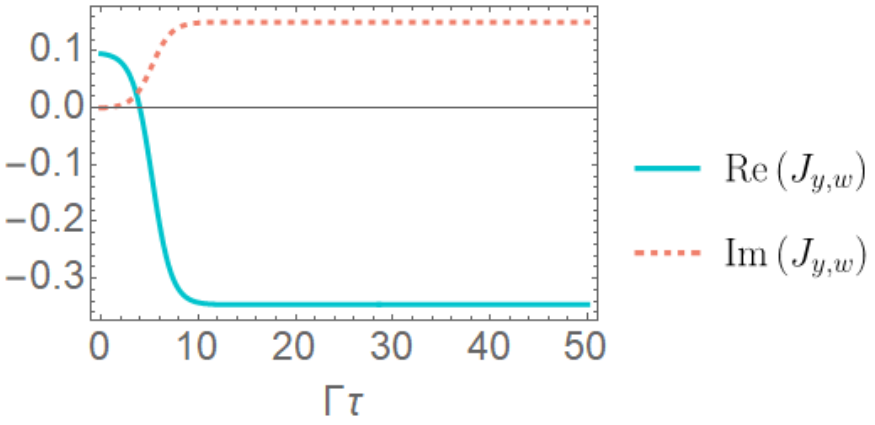

Figure 8.3: Real and imaginary parts of the weak value of $\hat{J}_y$ as a function of the product of the dissipation time and the dissipation rate. The pre- and post-selected states are detailed in the text and chosen to illustrate the occurrence of an increasing anomaly due to dissipation.

with $\alpha = 0.0498$. We choose again a state that is constant in the interaction picture to analyze solely the effects of the dissipation. The chosen observable to be measured is the angular momentum $\hat{A}_S \approx \hat{A}_{SI}(t/2) = \hat{J}_y$, or by setting $\hbar = 1$,

$$\hat{J}_y = \begin{pmatrix} 0 & i\frac{\sqrt{3}}{2} & 0 & 0 & 0 & 0 \\ -i\frac{\sqrt{3}}{2} & 0 & i & 0 & 0 & 0 \\ 0 & -i & 0 & i\frac{\sqrt{3}}{2} & 0 & 0 \\ 0 & 0 & -i\frac{\sqrt{3}}{2} & 0 & 0 & 0 \\ 0 & 0 & 0 & 0 & 0 & \frac{i}{2} \\ 0 & 0 & 0 & 0 & -\frac{i}{2} & 0 \end{pmatrix}, \tag{8.37}$$

in a basis ordered by decreasing magnetic quantum number m starting from the four excited states and ending with the two ground states (see Fig. 8.2).

Using the chosen pre- and post-selected states and observable, we find that the weak value without dissipation is $A_w(\tau = 0) = 0.0954$. This weak value is not anomalous, as its imaginary part is zero and its modulus, 0.0954, lies in the range of the spectrum of $\hat{J}_y$, whose smallest and largest eigenvalues are $\pm\frac{3}{2}$. At infinite dissipation time, the modulus and the imaginary part of the weak value increase in magnitude to $A_w(\tau \to \infty) = -0.346 + 0.151i$. The dissipation generates an anomalous behavior of the weak value, by increasing the imaginary part from 0 to 0.151. In Fig. 8.3, we show the evolution of the real and imaginary parts of the weak value as a function of the product $\Gamma\tau$ of dissipation time and dissipation rate. One can appreciate that, at very long times, the imaginary part of the weak value is not zero and the real part is larger in modulus than it was at null dissipation time.
We can also obtain an anomalous weak value that is preserved and completely constant over time,

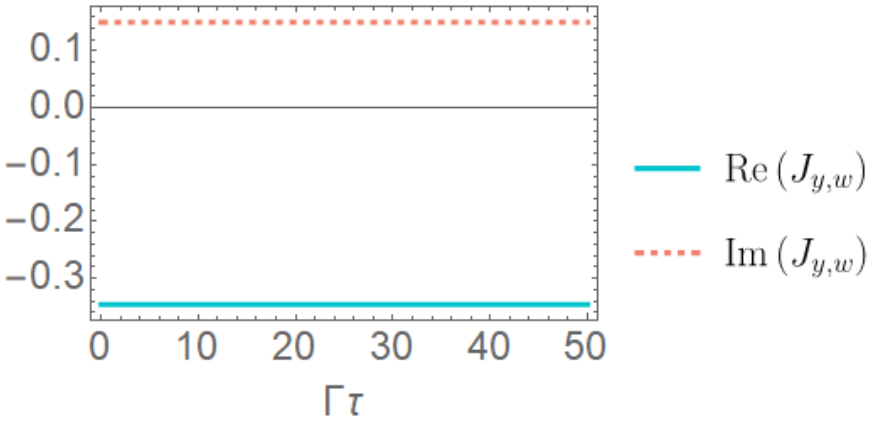

Figure 8.4: Real and imaginary parts of the weak value of $\hat{J}_y$ as a function of the product of the dissipation time and the dissipation rate. The pre- and post-selected states are detailed in the text and are chosen to create a constant anomalous weak value.

by choosing the following pre- and post-selected states for the same system:

$$\begin{aligned} |\psi_i\rangle &= \frac{1}{2}\left(|J_e,-3/2\rangle + i\,|J_e,-1/2\rangle + |J_e,1/2\rangle + |J_e,3/2\rangle\right), \\ |\psi_{fI}\rangle &= 0.989\,|J_g,-1/2\rangle + (-0.146+0.0226i)\,|J_g,1/2\rangle\,. \end{aligned} \tag{8.38}$$

Despite the orthogonality of the pre- and post-selected states, as defined in Eq. 8.38, the presence of dissipation in the system ensures that the weak value denominator is non-zero for $\tau > 0$. Fig. 8.4 depicts the evolution of the real and imaginary part of the weak value of $\hat{J}_y$. As one can see, the weak value is constant and has an imaginary part different from 0.

Anomalous weak values, which are quantities different from any possible expectation value (i.e., larger than the maximum expectation value, smaller than the minimal expectation value, or complex values), are linked to contextuality [31, 32], a non-classical property. Dissipation generally destroys the quantum superposition and coherence of a system, and without these quantum properties, there is no amplification through anomalous weak values. However, in systems with a degenerate ground state, the final state can still present quantum superposition and coherence, which allows us to maintain the anomalous character of the weak value even in the limit of infinite dissipation times.

In non-degenerate systems, dissipation inevitably eliminates the anomalous properties of weak values over time, preventing amplification in this regime. Nonetheless, weak values can still be leveraged to extract information about the system evolution over short dissipation times. During the early stages of dissipation, the Lindbladian can be approximated by a Taylor series, enabling us to extract parameters related to the dynamics from the weak value evolution. In the upcoming sections, we will examine a few examples.

8.3 Weak measurement in the Rabi model

In this section, we apply the theoretical principles of weak measurements under dissipation to a specific setup involving a two-level atom system. In this system, a weak measurement of the

internal state of the atom is performed using the field of a cavity. The cavity mode serves as the meter or ancilla, and the atom-cavity dynamics are governed by the Rabi model. Fig. 8.5 illustrates the various steps in this process. Initially, the atom is pre-selected, for example by pumping it with a laser pulse of appropriate frequency and intensity, leaving it in a superposition of its ground and excited states, as shown in (a). Following pre-selection, the weak interaction occurs with a cavity mode whose initial quantum state is known, as shown in (b). Dissipation then occurs as soon as the atom leaves the cavity, as a result of its interaction with a quantized radiation field (either the free field or the field of a second lossy cavity into which it moves) acting as an environment with an infinite number of degrees of freedom, as shown in (c). Finally, post-selection is performed on the atom and the bosonic cavity mode is read out. By measuring the field quadratures of the cavity mode, $\hat{Q}$ and $\hat{P}$, we can extract the real and imaginary components of the weak value from the shift in the expectation value of the quadratures.

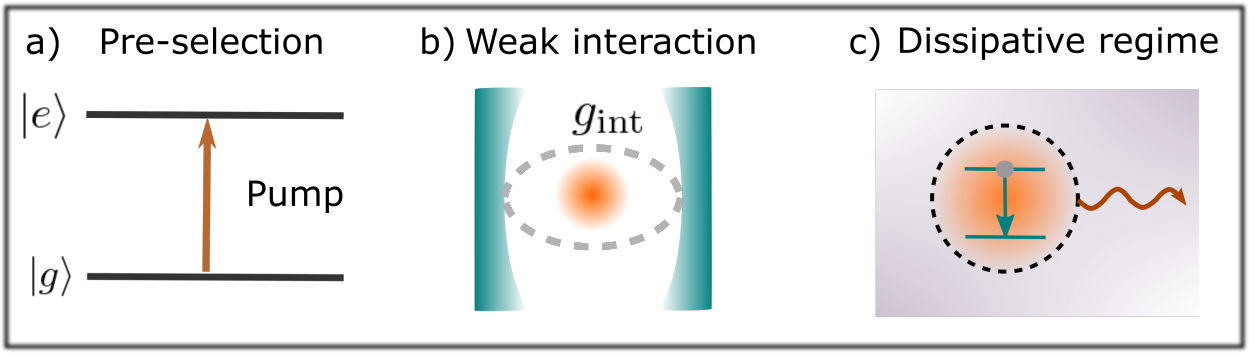

Figure 8.5: The weak measurement under dissipation scheme involves four stages. Firstly, pre-selection of the system is achieved by pumping the atom, as shown in (a), leaving it in a chosen superposition of the ground and excited states. Secondly, a weak interaction occurs in a closed single-mode cavity, as depicted in (b). Thirdly, after the weak interaction, the atom undergoes dissipation, as shown in (c). Finally, post-selection is performed on the atom.

When the atom is in the cavity, its interaction with the field mode is described by the Rabi model, corresponding to the atom-field Hamiltonian $\hat{H} = \hat{H}_{\text{atom}} + \hat{H}_{\text{field}} + \hat{H}_{\text{int}}$ with

$$\begin{aligned} \hat{H}_{\text{atom}} &= \frac{1}{2}\omega_a \hat{\sigma}_z, \\ \hat{H}_{\text{field}} &= \omega_f \hat{a}^\dagger \hat{a}, \\ \hat{H}_{\text{int}} &= g_{\text{int}} \hat{\sigma}_x \otimes \left(\hat{a}^\dagger + \hat{a}\right). \end{aligned} \tag{8.39}$$

where ω_a and ω_f are respectively the frequencies of the atom and the cavity, g_{int} is the atom-cavity coupling constant, $\hat{a}^\dagger$ and $\hat{a}$ are the creation and annihilation operators of the field, $\hat{\sigma}_j$ the Pauli matrices, and $\hbar = 1$. The field quadratures are defined by $\hat{Q} = \sqrt{\frac{1}{2\omega_f}}\left(\hat{a}^\dagger + \hat{a}\right)$ and $\hat{P} = i\sqrt{\frac{\omega_f}{2}}\left(\hat{a}^\dagger - \hat{a}\right)$. In this model, the pointer $\hat{N}$ from Eq. 8.3 is thus given by $\hat{N} = \sqrt{2\omega_f}\hat{Q}$. ($\hat{N}$ should not to be confused here with the number operator $\hat{a}^\dagger\hat{a}$.)

8.3.1 Usual weak measurement approximation

To begin, the atomic system is pre-selected in the state $\hat{\sigma}_i$. The meter initial state is denoted by $\hat{\mu}_0$. For an arbitrary initial state of the meter, the weak measurement results are provided by the general expressions Eq. 8.18 or Eq. 8.24. In order to use the corresponding simpler results Eq. 8.19 or Eq. 8.21 for the measurement average, we can require that $\langle \hat{N}_I(t/2)\rangle_0 = 0$; we can also take advantage of Eq. 8.20 when the initial meter state commutes with $\hat{H}_{\text{field}}$. The simplest meter state to consider is the vacuum state, denoted by $|0\rangle\langle 0|$, but the meter shifts observed with energy eigenstates, coherent states, squeezed states, and thermal-equilibrium states can all be evaluated straightforwardly, enabling the determination of the weak value. In the following, we will determine the meter shifts for a general meter state at first. Then, we will discuss a few simple examples.

The observable weakly measured as a result of the interaction $\hat{H}_{\text{int}}$ Eq. 8.39 of the Rabi model is the operator $\hat{\sigma}_x$, at least if we assume an instantaneous weak interaction (equivalent to adding a Dirac distribution $\delta(t)$ in the interaction Hamiltonian). For a short –but not instantaneous– interaction time with respect to the free evolution of the atom ($\omega_a t \ll 1$) and cavity field ($\omega_f t \ll 1$), we can use the weak measurement approximation Eq. 8.8–8.9 on which relies our general theory. In that case, we showed that the operator effectively probed is

$$\hat{\sigma}_{xI}(t/2) = e^{\frac{i}{4}\omega_a t\hat{\sigma}_z}\hat{\sigma}_x e^{-\frac{i}{4}\omega_a t\hat{\sigma}_z} = \cos\left(\frac{\omega_a t}{2}\right)\hat{\sigma}_x - \sin\left(\frac{\omega_a t}{2}\right)\hat{\sigma}_y. \tag{8.40}$$

We see that it corresponds to a small clockwise rotation of the $\hat{\sigma}_x$ operator around the z axis. We will use the notation $\hat{\sigma}_{xI} = \vec{n}_I \cdot \hat{\vec{\sigma}}$ to represent this operator, with $\vec{n}_I = (\cos\frac{\omega_a t}{2}, -\sin\frac{\omega_a t}{2}, 0)$ a three-dimensional real vector representing $\hat{\sigma}_{xI}$ on the Bloch sphere.

We use Eq. 8.24 to determine the shifts in terms of the real and imaginary parts of the weak value. Therefore, we need to compute the meter observables $\hat{N}_I$ and $\hat{L}_I$ in the interaction picture, as well as the commutator $\left[\hat{L}_I, \hat{N}_I\right]$ and anti-commutator $\left\{\hat{L}_I, \hat{N}_I\right\}$ for both cases $\hat{L}_I = \hat{Q}_I$ and $\hat{L}_I = \hat{P}_I$, since the two field quadratures serve as our conjugate meter observables. In the interaction picture, the creation and annihilation operators are represented as $\hat{a}_I(t') = e^{-i\omega_f t'}\hat{a}$ and $\hat{a}_I^\dagger(t') = e^{i\omega_f t'}\hat{a}^\dagger$. Thus, we can promptly determine the observables

$$\hat{N}_I(t/2) = \left[\hat{a}^\dagger e^{i\omega_f(t/2)} + \hat{a}e^{-i\omega_f(t/2)}\right], \tag{8.41}$$

$$\hat{Q}_I(t+\tau) = \sqrt{\frac{1}{2\omega_f}}\left[\hat{a}^\dagger e^{i\omega_f(t+\tau)} + \hat{a}e^{-i\omega_f(t+\tau)}\right], \tag{8.42}$$

$$\hat{P}_I(t+\tau) = \sqrt{\frac{\omega_f}{2}}i\left[\hat{a}^\dagger e^{i\omega_f(t+\tau)} - \hat{a}e^{-i\omega_f(t+\tau)}\right], \tag{8.43}$$

the commutators

$$\left[\hat{Q}_I(t+\tau), \hat{N}_I(t/2)\right] = -2i\sqrt{\frac{1}{2\omega_f}}\sin\left[\omega_f(t/2+\tau)\right]\hat{I}, \tag{8.44}$$

$$\left[\hat{P}_I(t+\tau), \hat{N}_I(t/2)\right] = -2i\sqrt{\frac{\omega_f}{2}}\cos\left[\omega_f(t/2+\tau)\right]\hat{I}, \tag{8.45}$$

as well as the anti-commutators

$$\begin{aligned}\left\{\hat{Q}_I(t+\tau),\hat{N}_I(t/2)\right\} &= 2\sqrt{\frac{1}{2\omega_f}}\cos\left[\omega_f(t/2+\tau)\right]\left(2\hat{a}^\dagger\hat{a}+\hat{I}\right)\\ &+ 2\sqrt{\frac{1}{2\omega_f}}\left[\hat{a}^{\dagger 2}e^{i\omega_f(3t/2+\tau)}+\hat{a}^2e^{-i\omega_f(3t/2+\tau)}\right], \qquad (8.46)\\ \left\{\hat{P}_I(t+\tau),\hat{N}_I(t/2)\right\} &= -2\sqrt{\frac{\omega_f}{2}}\sin\left[\omega_f(t/2+\tau)\right]\left(2\hat{a}^\dagger\hat{a}+\hat{I}\right)\\ &+ 2i\sqrt{\frac{\omega_f}{2}}\left[\hat{a}^{\dagger 2}e^{i\omega_f(3t/2+\tau)}-\hat{a}^2e^{-i\omega_f(3t/2+\tau)}\right]. \qquad (8.47)\end{aligned}$$

Now, we can simply evaluate the expectation values of these quantities in the meter initial state to determine the meter shifts Eq. 8.24. Interestingly, we can already observe that the expectation value of the commutators Eq. 8.44 and Eq. 8.45 do not depend on the meter initial state since they are proportional to the identity. This means that the initial meter state does not influence the meter shift arising from the real part of the weak value (at least when we can neglect the effect of the denominator in the shift expression). In contrast, the expectation value of the anti-commutators depends on the initial meter state. Thus, the choice of the initial meter state will influence the meter shift associated to the imaginary part of the weak value. It is worth noticing that the expectation value of the operator $2\hat{a}^\dagger\hat{a}+\hat{I}$ present in Eq. 8.46 and Eq. 8.47 is proportional to the average energy in the initial meter state (including the zero-point energy term). Using an initial meter state with an average energy larger than the energy of the vacuum state will thus generally increase the meter shift resulting from the imaginary part of the weak value, relatively to the shift due to the real part (at least, when we can ignore the contributions of the $\hat{a}^2$ and $\hat{a}^{\dagger 2}$ terms).
For simplicity, let us now assume that the meter initial state is an energy eigenstate $\hat{\mu}_0 = |n\rangle\langle n|$. In that case, all the expectation values of the meter observables $\hat{N}_I$, $\hat{Q}_I$, and $\hat{P}_I$ Eq. 8.41–8.43 are 0, while terms in $\hat{a}^2$ and $\hat{a}^{\dagger 2}$ in Eq. 8.46 and Eq. 8.47 average to zero as well. As a result, we find the following meter shifts at the end of the weak measurement:

$$\langle\hat{Q}\rangle_f = -2gt\sqrt{\frac{1}{2\omega_f}}\left[\sin\omega_f(t/2+\tau)\,\mathrm{Re}\sigma_{S,w}(\tau)-(2n+1)\cos\omega_f(t/2+\tau)\,\mathrm{Im}\sigma_{S,w}(\tau)\right], \qquad (8.48)$$

$$\langle\hat{P}\rangle_f = -2gt\sqrt{\frac{\omega_f}{2}}\left[\cos\omega_f(t/2+\tau)\,\mathrm{Re}\sigma_{S,w}(\tau)+(2n+1)\sin\omega_f(t/2+\tau)\,\mathrm{Im}\sigma_{S,w}(\tau)\right]. \qquad (8.49)$$

As just discussed before, the shifts proportional to the real part of the weak value are identical for all the energy eigenstates, while the shifts proportional to the imaginary part increase linearly with the energy level n. In these expressions, the weak value $\sigma_{S,w}(\tau)$ is the weak value of the observable $\vec{n}_I\cdot\hat{\vec{\sigma}}$ Eq. 8.40 under dissipation, defined as in Eq. 8.14 by imposing $\hat{A}_{SI}=\hat{\sigma}_{xI}$. The expressions Eq. 8.48 and Eq. 8.49 would remain essentially identical for a meter initial state in thermal equilibrium: in that case, the energy level n should be replaced by the average energy level in the thermal state $n_{\mathrm{eq}}(T)$, with $2n_{\mathrm{eq}}+1=\coth\left[\omega_f/(2k_BT)\right]$ where k_B is the Boltzmann constant and T the temperature. We see thus that the meter shift due to the imaginary part of the weak value is temperature dependent, while the shift due to the real part is not. For a squeezed vacuum

state as the meter initial state, it is theoretically possible to amplify or attenuate exponentially the shift due to the imaginary part of the weak value as a function of the squeezing parameter z (with a factor $e^{\pm 2|z|}$ replacing $(2n+1)$ in Eq. 8.48 and Eq. 8.49 for the particular argument $\arg z = \omega_f t$; also, because the terms $\hat{a}^2$ and $\hat{a}^{\dagger 2}$ contribute to the anti-commutator average for squeezed states, the factor $e^{\pm 2|z|}$ is not proportional to the mode average energy $\sinh|z|$). When choosing a coherent state for the meter initial state, the shift expressions remain straightforward to compute. However, they become much less practical to handle because the expectation values of the meter observables $\hat{N}_I$, $\hat{Q}_I$, and $\hat{P}_I$ are generally non-zero and then contribute to Eq. 8.24 by adding a term independent on the weak value on the numerator and by preserving the term proportional to the imaginary part of the weak value in the denominator. From that perspective, coherent states do not seem ideal to retrieve the weak values from the experimental meter shifts.

Now, we turn our attention to the dependence of the meter shifts on the dissipation duration τ, which determines the post-selection time. For reasons that will soon become apparent, we define the polar representation of the weak value [18, 19, 112] by $\sigma_{S,w}(\tau) = \left|\sigma_{S,w}(\tau)\right| e^{i\varphi_w(\tau)}$, where $\left|\sigma_{S,w}(\tau)\right|$ is its modulus and $\varphi_w(\tau)$ is its argument as a function of the dissipation duration τ. We consider that the meter initial state is the vacuum state for simplicity. After setting $n = 0$ in Eq. 8.48 and Eq. 8.49, the expectation values of the $\hat{Q}$ and $\hat{P}$ field quadratures become

$$\langle \hat{Q} \rangle_f = 2 g_{\text{int}} t \sqrt{\frac{1}{2\omega_f}} \left|\sigma_{S,w}(\tau)\right| \sin\left[\varphi_w(\tau) - \omega_f(t/2+\tau)\right], \tag{8.50}$$

$$\langle \hat{P} \rangle_f = -2 g_{\text{int}} t \sqrt{\frac{\omega_f}{2}} \left|\sigma_{S,w}(\tau)\right| \cos\left[\varphi_w(\tau) - \omega_f(t/2+\tau)\right]. \tag{8.51}$$

In the limit of negligible free evolution of the meter, i.e. when $\omega_f(t/2+\tau) \approx 0$, the expectation value of the $\hat{Q}$ field quadrature is proportional to the imaginary part of the weak value $\left|\sigma_{S,w}(\tau)\right| \sin\varphi_w(\tau)$, as seen from Eq. 8.22. In the same limit, the expectation value of the $\hat{P}$ quadrature, associated with the canonical conjugate of the weak measurement pointer, is proportional to the real part of the weak value $\left|\sigma_{S,w}(\tau)\right| \cos\varphi_w(\tau)$, as seen from Eq. 8.23. When the meter evolution due to its Hamiltonian $\hat{H}_{\text{field}}$ can be neglected, the shifts in position and momentum are proportional to the real and imaginary parts of the weak value, respectively. When the contributions from the term $\omega_f(t/2+\tau)$ cannot be neglected in Eqs. 8.50 and 8.51, then the weak value rotates with time τ in the meter phase space defined by the $\hat{Q}$–$\hat{P}$ quadratures (assuming that the contribution $\omega_f\tau$ varies much faster than the weak value argument $\varphi_w(\tau)$). This apparent rotation of the weak value results purely from the free meter evolution with time and does not arise from a modification of the weak value itself. Consequently, practical measurements need to be implemented differently for cases where the weak value evolution is much faster than the free-meter evolution, and for cases where the free-meter evolution significantly outpaces the weak value evolution. Nevertheless, in both situations, by knowing the parameters of the weak measurement, t and g_{int}, we can determine the weak value as a function of the dissipation time τ from the weak measurement results and, in turn, use it to extract information about the dissipative evolution. Even for more complex initial meter states, it is possible to invert the expressions linking the two meter expectation values to the complex weak value (see appendix N).

In the upcoming sections, we examine how to use the weak value expression to extract information regarding the dissipative dynamics of the atom. In this section, we provide a more comprehensive treatment of the weak measurement in the presence of dissipation, illustrating the general theory

in depth.

8.3.2 General expression of the weak value for two-level systems with dissipation

The Rabi model allows us to investigate analytically how the weak value evolves with the dissipation duration τ. Indeed, taking a single dissipation channel characterized by the time-independent damping constant γ and the jump operator $\hat{\sigma}_-$ in the dissipator $\mathscr{D}$ defined in Eq. 8.1, an arbitrary matrix $C = c_{gg}|g\rangle\langle g| + c_{ge}|g\rangle\langle e| + c_{eg}|e\rangle\langle g| + c_{ee}|e\rangle\langle e|$ becomes

$$e^{\mathscr{D}\tau}(C) = \begin{pmatrix} c_{ee}e^{-\gamma\tau} & c_{eg}e^{-\frac{1}{2}\gamma\tau} \\ c_{ge}e^{-\frac{1}{2}\gamma\tau} & c_{gg} + c_{ee}(1-e^{-\gamma\tau}) \end{pmatrix}. \tag{8.52}$$

Therefore, computing the weak value under dissipation Eq. 8.14 becomes straightforward. We choose arbitrary initial and final states characterized by the three-dimensional, real Bloch sphere vectors $\vec{i}$ and $\vec{f}$, respectively: $\hat{\sigma}_i = \frac{1}{2}(\hat{I} + \vec{i}\cdot\hat{\vec{\sigma}})$ and $\hat{\sigma}_f = \frac{1}{2}(\hat{I} + \vec{f}\cdot\hat{\vec{\sigma}})$. Unit vectors corresponds to arbitrary pure states of the atom, while vectors of length < 1 describe arbitrary mixed states of the two-level system. In the weak value expression, the post-selected state should be evaluated in the interaction representation at time $t+\tau$. In particular, $\hat{\sigma}_{fI}(t+\tau) = \left\{\cos\left[\frac{\omega_a}{2}(t+\tau)\right]\ \hat{I} + i\sin\left[\frac{\omega_a}{2}(t+\tau)\right]\ \hat{\sigma}_z\right\}\hat{\sigma}_f\left\{c\right.$
If we denote $\vec{f} = (f_x, f_y, f_z)$, then $\hat{\sigma}_{fI}$ is described by the vector

$$\vec{f}_I(t+\tau) = \begin{pmatrix} f_{Ix} \\ f_{Iy} \\ f_{Iz} \end{pmatrix} = \begin{pmatrix} f_x\cos[\omega_a(t+\tau)] + f_y\sin[\omega_a(t+\tau)] \\ f_y\cos[\omega_a(t+\tau)] - f_x\sin[\omega_a(t+\tau)] \\ f_z \end{pmatrix}, \tag{8.53}$$

which corresponds to a clockwise rotation of the initial vector $\vec{f}$ over time around the z axis of the Bloch sphere. We thus see that the actual time of post-selection influences the state that is effectively post-selected in practice. Since the weakly measured operator is given by Eq. 8.40 and characterized by the vector $\vec{n}_I$, we now have the following expression for the weak value

$$\hat{\sigma}_{S,w}(\tau) = \frac{\vec{f}_I^{\gamma}\cdot\vec{n}_I + \vec{i}\cdot\vec{n}_I\left(1 + f_{Iz}^{\gamma} - f_{Iz}\right) + i\vec{f}_I^{\gamma}\cdot\left(\vec{n}_I\times\vec{i}\right)}{1 + \vec{f}_I^{\gamma}\cdot\vec{i} + \left(f_{Iz}^{\gamma} - f_{Iz}\right)}, \tag{8.54}$$

where the vector $\vec{f}_I^{\gamma}$ is defined as

$$\vec{f}_I^{\gamma}(t+\tau) = \begin{pmatrix} f_{Ix}e^{-\frac{1}{2}\gamma\tau} \\ f_{Iy}e^{-\frac{1}{2}\gamma\tau} \\ f_{Iz}e^{-\gamma\tau} \end{pmatrix} = e^{-\frac{1}{2}\gamma\tau}\begin{pmatrix} f_x\cos[\omega_a(t+\tau)] + f_y\sin[\omega_a(t+\tau)] \\ f_y\cos[\omega_a(t+\tau)] - f_x\sin[\omega_a(t+\tau)] \\ f_z\ e^{-\frac{1}{2}\gamma\tau} \end{pmatrix}. \tag{8.55}$$

It is quite interesting to note that the consequences of the quantum system evolution under the full Lindbladian Eq. 8.1 can be taken into account by specifying an attenuated post-selected state $\vec{f}_I^{\gamma}(t+\tau)$ that picks up the complete evolution after the weak interaction, including the free evolution and the dissipation. We see that the effect of dissipation for a long time τ is to drive the attenuated post-selected state to $\vec{f}_I^{\gamma} = 0$. In that case, the density operator associated with the

attenuated post-selected state becomes the maximally mixed state $\hat{I}/2$. This explains why anomalousness disappears at long dissipation times. In that case, we also see that the weak value becomes real and converges towards the simple scalar product $\vec{i}\cdot\vec{n}_I$, which corresponds to the expectation value of the operator $\vec{n}_I\cdot\hat{\vec{\sigma}}$ in the initial state $\vec{i}$ expressed in terms of Bloch vectors (as shown in section 8.2). We should be careful, though, and note that the effect of dissipation is not strictly to post-select in $\vec{f}_I^{\gamma}$: indeed, the formula giving the weak value with dissipation is not exactly the same as the weak value without dissipation with $\vec{f}_I$ replaced by $\vec{f}_I^{\gamma}$. However, we see that the consequences of dissipation can always be anchored to the final state. In particular, if we set $\gamma=0$ to cancel the effects of dissipation, we recover the expression of a standard weak value of a Pauli operator [18, 19]:

$$\lim_{\gamma\to 0}\sigma_{S,w}(\tau)=\frac{\vec{f}_I\cdot\vec{n}_I+\vec{i}\cdot\vec{n}_I+i\vec{f}_I\cdot\left(\vec{n}_I\times\vec{i}\right)}{1+\vec{f}_I\cdot\vec{i}}. \tag{8.56}$$

The structure of the expressions Eq. 8.54 and Eq. 8.56 differ by the presence of two additional terms, proportional to the difference of the z components of $\vec{f}_I^{\gamma}$ and $\vec{f}_I$, in the case of dissipation.
In practice, the effect of the system free evolution during the time $t+\tau$ is to rotate the post-selected vector Eq. 8.53. In order to focus for the weak measurement specifically on the consequences of dissipation, we can choose to set, as done in section 8.2 and 8.4, a constant post-selected vector in the interaction representation: $\vec{f}_I(t+\tau)=\left(f_{Ix0},f_{Iy0},f_{Iz0}\right)$ and, thus, $\vec{f}_I^{\gamma}(t+\tau)=\left(f_{Ix0}\,e^{-\frac{\gamma}{2}\tau},f_{Iy0}\,e^{-\frac{\gamma}{2}\tau},f_{Iz0}\,e^{-\gamma\tau}\right)$. In that case, the post-selection must depend on time τ in the Schrödinger representation, meaning that the experimentalist must rotate its post-selection choice as a function of the dissipation duration τ:

$$\vec{f}=\begin{pmatrix}f_x\\f_y\\f_z\end{pmatrix}=\begin{pmatrix}f_{Ix0}\cos\left[\omega_a(t+\tau)\right]-f_{Iy0}\sin\left[\omega_a(t+\tau)\right]\\f_{Iy0}\cos\left[\omega_a(t+\tau)\right]+f_{Ix0}\sin\left[\omega_a(t+\tau)\right]\\f_{Iz0}\end{pmatrix}. \tag{8.57}$$

This time dependence in the Schrödinger representation requires the experimenter to choose a different post-selection depending on the time of post-selection.
Although we derived the expression of the weak value Eq. 8.54 in the context of the Rabi model, the expression is quite generally valid in the context of two-level systems. For an arbitrary observable of a two-level system undergoing dissipation as in Eq. 8.52, we can write $\hat{A}_S=a\,\hat{I}+b\,\vec{m}\cdot\hat{\vec{\sigma}}$. Then, for arbitrary initial and final states, the weak value expression is

$$A_{S,w}(\tau)=a+b\frac{\vec{f}_I^{\gamma}\cdot\vec{m}_I+\vec{i}\cdot\vec{m}_I\left(1+f_{Iz}^{\gamma}-f_{Iz}\right)+i\vec{f}_I^{\gamma}\cdot\left(\vec{m}_I\times\vec{i}\right)}{1+\vec{f}_I^{\gamma}\cdot\vec{i}+\left(f_{Iz}^{\gamma}-f_{Iz}\right)}. \tag{8.58}$$

with $\vec{f}_I$ the Bloch vector representing the post-selected state at time $t+\tau$ in the interaction picture and $\vec{f}_I^{\gamma}$, the attenuated post-selected vector, constructed from $\vec{f}_I$ as in the left-hand side of Eq. eq:attenuatedPostSelection, while $\vec{m}_I$ is the Bloch vector associated to $\hat{A}_{SI}(t/2)$ in the interaction picture. Within the weak value, the attenuated post-selection vector $\vec{f}_I^{\gamma}$ contains the information on the dissipation of the system after the weak interaction, which can be analyzed through the related weak measurement shifts.

8.3.3 Rotating-wave approximation

The standard weak measurement approximation enables expressing the final meter state as a function of the weak value of the weakly measured Hermitian operator in the pre- and post-selected quantum system. In the general Rabi model, this requires $\omega_a t \ll 1$ and $\omega_f t \ll 1$, meaning that the free evolution can be evaluated to first order during the short interaction time t. However, this assumption may not always be warranted. For example, the transit time of an atom passing through a cavity may be several orders of magnitude longer than the oscillation period of the cavity field. In that case, considering a weakly coupled atom–cavity system near resonance, the atomic Hamiltonian will also generate many oscillations during the interaction as $|\Delta| \ll \omega_a + \omega_f = 2\omega$ with $\Delta = \omega_a - \omega_f$. In order to make progress, we thus have to come back to the atom-field joint state after the weak interaction given by Eq. 8.7, knowing that the approximation Eq. 8.8 is now invalid. Then, we have to evaluate the integral of the interaction Hamiltonian in the interaction picture:

$$\begin{aligned}
\int_0^t \hat{V}\left(t'\right) dt' &= g_{\text{int}} \int_0^t \hat{\sigma}_{xI}\left(t'\right) \otimes \left[\hat{a}_I^\dagger\left(t'\right) + \hat{a}_I\left(t'\right)\right] dt' && (8.59)\\
&= g_{\text{int}} \int_0^t \left[\hat{\sigma}_+ e^{i\omega_a t'} + \hat{\sigma}_- e^{-i\omega_a t'}\right] \otimes \left[\hat{a}^\dagger e^{i\omega_f t'} + \hat{a} e^{-i\omega_f t'}\right] dt' && (8.60)\\
&\approx g_{\text{int}} \int_0^t \left[e^{i\left(\omega_a-\omega_f\right)t'} \hat{\sigma}_+ \otimes \hat{a} + e^{-i\left(\omega_a-\omega_f\right)t'} \hat{\sigma}_- \otimes \hat{a}^\dagger\right] dt' && (8.61)\\
&= g_{\text{int}} \frac{\sin \Delta t}{\Delta} \left[e^{i\Delta t/2} \hat{\sigma}_+ \otimes \hat{a} + e^{-i\Delta t/2} \hat{\sigma}_- \otimes \hat{a}^\dagger\right] && (8.62)\\
&\approx g_{\text{int}} t \left[e^{i\Delta t/2} \hat{\sigma}_+ \otimes \hat{a} + e^{-i\Delta t/2} \hat{\sigma}_- \otimes \hat{a}^\dagger\right], && (8.63)
\end{aligned}$$

where we used the fact that the atom and field Hamiltonians commute Eq. 8.59; we developed $\hat{\sigma}_x = \hat{\sigma}_+ + \hat{\sigma}_-$ Eq. 8.60; we neglected the fast oscillating terms $\hat{\sigma}_- \hat{a}^\dagger e^{2i\omega}$ and $\hat{\sigma}_+ \hat{a} e^{-2i\omega}$ with respect to the slow ones Eq. 8.61, as they will contribute a term in $1/(2\omega)$ in Eq. 8.62; where we expanded $\sin(\Delta t)$ to first order in Eq. 8.63, assuming that the interaction time is short with respect to the detuning $\Delta t \ll 1$, and $\hbar = 1$.

In practice, the rotating-wave approximation that we carried out leads to the conservation of the excitation number, by neglecting the non-resonant terms originating from $\hat{H}_{\text{int}}$ in Eq. 8.39. Note that the rotating-wave approximation also requires the condition $\omega_f \gg g_{\text{int}}$, which is met in most, if not all, atomic cavity QED experiments.

We observe that the effective interaction Hamiltonian in the weak measurement and rotating-wave approximations comprises two terms built from non-Hermitian operators. In the first one, the raising operator $\hat{\sigma}_+$ of the system is coupled to the annihilation operator $\hat{a}$ of the meter, while, in the second term, the lowering operator $\hat{\sigma}_-$ of the system is coupled to the creation operator $\hat{a}^\dagger$ of the meter. The sum of the two coupling terms is nevertheless a Hermitian operator. Starting from the effective interaction Hamiltonian $V_I(t/2)$ given by Eq. 8.63, by following the exact same theoretical developments performed in section 8.1, beginning from equation Eq. 8.10, we deduce immediately the equivalent of equation Eq. 8.18

$$\langle \hat{L} \rangle_f = \frac{\langle \hat{L}_I \rangle_0 + 2g_{\text{int}} t \,\text{Im}\left[e^{i\Delta t/2} \sigma_{+,w}(\tau) \langle \hat{L}_I \hat{a} \rangle_0\right] + 2g_{\text{int}} t \,\text{Im}\left[e^{-i\Delta t/2} \sigma_{-,w}(\tau) \langle \hat{L}_I \hat{a}^\dagger \rangle_0\right]}{1 + 2g_{\text{int}} t \,\text{Im}\left[e^{i\Delta t/2} \sigma_{+,w}(\tau) \langle \hat{a} \rangle_0\right] + 2g_{\text{int}} t \,\text{Im}\left[e^{-i\Delta t/2} \sigma_{-,w}(\tau) \langle \hat{a}^\dagger \rangle_0\right]}, \quad (8.64)$$

with $\hat{L}_I(t+\tau)$ and the weak values

$$\sigma_{\pm,w}(\tau) = \frac{\mathrm{Tr}\left[\hat{\sigma}_{fI}(t+\tau)\ e^{\mathscr{D}\tau}(\hat{\sigma}_{\pm}\hat{\sigma}_i)\right]}{\mathrm{Tr}\left[\hat{\sigma}_{fI}(t+\tau)\ e^{\mathscr{D}\tau}(\hat{\sigma}_i)\right]}. \tag{8.65}$$

We would like to point out that the operators $\hat{\sigma}_{\pm}$ appear in the Schrödinger representation, as their time dependence has been explicitly factored out in Eq. 8.63 and Eq. 8.64. The meter shift exhibits now two contributions, one from each coupling term. Very interestingly, the weak measurement result depends on the weak values of the non-Hermitian raising and lowering operators $\hat{\sigma}_{\pm}$ of the system.

To determine the weak values, we consider measuring the two meter quadratures $\hat{Q}_I(t+\tau)$ and $\hat{P}_I(t+\tau)$. Assuming that the initial meter state is an energy eigenstate $|n\rangle\langle n|$ or a thermal state, we have $\langle\hat{a}\rangle_0 = \langle\hat{a}^\dagger\rangle_0 = 0$ in the denominator, as well as $\langle\hat{L}_I\rangle_0 = 0$ in the numerator. We get thus the simple expressions

$$\langle\hat{Q}\rangle_f = 2g_{\mathrm{int}}t\sqrt{\frac{2}{\omega_f}}\mathrm{Im}\left[e^{i\Delta t/2+\omega_f(t+\tau)}\sigma_{+,w}(\tau)\langle\hat{a}^\dagger\hat{a}\rangle_0 + e^{-i\Delta t/2-i\omega_f(t+\tau)}\sigma_{-,w}(\tau)\langle\hat{a}\hat{a}^\dagger\rangle_0\right], \tag{8.66}$$

$$\langle\hat{P}\rangle_f = 2g_{\mathrm{int}}t\sqrt{2\omega_f}\mathrm{Re}\left[e^{i\Delta t/2+\omega_f(t+\tau)}\sigma_{+,w}(\tau)\langle\hat{a}^\dagger\hat{a}\rangle_0 - e^{-i\Delta t/2-i\omega_f(t+\tau)}\sigma_{-,w}(\tau)\langle\hat{a}\hat{a}^\dagger\rangle_0\right], \tag{8.67}$$

with $\langle\hat{a}^\dagger\hat{a}\rangle_0 = n$ and $\langle\hat{a}\hat{a}^\dagger\rangle_0 = n+1$, where n labels the energy level in an energy eigenstate, or corresponds to the average energy level $n_{\mathrm{eq}} = \left[e^{\omega_f/(k_BT)}-1\right]^{-1}$ in a thermal-equilibrium state of the meter. We thus see that there are generally two contributions to the observed shifts, arising from two weak values.

The simplest case, yet fascinating, corresponds to a meter initially in the vacuum state $|0\rangle\langle 0|$, so that only the weak value of $\hat{\sigma}_-$ contributes to the shift since $\langle\hat{a}^\dagger\hat{a}\rangle_0 = 0$. In that case, the weak measurement expectation values are given by

$$\langle\hat{Q}\rangle_f = 2g_{\mathrm{int}}t\sqrt{\frac{1}{2\omega_f}}|\sigma_{-,w}(\tau)|\sin\left[\varphi_w(\tau) - \Delta t/2 - \omega_f(t+\tau)\right], \tag{8.68}$$

$$\langle\hat{P}\rangle_f = -2g_{\mathrm{int}}t\sqrt{\frac{\omega_f}{2}}|\sigma_{-,w}(\tau)|\cos\left[\varphi_w(\tau) - \Delta t/2 - \omega_f(t+\tau)\right], \tag{8.69}$$

where $\varphi_w(\tau)$ is the argument of the weak value of $\hat{\sigma}_-$ Eq. 8.65. These shifts should be compared to the results obtained before in the Rabi model Eq. 8.50 and Eq. 8.51, which are functions of the weak value of the operator $\hat{\sigma}_{xI}(t/2)$. In a weak measurement performed within the validity of the Jaynes-Cumming model with a meter initially in the vacuum state, the meter shifts depend on the single weak value of the lowering operator of the system, a non-Hermitian operator. This approach enables using the weak value approximation for interaction times t such that $\omega_f t \gg 1$ and $\omega_a t \gg 1$, on the condition that the interaction time remains short with respect to the frequency detuning $\Delta t \ll 1$. In these circumstances, it is possible to investigate the dissipation dynamics of the system through the weak value of the non-Hermitian operator $\hat{\sigma}_-$.

The general formula Eq. 8.58 for a two-level weak value affected by dissipation enables expressing the weak value of the non-Hermitian operators $\hat{\sigma}_{\pm}$ straightforwardly. By setting $a = b = 1$ and

using a complex three-dimensional vector $\vec{m}_\pm = (1, \pm i, 0)/2$ because $2\hat{\sigma}_\pm = \sigma_x \pm i\sigma_y$, we obtain

$$\sigma_{\pm,w}(\tau) = \frac{\vec{f}_I^{\gamma} \cdot \vec{m}_\pm + \vec{i} \cdot \vec{m}_\pm \left(1 + f_{Iz}^{\gamma} - f_{Iz}\right) + i\vec{f}_I^{\gamma} \cdot \left(\vec{m}_\pm \times \vec{i}\right)}{1 + \vec{f}_I^{\gamma} \cdot \vec{i} + \left(f_{Iz}^{\gamma} - f_{Iz}\right)}, \tag{8.70}$$

which becomes

$$\sigma_{-,w}(\tau) = \frac{i_x(1 - f_{Iz}) + f_{Ix}^{\gamma}(1 + i_z) - i\left[i_y(1 - f_{Iz}) + f_{Iy}^{\gamma}(1 + i_z)\right]}{2\left[1 + \vec{f}_I^{\gamma} \cdot \vec{i} + \left(f_{Iz}^{\gamma} - f_{Iz}\right)\right]}, \tag{8.71}$$

$$\sigma_{+,w}(\tau) = \frac{i_x\left(1 - f_{Iz} + 2f_{Iz}^{\gamma}\right) + f_{Ix}^{\gamma}(1 - i_z) + i\left[i_y\left(1 - f_{Iz} + 2f_{Iz}^{\gamma}\right) + f_{Iy}^{\gamma}(1 - i_z)\right]}{2\left[1 + \vec{f}_I^{\gamma} \cdot \vec{i} + \left(f_{Iz}^{\gamma} - f_{Iz}\right)\right]}. \tag{8.72}$$

These weak values appear relatively simple and symmetric, with only a few Bloch vector components involved in their numerators. These expressions are helpful to choose appropriate pre- and post-selected states $\vec{i}$ and $\vec{f}$ to probe the dissipation dynamics that are revealed through the contributions of the $\vec{f}_I^{\gamma}$ vectors to the meter shifts.

8.4 Exploiting weak values in dissipative systems

Dissipation has a negative impact on the amplification properties of the weak value. In systems with non-degenerate energy levels, weak values cannot provide amplification when the dissipation time is long. In general, the longer the dissipation time, the weaker the amplification of the weak value. Nevertheless, measuring the weak value at short dissipation times can still provide valuable information about the evolution of the system. For example, the rate of change of the weak value could be used to determine the dissipation rate, allowing shorter measurement times than those required by traditional methods.

It is often interesting to detect non-markovianity in the evolution of a quantum system, which may not always be straightforward. For certain non-Markovian evolutions, we show it is possible to differentiate Markovian dissipation from non-Markovian dissipation by analysing the evolution of the weak value. This result demonstrates the potential of weak measurement theory in identifying non-Markovian dynamics.

8.4.1 Effective amplification of the dissipation rate

In this section, we show that the dissipation rate can, in principle, be accurately determined from the evolution of weak values in a short interval of time. To begin with, let us examine the atom evolution in the dissipative regime in the interaction picture,

$$\dot{\hat{\sigma}}_{SI} = \mathscr{D}(\hat{\sigma}_{SI}) = \gamma\left[\hat{\sigma}_-\hat{\sigma}_{SI}\hat{\sigma}_+ - \frac{1}{2}\left(\hat{\sigma}_+\hat{\sigma}_-\hat{\sigma}_{SI} + \hat{\sigma}_{SI}\hat{\sigma}_+\hat{\sigma}_-\right)\right], \tag{8.73}$$

where dissipation is assumed to be Markovian.

For this illustration, we will consider a weak measurement of the $\hat{\sigma}_x$ operator, i.e. $\hat{A}_{SI}(t/2) = \hat{\sigma}_x$

in the weak value expression Eq. 8.14 and, equivalently, $\vec{n}_I = (1,0,0)$ in Eq. 8.54. We also take a post-selected state that is constant in the interaction representation, namely $\hat{\sigma}_{fI}(t+\tau) = \hat{\sigma}_{fI0}$. As a result, we focus our attention exclusively on measuring the dissipation, without probing the free Hamiltonian evolution. Since the dissipation time is short, we can expand the weak value of the spin operator $\hat{\sigma}_x$ in a Taylor series up to the first order in τ,

$$\begin{aligned} \sigma_{x,w}(\tau) &= \frac{\mathrm{Tr}\left[\hat{\sigma}_{fI0}\, e^{\mathscr{D}\tau}(\hat{\sigma}_x\hat{\sigma}_i)\right]}{\mathrm{Tr}\left[\hat{\sigma}_{fI0}\, e^{\mathscr{D}\tau}(\hat{\sigma}_i)\right]} \\ &\approx \frac{\mathrm{Tr}\left[\hat{\sigma}_{fI0}\,\hat{\sigma}_x\hat{\sigma}_i\right]}{\mathrm{Tr}\left[\hat{\sigma}_{fI0}\,\hat{\sigma}_i\right]} + \tau\,\frac{d}{d\tau}\left(\frac{\mathrm{Tr}\left[\hat{\sigma}_{fI0}\, e^{\mathscr{D}\tau}(\hat{\sigma}_x\hat{\sigma}_i)\right]}{\mathrm{Tr}\left[\hat{\sigma}_{fI0}\, e^{\mathscr{D}\tau}(\hat{\sigma}_i)\right]}\right)\Bigg|_{\tau=0}, \end{aligned} \tag{8.74}$$

where the derivative can be computed using Eq. 8.73. Let $\varepsilon \ll 1$ be a small number, which we will show is inversely proportional to the amplification of the weak value. When the initial and the post-selected atomic states are chosen, to first order in ε, as

$$\begin{aligned} |\psi_i\rangle &= -\mathrm{sign}(\varepsilon)\,|g\rangle + \frac{|\varepsilon|}{2}\,|e\rangle, \\ |\psi_{fI0}\rangle &= \frac{1}{\sqrt{2}}\left(\varepsilon\,|g\rangle + (1-i)\,|e\rangle\right), \end{aligned} \tag{8.75}$$

with $\hat{\sigma}_{fI0} = |\psi_{fI0}\rangle\langle\psi_{fI0}|$, then the probability of post-selection (i.e. the denominator of Eq. 8.74) is $p = \varepsilon^2/4$ for $\tau = 0$ and the weak value at first order in $\gamma\tau$ and ε is given by[2]

$$\sigma_{x,w} \approx \frac{\tau\gamma}{\varepsilon} + i\frac{2-\tau\gamma}{\varepsilon}. \tag{8.76}$$

We see that for a given time τ, the dissipation rate γ is effectively amplified by the small parameter ε in the denominator of the real part of the weak value. At $\tau = 0$, the weak value is purely imaginary. However, when dissipation is introduced ($\tau \neq 0$), the weak value becomes a complex number that varies linearly with time, $\tau\gamma$. In principle, the dissipation rate can be extracted by measuring the real part of the weak value at different short times. This approach takes advantage of the weak value amplification, proportional to $\frac{1}{\varepsilon}$, which opens up the possibility of using much shorter dissipation times. This is especially relevant for experiments where it may be difficult to obtain long dissipation times. In particular, by resorting to amplification, we reduce the measurement duration, which may be helpful if the meter undergoes some dissipation in practice (contrary to our model assumptions). We note that it is also possible to extract the dissipation rate by measuring the weak value for several values of the small parameter ε for a fixed duration τ of the dissipation, if this proves more convenient.

8.4.2 Revealing non-markovianity

In this section, we show that weak values can provide a valuable tool to distinguish between certain Markovian and non-Markovian dynamics. More specifically, we consider here a modified experimental setting in which a two-level atom undergoes a weak interaction in a cavity and then enters

[2] A few technical considerations on the joint series developments are provided in appendix O

a second leaky cavity. Inside the second cavity, the atom is coupled to a single cavity mode which is itself coupled to the bosonic bath in vacuum associated with the field outside the cavity. The dynamics of the atom in this cavity is described by the Jaynes-Cummings model on resonance, where the Hamiltonian of the atom is proportional to $\hat{\sigma}_z$, as explained in section 8.3. In this model, the non-Markovian dissipator is given by [174]

$$\mathscr{D}(\hat{\sigma}_{SI}) = \gamma(\tau)\left[\hat{\sigma}_-\hat{\sigma}_{SI}\hat{\sigma}_+ - \frac{1}{2}\left(\hat{\sigma}_+\hat{\sigma}_-\hat{\sigma}_{SI} + \hat{\sigma}_{SI}\hat{\sigma}_+\hat{\sigma}_-\right)\right], \tag{8.77}$$

with the time-dependent dissipation rate

$$\gamma(\tau) = \frac{2\gamma_0\lambda\sinh\left(d\frac{\tau}{2}\right)}{d\cosh\left(d\frac{\tau}{2}\right) + \lambda\sinh\left(d\frac{\tau}{2}\right)}, \tag{8.78}$$

where $d = \sqrt{\lambda^2 - 2\gamma_0\lambda}$, λ defines the spectral width of the coupling, in other words, the inverse of the bath correlation time, and γ_0 is the typical atomic decay rate in the Markovian limit. The nature of the parameter d in the Jaynes-Cummings model on resonance varies based on specific conditions [174]. In cases of moderate or weak coupling ($\lambda^2 > 2\gamma_0\lambda$), d takes on a real value, resulting in the absence of oscillations in the system dynamics. On the other hand, under strong coupling conditions ($\lambda^2 < 2\gamma_0\lambda$), d is imaginary and the characteristic oscillatory behavior emerges. The dynamics generated by this model is non-Markovian [174], which means that the evolution of the system at each time step depends on its past evolution, not just its present state. If we select the pre- and post-selected states as in the previous Markovian case Eq. 8.75, the weak value of $\hat{\sigma}_x$ at second order in τ and first order in ε is

$$\sigma_{x,w}(\tau) \approx \frac{\lambda\tau^2\gamma_0}{2\varepsilon} + i\frac{4-\lambda\tau^2\gamma_0}{2\varepsilon}, \tag{8.79}$$

where the exact analytical solution of the non-Markovian evolution of the weak value as a function of τ was used and expanded in Taylor series for small values of τ (see appendix P for details). The above expression is valid if

$$\lambda\tau \ll 1 \quad \text{and} \quad \gamma_0\tau \ll 1. \tag{8.80}$$

The non-Markovian expression Eq. 8.79 can be recovered from the Markovian case if we replace γ in Eq. 8.76 by $\frac{1}{2}\gamma_0\lambda\tau$, which corresponds to the series expansion of $\gamma(\tau)$ to first order in $\lambda\tau$ in Eq. 8.78.

We can see from Eq. 8.79 that the weak value exhibits a quadratic evolution with respect to τ, with no linear term in τ. This behavior is characteristic of non-Markovian dynamics described by the above dissipator, provided that $\gamma(\tau = 0) = 0$. To consider the transition from non-Markovian to Markovian dynamics in this system, we highlight that the Jaynes-Cummings model becomes Markovian as λ approaches infinity, with $\lim_{\lambda\to\infty}\gamma(\tau) = \gamma_0$. Consequently, the series expansion leading to Eq. 8.79 becomes invalid. Hence, the weak value Eq. 8.79 corresponds to the strongly non-Markovian case.

By comparing the evolution of the weak value as a function of τ at short dissipation times, it is possible to distinguish between Markovian and non-Markovian dynamics. Identically to the Markovian case, amplification occurs when $\varepsilon \ll 1$. However, in strongly non-Markovian systems, the weak value is proportional to τ^2 instead of τ. The real part of the weak value Eq. 8.79 is null

at $\tau = 0$, making detection of the quadratic dependence easier.
By examining the relationship between Eq. 8.76 and Eq. 8.79, we can obtain valuable information about λ, especially when $\gamma_0 = \gamma$. By incorporating a leaky cavity and comparing the weak value evolution to its free space counterpart (without the cavity), we can extract information about the leaky cavity parameters.
In summary, we have shown that the weak value at short times provides valuable information about dissipation in a system through an amplified decay rate, the effects of which are felt over a shorter evolution time in practice.

8.5 Conclusions

In this chapter, we outlined a few benefits that weak measurements and, in particular, weak values bring to the study of open quantum systems. We have shown that dissipation impedes the amplification produced by weak values at long times, unless the system's ground state is degenerate. More specifically, we have considered a pre-selection, weak interaction, dissipation, and post-selection scheme. In non-degenerate cases, we have shown that the limit of the weak value at infinite dissipation time is the expectation value of the operator in the initial state, so that dissipation suppresses the anomalous character associated with weak values and prevents amplification. However, in systems with a degenerate ground state, amplification can still occur at very long time-scales, as we have illustrated with a specific system.
Dissipation-induced decay to a degenerate ground state can even increase the anomalous properties of the weak value until it stabilizes. This is possible because not all quantum properties are lost through dissipation and the final state reached after long dissipation times can still be a combination of different ground states that retain some coherence. In particular, observing anomalous weak values at long dissipation time requires that the unperturbed initial state and its perturbation provoked by the weak interaction evolve differently under dissipation.
In addition, weak values can be used to measure various properties of the evolution of open quantum systems. For example, by choosing appropriate pre- and post-selected states, we can extract information about the dissipation rate through the weak value at short dissipation times, in the weak value amplification regime. This is particularly helpful if experimental constraints require a short measurement duration of each quantum system.
We also explained how it is possible to distinguish between Markovian and non-Markovian evolutions by measuring with our scheme the growth rate of the weak value. For Markovian evolutions, the weak value always increases linearly with time. On the other hand, in the strongly non-Markovian regime, the weak value at small times increases quadratically with time. Consequently, a measure of the growth rate of the weak value is sufficient to distinguish the two contrasting cases.
Besides, we observed that using a cavity mode as the meter of a weak measurement of an atom's internal degrees of freedom may yield meter measurement results that depend on weak values of the non-Hermitian raising and lowering operators of the atom. These applications demonstrate the usefulness of weak values in open quantum systems. We hope that this work will set the stage for other applications connecting weak values and open quantum systems.

Chapter 9

Exploiting modular values in quantum algorithms

Moore's law posits that the number of transistors on a microchip forming a computer doubles every two years [186]. This prediction has been a reality for the past five decades. However, it appears that this law may now be reaching a plateau.

The ability to increase our computational capacities is crucial for the continuous development of society. This progress allows for the creation of better materials and the discovery of more specialized drugs. Unfortunately, the plateau in Moore's law could halt the rapid advances we have seen in recent years.

To address this issue, scientists have proposed various solutions. Among the most promising is the quantum computer, which utilizes qubits to replace traditional bits and operates in a state of superposition. By leveraging this property, quantum computers are expected to provide faster solutions for specific problems.

In recent years, several quantum algorithms have demonstrated superior performance compared to their classical counterparts for specific tasks, meaning that the quantum computer needs less repetitions than the classical one. For instance, the search for a particular item in a database [187] and integer factorization [188] are examples of such tasks. One of the earliest examples of this quantum advantage is the Deutsch algorithm [189] and its generalization, the Deutsch-Jozsa algorithm [190]. These algorithms aim to determine whether a function $f : \{0,1\}^{n-1} \to \{0,1\}$ is constant, meaning that all outputs are either uniformly equal to 1 or uniformly equal to 0, or if it is balanced, where half of the outputs are equal to 1 and the other half are equal to 0. In the quantum case, this problem can be resolved in a single step, whereas in the classical case, it requires up to 2^{n-1} repetitions in the worst-case scenario.

This chapter introduces a novel approach to implementing quantum algorithms using modular values. This method leverages the degrees of freedom and complex properties of modular values. The modular value, denoted as

$$A_m = \frac{\langle \psi_f | e^{-ik\hat{A}} | \psi_i \rangle}{\langle \psi_f | \psi_i \rangle}, \tag{9.1}$$

is similar to the weak value expression but involves a unitary operator instead of an observable. In some cases, such as when k is small, and the exponential can be expressed using a Taylor series,

they share the same expression. Nonetheless, modular values are associated with interactions of any strength; a weak coupling between the system and the ancilla is not necessary. It is important to note that the method requires a qubit as the ancilla [191]. Although some works have explored the possibility of developing quantum algorithms using modular values [192], a complete theoretical framework is still lacking. We anticipate that this approach could reduce the number of gates required as the quantum algorithm can be executed by simply evaluating the modular value of the oracle, and, therefore, minimize errors in executing the algorithm. However, it always requires an additional qubit to read out the result of the quantum modular value, and the probability of post-selection should always be considered.
In this chapter, we explore the application of modular values in executing quantum algorithms. We begin by introducing the general method for performing quantum algorithms using modular values. Next, we dive into the Deutsch-Jozsa problem and demonstrate how it can be solved using this approach. Furthermore, we delve into the choice of pre- and post-selected states in the Deutsch-Jozsa problem. To provide further clarity, we also provide an example of how to run this algorithm on a quantum computer. Moving on, we introduce Grover's search problem and demonstrate how modular values can be used to solve it. Subsequently, we introduce the phase estimation problem and highlight the numerous advantages it offers when addressed using modular values. Particularly, we emphasize the improvements in precision compared to the conventional approach. We also discuss the implications and benefits of using modular values in quantum computing. Finally, we conclude the chapter by providing some future perspectives on the application of modular values in implementing quantum algorithms.

9.1 General method using modular values

In this section, we provide a detailed procedure for tackling quantum algorithms using modular values. Our method involves carrying out a measurement with pre- and post-selection to the oracle. Oracles play a critical role in constructing algorithms in quantum computers [193, 194]. Essentially, an oracle is a black box that contains unknown operations to the person executing the experiment. Oracles are implemented using unitary operations and are commonly employed in quantum algorithms such as the Deutsch-Jozsa algorithm and the Grover's algorithm [187, 190].
As illustrated in Fig. 9.1, the system used in our algorithm comprises $n+1$ qubits, with n qubits for executing the oracle and one for the readout process. The algorithm consists of three main parts: pre-selection of the oracle input state and preparation of the ancilla's state, controlled oracle application, and post-selection on the system. Finally, the measurement of the modular value unfolds. To begin, we take the system's n qubits to the pre-selected state

$$|\psi_i\rangle = |\psi_1\rangle \otimes |\psi_2\rangle \otimes ... \otimes |\psi_n\rangle\,, \tag{9.2}$$

using unitary operators. The initial state of the meter, denoted as $\hat{\rho}_m$, is defined as

$$\hat{\rho}_m = \frac{1}{2}\left(\hat{I} + P_m \vec{m}\cdot\vec{\sigma}\right), \tag{9.3}$$

where $\vec{m}$ represents the state on the Bloch sphere and P_m quantifies the purity of the meter state. To obtain this initial state, we employ a unitary operator. Subsequently, we apply the following

nonlocal unitary operator to the entire system, comprising the probe and the meter:

$$\hat{U}_{\text{GATE}} = \hat{\Pi}_r \otimes \hat{I} + \hat{\Pi}_{-r} \otimes \hat{U}_O. \tag{9.4}$$

In this expression, $\hat{U}_O$ represents the oracle employed in the experiment, while $\hat{\Pi}_r$ and $\hat{\Pi}_{-r}$ are projectors applied to the ancillary space. These projectors can be expressed in terms of the vector $\pm\vec{r}$ on the Bloch sphere as follows:

$$\hat{\Pi}_{\pm r} = \frac{1}{2}\left(\hat{I} \pm \vec{r}\cdot\vec{\hat{\sigma}}\right). \tag{9.5}$$

The unitary operator $\hat{U}_{\text{GATE}}$ facilitates a controlled evolution of the probe. When the ancillary projector is $\hat{\Pi}_r$, the probe undergoes only the identity operation. Conversely, when the ancillary projector is $\hat{\Pi}_{-r}$, the probe experiences the application of the operator $\hat{U}_O$. In the case of an ancillary state lying between these two scenarios, the superposed effect of both operators is applied to the probe.
To complete the procedure, we post-select the system qubits to $|\psi_f\rangle$. Finally, by measuring the spin operator in the direction $\vec{q}$,

$$\hat{\sigma}_q = \hat{\Pi}_{+q} - \hat{\Pi}_{-q}, \tag{9.6}$$

we extract the information on the modular value.

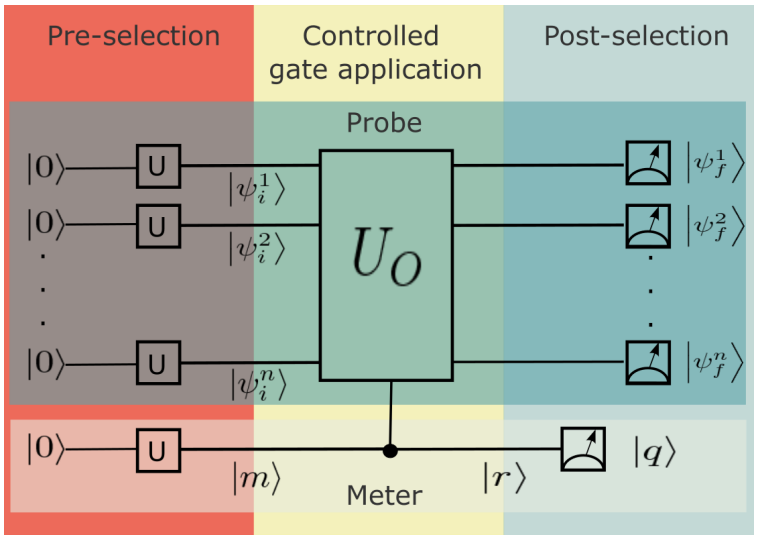

Figure 9.1: The proposed model consists of n qubits and a qubit meter that together form the full system. To prepare the system for the experiment, we first apply n unitary operators to the first n qubits to take them to the pre-selected state $|\psi_i\rangle$. We also use a unitary operator to set the qubit meter to its initial state. Next, we apply the controlled oracle to the system. To post-select, we apply additional unitary operators, and finally, we measure the state of the system in the computational basis.

After some mathematical development shown in [112], the joint probabilities are computed from,

$$P_{joint}^{\pm q} = \text{Tr}\left[\left(|\psi_f\rangle\langle\psi_f| \otimes \hat{\Pi}_{\pm q}\right)\hat{\rho}\right], \tag{9.7}$$

where $\hat{\rho}$ is the state of the full system. After applying the eraser condition $\vec{r}\cdot\vec{q}=0$[1], the joint probabilities take the form

$$\begin{aligned} P_{joint}^{\pm q} &= \frac{1}{4}\{(1+P_m\vec{r}\cdot\vec{m})\,|\langle\psi_f|\psi_i\rangle|^2 \\ &+ (1-P_m\vec{r}\cdot\vec{m})\,|\langle\psi_f|\hat{U}_O|\psi_i\rangle|^2 \\ &\pm 2P_m\,(\vec{m}\cdot\vec{q})\,\mathrm{Re}\left(\langle\psi_f|\hat{U}_O|\psi_i\rangle\langle\psi_i|\psi_f\rangle\right) \\ &\pm 2P_m\,[(\vec{r}\times\vec{m})\cdot\vec{q}]\,\mathrm{Im}\left(\langle\psi_f|\hat{U}_O|\psi_i\rangle\langle\psi_i|\psi_f\rangle\right)\}. \end{aligned} \tag{9.8}$$

The expected value of the spin operator in the meter is [112],

$$\bar{\sigma}_q^m = 2P_m\frac{(\vec{m}\cdot\vec{q})\,\mathrm{Re}O_m+[(\vec{r}\times\vec{m})\cdot\vec{q}]\,\mathrm{Im}O_m}{(1+P_m\vec{r}\cdot\vec{m})+(1-P_m\vec{r}\cdot\vec{m})\,|O_m|^2} = \frac{P_{\text{joint}}^{+q}-P_{\text{joint}}^{-q}}{P_{\text{joint}}^{+q}+P_{\text{joint}}^{-q}}, \tag{9.9}$$

where the modular value is

$$O_m = \frac{\langle\psi_f|\hat{U}_O|\psi_i\rangle}{\langle\psi_f|\psi_i\rangle}. \tag{9.10}$$

Since we use a qubit as the meter in this experiment, we can take advantage of the modular value properties to implement various algorithms.

To determine the required number of repetitions of the algorithm to obtain enough statistics to solve the initial problem, we need to evaluate the probability of post-selection, which is denoted at first order as

$$p = |\langle\psi_f|\psi_i\rangle|^2, \tag{9.11}$$

and the visibility that measures the contrast between joint probabilities that we measure, and which is given by

$$V = \frac{P_{max}-P_{min}}{P_{max}+P_{min}}. \tag{9.12}$$

P_{min} represents the minimum joint probability between P_{joint}^{+q} and P_{joint}^{-q}, while P_{max} corresponds to the maximum joint probability.

In each particular case, the determination of the maximum and minimum joint probabilities is essential and can be achieved by considering the expression provided in Eq. 9.8. When employing this approach, there exist various degrees of freedom that can be optimized based on specific experimental conditions. These include selecting the pre- and post-selected states, choosing the meter state, and determining the operator to be measured in the meter. Additionally, alternative experimental approaches can be explored, which may lead to the emergence of modular values and the development of novel methods for executing quantum algorithms. In the following sections, we will demonstrate the practical application of this approach by implementing three prominent quantum algorithms: the Deutsch-Jozsa algorithm, Grover's search algorithm, and the phase estimation algorithm.

[1]Selecting two quantum states that are orthogonal on the Bloch sphere, expressed as $\vec{r}\cdot\vec{q}=0$, maximizes the interference between different pathways during the meter measurement. In this configuration, the nonlocal gate action arises as a superposition of both $\hat{U}_O$ and $\hat{I}$, causing a loss of information about the gate action. This particular circumstance is referred to as the 'quantum eraser' condition, a term frequently employed in interferometer experiments to eliminate the knowledge of the particle's path. For instance, applying a linear polarizer can erase the information regarding whether the polarization is circular left or right. Linear polarization lies orthogonal on the Poincaré sphere to circular polarization (both left and right).

9.2 Deutsch-Jozsa algorithm

The Deutsch-Jozsa algorithm aims to determine whether a given function $f(x) : \{0,1\}^{n-1} \to \{0,1\}$ is constant or balanced. A constant function assigns the same value (either 0 or 1) to all the inputs, whereas a balanced function assigns the value 1 to exactly half of the inputs and the value 0 to the other half. Table 9.1 shows the different possibilities for the Deutsch-Jozsa algorithm for a function $f(x)$ with two inputs.

Balanced

$f(00)$	$f(01)$	$f(10)$	$f(11)$
0	0	1	1
0	1	0	1
0	1	1	0
1	1	0	0
1	0	1	0
1	0	0	1

Constant

$f(00)$	$f(01)$	$f(10)$	$f(11)$
0	0	0	0
1	1	1	1

Table 9.1: Here are all the possible combinations of two-bit inputs and single-bit outputs that result in either a constant or a balanced function.

In 1992, Deutsch and Jozsa introduced a groundbreaking quantum circuit that solves this problem in a single step, providing a significant advantage over the classical counterpart. In the worst-case scenario, the classical approach requires 2^{n-1} repetitions, where 2^{n-1} represents the total number of inputs for the function. However, by leveraging qubits, we can exploit the fact that 2^{n-1} corresponds to the dimensionality of the space formed by $n-1$ qubits. Thus, we can effectively employ $n-1$ qubits to generate the entire set of 2^{n-1} inputs. In stark contrast, the quantum circuit designed by Deutsch and Jozsa achieves the same result efficiently. The quantum circuit is depicted in Fig. 9.2, showcasing its elegance and simplicity. To tackle the problem with 2^{n-1} inputs, the algorithm mandates the utilization of n qubits. To address a problem involving a function with all possible combinations of $n-1$ qubits as input, it is necessary to utilize a total of n qubits. The first $n-1$ qubits are initialized in the state $|0\rangle$, while the remaining qubit is initialized in the state $|1\rangle$. This initialization results in the following state:

$$|\psi_0\rangle = |0\rangle^{\otimes n-1} |1\rangle \tag{9.13}$$

where $|0\rangle^{\otimes n-1}$ is a compact notation for the tensor product of $n-1$ $|0\rangle$ states, $|0\rangle \otimes |0\rangle \ldots \otimes |0\rangle$, and the basis has been chosen as

$$|0\rangle = \begin{pmatrix} 1 \\ 0 \end{pmatrix} \qquad |1\rangle = \begin{pmatrix} 0 \\ 1 \end{pmatrix}. \tag{9.14}$$

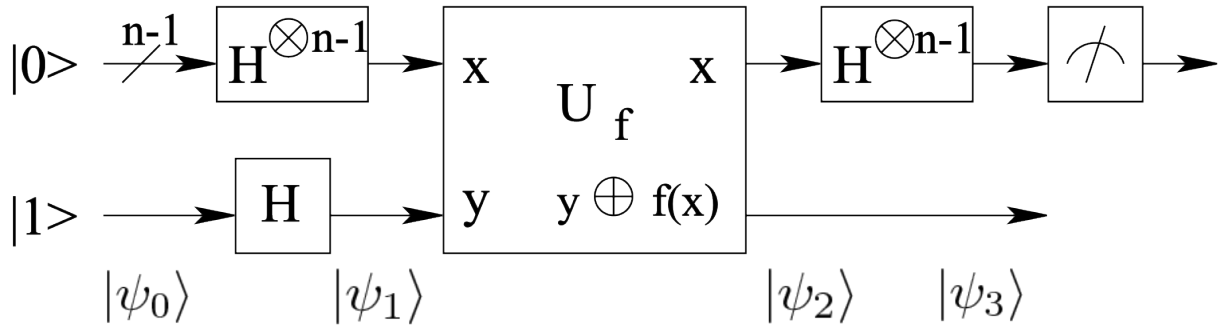

Figure 9.2: Deutsch-Jozsa quantum circuit, where U_f is the oracle, H is the Hadamard gate, and the states $|\psi_0\rangle$, $|\psi_1\rangle$, $|\psi_2\rangle$, and $|\psi_3\rangle$ are detailed in the text. Modified from Fran4004, https://commons.wikimedia.org/wiki/File:Deutsch-Jozsa__algorithm__circuit.svg, accessed on the 17th of August 2023.

The first step consists of applying the Hadamard gate, $\hat{H}$,

$$\hat{H} = \frac{1}{\sqrt{2}} \begin{pmatrix} 1 & 1 \\ 1 & -1 \end{pmatrix} \tag{9.15}$$

to all $n-1$ qubits. The state after the transformation is

$$|\psi_1\rangle = \frac{1}{\sqrt{2^n}} \left(|0\rangle + |1\rangle\right)^{\otimes n-1} \left(|0\rangle - |1\rangle\right) = \sum_{x\in\{0,1\}^{n-1}} \frac{1}{\sqrt{2^n}} |x\rangle \left(|0\rangle - |1\rangle\right), \tag{9.16}$$

where $|x\rangle$ are all the 2^{n-1} states of the basis with $n-1$ qubits.
After applying the Hadamard gates, the oracle is applied to the n qubits. The oracle acts as

$$\hat{U}_f |x, y\rangle \rightarrow |x, y \oplus f(x)\rangle, \tag{9.17}$$

where $\oplus$ represents the addition modulo 2, that is 0 if both terms are equal and 1 if both terms are different

$$\begin{aligned} 0 \oplus 0 &= 0 \\ 0 \oplus 1 &= 1 \\ 1 \oplus 0 &= 1 \\ 1 \oplus 1 &= 0. \end{aligned} \tag{9.18}$$

The resulting state after the application of the oracle is:

$$|\psi_2\rangle = \sum_{x\in\{0,1\}^{n-1}} \frac{1}{\sqrt{2^n}} |x\rangle \left(|0 \oplus f(x)\rangle - |1 \oplus f(x)\rangle\right) = \sum_{x\in\{0,1\}^{n-1}} \frac{(-1)^{f(x)}}{\sqrt{2^n}} |x\rangle \left(|0\rangle - |1\rangle\right). \tag{9.19}$$

In Eq. 9.19, we make use of the property that $|0 \oplus f(x)\rangle = |f(x)\rangle$, while $|1 \oplus f(x)\rangle = |1 - f(x)\rangle$. Subsequently, the Hadamard gate, denoted as $\hat{H}^{\otimes n-1}$, is applied to the first $n-1$ qubits. The

application of $n-1$ Hadamard gates to an $n-1$-qubit state can be expressed as:

$$\hat{H}^{\otimes n-1}|x_1,\ldots,x_{n-1}\rangle = \frac{\sum_{z_1,\ldots,z_{n-1}}(-1)^{x_1z_1+\ldots+x_{n-1}z_{n-1}}|z_1,\ldots,z_{n-1}\rangle}{\sqrt{2^{n-1}}}, \tag{9.20}$$

where x_i are the components of the state $|x\rangle$, while z_i are the ones of the state $|z\rangle$, hence every component is either a 0 or a 1.
The notation can be simplified as

$$\hat{H}^{\otimes n-1}|x\rangle = \frac{\sum_z(-1)^{x\cdot z}|z\rangle}{\sqrt{2^{n-1}}}, \tag{9.21}$$

where $x\cdot z$ is the inner product of x and z, modulo 2. Finally, the state $|\psi_3\rangle$ is after applying the Hadamard gate to the first $n-1$ qubits,

$$|\psi_3\rangle = \sum_{z_1,\ldots,z_{n-1}}\sum_{x_1,\ldots,z_{n-1}}\frac{1}{\sqrt{2^n}}(-1)^{x\cdot z+f(x)}|z\rangle(|0\rangle-|1\rangle) \tag{9.22}$$

Finally, if we measure in the $\{|0\rangle,|1\rangle\}^{n-1}$ basis the $n-1$ first qubits, the probability of obtaining the state $|0\rangle^{\otimes n-1}$ would be,

$$\left|\frac{1}{2^{n-1}}\sum_{x=0}^{2^{n-1}-1}(-1)^{f(x)}\right|. \tag{9.23}$$

Consequently, if the measurement result is $|0\rangle^{\otimes n-1}$, the function is constant, whereas if the measurement result is different from $|0\rangle^{\otimes n-1}$, the function is balanced. By applying the algorithm once, we can determine with certainty whether the function is balanced or constant.
Although the Deutsch-Jozsa algorithm does not have any real-world applications, it was one of the first quantum algorithms to demonstrate a clear advantage over its classical counterpart.

9.3 Deutsch-Jozsa problem using modular values

In the previous section, we discussed the conventional method for solving the Deutsch-Jozsa problem. In this section, we explore an alternative approach by calculating the modular value of the oracle operator, denoted as U. When solving the problem with 2^{n-1} inputs, the oracle is applied to n qubits. As a result, the pre- and post-selected states become n-qubit states. To extract the modular value, an additional qubit, known as the ancilla qubit, is required. Therefore, a total of $n+1$ qubits are needed for this approach. The application of the oracle can be expressed as

$$U(|x\rangle|y\rangle) = |x\rangle|y\oplus f(x)\rangle. \tag{9.24}$$

The algorithm can be implemented by calculating the modular value of the oracle in systems of any dimension. The Deutsch-Jozsa problem for a function of 4 inputs, hence the dimension of two qubits, employs three qubits, as seen in the previous section. In the modular value approach, we implement the modular value of the oracle with three qubits and we need an extra qubit to act as

the ancilla. The chosen pre- and post-selected states are:

$$\begin{aligned} |\psi_i\rangle &= \frac{1}{\sqrt{8}}(|0\rangle+|1\rangle)\otimes(|0\rangle+|1\rangle)\otimes(|0\rangle-|1\rangle) \\ &= \frac{1}{\sqrt{8}}(|000\rangle+|010\rangle+|100\rangle+|110\rangle-|001\rangle-|011\rangle-|101\rangle-|111\rangle) \\ |\psi_f\rangle &= \frac{1}{\sqrt{11}}(-2i|000\rangle-i|010\rangle+i|001\rangle+i|011\rangle+|100\rangle+|110\rangle-|101\rangle-|111\rangle). \end{aligned} \tag{9.25}$$

The probability of post-selection in this case is given by $p = |\langle\psi_f|\psi_i\rangle|^2 = \frac{41}{88} \approx 0.47$, which is slightly below one-half. Consequently, on average, two attempts are needed to achieve successful post-selection. When the function $f(x) : \{0,1\}^{n-1} \to \{0,1\}$ is constant, meaning that $f(x)$ is either 0 or 1 for all x, the numerator of the modular value is equal to the denominator or its opposite. Thus, the modular value is either 1 or -1, resulting in a purely real value. On the other hand, when the function $f(x) : \{0,1\}^n \to \{0,1\}$ is balanced, with half of the terms $f(x)$ equal to 1 and the other half equal to 0, the modular values possess an imaginary part for all possible balanced combinations of $f(x)$.

$f(00)$	$f(01)$	$f(10)$	$f(11)$	U_w	$\mathrm{Re}(U_w)$	$\mathrm{Im}(U_w)$
0	0	1	1	$\frac{5i-4}{5i+4}$	$\frac{9}{41}$	$\frac{40}{41}$
0	1	0	1	$\frac{i}{5i+4}$	$\frac{5}{41}$	$\frac{4}{41}$
0	1	1	0	$\frac{i}{5i+4}$	$\frac{5}{41}$	$\frac{4}{41}$
1	1	0	0	$\frac{-5i+4}{5i+4}$	$-\frac{9}{41}$	$-\frac{40}{41}$
1	0	1	0	$\frac{-i}{5i+4}$	$-\frac{5}{41}$	$-\frac{4}{41}$
1	0	0	1	$\frac{-i}{5i+4}$	$-\frac{5}{41}$	$-\frac{4}{41}$

Table 9.2: All the possible combinations to have a balanced function with three qubits and the corresponding modular values.

In table 9.2, all balanced possibilities using three qubits are presented. All modular values have an imaginary part, which allows for discrimination between balanced and constant functions by measuring this part. This process is easily generalized to the algorithm with $n+1$ qubits (the n qubits of the Deutsch-Jozsa algorithm plus the ancilla). In this case, the pre-selected state is the natural generalization of the previous case

$$|\psi_i\rangle = \frac{1}{\sqrt{2^n}}(|0\rangle+|1\rangle)^{\otimes(n-1)}(|0\rangle-|1\rangle). \tag{9.26}$$

The post-selected state is generalized from the three-qubit case,

$$\begin{aligned}\left|\psi_f\right\rangle &= \frac{1}{\sqrt{2^n+3}}(-2i\left|00...0\right\rangle + i\left|00...0...01\right\rangle + (-i\sum_{j=2}^{2^{n-2}} \underbrace{\left|0a_2...a_{(2^{n-1})}\right\rangle_j}_{(2^{n-1})/2-1 \text{ first terms with } n-1 \text{ qubits removing } |000...0\rangle} \\ &+ \sum_{k=2^{n-2}+1}^{2^{n-1}} \underbrace{\left|1b_2...b_{(2^{n-1})}\right\rangle_k}_{(2^{n-1})/2 \text{ last terms with } n-1 \text{ qubits}})\times(\left|0\right\rangle - \left|1\right\rangle))\end{aligned} \tag{9.27}$$

The probability of post-selection using the states Eq. 9.26 and Eq. 9.27 is

$$p = \frac{2^n\left(1+2^{n-1}\right)+1}{2^n\left(3+2^n\right)}, \tag{9.28}$$

whose limit when n tends to infinity is $\frac{1}{2}$. Therefore, on average, two attempts are required for successful post-selection. In the case where the function $f(x) : \{0,1\}^{n-1} \rightarrow \{0,1\}$ is constant, the numerator and denominator of the modular value take the same value or the opposite value, resulting in a modular value of either 1 or -1. Conversely, when the function is balanced, the modular value presents always an imaginary part. Discrimination between a real and complex modular value can be accomplished by observing whether there is a term proportional to $(\vec{r}\times\vec{m})\cdot\vec{q}$ in Eq. 9.9. We can access this term by choosing $\vec{m}$ and $\vec{q}$ perpendicular, so that $\vec{m}\cdot\vec{q}=0$. Additionally, by selecting different pre- and post-selected states, it is possible to determine in which of the possible ways the function is balanced.

9.4 Choice of pre- and post-selected states in the Deutsch-Jozsa problem using modular values

In the previous section, we introduced the pre- and post-selected states for solving the Deutsch-Jozsa problem using modular values, as described in Eq. 9.27. However, one might question the rationale behind this particular choice. Our objective is to find two quantum states (pre-selected and post-selected) that yield a non-zero imaginary part of the weak value of the oracle for all possible combinations of balanced function $f(x)$, as given in table 9.1. Ideally, we aim to maximize this imaginary part while minimizing the real part of the weak value, in order to enhance the visibility defined in Eq. 9.12. Additionally, we strive to maximize the probability of successful post-selection. Hence, we are confronted with an optimization problem.
In order to explore the entire quantum space, we conducted a random mapping of the complete state space for the pre-selected and post-selected states, both consisting of four-level states (two qubits). The pseudorandom numbers used were integer values drawn from a discrete uniform distribution. Fig. 9.3 showcases the resulting average visibility of all combinations of the balanced function, which are further detailed in table 9.1, as a function of the probability of post-selection. In this particular case, we have chosen to focus on separable states, as they are easier to generate

using quantum gates, such as those available in the IBM quantum computer. As depicted in the plot, there is a trade-off that needs to be considered. On one hand, we can achieve a very high probability of post-selection, but at the cost of lower visibility. On the other hand, we can enhance the visibility, but with a decrease in the probability of successful post-selection.

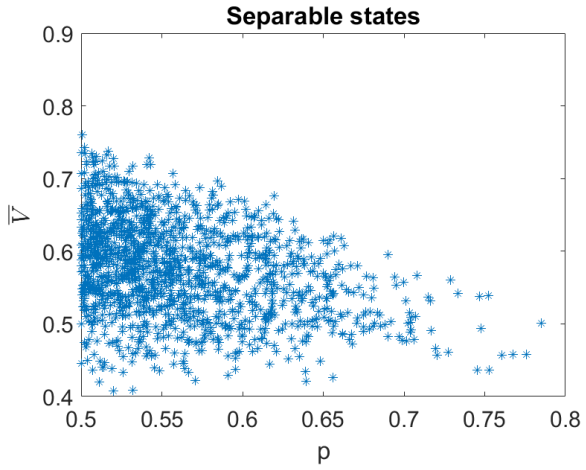

Figure 9.3: Average visibility as a function of the probability of post-selection for randomly generated two-qubit separable pre-selected and post-selected states in the Deutsch-Jozsa problem. Our criteria for selecting these states were to ensure that the imaginary part of the weak value of the oracle, corresponding to each balanced function, is greater than 0.1, each individual visibility is greater than 0.4, and the probability of post-selection is greater than 0.5. By imposing these conditions, we aim to strike a balance between a high post-selection probability, and strong visibility to ensure the ability to distinguish between constant and balanced functions.

Alternatively, we can explore the space of non-separable states as a potential solution. In Fig. 9.4, we present a denser plot where we consider both separable and non-separable states. This broader range of states offers more possibilities for achieving intermediate values of average visibility in relation to the probability of post-selection. It was expected that including non-separable states would provide additional options beyond the separable ones. When aiming for low visibility (around 0.4) and high post-selection probability (around 0.8), the benefit of incorporating non-separable states is limited. However, when targeting a low probability of post-selection (around 0.5), we observe points on the plot that yield improved average visibility values exceeding 0.8.
Interestingly, we observe the emergence of a distinct trend in the form of a straight line, which seems to move up when non-separable states are considered. This suggests that there is a clear boundary beyond which points are not found above the line. It is worth noting that choosing non-separable states introduces additional complexity in generating such states on a quantum computer. This typically involves utilizing multi-qubit gates such as the CNOT or the TOFFOLI gates. Despite the challenges involved, non-separable states offer potential advantages, as demonstrated by the improved average visibility and probability of post-selection in certain regions of the plot. Given the trade-off between selecting separable and non-separable states, we opted for simplicity in the implementation of the Deutsch-Jozsa problem on the IBM quantum computer in the subsequent section. We specifically chose straightforward pre- and post-selected states that enable differentiation between only one way to balance the function, and constant. This decision was

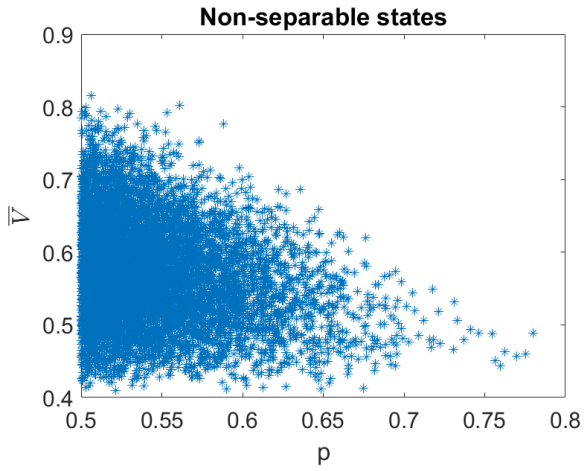

Figure 9.4: Average visibility in terms of the probability of post-selection for randomly generated two-qubit non-separable pre- and post-selected states in the context of the Deutsch-Jozsa problem. For this analysis, we have imposed a minimum threshold of 0.1 for the imaginary part of each weak value of the oracle, considering all balanced functions. Additionally, each individual visibility is required to exceed 0.4, and the probability of post-selection must be greater than 0.5.

motivated by the difficulty of implementing more complex states using the available gates.

9.5 Implementation of the Deutsch-Jozsa problem using modular values in the IBM quantum computer

To experimentally implement the Deutsch-Jozsa algorithm, we can follow the scheme shown in Fig. 9.1. In this approach, we need to select the initial state of the meter, denoted by $|m\rangle$, the applied Pauli matrix $\hat{\sigma}_r$, and the final state measured in the meter, denoted by $|q\rangle$. We should impose $\vec{r}\cdot\vec{q}=0$ to satisfy the eraser condition explained in the previous section. Additionally, we choose to enforce $\vec{m}\cdot\vec{q}=0$ in order to have direct access to the imaginary part of the weak value.

$$\hat{\rho}_m = \frac{1}{2}\left(\hat{I}+\hat{\sigma}_z\right), \tag{9.29}$$

where $\vec{m}=(0,0,1)$. The projector controlling the application of the oracle is

$$\hat{\Pi}_r = \frac{1}{2}\left(\hat{I}+\hat{\sigma}_x\right), \tag{9.30}$$

where $\vec{r}=(1,0,0)$. The observable to measure in the meter is $\hat{\sigma}_y$, with $\vec{q}=(0,1,0)$.
Applying the selected states, the average measured value of $\hat{\sigma}_y$ in the probe is

$$\bar{\sigma}_y^m = \frac{-2\mathrm{Im}\left(U_{0m}\right)}{1+|U_{0m}|^2}. \tag{9.31}$$

Taking into account the joint probability values in this scenario, the visibility is given by

$$V = \frac{2|\mathrm{Im}\left(U_{0m}\right)|}{1+|\mathrm{Im}\left(U_{0m}\right)|^2+|\mathrm{Re}\left(U_{0m}\right)|^2}. \tag{9.32}$$

It is desirable to achieve a high visibility to distinguish in less repetitions of the experiment the real part from the imaginary one. In particular, the maximum visibility $V = 1$ is reached for $\mathrm{Im}(A_m) = \pm 1$ and $\mathrm{Re}(A_m) = 0$. The closer the real part to 0, the better; the closer the imaginary part to 1, the better. This is equivalent to maximizing $\frac{2x}{x^2+y^2+1}$ with respect to x and y. For the case of the Deutsch-Jozsa problem with two qubits, $f(x) : \{0,1\}^2 \to \{0,1\}$ shown in table 9.2, the first and third possibilities to balance the system have a good visibility, while the others do not. These values can be optimized at the expense of losing some visibility on the first and third cases. The number of times the algorithm should be run depends on the level of uncertainty one is willing to accept.

We ran the modular value algorithm to solve the Deutsch-Jozsa problem on the Quito IBM quantum computer, using modular values, for one constant and one balanced case. The pre-selected state is chosen as described in Eq. 9.25, and we simplified the post-selected state by choosing it as

$$\left|\psi_f\right\rangle = \frac{1}{\sqrt{8}}\left(|000\rangle + |010\rangle + i|100\rangle + i|110\rangle - |001\rangle - |011\rangle - i|101\rangle - i|111\rangle\right). \tag{9.33}$$

This post-selected state has been chosen for simplicity to obtain the state through gates on the IBM quantum computer. In this case, only one way of balanced function can be discriminated, which means only one row of the balanced function can be differentiated from the constant one in table 9.1. In a next step, it would be desirable to implement the post-selected state expressed in Eq. 9.25. The probability of post-selection using the state described in Eq. 9.33 is $p = \frac{1}{2}$. The states $|m\rangle$, $|r\rangle$, and $|q\rangle$ were chosen as described earlier. The circuit applied when the function was constant is shown in Fig. 9.5, where no gate was used to create the oracle, as the circuit is constant, mathematically represented by the identity operator, $\hat{I}$. The unitary operators present in that image are used to post-select.

Basically, we send the post-selected state to the $|000\rangle$, which implies that finding the system in that state would be equivalent to having post-selected on the state $\left|\psi_f\right\rangle$.

The circuit applied when the function was balanced, with $f(00) = f(01) = 0$ and $f(10) = f(11) = 1$, is shown in Fig. 9.6, where the unitary operator is defined as,

$$\hat{U}(\theta,\phi,\lambda) = \begin{pmatrix} \cos\frac{\theta}{2} & -e^{-i\lambda}\sin\frac{\theta}{2} \\ e^{i\phi}\sin\frac{\theta}{2} & e^{\phi+\lambda}\cos\frac{\theta}{2} \end{pmatrix}. \tag{9.34}$$

The modular value is equal to 1 when the function is constant, with $\hat{\sigma}_y^m = 0$, and equal to i when the function is balanced, with $\hat{\sigma}_y^m = -1$. The visibility was 1 for the balanced case and 0 for the constant case.

Fig. 9.7 portrays the outcomes attained of the average $\hat{\sigma}_y$ measurements within the framework of the Deutsch-Jozsa algorithm when executed on the IBM Quito quantum computer. These results are exhibited as a function of the repetition count. Correspondingly, Fig. 9.8 presents the plotted post-selection rates for both the balanced and constant cases. It is noteworthy that the theoretical post-selection probability stands at $\frac{1}{2}$, while the value computed through the IBM quantum simulator reaches 0.51. In the realm of experimentation, the post-selection rate manifests itself between 0.4 and 0.6. The determination of the requisite number of repetitions is contingent upon the desired data quality and the precision of the experimental setup. Remarkably, the distinction between the two cases—constant and balanced—was successfully accomplished with 32 shots, incorporating unsuccessful post-selections as well. A pivotal observation is that the IBM Quito system is

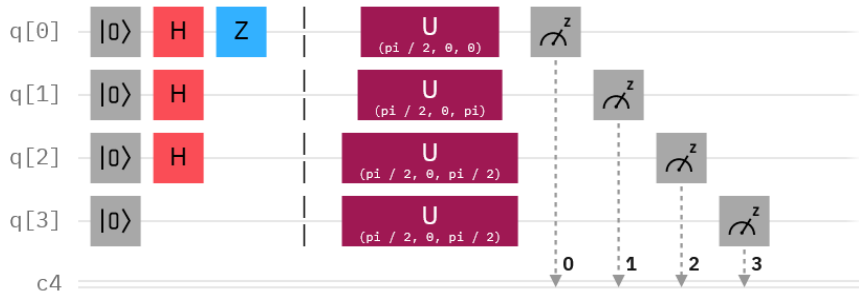

Figure 9.5: Circuit diagram for the Deutsch-Jozsa algorithm with a constant function using 3 qubits and one ancilla qubit. The circuit applies the unitary operator $\hat{U}\left(\frac{\pi}{2},0,0\right)$ to qubit 0, $\hat{U}\left(\frac{\pi}{2},0,\pi\right)$ to qubit 1, $\hat{U}\left(\frac{\pi}{2},0,\frac{\pi}{2}\right)$ to qubit 2, and $\hat{U}\left(\frac{\pi}{2},0,\frac{\pi}{2}\right)$ to qubit 3. Figure produced with https://quantum-computing.ibm.com.

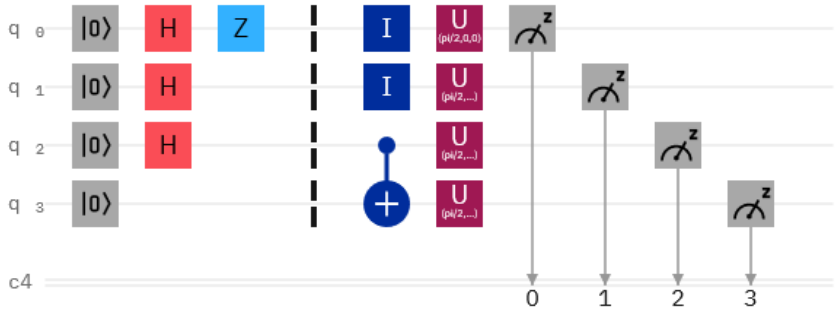

Figure 9.6: The circuit diagram illustrates the implementation of the Deutsch-Jozsa algorithm for the balanced case, using a 3-qubit system and one ancilla qubit. The gates applied to each qubit are $\hat{U}\left(\pi/2,0,\pi\right)$ to qubit 0, $\hat{U}\left(\pi/2,0,\pi\right)$ to qubit 1, $\hat{U}\left(\pi/2,0,\pi/2\right)$ to qubit 2, and $\hat{U}\left(\pi/2,0,\pi/2\right)$ to qubit 3. Figure produced with https://quantum-computing.ibm.com.

markedly influenced by substantial noise, as evidenced by a median CNOT error of 6.895e-3 and a median readout error of 3.920e-2. It is worth emphasizing that this procedure can also be conducted utilizing alternative experimental configurations, such as optical systems.

9.6 Grover's search algorithm

In this section, we present the quantum circuit for Grover's search algorithm, which aims to search for an element in a database of 2^n elements. The designed quantum algorithm to solve this problem requires a number of evaluations of the oracle, followed by the Grover diffusion operator, equal only to the integer the closest to $\frac{\pi}{4}\sqrt{2^n}$ Fig. 9.9, whereas a classical algorithm requires in average $\frac{2^n+1}{2}$, and 2^n in the worst scenario. The circuit, as shown in Fig. 9.9, starts with all qubits initialized on the fundamental state, $|0\rangle$. Next, a Hadamard gate is applied to all qubits, Eq. 9.15, resulting in

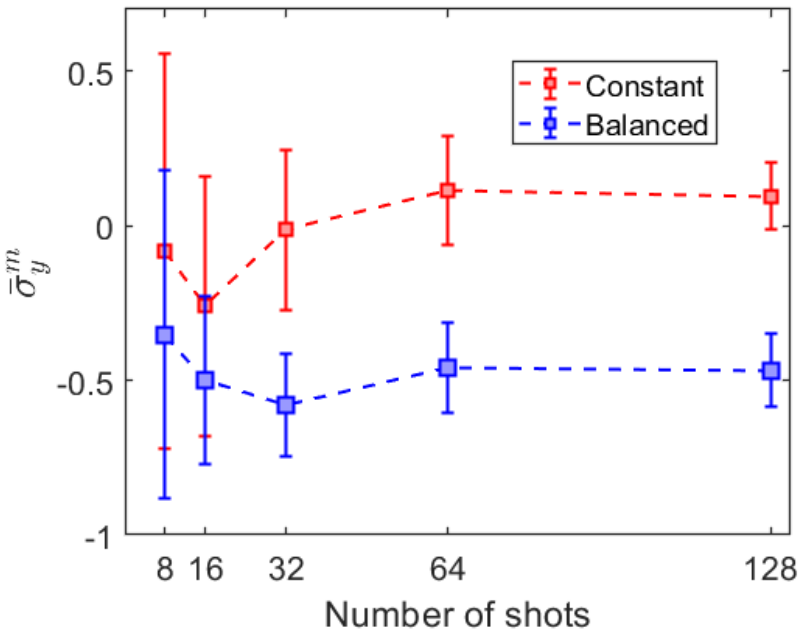

Figure 9.7: Mean $\hat{\sigma}_y$ operator measurement outcomes are presented for both the constant and balanced cases across a range of shots: 8, 16, 32, 64, and 128. The entire procedure has been iterated a total of 12 times for each distinct run count. Furthermore, to provide a comprehensive representation, the standard deviation has been incorporated in the form of error bars.

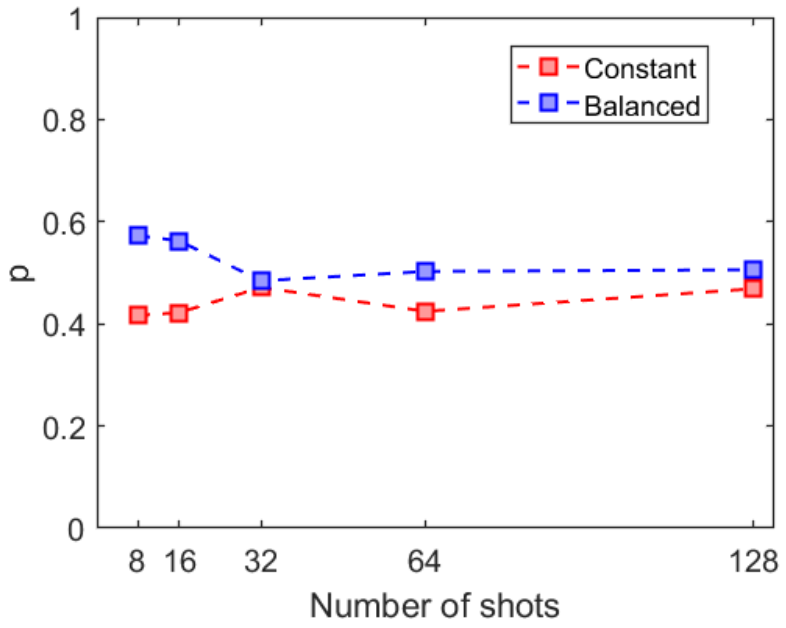

Figure 9.8: Experimental average post-selection rate, p, for varying number of shots: 8, 16, 32, 64, and 128, encompassing both the constant and balanced scenarios.

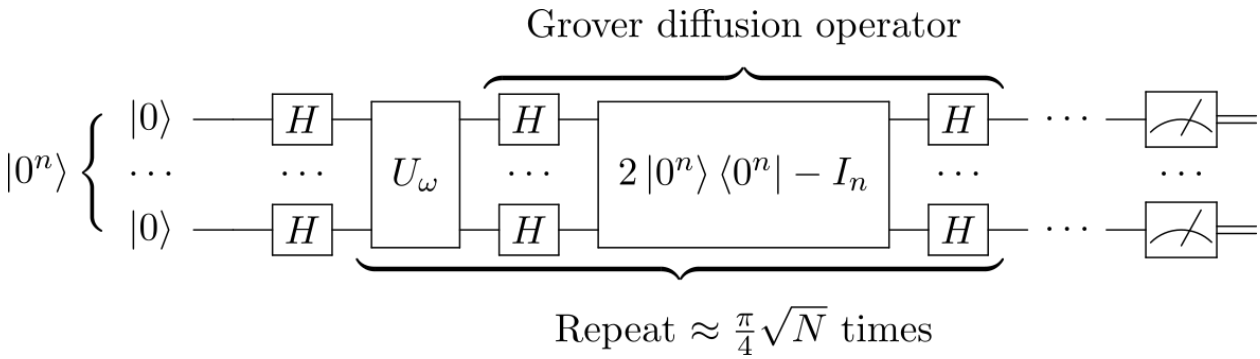

Figure 9.9: The circuit diagram illustrates the implementation of the Grover's search algorithm. The state $|\omega\rangle$ represents the desired target state, while $|s\rangle$ denotes the initial state obtained after applying the Hadamard gate to all the n qubits. This results in a superposition of all n-level states. Reproduced from Fawly, https://upload.wikimedia.org/wikipedia/commons/b/b9/Grover's_algorithm_circuit.svg, accessed on the 15th of May 2023.

the following state of the system

$$|s\rangle = \left(\frac{|0\rangle + |1\rangle}{\sqrt{2}}\right)^{\otimes n} = \frac{1}{\sqrt{2^n}} \sum_{x=0}^{2^n-1} |x\rangle \,. \tag{9.35}$$

After the preliminary step, we apply the oracle unitary operator to the system, which acts as follows:

$$\hat{U}_\omega |x\rangle = (-1)^{f(x)} |x\rangle \,, \tag{9.36}$$

where $f(x)$ equals 0 for all elements except the one we are searching for, denoted by ω. The oracle $\hat{U}_\omega$ can be expressed in terms of quantum states as

$$\hat{U}_\omega = \hat{I} - 2|\omega\rangle\langle\omega| \,. \tag{9.37}$$

This operation is equivalent to a Householder reflection over the state $|s'\rangle$,

$$|s'\rangle = \frac{1}{\sqrt{n-1}} \sum_{x \neq \omega} |x\rangle \tag{9.38}$$

This transformation flips the phase of the target element ω in the computational basis, leaving the other elements unchanged. The resulting state of the system is

$$|s_2\rangle = \frac{1}{\sqrt{2^n}} \left(\sum_{x \neq \omega} |x\rangle - |\omega\rangle \right). \tag{9.39}$$

Then, the Grover diffusion operator $\hat{U}_S$ should be applied,

$$\hat{U}_S = 2|s\rangle\langle s| - \hat{I}. \tag{9.40}$$

To execute the Grover algorithm, it is necessary to iterate the oracle and Grover diffusion operator multiple times, approximately $\frac{\pi}{4}\sqrt{2^n}$ times. Since $\frac{\pi}{4}\sqrt{2^n}$ is not an integer, we apply this sequence

of operators for the closest integer value. This represents the minimum number of steps required for the state to approach the desired target state. The algorithm provides an estimation of the state and not a precise value.
The operator $\hat{U}_S$ is a reflection over the state $|s\rangle$, while $\hat{U}_\omega$ is a reflection over the state $|s'\rangle$. When we apply $\hat{U}_S\hat{U}_\omega$, the state $|s\rangle$ rotates by an angle of $\theta = 2\arcsin\frac{1}{\sqrt{n}}$, as shown in Fig. 9.10.

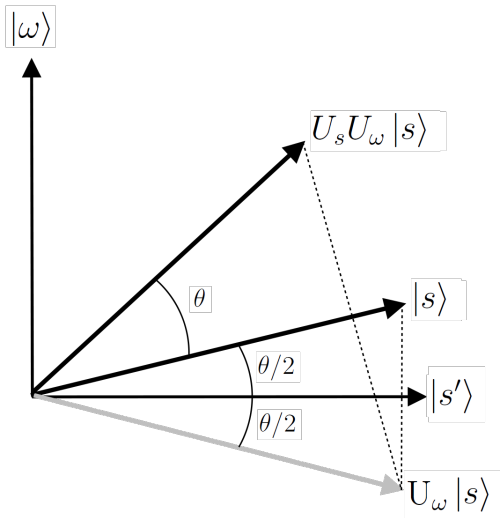

Figure 9.10: Rotation produced by the application of the oracle and the Grover's diffusion. The initial state is $|s\rangle$, the searched state is $|\omega\rangle$. The operators $\hat{U}_\omega$, and $\hat{U}_S$ are detailed on the text as well as the state $|s'\rangle$. Reproduced from Danski14, https://upload.wikimedia.org/wikipedia/commons/1/16/Grovers_algorithm_geometry.png, accessed on the 15th of May 2023.

The angle between the states $|s\rangle$ and $|\omega\rangle$ is $\arccos\frac{1}{\sqrt{2^n}}$, which means that when we apply the operator, we should apply it the integer number that is closest to r,

$$r = \frac{\arccos\frac{1}{\sqrt{2^n}}}{2\arcsin\frac{1}{\sqrt{2^n}}} \approx \frac{\pi}{4}\sqrt{2^n} \tag{9.41}$$

After applying the operator $\hat{U}_S\hat{U}_\omega$ the integer number of times the closest to r, we read out the state, which is then the closest it will be to $|\omega\rangle$. Further applications of the unitary operator will move the state away from $|\omega\rangle$.
Compared to the Deutsch-Jozsa algorithm, this method is less precise, as the state reached after the integer the closest to $\frac{\pi}{4}\sqrt{2^n}$ is the closest to the searched state $|\omega\rangle$, but it is not exactly it. The algorithm only provides an estimation. Additionally, it requires more iterations to solve the problem. In contrast to the Deutsch-Jozsa algorithm, the Grover's algorithm offers greater potential for improvement and optimization.

9.7 Grover's algorithm using modular values

Grover's algorithm is used to search for a specific element in an unstructured list of elements, as discussed in the previous section [195]. The algorithm employs the oracle, described in Eq. 9.36,

and Grover's diffusion operator, described in Eq. 9.40. By using the method outlined in section 9.1, we can find as many elements of the list as needed without knowing the number of elements beforehand. This is known as the Grover's generalized algorithm [195]. To obtain an experimental setup, we should choose the pre- and post-selected state along with the states $|m\rangle$, $|r\rangle$, and $|q\rangle$. The pre- and post-selected state in the three-qubit case are chosen as,

$$\begin{aligned} |\psi_i\rangle &= \frac{1}{\sqrt{8}}(|000\rangle+|010\rangle+|100\rangle+|110\rangle+|001\rangle+|011\rangle+|101\rangle+|111\rangle) \\ |\psi_f\rangle &= \frac{1}{\sqrt{21845}}(-i|000\rangle-2i|010\rangle-4i|001\rangle-8i|011\rangle+16|100\rangle+32|110\rangle+64|101\rangle+128|111\rangle). \end{aligned} \tag{9.42}$$

By measuring the modular value of the oracle $\hat{U}_\omega$ using the pre- and post-selected states described in Eq. 9.42, one can effectively distinguish the selected elements. To ensure distinct modular values for each possible combination of terms, the post-selected state is carefully chosen. This approach allows for a precise determination of both the number and identity of the selected elements, without requiring any prior knowledge.

It is noteworthy that it is possible to verify the distinctness of the modular values for all possible combinations of selected elements. The probability of post-selection in this case is $\frac{45}{136}$. However, one of the challenges of this procedure is that selecting certain states may result in modular values that are close to those obtained when selecting other states. Therefore, to gather sufficient statistical data, the algorithm needs to be repeated multiple times. Additionally, it is necessary to measure both the real and imaginary parts of the modular values. Consequently, two separate algorithms need to be executed. Nevertheless, if a higher level of precision is required beyond what the standard procedure offers, this approach can deliver exact results.

These states can be generalized to n-qubit systems,

$$\begin{aligned} |\psi_i\rangle &= \frac{1}{\sqrt{2^n}}(|0\rangle+|1\rangle)^{\otimes n} \\ |\psi_f\rangle &= \frac{1}{\sqrt{\sum_{k=0}^{2^n-1}2^{2k}}}\Big(\sum_{j=1}^{2^{n-1}}\underbrace{-i2^{j-1}\left|0a_2\ldots a_{(2^{n-1})}\right\rangle_j}_{2^{n-1}\text{ first terms with }n\text{ qubits}}+\Big(\sum_{j=2^{n-1}+1}^{2^n}\underbrace{2^{j-1}\left|1b_2\ldots b_{(2^{n-1})}\right\rangle_j}_{2^{n-1}\text{ last terms with }n\text{ qubits}}. \end{aligned} \tag{9.43}$$

By utilizing these states, we can ensure that every possible combination of elements produces a distinct modular value, allowing us to identify both the number and identity of selected elements without any prior knowledge. This property holds true for any number of qubits. The probability of post-selection is,

$$p=\frac{2^{2^{n+1}}-2^{3\cdot 2^{n-1}}+2}{\sum_{k=1}^{n}2^{2^{n+1}-2}}. \tag{9.44}$$

As the value of n increases, the probability of achieving successful post-selection diminishes rapidly towards zero. The visibility should be evaluated based on the experimental scheme that should be chosen. In this particular scheme, both the real and imaginary parts play a crucial role in the calculations. It is important to emphasize that in this particular scheme, the Grover diffusion operator is unnecessary. This leads to a potential reduction in the number of gates required, which can help mitigate noise in the system as each gate introduces an error in the range of 10^{-3} to 10^{-2}.

Furthermore, this approach enables precise determination of the states. However, it is important to note that a larger number of shots is likely necessary compared to the standard procedure in order to gather sufficient statistical data.

9.8 Quantum phase estimation algorithm

Quantum phase estimation is a captivating problem within the field of quantum computing, essential for implementing various algorithms like Shor's algorithm [188, 196]. The goal is to measure the phase θ that a unitary transformation $\hat{U}$ imparts onto a quantum state, given by $\hat{U}|\psi\rangle = e^{i2\pi\theta}|\psi\rangle$, where $0 \leq \theta \leq 1$, and $|\psi\rangle$ is an eigenstate of the unitary operator.

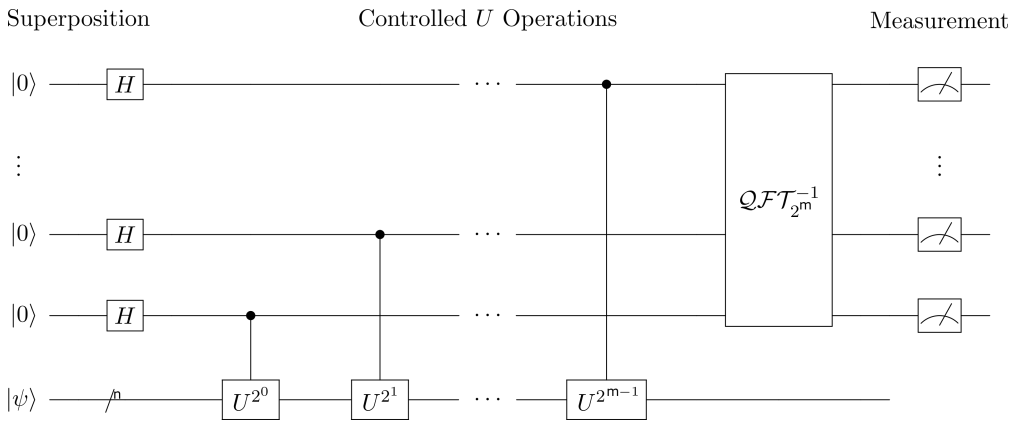

Figure 9.11: The phase estimation circuit begins by preparing an eigenstate of the unitary operator on n qubits, denoted as $|\psi\rangle$, along with m qubits initialized to $|0\rangle$ for readout. H represents a Hadamard gate, while each unitary operator U^{2j} represents a controlled unitary operation. Additionally, the inverse quantum Fourier transform ($\mathcal{QFT}^{-1}_{2^m}$) is applied to the first m qubits. Reproduced from Omrika, https://commons.wikimedia.org/wiki/File:PhaseCircuit.svg, accessed on the 21th of May 2023.

The quantum phase estimation problem is a fundamental task that involves determining the eigenvalue of a specific Hamiltonian and serves as a crucial component in a variety of algorithms. To kickstart the algorithm, we consider an initial state $|\psi\rangle$ consisting of n qubits, along with additional m qubits dedicated to measurement. The precision and accuracy of our results improve as we increase the number of measurement qubits, denoted by m. The initial state can be mathematically represented as follows:

$$|\psi_0\rangle = |0\rangle^{\otimes m}|\psi\rangle\,. \tag{9.45}$$

Subsequently, the first m qubits undergo the application of the Hadamard gate, resulting in the following state:

$$|\psi_1\rangle = \frac{1}{\sqrt{2^m}}(|0\rangle + |1\rangle)^{\otimes m} = \frac{1}{\sqrt{2^m}}\sum_{k=0}^{2^m-1}|k\rangle|\psi\rangle\,. \tag{9.46}$$

Next, a controlled unitary operation is implemented between the state $|\psi\rangle$ and each of the m qubits, as shown in Fig. 9.11. The state after this transformation is

$$|\psi_2\rangle = \frac{1}{\sqrt{2^m}} \sum_{j=0}^{2^m-1} e^{2i\pi j\theta} |j\rangle |\psi\rangle . \tag{9.47}$$

The next step in the process entails applying the inverse quantum Fourier transform to the m measuring qubits, resulting in the following state:

$$|\psi_3\rangle = \frac{1}{2^m} \left(\sum_{x=0}^{2^m-1} \sum_{k=0}^{2^m-1} e^{-\frac{2\pi ik}{2^m}(x-2^m\theta)} |x\rangle \right) |\psi\rangle . \tag{9.48}$$

By performing measurements on the m measuring qubits in the computational basis, the probability to obtain each of the state $|x\rangle$ is

$$P = \left| \frac{1}{2^m} \sum_{k=0}^{2^m-1} e^{-\frac{2\pi ik}{2^m}(x-2^m\theta)} \right|^2 . \tag{9.49}$$

We can reframe the probability expression by introducing a new notation: $2^m\theta = a + 2^m\delta$, where a represents the nearest integer to $2^m\theta$, and $0 \leq |2^m\delta| \leq \frac{1}{2}$. Subsequently, we proceed to measure the probability of obtaining the specific output a in the computational basis.

$$P(a) = \left| \frac{1}{2^m} \sum_{k=0}^{2^m-1} e^{-\frac{2\pi ik}{2^m}(x-a)} e^{2\pi i\delta k} \right|^2 . \tag{9.50}$$

Consequently, the probability $P(a)$ equals 1 if $2^m\theta = a$. Otherwise, the algorithm delivers the correct result with a probability of at least $P(a) \geq \frac{4}{\pi^2} \approx 0.405$. In most cases, after executing the algorithm multiple times, the outcome lie between two values, specifically the two outputs with the highest probabilities. Increasing the value of m amplifies the likelihood of obtaining an intermediate output that satisfies the condition $2^m\theta = a$.

9.9 Quantum phase estimation using modular values

The quantum phase estimation problem can be effectively addressed by employing the modular value-based procedure outlined before. In contrast to the standard approach, utilizing modular values allows theoretically for precise attainment of the phase. Moreover, it enables setting the probability of post-selection to unity while significantly reducing the number of required qubits. However, it should be noted that considering both the real and imaginary parts is crucial, necessitating the implementation of two separate algorithms to calculate the argument of the modular value.

Now, let us delve into a comprehensive examination of the proposed scheme. The problem can be directly resolved by leveraging the argument of the modular value associated with the operator $\hat{U}$ as

$$U_m = \frac{\langle \psi_f | \hat{U} | \psi_i \rangle}{\langle \psi_f | \psi_i \rangle} = e^{i2\pi\theta} = i \sin 2\pi\theta + \cos 2\pi\theta . \tag{9.51}$$

By measuring the argument of the modular value, we gain direct access to the phase that needs to be measured. The argument of the modular value is

$$\arg(U_m) = \text{atan2}\left(\frac{\sin 2\pi\theta}{\cos 2\pi\theta}\right) = \arg\left(e^{i2\pi\theta}\right) = 2\pi\theta, \tag{9.52}$$

where atan2 is the 2-argument arctangent.
As one can observe, in this particular case, the post-selected states become irrelevant since the scalar products cancel out both in the numerator and denominator. Consequently, we have the flexibility to choose the same pre- and post-selected states, leading to a post-selection probability of unity at the first order. Thus, the pre- and post-selected state would be as follows:

$$|\psi_i\rangle = |\psi_f\rangle = |\psi\rangle, \tag{9.53}$$

with $|\psi\rangle$ the considered eigenstate of the unitary operator.
Two different routines should be run. A first one to obtain the value of the imaginary part of the modular value, by setting $\vec{m}\cdot\vec{q} = 0$ from Eq. 9.9, and a second one setting $\vec{m}\times\vec{q} = 0$ to obtain the real part. Once both parts have been accessed, the phase can be easily calculated by obtaining the argument of the modular value as in Eq. 9.52.
In this scenario, the probability of post-selection is not a concern since the pre- and post-selected states are identical. However, to extract the real and imaginary parts of the modular value, we rely on averaging, which necessitates multiple measurements to gain sufficient confidence in the result. Nevertheless, this is also the case with the conventional quantum algorithm. The significant advantage of utilizing modular values is the substantial reduction in the number of required qubits. Only $n+1$ qubits are necessary, in contrast to the common algorithm that demands $n+m$ qubits. Furthermore, this modular value-based algorithm could deliver an accurate result for the phase.

9.10 Conclusions and perspectives

We have introduced a novel approach for executing quantum algorithms using modular values. This technique is applicable to various quantum algorithms that involve an oracle. An additional qubit is needed to read out the modular value result. The number of shots required depends on the post-selection probability and visibility. This procedure can be applied to different experimental setups such as quantum computers or optical systems.
This chapter presents a method for implementing algorithms using modular values in quantum computers. Despite the considerable noise in the Quito IBM quantum computer, with errors on the order of 10^{-3} for quantum gates and 10^{-2} for measuring, we have achieved initial results for the Deutsch-Jozsa problem using modular values. No advantages were observed in that particular case. It requires a significantly larger number of shots compared to the standard algorithm, where only one shot is typically sufficient. While there are various ways to potentially improve the algorithm, such as selecting appropriate pre- and post-selected states, it is unlikely to yield any significant advantages in this scenario. The probability of post-selection consistently hinders the efficiency of the modular value-based algorithm in reaching the correct result expeditiously.
In specific cases, the modular value approach has the potential to reduce the overall number of gates required, and, thus, to potentially mitigate noise, considering that each applied gate introduces a certain level of error to the final result. For instance, in the context of Grover's problem,

the Grover diffusion operator becomes unnecessary when modular values are employed. However, it is important to take into account the gates involved in creating the pre- and post-selected states when assessing the gate count. Moreover, the utilization of modular values in quantum algorithms potentially allows for the precise determination of the desired state, whereas conventional Grover's algorithm only provide estimations. This could represent a notable advancement, particularly in cases where exact results are required. The application of modular values is not limited to a specific algorithm and can be extended to other estimation algorithms as well, offering the potential for enhanced accuracy and precision in quantum computations.

However, it is essential to acknowledge that the modular value approach may necessitate a larger number of measurement shots compared to the standard quantum algorithm. This is primarily due to factors such as the post-selection probability and the visibility. To differentiate between distinct modular values effectively, it is crucial that they are as far apart from each other as possible. Furthermore, the practical implementation of the modular value-based Grover's algorithm using quantum gates still requires further development and refinement. In particular, the challenge lies in creating a non-separable post-selected state, which adds considerable complexity to the circuit design. As a result, calculating the circuit's exact configuration becomes significantly more challenging.

Nonetheless, the most promising application of modular-based algorithms resides in the estimation of the quantum phase. In this particular scenario, the probability of post-selection does not pose a problem since it is feasible to choose identical pre- and post-selected states, thereby increasing the probability of post-selection to unity at first order. Additionally, the number of qubits needed is reduced, as the original algorithm necessitates $n+m$ qubits while the modular-based procedure only requires $n+1$ qubits. Moreover, it provides the exact value of the phase, whereas the conventional algorithm only provides an estimate. The main drawback is the need to run two separate algorithms, one to measure the real part and one to measure the imaginary part. However, overall, this modular-based approach appears to be a highly promising alternative to the commonly used procedures.

The next step involves developing the concrete algorithm for execution on a quantum computer. A comparison between the standard approach and this new approach is necessary to validate its advantages.

In general, the modular value-based approach demonstrates significant potential as a more precise alternative for various algorithms and could facilitate the development of new ones. However, this potential has to be confirmed quantitatively.

In general, we have not yet found any experimental computational advantage over conventional quantum algorithm. Several questions need to be addressed to explore this approach further. First, we need to study all the information provided by the measurements in the computational basis to reduce the number of shots required. Post-selection in the different states of the computational basis simultaneously could be a possible approach, as we directly obtain the information when running an algorithm on a quantum computer. Additionally, we need to investigate the selection of pre- and post-selected states to increase the algorithm's efficiency, specifically by examining the states' separability. As we have seen, non-separable states provide a larger parameter space. However, these sates are much more complicated to create using the common quantum gates. Separable states can be created using an individual unitary transformation in each qubit. This approach is not possible for non-separable states. From a computational perspective, we need to improve our ability to create non-separable states using standard gates.

Finally, modular values are expected to yield good results in algorithms that search for small quantities due to their amplification capability. For example, we could differentiate between two almost identical gates. Even though, in that case the probability of post-selection would be very small, the precision that one can reach using a modular value-based approach could be better than using other standard approaches, at least in the presence of technical limitations. In the counterpart, the required number of repetitions of the algorithm could be very large.
In summary, the global phase estimation problem presents several notable advantages. It is imperative to continue further research in this direction, as it holds the potential for significant progress and may pave the way for discovering other problems where the modular value-based approach can offer advantages in different aspects. Exploring the applicability of modular values in various contexts could yield valuable insights and advancements in the field of quantum computing.

Chapter 10

Conclusions and perspectives

In this thesis, we undertook a comprehensive analysis of the geometrical and mathematical properties of post-selected measurements, as well as their applications such as weak values in open quantum systems and the use of modular values in quantum computing. Our research focused on the geometrical properties of the argument of weak values and their non-normal properties, as well as the relationship of non-normality with the modulus of the weak value. By re-analysing weak values as the expectation value of the observable in a Krein space, we were able to establish a link between weak values and a paraconsistent and paracomplete logic. Furthermore, we investigated the impact of dissipation between the weak interaction and post-selection on weak values, and discovered an approach to obtain anomalous weak values, which fall outside the range of the observable's spectrum, at infinite dissipation time. Lastly, we presented a novel approach for implementing algorithms using modular values. Overall, our study offers valuable insights into the fundamental properties of post-selected measurements and their applications in quantum systems.
In the first part of the thesis, we delved into the geometrical properties of weak values. Rather than the conventional approach of examining the real and imaginary parts, we concentrated on the polar description of these quantities. Specifically, we explored the argument of the weak value of an N-level projector, which reveals a geometric phase linked to the symplectic area of the triangle formed by the geodesics connecting the three-vectors representing the initial state, the projector state, and the post-selected state in the complex projective space $\mathbb{C}\mathrm{P}^{N-1}$. When reducing the analysis to the two-level case, the symplectic area and the common Riemannian area are equal. Since $\mathbb{C}\mathrm{P}^{N-1}$ can be bijectively mapped to the surface of a unit sphere, the Bloch sphere, the symplectic area translates into the solid angle subtended by the triangle spanned by the three quantum states on the sphere. We also established that the weak value of any discrete N-level observable is proportional to that of a specific projector linked to the state resulting from the normalized application of the observable to the pre-selected state. This discovery enabled us to associate the weak value of any N-level observable with a geometric phase and express it in terms of the symplectic area of the triangle formed by the geodesics connecting the initial state, the state arising from the normalized application of the observable to the pre-selected state, and the post-selected state. Although it is generally not easy to interpret the new vector arising from the application of the observable to the initial state, the two-level case provides an insightful illustration. Here, the vector lies on the geodesic (or great circle) connecting the pre-selected state and its mirror image over the projector state.

As we showed, it is possible to provide a full geometrical description of the argument of weak values in the complex projective space. Nonetheless, this description is not easily visualizable. To address this, we can use the Majorana description to map the problem onto the Bloch sphere. By doing this, we can express the argument of weak values of any N-level observable as the sum of $N-1$ arguments of weak values of qubit projectors. Each of these arguments is associated with the solid angle on the Bloch sphere of the triangle formed by the pre-selected state, the projector, and the post-selected state. A remarkable property of weak values is that they remain invariant under the application of unitary operators. This allows us to reduce the weak value of any N-level observable to a three-level problem. By leveraging this property, we can express the argument of weak values of any N-level observable in terms of two solid angles on the Bloch sphere.

We have successfully developed a comprehensive geometric framework for understanding the argument of weak values of discrete observables. Moving forward, there are two main areas of inquiry to explore. Firstly, the current study has exclusively focused on pure pre- and post-selected states. Generalizing this geometrical description to mixed states would be highly desirable. However, as we can no longer work with complex projective spaces, this requires a new approach. Secondly, investigating weak values in continuous space would be an intriguing avenue to pursue. This approach would enable us to study observables related to essential properties such as position or momentum. Additionally, studying the geometrical properties of the argument of weak values in the quantum phase space could offer new insights into the topic.

In the second part of our analysis, we leveraged various properties of weak values by re-expressing them in terms of expectation values. Firstly, we demonstrated that the weak value of any observable can be expressed as the expectation value of a non-normal operator. While all non-normal operators are non-Hermitian, some non-Hermitian operators can still be normal. Therefore, non-normality is a more stringent condition than non-Hermiticity. We established that in order to obtain a weak value that differs from an eigenvalue of the original observable, the corresponding operator must necessarily be non-normal. This implies that post-selecting changes the expectation value of a Hermitian operator to that of a non-Hermitian one. Non-Hermitian Hamiltonians describe the evolution of systems that undergo energy exchanges. This highlights the relevance of post-selection, which can also lead to energy exchanges in the system. To gain further insight, we compared the modulus of the weak value with the Henrici departure from normality, a quantity that measures the deviation of a matrix from normality. Our analysis revealed a striking correlation between these two parameters, which held across various pure pre- and post-selected states in the strong amplification regime. We extended our investigation to a family of observables and found that the modulus of the weak value exhibited an intermediate behavior with respect to the Henrici departure from normality of the two possible definitions of the non-normal operator. We also determined that the maximum modulus of the weak value in the anomalous regime was achieved at the arithmetic average of the point of the maximum Henrici departure from normality of both operators. Furthermore, we observed that the maximum value was reached when both matrices shared the same nilpotent point parameter value. This implies that all eigenvalues become zero at the same values of the angles associated with the observable.

The presence of non-normality has been observed to be closely linked with phase transitions across various domains of physics. Moving forward, our research aims to investigate weak measurements in diverse settings and identify phase transitions in the properties of the ancilla. An initial approach, stemming from the collaborative effort that initiated this study, could involve examining weak measurements within quantum networks.

Looking at weak values from another angle, we can express them as the expectation values of observables, but employing a pseudo-projector instead of the usual projector. This pseudo-projector is idempotent, but not Hermitian; it is actually η-Hermitian, which means Hermitian with respect to the η metric. Representing the weak value this way allows us to obtain a metric that characterizes an indefinite inner product space, also known as Krein space. In this newly defined Krein space, the weak value corresponds to the expectation value of the observable in the pre-selected state. Notably, this space may contain subspaces whose intersection with their η-orthogonal complements is not simply the zero vector. In non-classical logics, the orthogonal complement can be connected to negation. As a result, the logic of this space naturally incorporates paraconsistency.
In classical logics, the intersection of a proposition and its negation is always false, the probability that a bridge exists and does not exist simultaneously is zero. However, in the context of quantum physics, such situations can seem more natural. Schrödinger's cat, for instance, can be both dead and alive simultaneously. Similarly, in Krein spaces, subspaces can exist whose disjunction with their orthogonal complements does not cover the entire space. This property defies our intuition; in classical logic, the probability that a bridge exists or does not exist should be one, not something different. The non-classical logic is paracomplete. These findings represent a significant breakthrough in our understanding of the fundamental principles of quantum physics. Typically, the logic underlying the behavior of quantum systems is analyzed using either paraconsistent or paracomplete logic frameworks. In this study, we merge both approaches by leveraging the unique features of the Krein space. Moreover, we apply our combined approach to the investigation of the three-box paradox with pre- and post-selection, resulting in the identification of a logic with inherent contradictions from its definition. Our analysis provides valuable insights and opens up new avenues for future research in this field.
Our findings highlight the significant implications of the paraconsistent and paracomplete logic that arises from weak values. Moving forward, it is essential to explore the connections between this logic and other non-classical properties of weak values, such as contextuality, in more detail. Additionally, we need to extend our investigation to post-selected measurements beyond the realm of weak measurements, taking a consistent and rigorous approach. This will help us gain deeper insights into the underlying principles of quantum mechanics and provide novel perspectives on various interpretations of quantum physics, including the hidden variable and Bohmian interpretations. By pursuing these avenues of research, we can enhance our understanding of the foundations of quantum physics and pave the way for future advancements in this exciting field.
Quantum systems are never fully isolated and always interact with their surrounding environment, including during the weak measurement process. In our research, we examined weak measurements under dissipation, focusing specifically on weak measurements with dissipation between the weak interaction and the post-selection. This moment of dissipation is the most critical as it can have the greatest impact. If dissipation occurs before the weak interaction, it only affects the initial state, and with enough information, we can still obtain amplifying weak values by choosing an appropriate post-selected state, unless the state after the dissipation process is completely mixed. Nevertheless, if dissipation occurs after the weak interaction, the weak value at infinite dissipation time tends to converge to the expectation value of the observable on the pre-selected state, regardless of the post-selected state. As a result, these two types of dissipation should be treated separately.
In our study of degenerate ground states, we discovered that amplifying weak values can still occur even at infinite dissipation time. This surprising result can be explained by the fact that a degener-

ate ground state can still exhibit coherences, which are essential for obtaining weak values.
Conversely, at very short dissipation times, we can exploit the amplifying properties of weak values to extract information on the dissipative evolution of the system. For instance, we can determine the dissipation rate and distinguish between Markovian and non-Markovian evolutions. This can be particularly useful for experimentalists working with systems where the available dissipation path is limited.
Exploring weak values under dissipation in various specific systems could yield intriguing insights and reveal additional properties of the system. Another avenue for investigation would be to examine the geometrical interpretation of the argument in this case and observe how it is affected. However, to undertake this, it is necessary to extend previous geometrical work to mixed quantum states. Additionally, from a technical standpoint, it would be valuable to experimentally implement our proposal and compare its effectiveness to that of more conventional approaches.
After exploring weak values, we turned our attention to the use of modular values in implementing quantum algorithms. Our proposed method involves employing modular values to perform a direct evaluation of the oracle, and exploiting the amplifying and complex properties of modular values to execute the algorithm. By utilizing pre- and post-selection, numerous degrees of freedom are introduced, which can be employed to improve the efficiency of the algorithm. We then applied this method to three well-known algorithms: the Deutsh-Jozsa algorithm, the Grover's algorithm, and the quantum phase estimation protocol. In the first one, we utilized the complex behavior of modular values to distinguish between constant and balanced oracles, enabling the algorithm to be implemented on any platform, including an optics laboratory. We tested this approach on the IBM quantum computer for two qubits, but the results were not superior to those obtained through conventional quantum algorithms. However, there is still much potential for improving the method, such as by considering post-selection across all the computational bases simultaneously.
We also theoretically applied our method to the Grover's algorithm, which involves finding a specific object in a list. We achieved this by carefully selecting the pre- and post-measurement states, which enabled us to identify the desired object based on the result of the modular value of the oracle. Notably, this approach obviates the need for the Grover's diffusion operator, potentially offering an advantage by reducing the number of gates required and, consequently, the noise introduced.
Lastly, we devised a protocol for estimating the quantum global phase using modular values. Notably, our protocol requires fewer qubits compared to the standard algorithm, while maintaining a post-selection probability of unity. Moreover, it has the potential to yield precise phase values, unlike the conventional algorithm, which can only provide estimations. It is worth mentioning that our protocol necessitates running two subroutines for measuring both the real and imaginary components of the modular value. Given these advantages, it is highly promising and warrants implementation on the IBM quantum computer to validate its advantages.
While our approach did not prove experimentally advantageous over conventional quantum methods, we introduced a novel method for addressing quantum algorithms that can be applied broadly. There are numerous opportunities to improve the method's efficiency, such as by exploiting the amplifying properties of modular values. To that end, we could explore differentiating between quantum gates that are nearly identical.
This thesis has explored a variety of theoretical properties of post-selected measurements and their applications. Moving forward, numerous additional fundamental properties, particularly related to quantum foundations, could be explored. As more and more applications arise each year for quan-

tum weak measurements, particularly due to their amplifying nature, we believe that our work has paved the way for new applications and fundamental studies in the field.

Appendix A

Density operator

A density operator, denoted as $\hat{\rho}$, characterizes a classical mixture of quantum states and should not be confused with a quantum superposition of states. Mixed states arise from the interaction between a quantum system and its environment, through decoherence and measurement.
In contrast to a quantum superposition, which is expressed as a linear combination of quantum states, a mixed state is mathematically described as a linear combination of projectors, as shown in Eq. A.1,

$$\hat{\rho} = \sum_{i=1}^{N} \alpha_i \hat{\Pi}_i, \tag{A.1}$$

where α_i corresponds to the probability of having the pure state projector $\hat{\Pi}_i$ in the mixture, $\sum_{i=1}^{N} \alpha_i = 1$, and $\alpha_i > 0$. Each quantum pure projector, $\hat{\Pi}_i$, satisfies the condition $\hat{\Pi}_i^2 = \hat{\Pi}_i$, indicating a pure state. However, a density operator does not fulfill this condition since it represents a mixed state.
The purity of a density operator, denoted as p, can be computed as the trace of the squared density operator, as shown in Eq. A.2,

$$p = \mathrm{Tr}\left[\hat{\rho}^2\right]. \tag{A.2}$$

The purity value, ranging between 1 (representing a pure state) and $\frac{1}{n}$ (representing a completely mixed state), provides a quantification of the purity of the system. A completely mixed state can be represented by the normalized identity matrix, $\frac{1}{n}\hat{I}$.
For two-level systems, a mixed state can be visualized in the Bloch ball, considering the volume inside the sphere surface (Bloch sphere). The closer the state is to the surface, the purer it is, while a state closer to the center indicates greater mixing. The radius of the state on the Bloch sphere also serves as a measure of purity.
Considering an observable $\hat{O}$, the expectation value of the observable on a mixed state can be calculated following the formula:

$$\langle O \rangle = \mathrm{Tr}\left[\hat{\rho}\hat{O}\right] = \mathrm{Tr}\left[\sum_{i=1}^{N} \alpha_i \hat{\Pi}_i \hat{O}\right] = \sum_{i=1}^{N} \alpha_i \mathrm{Tr}\left[|\psi_i\rangle\langle\psi_i|\hat{O}\right] = \sum_{i=1}^{N} \alpha_i \langle\psi_i|\hat{O}|\psi_i\rangle, \tag{A.3}$$

where the expression of the pure projector $\hat{\Pi}_i = |\psi_i\rangle\langle\psi_i|$ has been employed. Eq. A.3 lucidly illustrates the classical mixture of expectation values of the different quantum pure states that composed the mixed state, $\hat{\rho}$.

Appendix B

Gell-Mann matrices

The order of the Gell-Mann matrices used in this thesis is,

$$\begin{aligned}
\hat{\lambda}_1 &= \begin{pmatrix} 0 & 1 & 0 \\ 1 & 0 & 0 \\ 0 & 0 & 0 \end{pmatrix} \qquad \hat{\lambda}_2 = \begin{pmatrix} 0 & -i & 0 \\ i & 0 & 0 \\ 0 & 0 & 0 \end{pmatrix} \qquad \hat{\lambda}_3 = \begin{pmatrix} 1 & 0 & 0 \\ 0 & -1 & 0 \\ 0 & 0 & 0 \end{pmatrix} \\
\hat{\lambda}_4 &= \begin{pmatrix} 0 & 0 & 1 \\ 0 & 0 & 0 \\ 1 & 0 & 0 \end{pmatrix} \qquad \hat{\lambda}_5 = \begin{pmatrix} 0 & 0 & -i \\ 0 & 0 & 0 \\ i & 0 & 0 \end{pmatrix} \qquad \hat{\lambda}_6 = \begin{pmatrix} 0 & 0 & 0 \\ 0 & 0 & 1 \\ 0 & 1 & 0 \end{pmatrix} \\
\hat{\lambda}_7 &= \begin{pmatrix} 0 & 0 & 0 \\ 0 & 0 & -i \\ 0 & i & 0 \end{pmatrix} \qquad \hat{\lambda}_8 = \frac{1}{\sqrt{3}} \begin{pmatrix} 1 & 0 & 0 \\ 0 & 1 & 0 \\ 0 & 0 & -2 \end{pmatrix}
\end{aligned} \tag{B.1}$$

Appendix C

Conventions for star product and projectors

From the symmetric constants d_{abc} of SU(N), we can construct a symmetric product called the star product. Given two (N^2-1)-dimensional vectors, the $\star$ product produces a vector with components $(\vec{\alpha}\star\vec{\beta})_c = c_s \sum_{ab} d_{abc}\alpha_a\beta_b$, where c_s is a proportionality constant. It would be convenient to simply set $c_s = 1$ (as done for the definition of the anti-symmetric wedge product $(\vec{\alpha}\wedge\vec{\beta})_c = \sum_{ab} f_{abc}\alpha_a\beta_b$, which is built on the structure constants). However, the original definition of the star product in the literature [84, 85] used another convention: the star product identified a proper quantum state from $\mathbb{C}P^2$ on the S^7 sphere. In the following, we explain thus how we generalized the star product from SU(3) to SU(N), based on this earlier choice. We also explain our normalization convention for projectors, as they are related.

A general projector $\hat{P}$ in $\mathbb{C}^N \times \mathbb{C}^N$ acting on states in $\mathbb{C}^N$ is defined by the relation $\hat{P}^2 = \hat{P}$. In addition, its trace is an integer number that is lower or equal to the dimension N: $\mathrm{Tr}\,\hat{P} = k$, with $1 \leq k \leq N$ representing the dimension of the projector subspace (essentially the degeneracy of the eigenvalue 1). We pose $\hat{P} = \frac{k}{N}\hat{I}_N + c_p\,\vec{\beta}\cdot\hat{\vec{L}}$ to meet the trace condition. The positive constant

$$c_p = \sqrt{\frac{k(N-k)}{2N}} \tag{C.1}$$

ensures that $\vec{\beta}$ is always a normalized vector ($\vec{\beta}\cdot\vec{\beta} = 1$) on the S^{N^2-2} unit sphere. Its value originates from the projector condition

$$\hat{P}^2 = (\frac{k^2}{N^2} + \frac{2}{N}c_p^2)\hat{I}_N + \frac{2k}{N}c_p\;\vec{\beta}\cdot\hat{\vec{L}} + c_p^2\sum_{abc} d_{abc}\beta_a\beta_b\hat{L}_c = \frac{k}{N}\hat{I}_N + c_p\,\vec{\beta}\cdot\hat{\vec{L}}, \tag{C.2}$$

where we used Eq. G.2 to expand the SU(N) generator square $(\vec{n}\cdot\hat{\vec{L}})^2$. Additionaly, Eq. C.2 constraints the vector $\vec{\beta}$ through the star product

$$\frac{1}{c_s}(\vec{\beta}\star\vec{\beta})_c = \sum_{ab} d_{abc}\beta_a\beta_b = (1-\frac{2k}{N})\frac{1}{c_p}\beta_c, \tag{C.3}$$

In the literature [84, 85], the star product was defined in SU(3) by imposing that this condition becomes $\vec{\beta}\star\vec{\beta} = \vec{\beta}$ for projectors on pure states (case $k = 1$). Therefore, imposing $\vec{\beta}\star\vec{\beta} = \vec{\beta}$ for

pure states, we find the value of the constant c_s in SU(N):

$$c_s = \frac{N c_p}{N-2} = \frac{1}{N-2}\sqrt{\frac{N(N-1)}{2}}, \tag{C.4}$$

which thus defines the star product in SU(N) [90]. As a result, an arbitrary projector takes the form

$$\hat{P} = \frac{k}{N}\hat{I}_N + \sqrt{\frac{k(N-k)}{2N}}\,\vec{\beta}\cdot\hat{\vec{L}}, \tag{C.5}$$

with the accompanying star product constraint resulting from Eq. C.3:

$$\vec{\beta}\star\vec{\beta} = \frac{N-2k}{N-2}\sqrt{\frac{N-1}{k(N-k)}}\,\vec{\beta}. \tag{C.6}$$

Note that, only when $k=1$, does this projector correspond to a quantum state from $\mathbb{C}\mathrm{P}^{N-1}$. For example, a projector on an $(N-1)$-dimensional subspace obeys $\vec{\beta}\star\vec{\beta} = -\vec{\beta}$; it is the opposite of the vector associated with the projection on the complementary 1-dimensional subspace (this one is a quantum state).

In summary, our convention sets the constant c_p defining an arbitrary projector so that we always work with vectors belonging to hyperspheres of unit radius when using the operators $\hat{\vec{L}}$ as generators of SU(N) [84, 85, 87, 88, 90]. Then, in order to define the star product, we follow the literature convention that the set of vectors representing pure quantum states is equivalent to the vectors invariant under the star product (in the sense of $\vec{r}\star\vec{r} = \vec{r}$) [84, 85, 87, 88, 90]. We note that, when working with generalized Bloch spheres, some authors prefer to set $c_p = 1$ and deal with unnormalized vectors [197, 198]. This would be inconvenient for us, as many expressions linked to weak values are invariant under permutations of the related vectors, some of which would be normalized and others not. Managing the vector normalization status complicates geometric descriptions as well. On the other hand, if the star product were defined initially with the constant $c_s = 1$, the constant c_s would not appear when the product of two generators is expressed in terms of the star product, such as in the weak value formula Eq. F.13. Were it the case, the projector condition for pure state would have been $\vec{r}\star\vec{r} = \frac{1}{c_s}\vec{r}$. A few authors working with unnormalized vectors chose to redefine to the star product with $c_s = 1$ [89, 91].

Appendix D

Properties of states on S^{N^2-2} and the $\star$ and $\wedge$ products

In this section, we review a few properties of the state representation on the generalized Bloch sphere, in connection to the $\star$ and $\wedge$ products of SU(N), as we believe this formalism is still unfamiliar to many. Our goal is to provide a glimpse on key aspects of the geometry and highlight information relevant to interpreting the various contributions to weak value formulas.
First of all, we consider the conditions defining an orthonormal basis of $\mathbb{C}\mathrm{P}^{N-1}$: the projector orthogonality relationship $\hat{\tilde{\Pi}}_i\hat{\tilde{\Pi}}_j = \delta_{ij}\hat{\tilde{\Pi}}_i$, as well as the resolution of the identity $\sum_{i=1}^{N}\hat{\Pi}_i = \hat{I}_N$. For orthogonal states, the former impose that the angles between the vectors are given by $\vec{n}_i\cdot\vec{n}_j = -\frac{1}{N-1}$ Eq. F.9. In addition, the later results in $\sum_i \vec{n}_i = 0$. Thus, the vectors are all placed very symmetrically. For SU(2), these conditions show that vectors associated with orthogonal states are opposite, a well-known property of the standard Bloch sphere. For SU(3), the three vectors arising from a state basis all lie in a plane, with angles of 120° between them: their extremities form an equilateral triangle. For SU(4), the vectors build a tetrahedron. In larger dimensions, for SU(N), the arrangements remain extremely symmetric in a similar fashion, with the N vectors residing in a subspace of $N-1$ dimensions. We see thus that orthogonal states do not correspond to orthogonal vectors in the Euclidean sense. Actually, an orthogonal vector $\vec{r}$ verifying $\vec{r}\cdot\vec{n}_i = 0$ for all states of a given basis, obeys $\mathrm{Tr}\,(\hat{\Pi}_r\hat{\Pi}_i) = \frac{1}{N}$ Eq. F.9. It corresponds to a state with maximal relative uncertainty with respect to the measurement basis (such as between states belonging to two different mutually unbiased bases). Orthogonal quantum states verify the following two additional relationships for their associated vectors: their wedge product is nul $\vec{m}\wedge\vec{n} = 0$ and their star product is located on the angle bissector of the two vectors $\vec{m}\star\vec{n} = -\frac{1}{N-2}(\vec{m}+\vec{n})$. In the particular case of SU(3), the later results in the third basis vector being given by the star product of the other two ($\vec{n}_1\star\vec{n}_2 = \vec{n}_3$). The symmetric star product is not associative. The star product of an arbitrary normalized vector $\vec{\alpha}$ does not generally produce a normalized vector ($\|\vec{\alpha}\star\vec{\alpha}\| \neq 1$), with the exception of SU(3), where $\vec{\alpha}\star\vec{\alpha}$ always remains on S^7. Of course, all vectors associated with pure states also remain on S^{N^2-2} in this manner, following the choice set by the definition of the $\star$ product. As the star product defines the condition for a vector to represent a state ($\vec{r}\star\vec{r} = \vec{r}$), we consider the particular case of the star product between two vectors associated with states. In that particular case, we have $(\vec{q}\star\vec{r})\cdot\vec{q} = (\vec{q}\star\vec{r})\cdot\vec{r} = \vec{q}\cdot\vec{r}$ (thanks to the fully symmetric nature of the product). Therefore, the star product of two projectors lies in the median hyperplane lying between $\vec{q}$ and $\vec{r}$, which is orthogonal

to $\vec{q}-\vec{r}$, as could be expected from the symmetric properties of the product. In general, the star product of two vectors $\vec{q}$, $\vec{r}$ does not remain in the plane spanned by the two vectors (contrary to what we observed for two orthogonal states). Neither does it represent a state in general. We note that, operationally, an observable involving the vector $\vec{\alpha}\star\vec{\alpha}$ can be constructed from the square of an operator $(\vec{\alpha}\cdot\hat{\vec{L}})^2 = \frac{2}{N}\hat{I}_N + \frac{1}{c_s}[(\vec{\alpha}\star\vec{\alpha})\cdot\hat{\vec{L}}]$ Eq. F.6, so that this vector contributes to quantum fluctuations (see section 4.8).

The anti-symmetric wedge product is not associative. It produces a vector orthogonal to the initial ones: $\vec{\alpha}\wedge\vec{\alpha} = 0$ and, therefore, $\vec{\alpha}\wedge\vec{\beta}\cdot\vec{\alpha} = \vec{\alpha}\wedge\vec{\beta}\cdot\vec{\beta} = 0$. However, due to the large number of dimensions involved, the wedge product selects an orthogonal direction amongst many available (contrary to the cross-product in three dimensions, for which the orthogonal direction to two non-parallel vectors is unique). The wedge product is intimately associated with the commutator Eq. F.7. From the Baker-Campbell-Hausdorff formula, the wedge product gives the unitary operator associated with the non-commutativity of consecutive unitary transformations, such as the generators of rotations: $e^{-ig\vec{\beta}\cdot\hat{\vec{L}}}e^{-ig\vec{\alpha}\cdot\hat{\vec{L}}}e^{ig\vec{\beta}\cdot\hat{\vec{L}}}e^{ig\vec{\alpha}\cdot\hat{\vec{L}}} \approx e^{ig^2(\vec{\alpha}\wedge\vec{\beta})\cdot\hat{\vec{L}}}$. From a practical point of view, this allows to construct an observable linked to the wedge product. This product gives thus also the direction of the effective transformation of an observable undergoing a small unitary transformation (from Eq. F.7) as $e^{ig\hat{A}}\hat{B}e^{-ig\hat{A}} \approx \hat{B} + ig[\hat{A},\hat{B}]$).

The wedge and star products between two vectors representing states are orthogonal in the following sense: $(\vec{q}\star\vec{r})\cdot(\vec{q}\wedge\vec{r}) = 0$ (actually, we also checked up to SU(6) using brute force calculation with a computer algebra system that this is true for any two vectors). Other relationships connect the star and wedge products in the case of pure states. By imposing that a projector $\hat{\Pi}_r$ remains a projector after a unitary transformation with generator $\vec{\alpha}\cdot\hat{\vec{L}}$, to first order, we obtain $\vec{\alpha}\wedge\vec{r} = 2\vec{r}\star(\vec{\alpha}\wedge\vec{r})$ (and more complex relationships can be deduced from second-order contributions).

Appendix E

$\mathbb{C}P^2$ representation on S^7

Considering an arbitrary state $|\psi\rangle$, the coordinates on the corresponding hypersphere are obtained by $\mathrm{Tr}\hat{\Pi}_\psi\hat{\vec{L}}$. On S^7, the state $|\psi\rangle = \left(n_1 e^{i\chi_1}, n_2 e^{i\chi_2}, n_3 e^{i\chi_3}\right)^T$ would thus become the gauge-invariant vector

$$\begin{aligned}[n_1 n_2 \cos(\chi_1-\chi_2), -n_1 n_2 \sin(\chi_1-\chi_2), \frac{1}{2}(n_1^2-n_2^2), n_1 n_3 \cos(\chi_1-\chi_3),\\ -n_1 n_3 \sin(\chi_1-\chi_3), n_2 n_3 \cos(\chi_2-\chi_3), -n_2 n_3 \sin(\chi_2-\chi_3),\\ \frac{1}{2\sqrt{3}}(n_1^2+n_2^2-2n_3^2)]^T.\end{aligned} \tag{E.1}$$

A closed geodesic $(0, \sin s, \cos s)^T$ ($s \in [0,\pi]$) appears therefore as a tilted circle of radius $\sqrt{3}/2$ on S^7 (it is not a great-circle):

$$[0,0,-\frac{\sqrt{3}}{4}(1-\cos 2s), 0, 0, \frac{\sqrt{3}}{2}\sin 2s, 0, -\frac{1}{4}(1+3\cos 2s)]^T. \tag{E.2}$$

Appendix F

Computation of the weak value and Bargmann invariant

Computing weak values involves the traces of products of two and three operators. Considering three arbitrary generators $\vec{\alpha}\cdot\hat{\vec{L}}$, $\vec{\beta}\cdot\hat{\vec{L}}$ and $\vec{\gamma}\cdot\hat{\vec{L}}$, using Eq. G.2, we find the products and traces

$$(\vec{\alpha}\cdot\hat{\vec{L}})(\vec{\beta}\cdot\hat{\vec{L}}) = \frac{2}{N}\vec{\alpha}\cdot\vec{\beta}\;\hat{I}_N+\frac{1}{c_s}(\vec{\alpha}\star\vec{\beta})\cdot\hat{\vec{L}}+i\,(\vec{\alpha}\wedge\vec{\beta})\cdot\hat{\vec{L}}, \tag{F.1}$$

$$\mathrm{Tr}\Big[(\vec{\alpha}\cdot\hat{\vec{L}})(\vec{\beta}\cdot\hat{\vec{L}})\Big] = 2\,\vec{\alpha}\cdot\vec{\beta}, \tag{F.2}$$

where c_s is defined in Eq. C.4. For three generators, we have

$$\begin{aligned}(\vec{\alpha}\cdot\hat{\vec{L}})(\vec{\beta}\cdot\hat{\vec{L}})(\vec{\gamma}\cdot\hat{\vec{L}}) = \frac{2}{N}\left[\frac{1}{c_s}(\vec{\alpha}\star\vec{\beta})\cdot\vec{\gamma}+i(\vec{\alpha}\wedge\vec{\beta})\cdot\vec{\gamma}\right]\hat{I}_N\\ +\frac{2}{N}\vec{\alpha}\cdot\vec{\beta}\;(\vec{\gamma}\cdot\hat{\vec{L}})+\frac{1}{c_s^2}[(\vec{\alpha}\star\vec{\beta})\star\vec{\gamma}]\cdot\hat{\vec{L}}-\;[(\vec{\alpha}\wedge\vec{\beta})\wedge\vec{\gamma}]\cdot\hat{\vec{L}}\\ +i\frac{1}{c_s}\left\{[(\vec{\alpha}\wedge\vec{\beta})\star\vec{\gamma}]\cdot\hat{\vec{L}}+[(\vec{\alpha}\star\vec{\beta})\wedge\vec{\gamma}]\cdot\hat{\vec{L}}\right\},\end{aligned} \tag{F.3}$$

$$\mathrm{Tr}\Big[(\vec{\alpha}\cdot\hat{\vec{L}})(\vec{\beta}\cdot\hat{\vec{L}})(\vec{\gamma}\cdot\hat{\vec{L}})\Big] = \frac{2}{c_s}(\vec{\alpha}\star\vec{\beta})\cdot\vec{\gamma}+2i\,(\vec{\alpha}\wedge\vec{\beta})\cdot\vec{\gamma}. \tag{F.4}$$

As the trace is invariant under unitary transformations, we see that the two quantities $(\vec{\alpha}\star\vec{\beta})\cdot\vec{\gamma}$ and $(\vec{\alpha}\wedge\vec{\beta})\cdot\vec{\gamma}$ present in Eq. F.4 are also invariant under unitary transformations. From the properties of the d_{abc} and f_{abc} constants of SU(N), the former is fully symmetric under permutations, while the latter is antisymmetric and changes sign under permutation of two vectors.
Now we define two projectors on pure states $\hat{\Pi}_i=\frac{1}{N}\hat{I}_N+c_p\;\vec{i}\cdot\hat{\vec{L}}$ and $\hat{\Pi}_f=\frac{1}{N}\hat{I}_N+c_p\;\vec{f}\cdot\hat{\vec{L}}$ (with c_p given by Eq. C.1 with $k=1$), as well as two arbitrary Hermitian operators $\hat{A}=a_I\hat{I}_N+a_L\;\vec{\alpha}\cdot\hat{\vec{L}}$ and

$\hat{B} = b_I \hat{I}_N + b_L \, \vec{\beta} \cdot \hat{\vec{L}}$. Following Eq. F.1, the product of the operators $\hat{A}$ and $\hat{B}$ becomes

$$\begin{aligned} \hat{A}\hat{B} &= a_I b_I \hat{I}_N + a_L b_I \, \vec{\alpha} \cdot \hat{\vec{L}} + a_I b_L \, \vec{\beta} \cdot \hat{\vec{L}} + a_L b_L (\vec{\alpha} \cdot \hat{\vec{L}})(\vec{\beta} \cdot \hat{\vec{L}}) \\ &= (a_I b_I + \frac{2}{N} a_L b_L \, \vec{\alpha} \cdot \vec{\beta}) \hat{I}_N + a_L b_I \, \vec{\alpha} \cdot \hat{\vec{L}} + a_I b_L \, \vec{\beta} \cdot \hat{\vec{L}} \\ &+ a_L b_L \frac{1}{c_s} \, (\vec{\alpha} \star \vec{\beta}) \cdot \hat{\vec{L}} + i a_L b_L \, (\vec{\alpha} \wedge \vec{\beta}) \cdot \hat{\vec{L}}. \end{aligned} \tag{F.5}$$

When $\hat{A} = \hat{B}$, the latter simplifies to

$$\hat{A}^2 = (a_I^2 + \frac{2}{N} a_L^2) \hat{I}_N + 2 a_I a_L \, \vec{\alpha} \cdot \hat{\vec{L}} + a_L^2 \frac{1}{c_s} \, (\vec{\alpha} \star \vec{\alpha}) \cdot \hat{\vec{L}}. \tag{F.6}$$

These expressions also allow us to compute the commutator and anti-commutator

$$[\hat{A}, \hat{B}] = 2 i a_L b_L \, (\vec{\alpha} \wedge \vec{\beta}) \cdot \hat{\vec{L}} \tag{F.7}$$

$$\begin{aligned} \{\hat{A}, \hat{B}\} &= 2(a_I b_I + \frac{2}{N} a_L b_L \, \vec{\alpha} \cdot \vec{\beta}) \hat{I}_N + 2 a_L b_I \, \vec{\alpha} \cdot \hat{\vec{L}} + 2 a_I b_L \, \vec{\beta} \cdot \hat{\vec{L}} \\ &+ 2 a_L b_L \frac{1}{c_s} \, (\vec{\alpha} \star \vec{\beta}) \cdot \hat{\vec{L}} \end{aligned} \tag{F.8}$$

The latter were used in section 4.8 to compute the variance and covariance of operators. Formula Eq. F.5 gives the product $\hat{\Pi}_f \hat{\Pi}_i$ of the two projectors, by simply setting $a_I = b_I = \frac{1}{N}$ and $a_L = b_L = c_p$, so that the trace of two projectors is

$$\mathrm{Tr}\,(\hat{\Pi}_f \hat{\Pi}_i) = \frac{1}{N} + 2 c_p^2 \, \vec{f} \cdot \vec{i} = \frac{1}{N} [1 + (N-1) \, \vec{f} \cdot \vec{i}]. \tag{F.9}$$

This is the denominator of the weak value Eq. 2.29. To obtain its numerator, we evaluate

$$\begin{aligned} \hat{\Pi}_f \hat{A} \hat{\Pi}_i &= \frac{a_I}{N^2} \hat{I}_N + \frac{a_I}{N} c_p \, \vec{i} \cdot \hat{\vec{L}} + \frac{a_L}{N^2} \, \vec{\alpha} \cdot \hat{\vec{L}} + \frac{a_L}{N} c_p (\vec{\alpha} \cdot \hat{\vec{L}})(\vec{i} \cdot \hat{\vec{L}}) \\ &+ \frac{a_I}{N} c_p \, \vec{f} \cdot \hat{\vec{L}} + a_I c_p^2 (\vec{f} \cdot \hat{\vec{L}})(\vec{i} \cdot \hat{\vec{L}}) + \frac{a_L}{N} c_p (\vec{f} \cdot \hat{\vec{L}})(\vec{\alpha} \cdot \hat{\vec{L}}) \\ &+ a_L c_p^2 (\vec{f} \cdot \hat{\vec{L}})(\vec{\alpha} \cdot \hat{\vec{L}})(\vec{i} \cdot \hat{\vec{L}}). \end{aligned} \tag{F.10}$$

Then, the trace formulas Eq. F.2 and Eq. F.4 yield

$$\begin{aligned} \mathrm{Tr}\,(\hat{\Pi}_f \hat{A} \hat{\Pi}_i) &= \frac{a_I}{N} + 2 \frac{a_L}{N} c_p \, \vec{\alpha} \cdot \vec{i} + 2 a_I c_p^2 \, \vec{f} \cdot \vec{i} + 2 \frac{a_L}{N} c_p \, \vec{f} \cdot \vec{\alpha} \\ &+ 2 a_L c_p^2 \left[\frac{1}{c_s} (\vec{f} \star \vec{\alpha}) \cdot \vec{i} + i \, (\vec{f} \wedge \vec{\alpha}) \cdot \vec{i} \right]. \end{aligned} \tag{F.11}$$

The Bargmann invariant ensues from considering that $\hat{A} = \hat{\Pi}_r$ ($a_I = \frac{1}{N}$ and $a_L = c_p$),

$$\begin{aligned} \mathrm{Tr}\,(\hat{\Pi}_f \hat{\Pi}_r \hat{\Pi}_i) &= \frac{1}{N^2} + \frac{2}{N} c_p^2 (\vec{r} \cdot \vec{i} + \vec{f} \cdot \vec{i} + \vec{f} \cdot \vec{r}) \\ &+ 2 c_p^3 \left[\frac{1}{c_s} (\vec{f} \star \vec{r}) \cdot \vec{i} + i \, (\vec{f} \wedge \vec{r}) \cdot \vec{i} \right], \end{aligned} \tag{F.12}$$

while the weak value is simply given by the ratio of Eq. F.11 with Eq. F.9. The real and imaginary part of the weak value are thus

$$\mathrm{Re}A_w = \frac{\frac{a_I}{N} + \frac{2a_L}{N} c_p(\vec{\alpha}\cdot\vec{i} + \vec{f}\cdot\vec{\alpha}) + 2a_I c_p^2\, \vec{f}\cdot\vec{i} + 2a_L c_p^2 \frac{1}{c_s}(\vec{f}\star\vec{\alpha})\cdot\vec{i}}{\frac{1}{N} + 2c_p^2\, \vec{f}\cdot\vec{i}}, \tag{F.13}$$

$$\mathrm{Im}A_w = \frac{2i\, a_L c_p^2\, (\vec{f}\wedge\vec{\alpha})\cdot\vec{i}}{\frac{1}{N} + 2c_p^2\, \vec{f}\cdot\vec{i}}. \tag{F.14}$$

The argument of the weak value is determined by $\arctan(\mathrm{Im}A_w/\mathrm{Re}A_w)$ while simultaneously taking the signs of Eq. F.13 and Eq. F.14 into account to recover the appropriate quadrant. The latter expressions allow for an easy conversion between possibly different conventions for the c_p and c_s constants, as discussed in appendix C.

Appendix G

Conventions for generators of SU(N)

In this thesis, as a convention, we have chosen to use the N^2-1 traceless Hermitian generators of SU(N) that arise from the generalization of the Pauli and Gell-Mann matrices, thereafter noted $\hat{\vec{L}}$. From a strictly formal point of view, these operators would probably be best seen as twice the proper generators of SU(N), typically noted $\hat{\vec{T}}$. However, we think this choice is natural in order to express quantum states on the Bloch sphere and generalized Bloch spheres in terms of standard operators. The generators usually defined by $\hat{\vec{T}}$ follow the properties

$$\begin{aligned}
\left[\hat{T}_a,\hat{T}_b\right] &= i\sum_c f_{abc}\hat{T}_c, \\
\{\hat{T}_a,\hat{T}_b\} &= \frac{1}{N}\delta_{ab}\hat{I}_N+\sum_c d_{abc}\hat{L}_c, \\
\mathrm{Tr}\,\hat{T}_a\hat{T}_b &= \frac{1}{2}\delta_{ab}, \\
\hat{T}_a\hat{T}_b &= \frac{1}{2N}\delta_{ab}\hat{I}_N+\frac{1}{2}\sum_c (d_{abc}+if_{abc})\,\hat{T}_c.
\end{aligned} \tag{G.1}$$

Even though these generators are mathematically convenient, quantum physics makes extensive use of the Pauli matrices $\hat{\vec{\sigma}}$. Their SU(3) counterparts are the well-known Gell-Mann matrices $\hat{\vec{\lambda}}$. They share the following properties with their SU(N) generalization $\hat{\vec{L}}$:

$$\begin{aligned}
\left[\hat{L}_a,\hat{L}_b\right] &= 2i\sum_c f_{abc}\hat{L}_c, \\
\{\hat{L}_a,\hat{L}_b\} &= \frac{4}{N}\delta_{ab}\hat{I}_N+2\sum_c d_{abc}\hat{L}_c, \\
\mathrm{Tr}\,\hat{L}_a\hat{L}_b &= 2\delta_{ab}, \\
\hat{L}_a\hat{L}_b &= \frac{2}{N}\delta_{ab}\hat{I}_N+\sum_c (d_{abc}+if_{abc})\,\hat{L}_c.
\end{aligned} \tag{G.2}$$

The anti-symmetric structure constants and the symmetric constants of SU(N) are connected to the generators using

$$f_{abc} = -\frac{1}{4} i \,\mathrm{Tr}\big(\hat{L}_a[\hat{L}_b,\hat{L}_c]\big) = -2i\,\mathrm{Tr}\big(\hat{T}_a[\hat{T}_b,\hat{T}_c]\big), \tag{G.3}$$

$$d_{abc} = \frac{1}{4}\,\mathrm{Tr}\big(\hat{L}_a\{\hat{L}_b,\hat{L}_c\}\big) = 2\,\mathrm{Tr}\big(\hat{L}_a\{\hat{L}_b,\hat{L}_c\}\big), \tag{G.4}$$

so that $\hat{\vec{L}} = 2\,\hat{\vec{T}}$. This simple proportionality relationship provides the conversion rule between the two conventions, should anyone wish to use expressions with the $\hat{\vec{T}}$ generators. In this document, we will exclusively work with the $\hat{\vec{L}}$ generators.

Appendix H

Calculation of the expression of the Henrici departure from normality

Let us consider the non-normal operator $\hat{A}$ defined in Eq. 6.3. The square of this operator is

$$\hat{A}^2 = \frac{1}{\mathrm{Tr}\left[\hat{\Pi}_f \hat{\Pi}_i\right]^2} \hat{O}\left|\psi_i\right\rangle \left\langle\psi_i\right| \hat{O}\left|\psi_i\right\rangle \left\langle\psi_i\right| = \frac{\left\langle\psi_i\right| \hat{O}\left|\psi_i\right\rangle}{\left|\left\langle\psi_f\middle|\psi_i\right\rangle\right|^2} \hat{A}, \tag{H.1}$$

which implies that the N^{th} power of the operator $\hat{A}$ is

$$\hat{A}^N = \frac{\left\langle\psi_i\right| \hat{O}\left|\psi_i\right\rangle^{N-1}}{\left|\left\langle\psi_f\middle|\psi_i\right\rangle\right|^{2(N-1)}} \hat{A}. \tag{H.2}$$

The matrix $\hat{A}$ is almost idempotent, as $\hat{A}^2 = \alpha\hat{A}$. Consequently, we can redefine a matrix $\tilde{\hat{A}}$ that is idempotent, i.e. $\tilde{\hat{A}}^2 = \tilde{\hat{A}}$,

$$\tilde{\hat{A}} = \frac{\hat{O}\hat{\Pi}_i \left|\left\langle\psi_f\middle|\psi_i\right\rangle\right|^2}{\left\langle\psi_i\right| \hat{O}\left|\psi_i\right\rangle}. \tag{H.3}$$

The eigenvalues of an idempotent matrix are either 0 or 1. As the trace of the matrix $\tilde{\hat{A}}$ is 1, one eigenvalue should be 1 and the rest 0. Consequently, one eigenvalue of the matrix $\hat{A}$ is $\frac{\left\langle\psi_i\right|\hat{O}\left|\psi_i\right\rangle}{\left\langle\psi_f\middle|\psi_i\right\rangle^2}$ and the rest are 0. Obviously, when the expectation value of the observable in the initial state is 0, all eigenvalues are 0.
The Frobenious norm of the matrix $\hat{A}$ is

$$\begin{aligned} ||\hat{A}||_F^2 &= \frac{1}{\left|\left\langle\psi_f\middle|\psi_i\right\rangle\right|^4} \mathrm{Tr}\left[\left(\hat{O}\hat{\Pi}_i\right)\left(\hat{O}\hat{\Pi}_i\right)^\dagger\right] = \frac{1}{\left|\left\langle\psi_f\middle|\psi_i\right\rangle\right|^4} \mathrm{Tr}\left[\hat{O}\hat{\Pi}_i\hat{\Pi}_i\hat{O}\right] \\ &= \frac{1}{\left|\left\langle\psi_f\middle|\psi_i\right\rangle\right|^4} \mathrm{Tr}\left[\hat{O}\hat{\Pi}_i\hat{O}\right] = \frac{\left\langle\psi_i\right| \hat{O}^2\left|\psi_i\right\rangle}{\left|\left\langle\psi_f\middle|\psi_i\right\rangle\right|^4}. \end{aligned} \tag{H.4}$$

The Henrici departure from normality of the matrix $\hat{A}$ is

$$d_f\left(\hat{A}\right) = \sqrt{\frac{\left\langle\psi_i\right| \hat{O}^2\left|\psi_i\right\rangle}{\left|\left\langle\psi_f\middle|\psi_i\right\rangle\right|^4} - \frac{\left\langle\psi_i\right| \hat{O}\left|\psi_i\right\rangle^2}{\left|\left\langle\psi_f\middle|\psi_i\right\rangle\right|^4}} = \frac{\Delta_i \hat{O}}{\left|\left\langle\psi_f\middle|\psi_i\right\rangle\right|^2}, \tag{H.5}$$

which is proportional to the uncertainty of the operator $\hat{O}$ in the initial state $|\psi_i\rangle$.
Following the same procedure, one can obtain the Henrici departure from normality of the operator $\hat{A}'$,

$$d_f\left(\hat{A}'\right) = \sqrt{\frac{\langle\psi_f|\,\hat{O}^2\,|\psi_f\rangle}{|\langle\psi_f|\psi_i\rangle|^4} - \frac{\langle\psi_f|\,\hat{O}\,|\psi_f\rangle^2}{|\langle\psi_f|\psi_i\rangle|^4}} = \frac{\Delta_f\hat{O}}{|\langle\psi_f|\psi_i\rangle|^2}\,, \tag{H.6}$$

which is proportional to the uncertainty of the operator $\hat{O}$ in the final state $|\psi_f\rangle$.

Appendix I

Some analytical formulas for $\hat{\sigma}_x$

The aim of this appendix is to present the analytical expressions relating O_w and d_f for the cases numerically studied in the main text.
Let us assume the pre- and post-selected states to be given in the general form

$$|\psi_a\rangle = \begin{pmatrix} \cos\theta_a \\ e^{i\xi_a}\sin\theta_a, \end{pmatrix} \tag{I.1}$$

where for $a \in \{i,f\}$ we assume $0 \leq \theta_a \leq \frac{\pi}{2}$ and $0 \leq \xi_a \leq 2\pi$. For sake of definitiveness, let us consider the case of the x-Pauli matrix. Because $\hat{\sigma}_x^2 = 1$ and the normalization of the initial state, we get from Eq. H.5

$$d_f\left(\hat{A}_x\right) = \frac{\sqrt{1-\sin^2(2\theta_i)\cos^2\xi_i}}{|\langle\psi_f|\psi_i\rangle|^2}, \tag{I.2}$$

where

$$|\langle\psi_f|\psi_i\rangle|^2 = \cos^2\theta_f\cos^2\theta_i + \sin^2\theta_f\sin^2\theta_i + 2\cos\left(\xi_i-\xi_f\right)\cos\theta_f\cos\theta_i\sin\theta_f\sin\theta_i\,. \tag{I.3}$$

To compute the weak value we use the very first definition Eq. 6.1 to obtain

$$|\sigma_{x,w}|^2 = \frac{\sin^2\theta_f\cos^2\theta_i + \cos^2\theta_f\sin^2\theta_i + 2\cos\left(\xi_i+\xi_f\right)\cos\theta_f\cos\theta_i\sin\theta_f\sin\theta_i}{|\langle\psi_f|\psi_i\rangle|^2}\,. \tag{I.4}$$

Both $d_f\left(\hat{A}_x\right)$ and $|\sigma_{x,w}|^2$ depend on the angles, θ_f and θ_i, and the phases ξ_i and ξ_f. In the following, we will assume the last three quantities as fixed parameters and thus consider $X = d_f\left(\hat{A}_x\right)$ and $Y = |\sigma_{x,w}|^2$ to represent a curve parametrized by θ_f in the plane (X,Y).
In Fig. I.1, we report three typical behaviors of such a curve. In the left panel, we assume $\xi_i = \xi_f = 0$ and one clearly observes a positive correlation between $d_f(\hat{A}_x)$ and $|\hat{\sigma}_{x,w}|^2$, they both increases as θ_f varies from $\tilde{\theta}_f$, i.e., the values at which $|\hat{\sigma}_{x,w}|^2 = 1$ to $\theta_f = 0$, corresponding here to the maximum of both $d_f(\hat{A}_x)$ and $|\hat{\sigma}_{x,w}|^2$. The results shown in the middle panel have been obtained by setting $\xi_i = \pi/5$ and still $\xi_f = 0$ and we can observe the same behavior of the one presented in the left panel. A similar behavior persists once we increase ξ_i up to a point at which a new behavior emerges (see right panel) at which the relation between $d_f(\hat{A}_x)$ and $|\hat{\sigma}_{x,w}|^2$ is no longer monotonic.

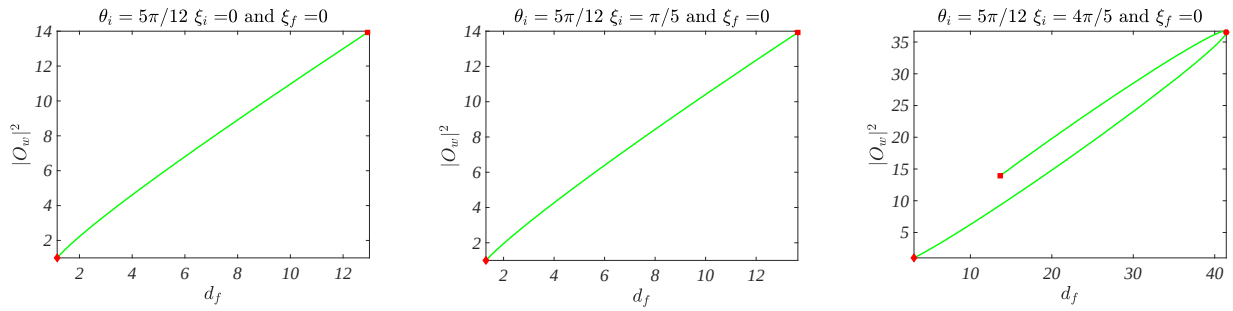

Figure I.1: We show the curves $d_f(\hat{A}_x)$ and $|\hat{\sigma}_{x,w}|^2$ as function of θ_f in the range $[0, \tilde{\theta}_f]$, where the upper bound is determined by the condition $|\hat{\sigma}_{x,w}|^2(\tilde{\theta}_f) = 1$ and it is marked with a red diamond. The value $\theta_f = 0$ is marked with a red square, while the value $\hat{\theta}_f$ at which d_f attains its maximum is denoted by a red circle denotes once the latter falls in the domain of anomalous weak value. The remaining parameters have been fixed to $\theta_i = 5\pi/12$, $\xi_i = 0$ and $\xi_f = 0$ (left panel), $\theta_i = 5\pi/12$, $\xi_i = \pi/5$ and $\xi_f = 0$ (middle panel), $\theta_i = 5\pi/12$, $\xi_i = 4\pi/5$ and $\xi_f = 0$ (right panel).

In this panel, we can indeed observe the existence of a value $\hat{\theta}_f$ at which d_f attains its maximum and this value is in the region of anomalous weak values. The value $\tilde{\theta}_f$ can be setting Eq. I.4 equal to 1 and solving the resulting relation for $\tan\theta_f$. A straightforward computation returns if $\tan^2\theta_i \neq 1$

$$\tan\tilde{\theta}_f = \tan(2\theta_i)\sin\xi_i\sin\xi_f \pm \sqrt{\tan^2(2\theta_i)\sin^2\xi_i\sin^2\xi_f + 1}\,, \tag{I.5}$$

and we have to select the angle lying in $[0,\pi/2]$.
To determine the angle $\hat{\theta}_f$ that maximizes d_f one can observe that the numerator of Eq. I.2 does not depend on θ_f and thus this is equivalent to minimize the denominator. By doing so, we can obtain

$$\tan\big(2\hat{\theta}_f\big) = \tan(2\theta_i)\cos\big(\xi_i - \xi_f\big)\,, \tag{I.6}$$

if $\cos(2\theta_i) \neq 0$ and $\hat{\theta}_f = \pi/4 + k\pi/2$ if if $\cos(2\theta_i) = 0$.
Having those two angles, $\hat{\theta}_f$ and $\tilde{\theta}_i$, we can obtain conditions on ξ_f, ξ_i and θ_i to determine if there is or not a monotonic dependence between $d_f(\hat{A}_x)$ and $|\hat{\sigma}_{x,w}|^2$.
To make some analytical progress we can explicitly express the dependence of $|\sigma_{x,w}|^2$ on $d_f(\hat{A}_x)$, again by removing θ_f. To do so, we first express Eq. I.2 in terms of $\tan^2\theta_f$

$$d_f\left(\hat{A}_x\right) = \sqrt{1-\sin^2(2\theta_i)\cos^2\xi_i}\,\frac{(1+\tan^2\theta_i)(1+\tan^2\theta_f)}{1+\tan^2\theta_f\tan^2\theta_i + 2\cos\big(\xi_i-\xi_f\big)\tan\theta_i\tan\theta_f}\,, \tag{I.7}$$

and we solve the second degree equation in $\tan\theta_f$ to express the latter as a function of d_f and the remaining variables

$$\tan\theta_f = \frac{d_f\cos\big(\xi_i-\xi_f\big)\tan\theta_i \pm \sqrt{d_f^2\cos^2(\xi_i-\xi_f)\tan^2\theta_i - [d_f\tan^2\theta_i - (1+\tan^2\theta_i)S][d_f - (1+\tan^2\theta_i)S]}}{d_f\tan^2\theta_i - (1+\tan^2\theta_i)S}\,, \tag{I.8}$$

where $S = \sqrt{1-\sin^2(2\theta_i)\cos^2\xi_i}$.
Hence we insert the above value of $\tan\theta_f$ into Eq. I.4 that it has also be rewritten in terms of $\tan^2\theta_f$

$$|\hat{\sigma}_{x,w}|^2 = \frac{1}{1+\tan^2\theta_i}\frac{1}{1+\tan^2\theta_f}\frac{\tan^2\theta_f + \tan^2\theta_i + 2\cos\big(\xi_i+\xi_f\big)\tan\theta_f\tan\theta_i}{\sqrt{1-\sin^2(2\theta_i)\cos^2\xi_i}}d_f\,. \tag{I.9}$$

We can observe that the curves given parametrically by Eqs. I.2 and I.4 shown in Fig. I.1 correspond to the branch of $\tan\theta_f$ Eq. I.8 with the positive sign in front of the square root. In Fig. I.3 we propose a global view of $|\sigma_{x,w}|$ (top panels) and $d_f(\hat{A}_x)$ (bottom panels) as a function of θ_i and θ_f for three sets of values of (ξ_i,ξ_f), $(0,0)$ (left panel), $(\pi/5,0)$ (middle panel) and $(4\pi/5,0)$ (right panel). We can observe that as ξ_i increases so does the region corresponding to strong anomalous weak value, e.g., larger than 2. On the other hand (see Fig. I.4) increasing ξ_f reduces the region of anomalous weak values.

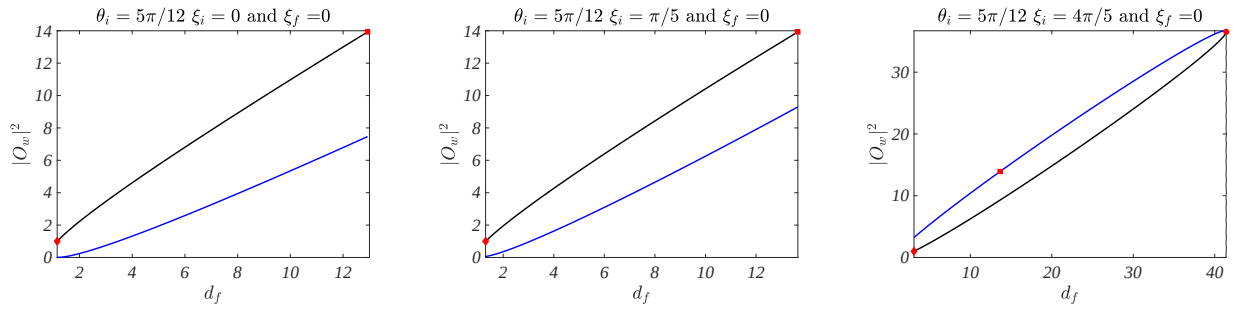

Figure I.2: We show the curve $|\hat{\sigma}_{x,w}|^2$ as a function of $d_f(\hat{A}_x)$, in the range of anomalous weak values. The black line corresponds to the root with the positive sign while the blue one to the negative sign. The red diamond marks the value of d_f for which $|\hat{\sigma}_{x,w}|^2 = 1$. The red square identifies the value of d_f associated to $\theta_f = 0$, while red circle determines the largest value of d_f. The remaining parameters have been fixed to $\theta_i = 5\pi/12$, $\xi_i = 0$ and $\xi_f = 0$ (left panel), $\theta_i = 5\pi/12$, $\xi_i = \pi/5$ and $\xi_f = 0$ (middle panel), $\theta_i = 5\pi/12$, $\xi_i = 4\pi/5$ and $\xi_f = 0$ (right panel).

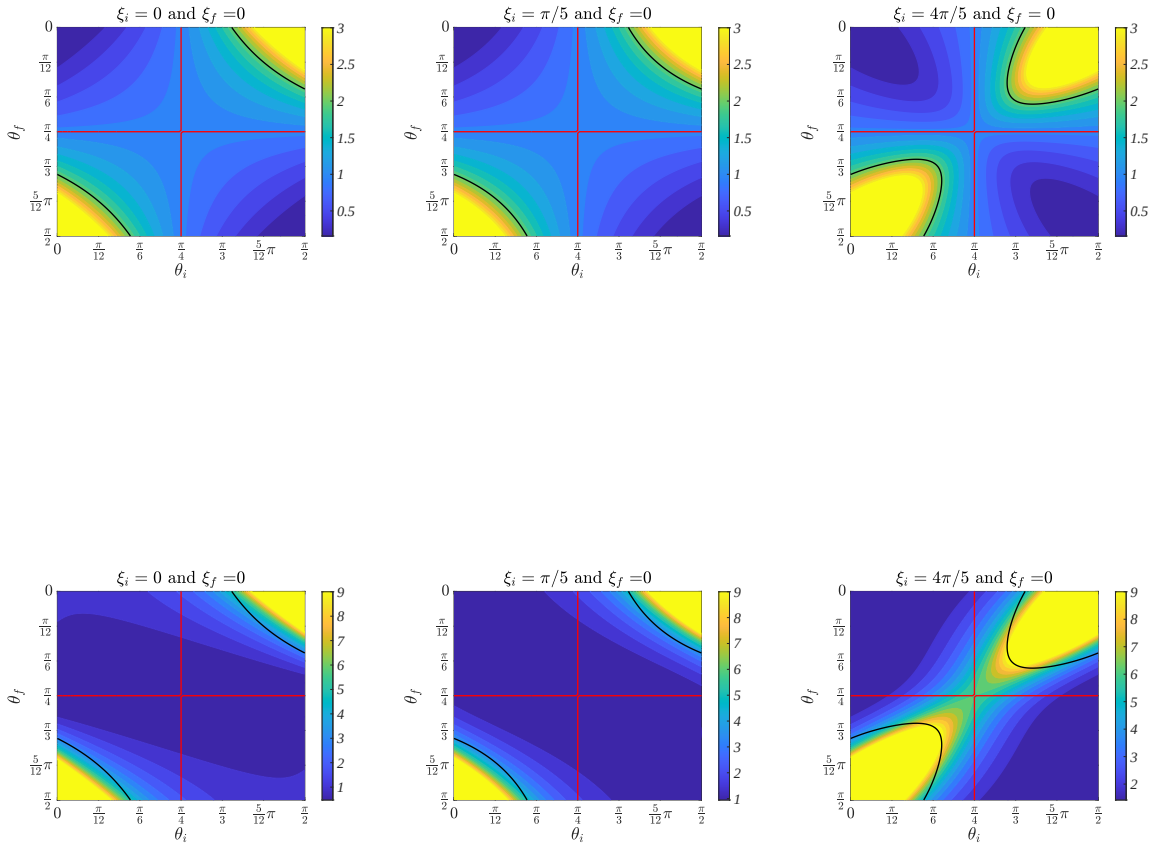

Figure I.3: We show in the plane (θ_i, θ_f) the level curves of the functions $|\hat{\sigma}_{x,w}|$ (top panels) and $d_f(\hat{A}_x)$ (bottom panels). The remaining parameters have been fixed to $(\xi_i, \xi_f) = (0,0)$ (left panel), $(\xi_i, \xi_f) = (\pi/5, 0)$ (middle panel) and $(\xi_i, \xi_f) = (4\pi/5, 0)$ (right panel).

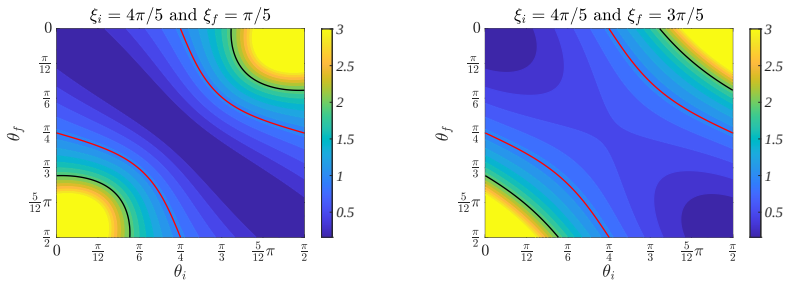

Figure I.4: We show in the plane (θ_i, θ_f) the level curves of the function $|\hat{\sigma}_{x,w}|$ for two sets of parameters $(\xi_i, \xi_f) = (4\pi/5, \pi/5)$ (left panel), $(\xi_i, \xi_f) = (4\pi/5, 3\pi/5)$ (right panel).

Appendix J

Analytical calculations considering null phases

Let us consider now the Pauli matrix $\hat{\sigma}_y$. In this case, the Henrici departure from normality of the matrix $\hat{A}$ is, assuming $\xi_i = \xi_f = 0$,

$$df\left(\hat{A}_y\right) = \frac{1}{\cos^2\left(\theta_f - \theta_i\right)}, \tag{J.1}$$

while the weak value is

$$\sigma_{y,w} = i\tan\left(\theta_f - \theta_i\right). \tag{J.2}$$

The Henrici departure from normality can be expressed in terms of the weak value as

$$|\sigma_{y,w}|^2 = \frac{1}{\cos^2\left(\theta_f - \theta_i\right)} - 1 = df\left(\hat{A}_y\right) - 1. \tag{J.3}$$

A comparison between Fig. J.1 and Fig. 6.2 reveals a remarkable agreement between the figures generated from the numerical and analytical studies. Finally, we also studied the Pauli matrix $\hat{\sigma}_z$, assuming $\xi_i = \xi_f = 0$. The Henrici departure from normality is in that case,

$$d_f\left(\hat{A}_z\right) = \sin^2 2\theta_i\left[1 + \tan^2\left(\theta_f - \theta_i\right)\right] \tag{J.4}$$

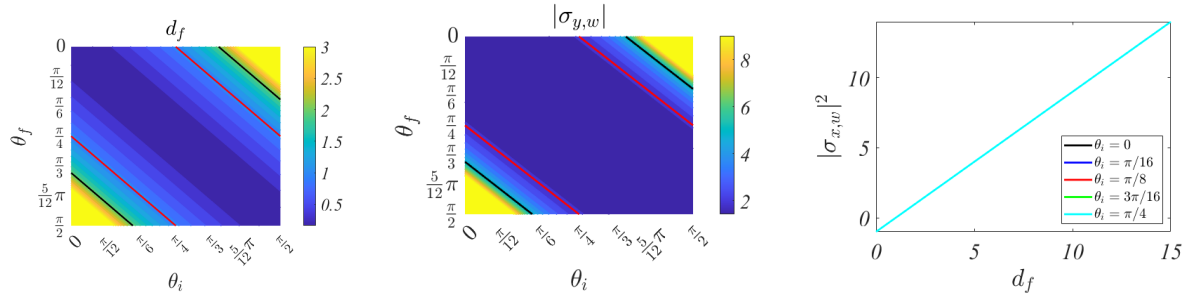

Figure J.1: Henrici departure from normality of $\hat{A}_y$ in terms of θ_i and θ_f, weak value of $\hat{\sigma}_y$ in terms of θ_i and θ_f, and weak value of $\hat{\sigma}_y$ in terms of the Henrici departure in the anomalous regime from normality for different values of θ_i from 0 to $\frac{\pi}{4}$.

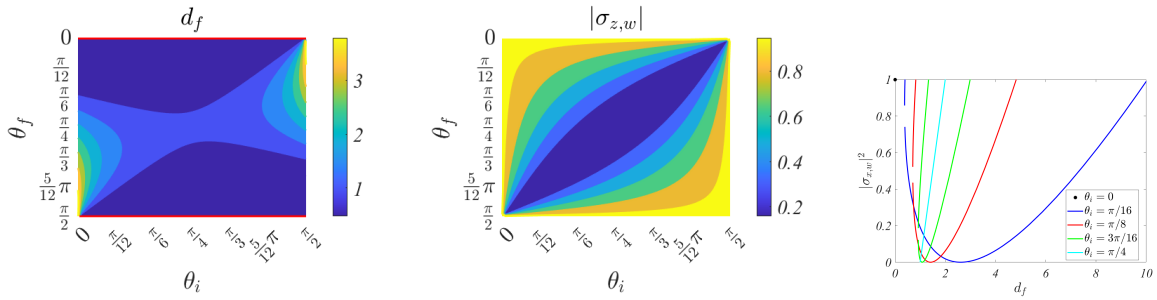

Figure J.2: Henrici departure from normality of $\hat{A}_z$ in terms of θ_i and θ_f, weak value of $\hat{\sigma}_z$ in terms of θ_i and θ_f, and weak value of $\hat{\sigma}_z$ in terms of the Henrici departure from normality for different values of θ_i from 0 to $\frac{\pi}{4}$.

while the weak value is

$$|\sigma_{z,w}| = |\cos 2\theta_i - \tan\left(\theta_f - \theta_i\right) \sin 2\theta_i| \tag{J.5}$$

The weak value can be expressed in terms of the Henrici departure from normality as,

$$|\sigma_{z,w}|^2 = \left| \cos 2\theta_i \pm \sin 2\theta_i \sqrt{-1 \pm \frac{df\left(\hat{A}_z\right)}{\sin 2\theta_i}} \right|^2. \tag{J.6}$$

Fig. J.2 and 6.3 depict the results of the theoretical and numerical calculations, and a striking similarity between the theoretical and numerical figures is immediately apparent.

Appendix K

Study of the point of maximum weak value and maximum Henrici departure from normality

In this appendix, we show some analytical results about the value of the observable parameter (θ) in which the weak value presents a maximum and the ones in which both matrices ($\hat{A}$ and $\hat{A}'$) present a Henrici departure from normality that is the largest.
Let us consider the specific example of Fig. 6.10. The studied observable is

$$\hat{O} = \begin{pmatrix} \cos\theta & \frac{(1-i)}{\sqrt{2}}\sin\theta \\ \frac{(1+i)}{\sqrt{2}}\sin\theta & -\cos\theta \end{pmatrix}. \tag{K.1}$$

The pre- and post-selected states are

$$|\psi_i\rangle = \begin{pmatrix} \cos\theta_i \\ \sin\theta_i \end{pmatrix}, \qquad |\psi_f\rangle = \begin{pmatrix} 1 \\ 0 \end{pmatrix}. \tag{K.2}$$

Both matrices $\hat{A}$ and $\hat{A}'$ have an eigenvalue that is equal to 0. The other eigenvalues are

$$\begin{aligned} \alpha_{\hat{A}} &= \cos\theta \\ \alpha_{\hat{A}'} &= \cos\theta\cos 2\theta_i + \sqrt{2}\cos\theta_i \sin\theta \sin\theta_i. \end{aligned} \tag{K.3}$$

The weak value is

$$|O_w| = \sqrt{\cos^2\theta + \sqrt{2}\cos\theta\sin\theta\tan\theta_i + \sin^2\theta\tan^2\theta_i}, \tag{K.4}$$

and the normalized Henrici departure from normality is

$$d_{f_n} = \sqrt{1 - \left(\cos\theta\cos 2\theta_i + \sqrt{2}\cos\theta_i\sin\theta\sin\theta_i\right)^2}. \tag{K.5}$$

At $\theta = 0$, the weak value is equal to 1 independently on the value of the initial polar angle, θ_i. When $0 \leq \theta \leq \frac{\pi}{4}$, the weak value is only anomalous for a section of values of θ, actually, with $0 \leq \theta \leq \arctan\frac{\sqrt{2}\tan\theta_i}{1-\tan^2\theta_i}$.

The Henrici departure from normality is the largest when the eigenvalue α is the smallest. In the case of $\alpha_{\hat{A}}$, it always decreases in the range of θ between 0 and $\frac{\pi}{2}$. Consequently, the maximum value of the Henrici departure from normality in the range of anomalous weak values would be at $\theta = \arctan \frac{\sqrt{2}\tan\theta_i}{1-\tan^2\theta_i}$.

The eigenvalue of $\hat{A}'$ that is different from zero, $\alpha_{\hat{A}'}$ increases when increasing θ in the range $0 \leq \theta \leq \arctan \frac{\sqrt{2}\tan\theta_i}{1-\tan^2\theta_i}$. The point of the largest Henrici departure from normality in the anomalous regime is at $\theta = 0$, for all values of $0 \leq \theta_i \leq \frac{\pi}{4}$.

The value of θ for which the weak value is maximum is exactly at the average of both points of the largest value of Henrici departure from normality, $\theta = \frac{1}{2}\arctan \frac{\sqrt{2}\tan\theta_i}{1-\tan^2\theta_i}$.

When moving to $\frac{\pi}{4} \leq \theta_i \leq \frac{\pi}{2}$, the weak value is anomalous for all values of θ in the range $0 \leq \theta \leq \frac{\pi}{2}$. The largest Henrici departure from normality of $\hat{A}$ in the anomalous regime is at $\theta = \frac{\pi}{2}$ for all values of θ_i, where the matrix is nilpotent, both eigenvalues are 0.

The Henrici departure from normality of $\hat{A}'$ reaches its maximum when the matrix is nilpotent, at $\theta = \arctan\left(-\sqrt{2}\cot 2\theta_i\right)$ which is in the anomalous regime when $\frac{\pi}{4} \leq \theta_i \leq \frac{\pi}{2}$.

The anomalous weak value reaches its maximum at $\theta = \frac{1}{2}\arctan\left(-\sqrt{2}\cot 2\theta_i\right)$.

Here, we have explained in detail how the value of θ in which the weak value is maximum is at the average between the one in which the Henrici departure from normality of $\hat{A}$ and $\hat{A}'$ are maximum for a specific case. However, this is valid for any two-dimensional quantum system.

Appendix L

Derivative of the normalized Henrici departure from normality and the numerator of the weak value

The numerator of the weak value of the operator defined in Eq. 6.17 is, assuming $\xi_i = \xi_f = 0$,

$$O_w = \sqrt{\left(\cos\theta\cos\left(\theta_f+\theta_i\right)+\cos\phi\sin\theta\sin\left(\theta_f+\theta_i\right)\right)^2+\sin^2\theta\sin^2\left(\theta_f-\theta_i\right)\sin^2\phi}. \tag{L.1}$$

The derivative with respect to θ is

$$\frac{dO_w}{d\theta} = \frac{-\sin 2\theta\left(\cos\left[2\left(\theta_f-\theta_i\right)\right]+3\cos\left[2\left(\theta_f+\theta_i\right)\right]-2\cos 2\phi\sin 2\theta_f\sin 2\theta_i\right)+4\cos 2\theta\cos\phi\sin\left[2\left(\theta_f+\theta_i\right)\right]}{8\sqrt{\left(\cos\theta\cos\left(\theta_f+\theta_i\right)+\cos\phi\sin\theta\sin\left(\theta_f+\theta_i\right)\right)^2+\sin^2\theta\sin^2\left(\theta_f-\theta_i\right)\sin^2\phi}}. \tag{L.2}$$

The Henrici departure of $\hat{A}$ is

$$df_n\left(\hat{A}\right) = \frac{1}{2}\sqrt{\left(3+2\cos 4\theta_f\cos^2\phi-\cos 2\phi\right)\sin^2\theta+4\cos^2\theta\sin^2 2\theta_f-2\cos\phi\sin 2\theta\sin 4\theta_f}. \tag{L.3}$$

The derivative of the normalized Henrici departure from normality of $\hat{A}$ is

$$\frac{df_n\left(\hat{A}\right)}{d\theta} = \frac{-4\cos 2\theta\cos\phi\sin 4\theta_f+\sin 2\theta\left(\cos 4\theta_f\left(3+\cos 2\phi\right)+2\sin^2\phi\right)}{4\sqrt{\left(3+2\cos 4\theta_f\cos^2\phi-\cos 2\phi\right)\sin^2\theta+4\cos^2\theta\sin^2 2\theta_f-2\cos\phi\sin 2\theta\sin 4\theta_f}}. \tag{L.4}$$

The Henrici departure of $\hat{A}'$ is

$$df_n\left(\hat{A}'\right) = \frac{1}{2}\sqrt{\left(3+2\cos 4\theta_i\cos^2\phi-\cos 2\phi\right)\sin^2\theta+4\cos^2\theta\sin^2 2\theta_i-2\cos\phi\sin 2\theta\sin 4\theta_i}\,. \tag{L.5}$$

The derivative of the normalized Henrici departure from normality of $\hat{A}'$ is

$$\frac{df_n\left(\hat{A}'\right)}{d\theta} = \frac{-4\cos 2\theta\cos\phi\sin 4\theta_i+\sin 2\theta\left(\cos 4\theta_i\left(3+\cos 2\phi\right)+2\sin^2\phi\right)}{4\sqrt{\left(3+2\cos 4\theta_i\cos^2\phi-\cos 2\phi\right)\sin^2\theta+4\cos^2\theta\sin^2 2\theta_i-2\cos\phi\sin 2\theta\sin 4\theta_i}}. \tag{L.6}$$

Appendix M

Expression of the jump operators for the degenerate ground state study

The expression of the jump operators $\hat{L}_q$ used in Eq. 8.34 are

$$\begin{aligned}
\hat{L}_0 &= \sqrt{\tfrac{2}{3}}\,|J_g,-\tfrac{1}{2}\rangle\langle J_e,-\tfrac{1}{2}| + \sqrt{\tfrac{2}{3}}\,|J_g,\tfrac{1}{2}\rangle\langle J_e,\tfrac{1}{2}|\,, \\
\hat{L}_- &= |J_g,-\tfrac{1}{2}\rangle\langle J_e,-\tfrac{3}{2}| + \tfrac{1}{\sqrt{3}}\,|J_g,\tfrac{1}{2}\rangle\langle J_e,-\tfrac{1}{2}|\,, \\
\hat{L}_+ &= \tfrac{1}{\sqrt{3}}\,|J_g,-\tfrac{1}{2}\rangle\langle J_e,\tfrac{1}{2}| + |J_g,\tfrac{1}{2}\rangle\langle J_e,\tfrac{3}{2}|\,.
\end{aligned} \tag{M.1}$$

Appendix N

Extracting the Weak value from the meter measurements in the Rabi model

To shorten the formulas, we denote the anti-commutator averages by $ACP = \langle \{ \hat{P}_I(t+\tau)), \hat{N}_I(t/2) \} \rangle_0$ and $ACQ = \langle \{ \hat{Q}_I(t+\tau)), \hat{N}_I(t/2) \} \rangle_0$; the commutator averages by $CP = \langle [\hat{P}_I(t+\tau)), \hat{N}_I(t/2)] \rangle_0$ and $CQ = \langle [\hat{Q}_I(t+\tau)), \hat{N}_I(t/2) \rangle_0$; the meter operators averages in the initial meter state by $N0 = \langle \hat{N}_I(t/2) \rangle_0$, $Q0 = \langle \hat{Q}_I(t+\tau) \rangle_0$, and $P0 = \langle \hat{P}_I(t+\tau) \rangle_0$. Then, the expression of the weak value in terms of the measurement results, namely the averages $\langle \hat{Q} \rangle_f$ and $\langle \hat{P} \rangle_f$ of the two meter quadratures, is

$$\mathrm{Re}A_{S,w} = \frac{i}{gt} \frac{ACQ\left(\langle \hat{P} \rangle_f - P0\right) - ACP\left(\langle \hat{Q} \rangle_f - Q0\right) + 2N0\left(P0 \langle \hat{Q} \rangle_f - \langle \hat{P} \rangle_f Q0\right)}{ACQ\,CP - ACP\,CQ + 2N0\left(CQ \langle \hat{P} \rangle_f - CP \langle \hat{Q} \rangle_f\right)}, \quad \text{(N.1)}$$

$$\mathrm{Im}A_{S,w} = -\frac{1}{gt} \frac{CQ\left(\langle \hat{P} \rangle_f - P0\right) - CP\left(\langle \hat{Q} \rangle_f - Q0\right)}{ACQ\,CP - ACP\,CQ + 2N0\left(CQ \langle \hat{P} \rangle_f - CP \langle \hat{Q} \rangle_f\right)}, \quad \text{(N.2)}$$

which is valid for an arbitrary initial meter state. These expressions are obtained by inverting Eq. 8.24 using both quadratures. In order to retrieve the weak value from the quadrature measurements, we see that it is preferable to choose an initial meter state verifying $N0 = 0$, as well as $P0 = Q0 = 0$.

Appendix O

Series expansion of the weak value (Markovian case)

We discuss here a few technical issues related to the series expansion of the weak value Eq. 8.76 in section 8.4.1. Let us consider the denominator of the two-level system weak value Eq. 8.54:

$$1+(f_{Ix}i_x+f_{Iy}i_y)\,e^{-\frac{1}{2}\gamma\tau}+f_{Iz}\,(1+i_z)\,e^{-\gamma\tau}-f_{Iz}. \tag{O.1}$$

Since we would like to exploit amplification, we require that the pre- and post-selected states are nearly orthogonal $\left|\left\langle\psi_{fI}\middle|\psi_i\right\rangle\right|^2=\varepsilon'^2$ for a small parameter ε'. In terms of Bloch vectors, we have thus $\vec{f}_I\cdot\vec{i}=-1+2\varepsilon'^2$. We can then eliminate the x and y components of the Bloch vectors in Eq. O.1:

$$1-e^{-\frac{1}{2}\gamma\tau}+2\varepsilon'^2e^{-\frac{1}{2}\gamma\tau}+f_{Iz}\left(e^{-\gamma\tau}-1\right)+f_{Iz}i_z\left(e^{-\gamma\tau}-e^{-\frac{1}{2}\gamma\tau}\right). \tag{O.2}$$

Now, a first-order series expansion in $\gamma\tau$ yields

$$2\varepsilon'^2+\frac{1}{2}\gamma\tau\left(1-2\varepsilon'^2-2f_{Iz}-f_{Iz}i_z\right)+\mathscr{O}\left(\gamma^2\tau^2\right). \tag{O.3}$$

This shows that we should be careful when making a series expansion of the full weak value with respect to $\gamma\tau$, as in Eq. 8.74, because we have to ensure that the first-order term in $\gamma\tau$ in the weak value denominator is smaller than the small term ε'^2 linked to the low post-selection probability. This would require $\gamma\tau\ll\varepsilon'^2$ in general (for example if choosing $f_{Iz}=0$), which could be an inconvenience as this imposes a bound on the amplification yield. However, if we ensure that the factor multiplying $\gamma\tau$ in Eq. O.3 is proportional to ε'^2, then the series expansion in $\gamma\tau$ is valid as long as $\gamma\tau\ll 1$, without constraining the amplification. Indeed, if we take the pre-and post-selected states with small components along x and y that are of the order of ε', then, to second-order in ε', we can write $f_{Iz}\approx 1-\alpha\varepsilon'^2$ and $i_z\approx -1+\beta\varepsilon'^2$ (exchanging the roles of f_{Iz} and i_z works as well), where α and β are unimportant proportionality constants related to the state normalization. This situation corresponds to pre- and post-selected states that nearly coincide with the basis states $|e\rangle$ and $|g\rangle$, respectively. Then, Eq. O.3 becomes

$$2\varepsilon'^2\left[1-\frac{1}{4}\gamma\tau\left(2-\alpha+\beta-\alpha\beta\varepsilon'^2\right)+\mathscr{O}\left(\gamma^2\tau^2\right)\right]. \tag{O.4}$$

The factorization of ε'^2 does not depend on the series expansion in $\gamma\tau$ and occurs also in Eq. O.2. With this choice of pre- and post-selected states, we obtain an amplification in $1/\varepsilon'$, while the series expansion to first order in $\gamma\tau$ is valid.

Appendix P

Computation of the weak value (non-Markovian case)

With the non-Markovian dynamics specified in section 8.4.2 with the dissipator $\mathscr{D}$ defined in Eq. 8.77 and the time-dependant dissipation rate given in Eq. 8.78, an arbitrary matrix $C = c_{gg}\,|g\rangle\langle g| + c_{ge}\,|g\rangle\langle e| + c_{eg}\,|e\rangle\langle g| + c_{ee}\,|e\rangle\langle e|$ becomes

$$e^{\mathscr{D}\tau}(C) = \begin{pmatrix} c_{ee}\,\Gamma^2 & c_{eg}\,\Gamma \\ c_{ge}\,\Gamma & c_{gg} + c_{ee}\left(1-\Gamma^2\right) \end{pmatrix}, \tag{P.1}$$

where

$$\Gamma = \frac{\sqrt{\lambda - \gamma_0 - \gamma_0 \cosh\left[\tau\sqrt{\lambda(\lambda-2\gamma_0)}\right]}}{\sqrt{\lambda-2\gamma_0}} \exp\left\{-\frac{\lambda\tau}{2} + \tanh^{-1}\left[\frac{\sqrt{\lambda}\tanh\left(\frac{1}{2}\sqrt{\lambda}\tau\sqrt{\lambda-2\gamma_0}\right)}{\sqrt{\lambda-2\gamma_0}}\right]\right\}. \tag{P.2}$$

This evolution should be compared with the Markovian result Eq. 8.52, which exhibits an exponential decay. Considering the similar structure of the solutions Eq. 8.52 and Eq. P.1, the two-level weak value in the non-Markovian case is identical to Eq. 8.54 and Eq. 8.58, if we redefine the attenuated post-selected Bloch vector Eq. 8.55 to

$$\vec{f}_I^{\,\gamma}(t+\tau) = \begin{pmatrix} f_{Ix}\,\Gamma \\ f_{Iy}\,\Gamma \\ f_{Iz}\,\Gamma^2 \end{pmatrix}. \tag{P.3}$$

Bibliography

[1] Amnon Yariv. *An introduction to theory and applications of quantum mechanics*. Courier Corporation, 2013.

[2] Timothy Jamieson, Raheleh Bakhshi, Daniela Petrova, Rachael Pocock, Mo Imani, and Alexander M Seifalian. Biological applications of quantum dots. *Biomaterials*, 28(31):4717–4732, 2007.

[3] Fabien Gatti, Benjamin Lasorne, Hans-Dieter Meyer, and André Nauts. *Applications of quantum dynamics in chemistry*, volume 98. Springer, 2017.

[4] Vladimir Bužek, Radoslav Derka, and Serge Massar. Optimal quantum clocks. *Physical Review Letters*, 82(10):2207, 1999.

[5] Rupak Biswas, Zhang Jiang, Kostya Kechezhi, Sergey Knysh, Salvatore Mandrà, Bryan O'Gorman, Alejandro Perdomo-Ortiz, Andre Petukhov, John Realpe-Gómez, Eleanor Rieffel, Davide Venturelli, Fedir Vasko, and Zhihui Wang. A NASA perspective on quantum computing: Opportunities and challenges. *Parallel Computing*, 64:81–98, 2017.

[6] Tim Sailer, Vincent Debierre, Zoltán Harman, Fabian Heiße, Charlotte König, Jonathan Morgner, Bingsheng Tu, Andrey V Volotka, Christoph H Keitel, Klaus Blaum, et al. Measurement of the bound-electron g-factor difference in coupled ions. *Nature*, 606(7914):479–483, 2022.

[7] Paul Busch, Pekka Lahti, Juha-Pekka Pellonpää, and Kari Ylinen. *Quantum measurement*, volume 23. Springer, 2016.

[8] Arthur Fine. Insolubility of the quantum measurement problem. *Physical Review D*, 2(12):2783, 1970.

[9] Anthony James Leggett. The quantum measurement problem. *Science*, 307(5711):871–872, 2005.

[10] Časlav Brukner. On the quantum measurement problem. In *Quantum [Un] Speakables II*, pages 95–117. Springer, 2017.

[11] Howard M Wiseman and Gerard J Milburn. *Quantum measurement and control*. Cambridge University Press, 2009.

[12] Pier A Mello. The von Neumann model of measurement in quantum mechanics. In *AIP Conference Proceedings*, volume 1575, pages 136–165. American Institute of Physics, 2014.

[13] Daniel E Platt. A modern analysis of the Stern–Gerlach experiment. *American Journal of Physics*, 60(4):306–308, 1992.

[14] IM Duck, Paul M Stevenson, and EC George Sudarshan. The sense in which a "weak measurement" of a spin-$1/2$ particle's spin component yields a value 100. *Physical Review D*, 40(6):2112, 1989.

[15] Yakir Aharonov, Eliahu Cohen, and Avshalom C Elitzur. Foundations and applications of weak quantum measurements. *Physical Review A*, 89(5):052105, 2014.

[16] Hong-Wei Li, Yong-Sheng Zhang, Xue-Bi An, Zheng-Fu Han, and Guang-Can Guo. Three-observer classical dimension witness violation with weak measurement. *Communications Physics*, 1(1):10, 2018.

[17] Yakir Aharonov, David Z Albert, and Lev Vaidman. How the result of a measurement of a component of the spin of a spin-1/2 particle can turn out to be 100. *Physical Review Letters*, 60(14):1351, 1988.

[18] Mirko Cormann and Yves Caudano. Geometric description of modular and weak values in discrete quantum systems using the Majorana representation. *Journal of Physics A: Mathematical and Theoretical*, 50(30):305302, 2017.

[19] Lorena Ballesteros Ferraz, Dominique L Lambert, and Yves Caudano. Geometrical interpretation of the argument of weak values of general observables in N-level quantum systems. *Quantum Science and Technology*, 7(4):045028, 2022.

[20] Lorena Ballesteros Ferraz, Dominique L Lambert, and Yves Caudano. Geometrical interpretation of the argument of Bargmann invariants and weak values in N-level quantum systems applying the Majorana symmetric representation. *arXiv preprint arXiv:2211.05692*, 2022.

[21] Lorena Ballesteros Ferraz, Riccardo Muolo, Yves Caudano, and Timoteo Carletti. Revisiting weak values through non-normality. *arXiv preprint arXiv:2306.01392*, 2023.

[22] Lorena Ballesteros Ferraz, John Martin, and Yves Caudano. On the relevance of weak measurements in dissipative systems. *arXiv preprint arXiv:2308.00722*, 2023.

[23] Eugene P Wigner. The problem of measurement. *American Journal of Physics*, 31(1):6–15, 1963.

[24] Philippe Grangier, Juan Ariel Levenson, and Jean-Philippe Poizat. Quantum non-demolition measurements in optics. *Nature*, 396(6711):537–542, 1998.

[25] John von Newman. *Mathematical Foundations of Quantum Mechanics*. Princenton University, 1955.

[26] Bengt EY Svensson. Pedagogical review of quantum measurement theory with an emphasis on weak measurements. *Quanta*, 2(1):18–49, 2013.

[27] Howard M Wiseman. Weak values, quantum trajectories, and the cavity-QED experiment on wave-particle correlation. *Physical Review A*, 65(3):032111, 2002.

[28] Francisco De Zela. Role of weak values in strong measurements. *Physical Review A*, 105(4):042202, 2022.

[29] John G Kirkwood. Quantum statistics of almost classical assemblies. *Physical Review Letters*, 44(1):31, 1933.

[30] Stephan De Bièvre. Complete incompatibility, support uncertainty, and kirkwood-dirac nonclassicality. *Physical Review Letters*, 127(19):190404, 2021.

[31] Matthew F Pusey. Anomalous weak values are proofs of contextuality. *Physical Review Letters*, 113(20):200401, 2014.

[32] Ravi Kunjwal, Matteo Lostaglio, and Matthew F Pusey. Anomalous weak values and contextuality: robustness, tightness, and imaginary parts. *Physical Review A*, 100(4):042116, 2019.

[33] Valentine Bargmann. Note on Wigner's Theorem on Symmetry Operations. *Journal of Mathematical Physics*, 5(7):862–868, 1964.

[34] Eqab M Rabei, Arvind, Narasimhaiengar Mukunda, and Rajiah Simon. Bargmann invariants and geometric phases: A generalized connection. *Physical Review A*, 60(5):3397, 1999.

[35] Michał Oszmaniec, Daniel J Brod, and Ernesto F Galvão. Measuring relational information between quantum states, and applications. *arXiv preprint arXiv:2109.10006*, 2021.

[36] Yakir Aharonov and Lev Vaidman. Properties of a quantum system during the time interval between two measurements. *Physical Review A*, 41(1):11, 1990.

[37] Yakir Aharonov, Sandu Popescu, and Jeff Tollaksen. A time-symmetric formulation of quantum mechanics. *Physics Today*, 63(11), 2010.

[38] Benni Reznik and Yakir Aharonov. Time-symmetric formulation of quantum mechanics. *Physical Review A*, 52(4):2538, 1995.

[39] Bengt EY Svensson. What is a quantum-mechanical "weak value" the value of? *Foundations of Physics*, 43:1193–1205, 2013.

[40] Bengt EY Svensson. Quantum weak values and logic: an uneasy couple. *Foundations of Physics*, 47:430–452, 2017.

[41] Justin Dressel and Andrew N Jordan. Significance of the imaginary part of the weak value. *Physical Review A*, 85(1):012107, 2012.

[42] Justin Dressel, Mehul Malik, Filippo M Miatto, Andrew N Jordan, and Robert W Boyd. Understanding quantum weak values: Basics and applications. *Reviews of Modern Physics*, 86(1):307–316, 2014.

[43] Lijian Zhang, Animesh Datta, and Ian A Walmsley. Precision metrology using weak measurements. *Physical Review Letters*, 114(21):210801, 2015.

[44] Liang Xu, Zexuan Liu, Animesh Datta, George C Knee, Jeff S Lundeen, Yan-Qing Lu, and Lijian Zhang. Approaching quantum-limited metrology with imperfect detectors by using weak-value amplification. *Physical Review Letters*, 125(8):080501, 2020.

[45] Xiao-Ye Xu, Yaron Kedem, Kai Sun, Lev Vaidman, Chuan-Feng Li, and Guang-Can Guo. Phase estimation with weak measurement using a white light source. *Physical Review Letters*, 111(3):033604, 2013.

[46] Matin Hallaji, Amir Feizpour, Greg Dmochowski, Josiah Sinclair, and Aephraim M Steinberg. Weak-value amplification of the nonlinear effect of a single photon. *Nature Physics*, 13:540–544, 2017.

[47] Xiaodong Qiu, Linguo Xie, Xiong Liu, Lan Luo, Zhiyou Zhang, and Jinglei Du. Estimation of optical rotation of chiral molecules with weak measurements. *Organic Letters*, 41(17):4032–4035, 2016.

[48] Dongmei Li, Zhiyuan Shen, Yonghong He, Yilong Zhang, Zhenling Chen, and Hui Ma. Application of quantum weak measurement for glucose concentration detection. *Applied Optics*, 55(7):1697–1702, 2016.

[49] Dongmei Li, Tian Guan, Yonghong He, Fang Liu, Anping Yang, Qinghua He, Zhiyuan Shen, and Meiguo Xin. A chiral sensor based on weak measurement for the determination of Proline enantiomers in diverse measuring circumstances. *Materials Today Bio*, 110:103–109, 2018.

[50] P Ben Dixon, David J Starling, Andrew N Jordan, and John C Howell. Ultrasensitive beam deflection measurement via interferometric weak value amplification. *Physical Review Letters*, 102(17):173601, 2009.

[51] Omar S Magaña-Loaiza, Mohammad Mirhosseini, Brandon Rodenburg, and Robert W Boyd. Amplification of angular rotations using weak measurements. *Physical Review Letters*, 112(20):200401, 2014.

[52] Jérémie Harris, Robert W Boyd, and Jeff S Lundeen. Weak value amplification can outperform conventional measurement in the presence of detector saturation. *Physical Review Letters*, 118(7):070802, 2017.

[53] Andrew N Jordan, Julián Martínez-Rincón, and John C Howell. Technical advantages for weak-value amplification: When less is more. *Physical Review X*, 4(1):011031, 2014.

[54] Gaurav Jayaswal, Giampaolo Mistura, and Michele Merano. Weak measurement of the Goos–Hänchen shift. *Optics Letters*, 38(8):1232–1234, 2013.

[55] Mark R Dennis and Jörg B Götte. The analogy between optical beam shifts and quantum weak measurements. *New Journal os Physics*, 14:073013, 2012.

[56] Xiaohui Ling, Xinxing Zhou, Kun Huang, Yachao Liu, Cheng-Wei Qiu, Hailu Luo, and Shuangchun Wen. Recent advances in the spin Hall effect of light. *Reports on Progress in Physics*, 80(6):066401, 2017.

[57] Onur Hosten and Paul Kwiat. Observation of the spin Hall effect of light via weak measurements. *Science*, 319(5864):787–790, 2008.

[58] Sacha Kocsis, Boris Braverman, Sylvain Ravets, Martin J Stevens, Richard P Mirin, L Krister Shalm, and Aephraim M Steinberg. Observing the average trajectories of single photons in a two-slit interferometer. *Science*, 332(6034):1170–1173, 2011.

[59] Konstantin Y Bliokh, Aleksandr Y Bekshaev, Abraham G Kofman, and Franco Nori. Photon trajectories, anomalous velocities and weak measurements: a classical interpretation. *New Journal of Physics*, 15:073022, 2013.

[60] Alexandre Matzkin. Observing trajectories with weak measurements in quantum systems in the semiclassical regime. *Physical Review Letters*, 109(15):150407, 2012.

[61] Kevin J Resch, Jeff S Lundeen, and Aephraim M Steinberg. Experimental realization of the quantum box problem. *Physics Letters A*, 324(2–3):125–131, 2004.

[62] Kazuhiro Yokota, Takashi Yamamoto, Masato Koashi, and Nobuyuki Imoto. Direct observation of Hardy's paradox by joint weak measurement with an entangled photon pair. *New Journal of Physics*, 11:033011, 2009.

[63] Tobias Denkmayr, Hermann Geppert, Stephan Sponar, Hartmut Lemmel, Alexandre Matzkin, Jeff Tollaksen, and Yuji Hasegawa. Observation of a quantum Cheshire Cat in a matter-wave interferometer experiment. *Nature Communications*, 5(1):1–7, 2014.

[64] Ming-Cheng Chen, Chang Liu, Yi-Han Luo, He-Liang Huang, Bi-Ying Wang, Xi-Lin Wang, Li Li, Nai-Le Liu, Chao-Yang Lu, and Jian-Wei Pan. Experimental demonstration of quantum pigeonhole paradox. *Proceedings of the National Academy of Sciences*, 116(5):1549–1552, 2019.

[65] Tamar Ravon and Lev Vaidman. The three-box paradox revisited. *Journal of Physics A: Mathematical and Theoretical*, 40(11):2873, 2007.

[66] Mehul Malik, Mohammad Mirhosseini, Martin P J Lavery, Jonathan Leach, Miles J Padgett, and Robert W Boyd. Direct measurement of a 27-dimensional orbital-angular-momentum state vector. *Nature Communications*, 5:3115, 2014.

[67] Shengjun Wu. State tomography via weak measurements. *Scientific Reports*, 3:1193, 2013.

[68] Jeff S Lundeen, Brandon Sutherland, Aabid Patel, Corey Stewart, and Charles Bamber. Direct measurement of the quantum wavefunction. *Nature*, 474:188–191, 2011.

[69] Arun Kumar Pati, Uttam Singh, and Urbasi Sinha. Measuring non-Hermitian operators via weak values. *Physical Review A*, 92(5):052120, 2015.

[70] Zafer Gedik. Weak measurement of Berry's phase. *Journal of Physics A: Mathematical and Theoretical*, 54(40):405301, 2021.

[71] Max F Riedel, Daniele Binosi, Rob Thew, and Tommaso Calarco. The European quantum technologies flagship programme. *Quantum Science and Technology*, 2(3):030501, 2017.

[72] Yoshihisa Yamamoto, Masahide Sasaki, and Hiroki Takesue. Quantum information science and technology in Japan. *Quantum Science and Technology*, 4(2):020502, 2019.

[73] Michael G Raymer and Christopher Monroe. The US national quantum initiative. *Quantum Science and Technology*, 4(2):020504, 2019.

[74] Christian L Degen, Friedemann Reinhard, and Paola Cappellaro. Quantum sensing. *Reviews of Modern Physics*, 89(3):035002, 2017.

[75] Miguel Herrero-Collantes and Juan Carlos Garcia-Escartin. Quantum random number generators. *Reviews of Modern Physics*, 89(1):015004, 2017.

[76] Andrew D Ludlow, Martin M Boyd, Jun Ye, Ekkehard Peik, and Piet O Schmidt. Optical atomic clocks. *Reviews of Modern Physics*, 87(2):637, 2015.

[77] N David Mermin. *Quantum computer science: an introduction*. Cambridge University Press, 2007.

[78] F Tito Arecchi, Eric Courtens, Robert Gilmore, and Harry Thomas. Atomic coherent states in quantum optics. *Physical Review A*, 6(6):2211, 1972.

[79] Sisi Zhou and Liang Jiang. Optimal approximate quantum error correction for quantum metrology. *Physical Review Research*, 2(1):013235, 2020.

[80] Sandeep K Goyal, B Neethi Simon, Rajeev Singh, and Sudhavathani Simon. Geometry of the generalized Bloch sphere for qutrits. *Journal of Physics A: Mathematical and Theoretical*, 49(16):165203, 2016.

[81] Michael A Nielsen and Isaac L Chuang. *Quantum computation and quantum information*. Cambridge university press, 2010.

[82] Simon J Devitt, William J Munro, and Kae Nemoto. Quantum error correction for beginners. *Reports on Progress in Physics*, 76(7):076001, 2013.

[83] Daniel A Lidar and Todd A Brun. *Quantum error correction*. Cambridge University Press, 2013.

[84] Aravind, KS Mallesh, and Narasimhaiengar Mukunda. A generalized Pancharatnam geometric phase formula for three-level quantum systems. *Journal of Physics A: Mathematical and General*, 30(7):2417, 1997.

[85] Gaurav Khanna, Saibal Mukhopadhyay, Rajiah Simon, and Narasimhaiengar Mukunda. Geometric Phases for SU(3) Representations and Three Level Quantum Systems. *Annals of Physics*, 253(1):55–82, 1997.

[86] Istok P Mendaš. The classification of three-parameter density matrices for a qutrit. *Journal of Physics A: Mathematical and General*, 39(36):11313, 2006.

[87] Sandeep K Goyal, B Neethi Simon, Rajeev Singh, and Sudhavathani Simon. Geometry of the generalized Bloch sphere for qutrits. *Journal of Physics A: Mathematical and Theoretical*, 49:165203, 2016.

[88] Mark Byrd. Differential geometry on SU(3) with applications to three state systems. *Journal of the Mechanics and Physics of Solids*, 39(11):6125–6136, 1998.

[89] Lech Jakóbczyk and M Siennicki. Geometry of Bloch vectors in two-qubit system. *Annals of Physics*, 286(6):383–390, 2001.

[90] Mark S Byrd and Navin Khaneja. Characterization of the positivity of the density matrix in terms of the coherence vector representation. *Physical Review A*, 68(6):062322, 2003.

[91] Ansgar Graf and Frédéric Piéchon. Berry curvature and quantum metric in N-band systems: An eigenprojector approach. *Physical Review B*, 104(8):085114, 2021.

[92] Ingemar Bengtsson and Karol Życzkowski. *Geometry of quantum states: an introduction to quantum entanglement*. Cambridge University Press, 2017.

[93] Usha A R Devi, Sudha, and Attipat K Rajagopal. Majorana representation of symmetric multiqubit states. *Quantum Information Processing*, 11(3):685–710, 2012.

[94] Michael V Berry. Quantal phase factors accompanying adiabatic changes. *Proceedings of the Royal Society of London. A. Mathematical and Physical Sciences*, 392(1802):45–57, 1984.

[95] Shivaramakrishnan Pancharatnam. Generalized theory of interference and its applications. In *Proceedings of the Indian Academy of Sciences-Section A*, volume 44, pages 398–417. Springer, 1956.

[96] Karin Everschor-Sitte and Matthias Sitte. Real-space Berry phases: Skyrmion soccer. *Journal of Applied Physics*, 115(17):172602, 2014.

[97] Joseph Samuel and Rajendra Bhandari. General setting for Berry's phase. *Physical Review Letters*, 60(23):2339, 1988.

[98] Eliahu Cohen, Hugo Larocque, Frédéric Bouchard, Farshad Nejadsattari, Yuval Gefen, and Ebrahim Karimi. Geometric phase from Aharonov–Bohm to Pancharatnam–Berry and beyond. *Nature Reviews Physics*, 1(7):437–449, 2019.

[99] Shuhei Tamate, Kazuhisa Ogawa, and Masao Kitano. Bloch-sphere representation of three-vertex geometric phases. *Physical Review A*, 84(5):052114, 2011.

[100] Carl L Siegel. *Symplectic geometry*. Elsevier, 2014.

[101] Richard Jozsa. Complex weak values in quantum measurement. *Physical Review A*, 76:044103, 2007.

[102] Erik Sjöqvist. Geometric phase in weak measurements. *Physics Letters A*, 359(3):187–189, 2006.

[103] S Tamate, H Kobayashi, T Nakanishi, K Sugiyama, and M Kitano. Geometrical aspects of weak measurements and quantum erasers. *New Journal of Physics*, 11:093025, 2009.

[104] Le Bin Ho and Nobuyuki Imoto. Various pointer states approaches to polar modular values. *Journal of the Mechanics and Physics of Solids*, 59(4):042107, 2018.

[105] Chandran T Samlan and Nirmal K Viswanathan. Geometric phase topology in weak measurement. *Journal of Optics*, 19(12):125401, 2017.

[106] Mandira Pal, Sudipta Saha, B S Athira, Subhasish Dutta Gupta, and Nirmalya Ghosh. Experimental probe of weak-value amplification and geometric phase through the complex zeros of the response function. *Physical Review A*, 99(3):032123, 2019.

[107] Young-Wook Cho, Yosep Kim, Yeon-Ho Choi, Yong-Su Kim, Sang-Wook Han, Sang-Yun Lee, Sung Moon, and Yoon-Ho Kim. Emergence of the geometric phase from quantum measurement back-action. *Nature Physics*, 15:665–671, 2019.

[108] Narasimhaiengar Mukunda and Rajiah Simon. Quantum Kinematic Approach to the Geometric phase. I. General Formalism. *Annals of Physics*, 228(2):205–268, 1993.

[109] Alan J Macfarlane, Anthony Sudbery, and PH Weisz. On Gell-Mann's λ-matrices, d- and f-tensors, octets, and parametrizations of SU(3). *Communications in Mathematical Physics*, 11(1):77–90, 1968.

[110] Yago P Porto-Silva and M C de Oliveira. Theory of neutrino detection: flavor oscillations and weak values. *The European Physical Journal C*, 81:330, 2021.

[111] Mirko Cormann, Mathilde Remy, Branko Kolaric, and Yves Caudano. Revealing geometric phases in modular and weak values with a quantum eraser. *Physical Review A*, 93(4):042124, 2016.

[112] Asher Peres. Two simple proofs of the Kochen-Specker theorem. *Journal of Physics A: Mathematical and General*, 24:L175–L178, 1991.

[113] Juan Maldacena, Stephen H. Shenker, and Douglas Stanford. A bound on chaos. *Journal of High Energy Physics*, 2016:106, 2016.

[114] Jeff S Lundeen and Kevin J Resch. Practical measurement of joint weak values and their connection to the annihilation operator. *Physics Letters A*, 334:337–344, 2005.

[115] Daniel R. Solli, Collin F McCormick, Raymond Y Chiao, Sandu Popescu, and Jandir M Hickmann. Fast light, slow light, and phase singularities: a connection to generalized weak values. *Physical Review Letters*, 92:043601, 2004.

[116] Michael JW Hall. Prior information: How to circumvent the standard joint-measurement uncertainty relation. *Physical Review A*, 69(5):052113, 2004.

[117] Justin Dressel. Weak values as interference phenomena. *Physical Review A*, 91(3):032116, 2015.

[118] Holger F Hofmann. Uncertainty limits for quantum metrology obtained from the statistics of weak measurements. *Physical Review A*, 83(2):022106, 2011.

[119] Holger F Hofmann. Direct evaluation of measurement uncertainties by feedback compensation of decoherence. *Physical Review Research*, 3:L012011, 2021.

[120] Ettore Majorana. Atomi orientati in campo magnetico variabile. *Il Nuovo Cimento (1924-1942)*, 9(2):43–50, 1932.

[121] J H Hannay. The Berry phase for spin in the Majorana representation. *Journal of Physics A: Mathematical and General*, 31(2):L53, 1998.

[122] Konstantin Y Bliokh, Miguel A Alonso, and Mark R Dennis. Geometric phases in 2D and 3D polarized fields: geometrical, dynamical, and topological aspects. *Reports on Progress in Physics*, 82(12):122401, 2019.

[123] Damian JH Markham. Entanglement and symmetry in permutation-symmetric states. *Physical Review A*, 83(4):042332, 2011.

[124] Jason Zimba. Anticoherent spin states via the Majorana representation. *Electronic Journal of Theoretical Physics*, 3(10):143–156, 2006.

[125] Diego Morachis Galindo and Jesús A Maytorena. Entangling power of symmetric two-qubit quantum gates and three-level operations. *Physical Review A*, 105(1):012601, 2022.

[126] KS Akhilesh, BG Divyamani, AR Usha Devi, and KS Mallesh. Spin squeezing in symmetric multiqubit states with two non-orthogonal Majorana spinors. *Quantum Information Processing*, 18(5):1–15, 2019.

[127] Felix Bloch and Isidor Isaac Rabi. Atoms in variable magnetic fields. *Reviews of Modern Physics*, 17(2-3):237, 1945.

[128] Reinhold A Bertlmann and Philipp Krammer. Bloch vectors for qudits. *Journal of Physics A: Mathematical and Theoretical*, 41(23):235303, 2008.

[129] Anton V Andreev, O A Shoutova, S M Trushin, and S Yu Stremoukhov. 3D Stokes parameters for vector focal fields. *Journal of the Optical Society of America B: Optical Physics*, 39(7):1775–1782, 2022.

[130] Antonio Acin, Thomas Durt, Nicolas Gisin, and José Ignacio Latorre. Quantum nonlocality in two three-level systems. *Physical Review A*, 65(5):052325, 2002.

[131] Vikash Mittal, K S Akhilesh, and Sandeep K Goyal. Geometric decomposition of geodesics and null-phase curves using Majorana star representation. *Physical Review A*, 105(5):052219, 2022.

[132] Robert Eisberg and Robert Resnick. *Quantum physics of atoms, molecules, solids, nuclei, and particles*. 1985.

[133] Sinem Binicioğlu, M Ali Can, Alexander A Klyachko, and Alexander S Shumovsky. Entanglement of a single spin-1 object: an example of ubiquitous entanglement. *Foundations of Physics*, 37(8):1253–1277, 2007.

[134] Alessandro Romito, Yuval Gefen, and Yaroslav M Blanter. Weak values of electron spin in a double quantum dot. *Physical Review Letters*, 100(5):056801, 2008.

[135] Steven J Van Enk. Single-particle entanglement. *Physical Review A*, 72(6):064306, 2005.

[136] Lan Luo, Xiaodong Qiu, Linguo Xie, Xiong Liu, Zhaoxue Li, Zhiyou Zhang, and Jinglei Du. Precision improvement of surface plasmon resonance sensors based on weak-value amplification. *Optics Express*, 25(18):21107–21114, 2017.

[137] Yakir Aharonov, Alonso Botero, Sandu Popescu, Benni Reznik, and Jeff Tollaksen. Revisiting Hardy's paradox: counterfactual statements, real measurements, entanglement and weak values. *Physics Letters A*, 301(3-4):130–138, 2002.

[138] Jeff S Lundeen and Aephraim M Steinberg. Experimental joint weak measurement on a photon pair as a probe of Hardy's paradox. *Physical Review Letters*, 102(2):020404, 2009.

[139] Alexandre Matzkin and Alok K Pan. Three-box paradox and 'Cheshire cat grin': the case of spin-1 atoms. *Journal of Physics A: Mathematical and Theoretical*, 46(31):315307, 2013.

[140] Aqsa Gul, Muhammad Imran, Muhammad Haroon Saeed, Rameez ul Islam, and Manzoor Ikram. Implementation of the quantum three box paradox through atomic internal states. *Optics Communications*, page 128587, 2022.

[141] L Nick Trefethen and Mark Embree. *Spectra and Pseudospectra: The Behavior of Nonnormal Matrices and Operators*. Princeton Univiversity Press, 2005.

[142] Riccardo Muolo, Timoteo Carletti, James P Gleeson, and Malbor Asllani. Synchronization dynamics in non-normal networks: the trade-off for optimality. *Entropy*, 23:36, 2021.

[143] Robert S MacKay, Steven Johnson, and B Sansom. How directed is a directed network? *Royal Society Open Science*, 7, 2020.

[144] Julia D O'Brien, K A Oliveira, James P Gleeson, and Malbor Asllani. Hierarchical route to the emergence of leader nodes in real-world networks. *Physical Review Research*, 3:023117, 2021.

[145] Malbor Asllani, Renaud Lambiotte, and Timoteo Carletti. Structure and dynamical behavior of non-normal networks. *Science Advances*, 4:eaau9403, 2018.

[146] Nimrod Moiseyev. *Non-Hermitian quantum mechanics*. Cambridge University Press, 2011.

[147] L Reichel and L Nick Trefethen. Eigenvalues and Pseudo-eigenvalues of Toeplitz Matrices. *Linear Algebra and its Applications*, pages 162–164, 1992.

[148] L Nick Trefethen, Anne E Trefethen, S C Reddy, and Tobin A Driscoll. Hydrodynamic stability without eigenvalues. *Science*, 261:578–584, 1993.

[149] Malbor Asllani and Timoteo Carletti. Topological resilience in non-normal networked systems. *Physical Review E*, 97, 2018.

[150] Michael G Neubert and Hal Caswell. Alternatives to resilience for measuring the responses of ecological systems to perturbations. *Mathematical Biosciences*, 78:653–665, 1997.

[151] Michael G Neubert, Hal Caswell, and James D Murray. Transient dynamics and pattern formation: Reactivity is necessary for turing instabilities. *Mathematical Biosciences*, 175(1):1–11, 2002.

[152] Riccardo Muolo, Malbor Asllani, Duccio Fanelli, Philip K Maini, and Timoteo Carletti. Patterns of non-normality in networked systems. *Journal of Theoretical Biology*, 480:81, 2019.

[153] Zachary G Nicolaou, Takashi Nishikawa, Schuyler B Nicholson, J R Green, and Adilson E Motter. Non-normality and non-monotonic dynamics in complex reaction networks. *Physical Review Research*, 2:043059, 2020.

[154] Dmitri Sokolovski. The meaning of "anomalous weak values" in quantum and classical theories. *Physics Letters A*, 379(16-17):1097–1101, 2015.

[155] Asger C Ipsen. Anomalous weak values are caused by disturbance. *Foundations of Physics*, 52(1):1–18, 2022.

[156] Nathan D Lemke, Andrew D Ludlow, ZW Barber, Tara M Fortier, Scott A Diddams, Yanyi Jiang, Steven R Jefferts, Thomas P Heavner, Thomas E Parker, and Christopher W Oates. Spin-1/2 Optical Lattice Clock. *Physical Review Letters*, 103(6):063001, 2009.

[157] Sebastian Eggert, Ian Affleck, and Minoru Takahashi. Susceptibility of the spin 1/2 Heisenberg antiferromagnetic chain. *Physical Review Letters*, 73(2):332, 1994.

[158] Mattias Marklund and Gert Brodin. Dynamics of spin-1/2 quantum plasmas. *Physical Review Letters*, 98(2):025001, 2007.

[159] Mihail Popescu. Control of affine nonlinear systems with nilpotent structure in singular problems. *Journal of optimization theory and applications*, 124:455–466, 2005.

[160] T Elmhirst and Marty Golubitsky. Nilpotent Hopf Bifurcations in Coupled Cell Systems. *SIAM J. APPLIED DYNAMICAL SYSTEMS*, 5:205–251, 2006.

[161] Geng-Li Zhang, Di Liu, and Man-Hong Yung. Observation of exceptional point in a PT broken non-Hermitian system simulated using a quantum circuit. *Scientific Reports*, 11:13795, 2021.

[162] Robert W Spekkens. Negativity and contextuality are equivalent notions of nonclassicality. *Physical Review Letters*, 101(2):020401, 2008.

[163] Mark Howard, Joel Wallman, Victor Veitch, and Joseph Emerson. Contextuality supplies the 'magic'for quantum computation. *Nature*, 510(7505):351–355, 2014.

[164] Juan Bermejo-Vega, Nicolas Delfosse, Dan E Browne, Cihan Okay, and Robert Raussendorf. Contextuality as a resource for models of quantum computation with qubits. *Physical Review Letters*, 119(12):120505, 2017.

[165] János Bognár. *Indefinite inner product spaces*, volume 78. Springer Science & Business Media, 2012.

[166] T Ya Azizov and Iosif Semenovich Iokhvidov. *Linear operators in spaces with an indefinite metric*. John Wiley & Sons, Incorporated, 1989.

[167] Rafael Wagner and Ernesto F Galvão. Anomalous weak values require coherence. *arXiv preprint arXiv:2303.08700*, 2023.

[168] Newton da Costa and Christian De Ronde. The paraconsistent logic of quantum superpositions. *Foundations of Physics*, 43:845–858, 2013.

[169] Majid Shahn. *Mathematical structures of the universe.*, chapter The self-representing Univers, page 357–387. Copernicus Center Press, Kraków, 2014.

[170] Arkadiusz Jadczyk. Geometry of indefinite metric spaces. *Reports on Mathematical Physics*, 2:263–276, 1971.

[171] Arkadiusz Jadczyk. Quantum logic and indefinite metric spaces. *Reports on Mathematical Physics*, 1(4), 1971.

[172] Nicolas Brunner and Christoph Simon. Measuring small longitudinal phase shifts: weak measurements or standard interferometry? *Physical Review Letters*, 105(1):010405, 2010.

[173] Heinz-Peter Breuer and Francesco Petruccione. *The theory of open quantum systems*. Oxford University Press, 2002.

[174] Inés De Vega and Daniel Alonso. Dynamics of non-Markovian open quantum systems. *Reviews of Modern Physics*, 89(1):015001, 2017.

[175] Angel Rivas and Susana F Huelga. *Open quantum systems*, volume 10. Springer, 2012.

[176] Ingrid Rotter and Jonathan P Bird. A review of progress in the physics of open quantum systems: theory and experiment. *Reports on Progress in Physics*, 78(11):114001, 2015.

[177] Marco Merkli. Dynamics of Open Quantum Systems II, Markovian Approximation. *Quantum*, 6:616, 2022.

[178] George C Knee, G Andrew D Briggs, Simon C Benjamin, and Erik M Gauger. Quantum sensors based on weak-value amplification cannot overcome decoherence. *Physical Review A*, 87(1):012115, 2013.

[179] Yutaka Shikano and Akio Hosoya. Weak values with decoherence. *Journal of Physics A: Mathematical and Theoretical*, 43(2):025304, 2009.

[180] Masashi Ban. Weak values influenced by environment. *Journal of Modern Physics*, 4(11):1–8, 2013.

[181] Masahiro Abe and Masashi Ban. Decoherence of weak values in a pure dephasing process. *Quantum Studies: Mathematics and Foundations*, 2(1):23–36, 2015.

[182] Masashi Ban. Weak measurement on a quantum system in contact with a thermal reservoir: projection operator method. *Quantum Studies: Mathematics and Foundations*, 4(4):339–355, 2017.

[183] Masahiro Abe and Masashi Ban. Decoherence of a weak value influenced by a non-Markovian environment. *Quantum Studies: Mathematics and Foundations*, 3(4):313–326, 2016.

[184] Daniel Manzano. A short introduction to the Lindblad master equation. *AIP Advances*, 10:025106, 2020.

[185] Robert R Schaller. Moore's law: past, present and future. *IEEE Spectrum*, 34(6):52–59, 1997.

[186] Lov K Grover. A fast quantum mechanical algorithm for database search. In *Proceedings of the twenty-eighth annual ACM symposium on Theory of computing*, pages 212–219. Association for Computing Machinery, 1996.

[187] Peter W Shor. Algorithms for quantum computation: discrete logarithms and factoring. In *Proceedings 35th annual symposium on foundations of computer science*, pages 124–134. Institute of Electrical and Electronics Engineers, 1994.

[188] David Deutsch and Richard Jozsa. Rapid solution of problems by quantum computation. *Proceedings of the Royal Society of London. Series A: Mathematical and Physical Sciences*, 439(1907):553–558, 1992.

[189] Richard Cleve, Artur Ekert, Chiara Macchiavello, and Michele Mosca. Quantum algorithms revisited. *Proceedings of the Royal Society of London. Series A: Mathematical, Physical and Engineering Sciences*, 454(1969):339–354, 1998.

[190] Yaron Kedem and Lev Vaidman. Modular values and weak values of quantum observables. *Physical Review Letters*, 105(23):230401, 2010.

[191] Arun Kumar Pati. Super quantum search algorithm with weak value amplification and post-selection. *arXiv preprint arXiv:1910.12390*, 2019.

[192] Elham Kashefi, Adrian Kent, Vlatko Vedral, and Konrad Banaszek. Comparison of quantum oracles. *Physical Review A*, 65(5):050304, 2002.

[193] Vikram Menon and Ayan Chattopadhyay. Quantum pattern matching oracle construction. *Pramana*, 95(1):1–3, 2021.

[194] Gilles Brassard, Peter Høyer, and Alain Tapp. Quantum counting. In *International Colloquium on Automata, Languages, and Programming*, pages 820–831. Springer, 1998.

[195] A Yu Kitaev. Quantum measurements and the Abelian stabilizer problem. *arXiv preprint quant-ph/9511026*, 1995.

[196] Gen Kimura. The Bloch vector for n-level systems. *Physics Letters A*, 314(5–6):339–349, 2003.

[197] Reinhold A Bertlmann and Philipp Krammer. Bloch vectors for qudits. *Journal of Physics A: Mathematical and Theoretical*, 41:235303, 2008.